1-1-1979

Small angle x-ray scattering studies of ionomers.

Edward J. Roche
University of Massachusetts Amherst

SMALL ANGLE X-RAY SCATTERING STUDIES OF IONOMERS

A Dissertation Presented

By

EDWARD J. ROCHE

Submitted to the Graduate School of the
University of Massachusetts in partial fulfillment
of the requirements for the degree of

DOCTOR OF PHILOSOPHY

February 1979

Polymer Science and Engineering Department

SMALL ANGLE X-RAY SCATTERING

STUDIES OF IONOMERS

A Dissertation Presented

By

EDWARD J. ROCHE

Approved as to style and content by:

Richard S. Stein
Chairperson of Committee

Frank E. Karasz, Member

William J. MacKnight, Member

Otto F. Vogl, Member

William J. MacKnight, Head
Polymer Science and Engineering

Dedicated to my parents

for all of their love and support

given to me over the last twenty-six years.

ACKNOWLEDGMENTS

The author wishes to express much appreciation to Dr. R.S. Stein for his guidance and many helpful ideas provided during the course of the work.

An expression of gratitude is extended to Dr. William J. MacKnight for introducing me to many of the interesting problems of ionomer morphology and also for his knowledge and encouragement.

Thanks is given to Dr. Adi Eisenberg for providing samples used in the studies and also for several very helpful discussions.

Acknowledgment and gratitude is extended to Drs. Frank E. Karasz and Otto F. Vogl for their knowledge and interest in the completion of this project.

Special appreciation is expressed to Drs. A. Wasiak, F.P. Warner, S. Baczek and students Thomas P. Russell and Jeffrey T. Koberstein for their help in SAXS data collection and analysis and also for their friendship.

The technical assistance of D.A. Keedy and Joseph DeCaro is acknowledged.

Appreciation is given to Dr. R.W. Hendricks and his staff for the use of their SAXS facility at the Oak Ridge National Laboratories.

Thanks is given to Dr. C. Azuma for synthesizing the samples discussed in Chapter III.

This work was supported in part by grants from the National Science Foundation and the Materials Research Laboratory at the University of Massachusetts.

ABSTRACT

Small Angle X-ray Scattering
Studies of Ionomers

(February 1979)

Edward J. Roche

B.S., Case Western Reserve University
M.S., University of Massachusetts
Ph.D., University of Massachusetts

Directed by: Dr. Richard S. Stein

The work consists of three studies:

1. Deformation studies of an ethylene-methacrylic acid ionomer. The small angle x-ray scattering from a cesium salt of an ethylene-methacrylic acid copolymer has been shown to become azimuthally dependent on sample elongation. The observed azimuthal dependence of scattering has been compared with the predictions of several scattering models. A model in which the ionic aggregates are arranged on a paracrystalline lattice gives a poor fit to the undeformed data and predicts scattering peak shifts which are much different than those observed experimentally. A spherical shell-core model and a lamellar model with short range order are capable of fitting the undeformed data. An ellipsoidal deformation scheme of the shell-core model predicts correctly a decrease in intensity at an azimuthal angle of 0° to the stretching

direction but fails to predict an increase at 90° azimuthal angle. The lamella model gives nearly correct intensity changes at both 0° and 90° azimuthal angle. The scattering at large elongations at 0° azimuthal angle is used to analyze the size distribution of one dimension of the ionic domain. This analysis is believed to be more correct than those previously done for ionomers because of the absence of any scattering maximum at this elongation and azimuthal angle.

2. Studies of styrene-methacrylic acid ionomers. SAXS has been measured for a series of styrene-methacrylic acid copolymers and corresponding cesium salts in the range of 2-10 mol % co-units. The extent of phase separation is analyzed in terms of the SAXS invariant and internal density scattering components. The angular dependence of scattering is used to analyze the size and shape of ionic domains. A scattering maximum is observed for salt samples with ion concentrations above about 6 mol %.

3. Studies of polypentenamer based ionomers containing phosphonate side groups. Small and wide angle x-ray scattering have been studied for polypentenamers and hydrogenated polypentenamers with pendant phosphonate side groups including ester, acid, and cesium salt forms. For the hydrogenated polymers, the unsubstituted material and samples with 5% of

the pentenamer units containing acid or ester side groups show pronounced SAXS maxima typical of semi-crystalline polymers. The SAXS pattern has been analyzed in terms of the Hosemann paracrystalline scattering model to determine crystalline, amorphous, and transition zone thicknesses. Samples with 10% side groups show no SAXS maxima. A combination of WAXS, SAXS, and density measurements has been used to analyze the density and volume fractions of the crystalline and amorphous phases. The analysis indicates the crystalline density to be relatively constant while the amorphous density increases which is consistent with exclusion of the phosphonate groups from the crystal lattice.

The cesium salts of the 5 and 10% hydrogenated samples show SAXS maxima similar to those observed for other ionomers. Acid and ester forms of unhydrogenated samples show no SAXS maxima. Cesium salts show a shoulder and peak in the SAXS pattern for the 5 and 10% samples, respectively.

TABLE OF CONTENTS

INTRODUCTION

The field of ion containing polymers has received a growing amount of attention in the past few decades. This attention has arisen from the increasing number of applications for these materials as well as the fundamental scientific importance of these polymers. Several review articles (1,4,5,6) and two books (2,3) have appeared on the subject.

Many schemes for the classification of ion containing polymers are possible. One useful one is that employed by Eisenberg (2) in which classification is made according to the degree of ionic character and the degree of ionic versus covalent crosslinking. According to the scheme linear hydrocarbon polymers such as polyethylene or polystyrene have the least amount of ionic character and crosslinking. An increased amount of ionic character is found in ionomers which are structural copolymers of hydrocarbon and small amounts of ionic co-units (less than about 10 mol %). A larger ionic character is found in polyelectrolytes for which the fraction of ionizable units is much larger. Polymers with moderate ionic character and a large degree of crosslinking include mixed cure rubbers, copolymers with moderate amounts of ionic units (10-50%). Minerals and water insoluble synthetics are materials with the largest ionic and

network character.

Ionomers represent the case of a polymer with two types of structural units which vary greatly in polarity. According to usual definitions the ionic units in an ionomer are present in concentrations of 10 mol % or less. These polymers are most usually formed through a copolymerization reaction although other routes have also been used or will be discussed further below. Ionomers achieved commercial importance in 1964 with the introduction of Surlyn^{R}, neutralized copolymers of ethylene and methacrylic acid, by the DuPont Company. These copolymers are flexible, tough and truly thermoplastic materials with good processibility in the range of temperatures from 150° to 250°C and outstanding melt strength. The unusually high clarity and larger impact strength of Surlyn have also contributed to its commercial success. While Surlyn is the outstanding example of a commercially successful ionomer other ionomers such as Hycar^{R} copolymers of butadiene and recently Nafron^{R} ionomers used as electrolytic membranes have also achieved importance.

The unusual properties of ionomers have led to intensive investigations trying to understand the physical arrangement and properties of the ionic co-units. Originally these investigations focused primarily on the ethylene-methacrylic acid system. More recently these have been expanded to many other chemically differing ionomers especially

to systems where the complication of hydrocarbon crystallization is not present as is the case for the ethylene-methacrylic acid copolymers.

Studies of ionomers have utilized wide and small angle x-ray scattering, electron microscopy, dynamic mechanical, dielectric and nuclear magnetic relaxation, infrared spectroscopy, and other techniques. Results of these studies with few exception have favored the idea that the ionic groups form microphase separated aggregates. Particularly supportive of this idea have been small angle x-ray studies in which a peak corresponding to a 20-30 Å Bragg spacing has been observed. The peak is found for many different salt forms but not for the acid. The peak persists to high temperatures. Low molecular weight polar additives can lead to a disappearance of the scattering peak. Several authors have reported that the peak is not affected by sample orientation.

The interpretation of this small angle x-ray maximum has varied greatly. Longworth and Vaughan (15) originally proposed that the peak arises from a repeated 20 Å spacing within 100 Å diameter ionic domains. Other authors have proposed that the peak arises from interference between different aggregates which are arranged on a paracrystalline lattice. The radial dimension of aggregates in these models is about 5-10 Å. More extensive studies of the scattering

curve and the corresponding radial distribution by MacKnight, Stein et al. have contradicted these models indicating instead ionic particles with radii of gyration of about 10-15 Å present at a volume fraction of 5-10%. These authors have suggested the scattering maximum arises from internal particle structure rather than interparticle interference. They have proposed a model in which a central ionic core of 3-13Å radius is surrounded by a shell of associated ions at a distance of ~30 Å. Other authors recently have interpreted the scattering maximum as arising from interference between "neighboring" ionic aggregates even though such an interpretation has little rigorous basis in small angle x-ray scattering theory.

Other aspects of the problem of the nature and degree of phase separation have also received much discussion. On the basis of thermodynamic arguments Eisenberg has predicted the formation of ionic multiplets containing about 8 ion pairs and layer ionic clusters consisting of several multiplets. The formation of such structures is favored by the reduction of energy in the system due to increased coulombic interactions but is opposed by chain entropic forces which favor a random coil conformation. Eisenberg has been successful in interpreting many of the properties of styrene-methacrylic acid ionomers and other systems on the basis of this model.

Recently the group of Pineri has also found evidence that the ions occur in several different levels of aggregation. Mössbauer spectroscopic studies of butadiene-styrene-4-vinyl l-pyridine terpolymers crosslinked by iron chloride have been interpreted to indicate the presence of ions in dimers, quasi-isolated complexes, and clusters. Analysis of small angle x-ray and neutron scattering have indicated a wide distribution of particle sizes.

In the present work several studies have been made to gain further understanding of the extent of phase separation in ionomers and the geometric structure of ionic aggregates. The studies have been made primarily on ionomers exhibiting no separate hydrocarbon crystallinity which can complicate the interpretation of small angle x-ray scattering. In the first study it is shown that ethylene-methacrylic acid ionomers at fairly high salt concentrations do show an azimuthally dependent scattering pattern on elongation. The observed azimuthal dependence is shown to be a powerful method of testing various models for ionomer structure. The results strongly favor local structure models. A deformation model involving rotation of a layered micelle or lamellar structure is largely consistent with the data although other geometries and mechanisms may also be possible.

An investigation of the styrene-methacrylic acid ionomer system is made. The scattering is shown to arise

from two contributions. The first contribution arises from phase separated ionic aggregates. A second contribution arising from internal density fluctuations is ascribed to non phase separated ions. The scattering is also used to estimate the size and geometric structures of the aggregates.

A similar investigation is made for phosphonated polypentenamers which contain either a hydrogenated backbone which can crystallize or an unhydrogenated backbone which does not. The effect of the phosphonate units on backbone crystallization is examined for the former. The pattern of ion aggregation is analyzed for phosphonate salts in both systems.

CHAPTER I

BACKGROUND AND THEORY

A. Ionomers--Structure and Properties

1. The problem of phase separation in ionomers. Ionomers are statistical copolymers containing ionizable co-units at a level of 10 mol % or less with the remaining units being non-ionizable. In most existing cases ionomers contain two types of units of greatly varying polarity. It is well known that in low molecular weight systems of this type phase separation will occur to minimize the coulombic energy. The resulting system will contain polar regions and non-polar regions arranged in a manner to minimize the high energy interfacial area. If the polar and non-polar units are molecularly connected increasing constraints are placed on the possible ways for phase separation to occur. In ionomers where many ionic and non-ionic units are part of the same molecule these constraints can be expected to be quite severe. The aggregation of a large number of ionic units will greatly decrease the entropy of the connected polymer chains. In addition the necessity of incorporating non-ionic units in ion-rich regions will decrease the loss in coulombic energy on aggregation. Based on these arguments one would expect that the

degree of phase separation and the size of phase separated regions to be significantly reduced for a high molecular weight ionomer.

The problem of phase separation in lipids has been extensively studied. Lipid molecules containing hydrocarbon segments with 11 to 17 carbon atoms connected to ionizable units have been shown by Luzzati to undergo remarkable polymorphism. These studies have been made primarily by x-ray diffraction techniques. Proposed structures include lamellae, disks, and spherical micelles. Some examples are shown in Figure 1. For lipids with flexible hydrocarbons, Luzzati has analyzed the energetics determining the extent of phase separation. He proposes that the controlling forces are (1) electrostatic interactions related to the exact spatial configuration of ions in the polar regions, (2) interfacial tension acting against an increase in the area per polar group at the interface, and (3) chain entropic energy which is affected by the degree of disorder of the hydrocarbon chain. These factors can be influenced by the bulkiness of the polar and non-polar moieties, heterogeneities in the hydrocarbon chains and the nature of the cation. To a large extent these same three factors can be expected to control the phase separation in ionomers.

A quantitative theory based on these ideas has been proposed by Eisenberg (12). This author considers the aggregation of ions in ionomers to occur in two steps. In the

first step ionic multiplets are formed which contain a maximum of eight ion pairs and have radii of 3-5 $\mathring{A}$ and thus volumes of about 100 $\mathring{A}^3$. Once such a multiplet has been formed it is completely coated with non-ionic material. The aggregation of such multiplets to form larger clusters is then controlled by the decrease in free energy caused by coulombic interactions on multiplet approach and the increase in chain entropy resulting from such approach. The force for chain stretching is calculated from the force law:

$$f = 3kTh/\overline{h^2} \qquad (1)$$

where $\overline{h^2}$ is the mean square end to end distance for the free chain and h the actual separation. The coulombic energy, W, per ion pair is given by:

$$W = -K'e^2 / r4\pi\varepsilon_o D \qquad (2)$$

where e is the electron charge, D is the polymer dielectric constant, r the distance between centers of positive and negative charge, K' is a geometrical constant, and $4\pi\varepsilon_o$ is the permitivity constant.

By equating the coulombic and chain entropic energies at some temperature T_c where the cluster free energy is zero, Eisenberg is able to solve for the number of ions present in such a cluster. It is necessary to assume a particular geometry to evaluate K'. To evaluate the resulting expression, a temperature of 50°C which corresponds to a

tan δ dynamical mechanical relaxation is selected as the temperature of cluster breakdown. The result gives a value of 160 ion pairs per cluster. The cluster volume calculated from the theory is of the order of 50,000 $\mathring{A}^3$. The calculated cluster volume fraction is approximately 30%.

Several criticisms of this theory can be made. Firstly, the assumption that an energy minimum is achieved for the system by first incorporating all ions in multiplets and then by the association of such multiplets is not necessarily correct. It may be that lower energy states occur by the exclusion of some ions entirely from aggregates so that others may aggregate more favorably. Secondly, the calculation of chain entropic energy is clearly underestimated in cluster formation. This is apparent in that in some cases separation distances between sequential ionic groups are required by the theory to be greater than the fully stretched out distance of the chain. This problem could be avoided by the use of the more accurate expression for the elastic force developed by Kuhn and Grün (14) in place of Equation 1. It is more probable that large chain elastic forces are not encountered in these systems due to the exclusion of a fraction of the ions from the ionic phase.

Thirdly the use of 50°C for the temperature of cluster instability is probably incorrect. SAXS studies have shown that the ionomer scattering peak persists to temperatures of 200-300°C without large changes in intensity. This

indicates the stability of whatever structures are present to temperatures much greater than 50°C. Despite these problems the Eisenberg approach has been quite useful in showing that there are strong tendencies for phase separation in ionomers and that the coulombic energies involved in aggregation are on a competitive level with chain entropic forces opposing aggregation.

One other attempt has been made to evaluate the thermodynamics of phase separation in ionomers (13). These authors have attempted to evaluate more exactly the Hamiltonian describing the energetics through the use of the non-equilibrium thermodynamic distribution function approach of Bogolyubov (14). The authors have also considered more exactly the effect of shielding by the non-ionic segments. However, the resulting equations are not presented in a tractable form and no real conclusions can be drawn from the extant work. The desire of the authors to achieve a more accurate evaluation of the configuration corresponding to the minimum free energy is admirable and should form the basis for future theoretical developments.

2. Experimental studies of ionomer structure and properties. A large number of experimental studies have been made on ionomers which give direct or indirect evidence on the problem of phase separation. Electron microscopy and small angle x-ray and neutron scattering have been used to attempt to

directly characterize the phase structure. Extensive studies have also been made of the rheological, relaxation, and spectroscopic properties of these polymers. The relaxation measurements have included dynamic mechanical, dielectric, nuclear magnetic resonance, and electron paramagnetic resonance studies. Although the interpretation of many of the results are not yet certain, the general view that has emerged from these studies is that the ionic groups in ionomers do phase separate to some extent. This phase separation appears to be the cause of the many unique characteristics of ionomers. The extent of phase separation varies for different ionomer systems depending on the nature of the hydrocarbon and ionic units.

a. Electron microscopy. Direct observation through electron microscopy would appear to be the simplest method of characterizing the phase structure. This method was used by the DuPont group in studies of the ethylene-methacrylic acid ionomers (15,16). Films used in these studies were prepared principally by casting from solution but also by thin sectioning. In the former case a dilute (0.1%) solution of the unneutralized copolymer was placed on either hot water or a dilute base. Observations were made as a function of acid co-unit concentration in the copolymer. For films cast on water, spherulitic and or lamellar structures were observed similar to those in low density polyethylenes. For films cast onto base such structures were absent for concentration

of 3 mol % acid units or higher. Instead an irregular grainy structure with grain sizes of about 150 Å in diameter were found. Since the method of solution casting cannot in general be expected to produce morphologies which are characteristic of the bulk of the method of thin sectioning was also used. The authors report that the grainy structure was also observed in this case but this seems less than obvious based on the published micrographs (15). Other electron microscopic studies of ionomers have been made. MacKnight et al. (17) studying the same ethylene-methacrylic acid system reported considerable variation in the grainy structure produced by using different sample preparation techniques. An examination of ionomers of butadiene-methacrylic acid was made by Marx et al. (18). A granular structure was also reported but in this case was found to be considerably smaller with ionic domain diameters in the range of 13-26 Å. Recently Pineri et al. (19,20) investigated the structure of a complexed terpolymer of butadiene, styrene, and 4-vinylpyridine. The polymer was complexed in benzene solution by mixing with methanolic $FeCl_3$ giving samples of different ion concentration. Electron microscopy showed the existence of heterogeneously distributed dark regions, which varied in size over a wide range of 100 Å to more than 1000 Å. Electron diffraction studies showed the dark regions to be noncrystalline. Accompanying x-ray and neutron scattering studies of this system, however, indicated particle size

distributions with most probable sizes in the range of 10-20 Å radius. In summary the electron microscopic studies of ionomers have indicated that there are differences in morphology between acid and neutralized copolymers. Additional contrast features appear to be present in the neutralized samples. The reason for the contrast is, however, not certain as is often the case in electron microscopy. A very useful experiment that may be done in the near future is to use recently developed x-ray spectrographic techniques to determine the concentrations of metal ions inside and outside contrast features. Another criticism that must be made of the microscopic studies is that in most cases sample preparation has consisted of casting from solution. This technique is well known to be non-representative of bulk materials based on microscopic studies of amorphous polymers.

b. Small angle x-ray and neutron scattering. The difficulty of interpretation of microscopic evidence has led to many studies of ionomers by scattering techniques. Scattering techniques have the advantage that the source of scattering contrast for a particular technique is known. The disadvantage of scattering is that the Fourier transform of the scattering object is obtained and not a direct image. In addition many different scattering objects can in principle give the same scattering pattern. Despite these problems the techniques of small angle x-ray scattering and re-

cently small angle neutron scattering have given what is probably the most important evidence on the nature of phase separation in ionomers. Initial studies on the ethylene-methacrylic acid system were made by Wilson et al. (21) and Longworth and Vaughan (13) as a function of copolymer composition and degree of neutralization. In the case of a polymer containing 6 mol % methacrylic acid no peaks were observed in the small angle x-ray scattering region while in the same material neutralized 90% a peak was observed at a scattering angle of about 4° 2θ using an incident wavelength of 1.54 Å. These authors report an increased peak intensity with increasing salt content. In copolymers with increasing acid co-unit content but neutralized to the same extent (5 mol %) the peak shifts to slightly smaller spacings. A similar peak was observed for all the alkali metals from lithium through cesium as well as other salts. The peak persists to temperatures above 300°C. Low levels of humidit- enhance the peak but saturating the sample with water destroys it. No change is reported in the peak with sample orientation although orientation effects were seen in the polyethylene lamellar peaks. These authors cite an optical rule of thumb that at least five repeat units must be present for a peak to be observed. On this basis they propose that ionic domains have a dimension of at least 100 Å and contain internal repeated structures separated by 20 Å.

Delf and MacKnight (22) made small angle x-ray

studies of 4 mol % ethylene-methacrylic acid copolymers and the corresponding 60% ionized cesium salt. They reported the same 20 Å peak but also a peak at 83 Å. This latter peak has been subsequently ascribed to lamellar periodicity (23).

Binsbergen and Kroon (24) suggested that the ionomer peak is due to a favored separation distance between ionic domains. Using the data of Wilson et al. (21) and assuming Bragg's law to characterize the separation distance these authors have calculated the number of carboxyl groups per domain as a function of copolymer content. The result indicates there are five to eleven groups per domain.

Marx et al. (25) have used an essentially similar interpretation in interpreting data also taken on the ethylene-methacrylic acid system. They propose the use of the equation:

$$d = C(V' f^{-1})^{1/3} \qquad (3)$$

where d is the Bragg spacing between scattering sites, C is a constant of the order of unity, V' is the volume per carboxyl group, and f^{-1} is the number of carboxyl groups per scattering site. On the basis of a light scattering analog they estimate C to be 0.9. The authors have also observed x-ray peaks in methacrylic acid and acetic acid after neutralization. Postulating that in these systems the ions are present as trimers they calculate a value of C in Equation 3

of 0.77. They then use the Bragg spacings observed in ionomers with this value of C to estimate f^{-1}. Values for this parameter range from 2-7. It is thus the opinion of these authors that the state of aggregation in ionomers is relatively low certainly much lower than that proposed by Longworth et al. (13). It should be pointed out that the use of Equation 3 essentially describes the system as containing crystalline or at least paracrystalline order. This implies that the spacing between the scattering sites is quite regular. No good explanation for why such regularity might occur has been given. In addition it has also been pointed out that the use of Equation 3 leads to contradictions with the known stoichiometry of the system, particularly at higher ion concentrations. For example one can calculate that the number of ion groups required for a homogeneous lattice satisfying Equation 3 for a 6 mol % copolymer is twice the existent number of ionic units present. To some extent this criticism may be answered by postulating that the homogeneous lattice exists only over limited regions in the sample. This point will be discussed more thoroughly in the discussion of models for ionomer structure presented in a subsequent chapter.

Two studies have been made of the radial distribution function (RDF) for ionomers which is the Fourier transform of the interference portion of the small angle x-ray scattering curve. In principle the radial distribution

function contains the same information as the scattering curve. The RDF approach has the advantage that the information is presented in a more readily interpretable form that can be related to structure. The RDF approach has the disadvantage that errors can be introduced in making the Fourier transform. Particularly troublesome are errors introduced by the necessary termination of data at small and large angles. Roe (26) calculated the RDF for an ethylene-acrylic acid containing 5.4 mol % acid and its 78% neutralized cesium salt. The calculation was based on data above $s = 0.6$ Å^{-1} and thus excluded the region of the small angle x-ray ionomer peak. Roe found evidence for Cs-O and Cs-Cs spacings. Spacings above 6 Å were absent. The author concluded that there was no evidence for the existence of ionic clusters but that there was evidence for dimer formation.

These conclusions have been challenged by Kao et al. (27). These authors have calculated the RDF for a 64% neutralized cesium salt of a 3.8 mol % ethylene-methacrylic acid copolymer. Data from the region of the small angle x-ray scattering peak was included. The RDF shows a high probability for interferences in the range of 4-14 Å with a shallow broad peak at about 35 Å. This RDF is consistent with cluster formation on a level intermediate between the 100 Å diameter aggregates proposed by Longworth et al. (13) and the 3-5 Å multiplets proposed by Marx et al. (25).

In subsequent studies MacKnight et al. (28,29)

analyzed the SAXS from a number of ethylene-methacrylic acid ionomers. Scattering peaks corresponding to Bragg spacings between 25 and 35 Å were observed in all dry salts but disappeared in water saturated polymers. The maximum was observed to decrease slightly in intensity and be unchanged in position above the melting temperature. In studies of orientation of a 3.8 mol % cesium salt by photographic methods no change in the peak was observed.

The angular dependence of scattering was analyzed by the method of Grunier to determine radii of gyration of particles in the system. Radius of gyration values ranged from 8-12 Å. The tail of the scattering curve was analyzed by the method of Porod. Results indicated positive deviations from Porod's law which are indicative of electron density fluctuations within phases. In principle this could either be due to the presence of ions in the non-ionic phase or due to hydrocarbon segments in the ionic phase. As will be shown later since the scattering from internal density fluctuations depends on the volume fraction of the phase the former possibility can be expected to be of greater importance than the latter. Values of the specific interface calculated from Porod's constant indicated aggregate sizes comparable in size to those found from the Guinier analysis. Analysis of the total scattering invariant indicated ionic phase volume fractions in the range of 2-5%. On the basis of these results these authors have proposed the model shown

in Figure 1. A central ionic core of radius 3-13 Å is surrounded by a shell of associated ions at a separation distance of 20-35 Å. The shell of associated ions may include either sequential ions along the polymer chains of ions included in the central core or may reflect the presence of non-directly connected ions from the surrounding matrix attracted to the central core by coulombic interactions. In this model the scattering system is essentially dilute that is the individual shell-core structures are widely separated so that no constructive interference occurs between them.

A study of SAXS from styrene-methacrylic acid ionomers has been made by Eisenberg and Navratil (30). For cesium salts containing more than 6 mol % of the ionic comonomer maxima were observed corresponding to spacings of 50-60 Å. These peaks were absent for cesium salts containing less than 6 mol % of co-units and were also not observed for un-ionized copolymers. For cesium salts with less than 6 mol % co-units SAXS peaks corresponding to spacings of 18-20 Å were observed. Eisenberg has proposed that these spacings may be due to interference between multiplets presumably forming a sub-cluster structure. The 50-60 Å spacings observed in salts above a 6 mol % concentration have been interpreted as arising from intercluster spacings. It should be again pointed out that such an interpretation can only be correct if the arrangement of clusters is quite regular or if the volume concentration is high above about 30%

as will be discussed further in a later section.

Pineri et al. (31) studied butadiene-methacrylic acid ionomers and carboxy terminated butadienes. In a low molecular weight butadiene polymer ($\bar{M}_n = 4.4 \times 10^3$) containing terminal acid groups neutralized with manganese acetate a SAXS peak was observed corresponding to a 70 Å spacing. The overall intensity increased greatly with increased degree of neutralization but the peak position was unchanged. An analysis of the angular dependence of scattering in the region following the maximum was used to evaluate the size distribution of particles in the system. The results indicate most probable radii in the range of 3-6 Å. The authors conclude that the system consists of ionic clusters arranged nearly equidistantly in some regions of the sample. The SAXS peak results from interference between these clusters. Other portions of the sample remain unneutralized. This interpretation is largely analogous to that of Marx et al. (25) except in this case the lattice of scattering sites is finite occupying only portions of the sample.

Very recently further studies of this system by SAXS have been reported (32). Telechelic polybutadiene-methacrylic acid copolymers containing 2 mol % acid groups and neutralized 5-100% by various cations were examined. SAXS maxima corresponding to 80 Å spacings were observed with again little change in spacing with increased neutralization. Radius of gyration values in the range of 8 Å were

reported. The tail of the scattering curve was analyzed and found to obey Porod's law. This agreement is the first reported for any ionomer system. All other studies have reported positive deviations. The SAXS invariant was then calculated and used to calculate electron densities for the ionic phase. It was assumed that the density of the non-ionic phase was unchanged with neutralization. This is a reasonable approximation in view of the observed obeyance with Porod's law which is indicative of the absence of ions from the non-ionic phase. Values of the ionic phase density in the range of 0.5-0.7 electrons/$\mathring{A}^3$ were reported. The correlation function was calculated for the system. This function contains essentially similar information to the radial distribution discussed previously. The correlation function exhibits a peak in the range of 20-40 $\mathring{A}$ and continued fluctuation about zero to values over 200 $\mathring{A}$. The authors have proposed that the ions appear in clusters possibly disk like with radii of 10-12 $\mathring{A}$. The 80 $\mathring{A}$ peak is assigned to intercluster distances.

Meyer and Pineri (20,33) used SAXS and small angle neutron scattering to analyze particle size distributions in the butadiene-styrene-4 vinylpyridine terpolymer crosslinked with iron (III)-chloride previously mentioned. Due to the different wavelengths of these two techniques these authors claim that the two techniques can be used to study complementary regions of particle size. To some extent this is

true. However since SANS results from differences in neutron scattering cross section rather than electron density differences the nature of particles seen by the two techniques may differ. The resulting size distribution as previously discussed shows particles to be most probably in the range of 10-20 Å radius of gyration. The tail of the curve has also been analyzed. A positive deviation is observed which is interpreted by the authors to be due to the presence of dimers, trimers, etc., giving rise to a constant diffuse intensity.

Studies of ionomers using techniques other than microscopy and small angle scattering have been interpreted of supermolecular structural models. However since these techniques usually have measured properties which are secondary consequences of structure rather than structure itself the results are usually not conclusive.

c. Spectroscopic techniques. Otocka and Davis (34) investigated the nuclear magnetic resonance of ethylene-acrylic acid copolymers and their lithium salts. They observed a decrease in the proton line width at a temperature lower than for lithium nuclei by about 20°C. These authors have concluded that this temperature difference is small enough to indicate effective transfer of motion from the matrix to the ions and thus that the ions are fairly well dispersed. This view has been challenged by Ovenall (35).

Electron paramagnetic resonance studies of a

butadiene-methacrylic acid copolymers have been recently reported by Pineri et al. (36). In a copolymer neutralized by 95% Zn^{2+} ions which are dismagnetic and 5% Cu^{2+} ions which are paramagnetic, the EPR spectrum was largely characteristic of that from isolated Cu^{2+} ions. In contrast the main fraction of the spectrum neutralized fully with Cu^{2+} ions was characteristic of Cu^{2+}-Cu^{2+} pairs. This indicates that the ions in this system are present in aggregates at least as large as dimers.

Mössbauer spectroscopy coupled with magnetic susceptibility measurements has been used successfully to characterize the environment of iron ions in the butadiene-styrene-vinylpyridine terpolymer system (20,33,37). Results were shown indicating the presence of iron ions in three distinct environments. Clustered complexes exhibiting a hyperfine spectrum indicative of superparamagnetic behavior were shown to contain 40 to 60% of the iron ions. Quasi-isolated complexes with weak ferromagnetic coupling were shown to contain about 20% of the ions. The remaining fraction of ions was assigned to dimers exhibiting antiferromagnetic coupling.

d. Relaxation and rheological behavior. Numerous studies of the relaxational and viscoelastic properties of ionomers have been made. Since these have been recently reviewed (2,3) only a brief summary will be made here.

MacKnight et al. (38) have interpreted the dynamic

mechanical behavior of the ethylene-methacrylic acid copolymers and ionomers in terms of microphase separation on neutralization. The occurrence of a new α relaxation which exhibits a strong dependence on the quantity and type of ions present is indicative of regions containing predominantly ionic material. The reasons for the appearance of a β relaxation at -10°C have been disputed (2,38,39). The dielectric relaxation properties of this system were also studied by MacKnight and coworkers (40,41,42). While interpretation was made difficult by problems of peak overlap and the presence of dipoles in the form of unneutralized acid units, the general conclusion of the dynamic mechanical studies that clustering of ions occurs was reinforced.

Studies of the viscoelasticity of the styrene-methacrylic acid system were made by Eisenberg and coworkers (43-46a). Stress relaxation results (43) showed the appearance of an upper inflection point in the modular-temperature curves for all salts and the failure of time-temperature superposition for salts above about 6 mol % concentration. These have been interpreted as being indicative of changes in structure with ionization particularly the occurrence of ionic clusters. Changes in the WLF constants necessary to achieve so-called pseudo-master curves in the region of time-temperature superposition and the broadening of relaxation times are also consistent with clustering. Previous studies of the viscoelastic properties of this system are

also largely consistent with these results (47,48). The dynamic mechanical loss tangent for this system exhibited two peaks in the glass transition region which were attributed to the glass transition of the clustered material and the matrix. The lower temperature relaxation attributed to the matrix exhibited a weak compositional dependence in contrast to the high temperature relaxation which increased steadily with ionic content.

Dielectric results on this system have been interpreted similarly (49). After conductivity subtractions two peaks were resolved. The low temperature peak was attributed to matrix dipoles, while the high temperature relaxation was assigned to dipoles in ionic clusters. The areas of the peaks were used to calculated the relative number of dipoles in the two environments. With uncertainties of 10-20% the percentage of ions in clusters varied from about 35-70% over the range of ion concentrations from 2-10 mol %.

Studies of light scattering (50,51) and x-ray relaxation (52) and optical relaxation (53,54) have been made on the ethylene-methacrylic acid ionomers by Stein et al. Static and dynamic light scattering studies (50,51) showed marked differences between an unneutralized 4.1 mol % copolymer and a 55% neutralized sodium salt. Differences in the angular dependence of static light scattering indicate a rod-like superstructure for quenched salt films but a spherulitic superstructure for annealed salts. The real and

imaginary components $\Delta I'$ and $\Delta I''$ of dynamic light scattering were measured on spherulitic acid and salt films in the temperature range 25-60°C. The acid film exhibited no transition in this region while one was observed for the salt at about 40°C. A similar transition was also observed in the strain optical coefficient (53), the amorphous orientation function as observed by x-ray diffraction (52), and in a number of infrared absorption bands (54). These results in connection with the dynamic-mechanical and dielectric results have led to the assignment of the 40°C α loss to a softening of ionic domains. The observation that both ionic and hydrocarbon groups orient more readily above this temperature suggests a parallel connection between these regions. This suggests a sandwich structure in which the ionic domains may occur between the crystalline lamellae in spherulites.

The melt rheological properties of acid copolymers and ionomers have also been extensively studied. Sakamato et al. (56) investigated a 4.1 mol % ethylene-methacrylic acid copolymer and its 55% neutralized salt. Time temperature superposition was found applicable for the un-ionized copolymer but not for the salt. Longworth and Vaughan (16) found a dramatic increase in the viscosity at low shear with increasing ionization for this system with the effect diminishing at higher shear rates. This suggests the breakdown of a flow unit at high shear rates involving the ionic domains.

Recently Earnest (57) has investigated the melt rheological properties of ester, acid, and salt forms of copolymers in this system at different co-unit concentrations in conjunction with infrared measurements. The results are consistent with the existence of phase separated ionic domains being formed on neutralization which persist to high temperatures. Shohamy and Eisenberg (58) investigated the melt rheology of styrene-methacrylic acid copolymers and ionomers. In the temperature range studied time temperature superposition was applicable. The temperatures required to achieve superposition varied greatly for un-ionized materials and salts (e.g., 8°C and 38°C for 1.5 mol % acid and salts). These differences may simply reflect the differences in enthalpies of interchain interactions. It was also observed that the ΔT difference between acid and salts changed with ion concentration showing a change in slope at about 5 mol % concentration. This was interpreted as being indicative of the onset of ionic clustering at this concentration.

In summary studies of the relaxational and rheological properties of ionomers show consistently that profound changes occur on ionization. The exact interpretation of these changes in terms of supermolecular structure is in most cases complicated. However the general indication is that in most cases the properties are most consistent with the formation of a separate ionic microphase. This microphase is seen to exhibit special properties of its own such as the

α loss mechanism observed in the ethylene-methacrylic acid ionomers. The phase apparently persists to high temperatures and effects greatly the melt rheology of these systems. In several studies evidence has also been found that indicates that a fraction of ions are not phase separated or at least are aggregated at a reduced structural level such as multiplets.

B. Non-Ionic Random Copolymers

The problem of the physical structure of non-ionic random copolymers has also received much attention in the past two decades. This problem has two aspects. The first deals with copolymers which contain a large percentage of a crystallizable co-unit. In this case it is desirable to describe the influence of the second co-unit on the crystallization of the first. In particular it is desirable to know whether the second co-unit is always excluded from the crystal or whether it may in some cases enter the crystal lattice of the first co-unit. This problem has been treated both theoretically and experimentally and remains a matter of some controversy. The second aspect of the problem of the structure of these copolymers concerns the co-units excluded from the crystal in semi-crystalline systems or the co-units in totally amorphous systems. In cases where the two co-units differ in polarity it might be expected that phase separation may occur similarly to the case of ionomers

but to a lesser extent. Direct spectroscopic evidence indicates the presence of dimers in such systems especially in cases where special interactions such as hydrogen bonding are possible. Some authors have interpreted other results as pointing to a greater level of aggregation than merely dimer formation. As will be seen these results may be incorrect in view of recent progress in the interpretation of small angle scattering.

Flory (58) has predicted the thermal properties of random copolymers in which type A units are completely excluded from type B crystals. In this case the melting point, T_m, differs from the melting point of pure B, T_m°, as described by the relation:

$$\left(\frac{1}{T_m^\circ} - \frac{1}{T_m}\right) = \frac{R}{\Delta H^\circ} \ln(1 - X) \qquad (4)$$

where ΔH° is the heat of fusion, R the gas constant, and X the concentration of A units in the system. This result is derived solely on entropic considerations. A more general approach has been described by Sanchez and Eby (59). These authors have analyzed the free energy of systems where A co-units may be included in the B crystal. In this case the melting behavior is described by:

$$\left(\frac{1}{T_m^\circ} - \frac{1}{T_m}\right) = \frac{-R}{\Delta H^\circ}\left[\frac{\varepsilon X_c}{RT} + (1 - X_c)\ln\left(\frac{1 - X_c}{1 - X}\right) + X_c \ln\left(\frac{X_c}{X}\right)\right] \quad (5)$$

where X_c denotes the concentration of A units in the B crystal and ε is the defect energy of such inclusions. The thickness of such crystals has also been predicted and compares well with data of Fischer et al. (60) for L- and DL-lactides. Unfortunately for most random copolymers not enough data is available to characterize the defect energy parameter and to predict whether Equations 4 or 5 best describes the system.

A number of experimental studies have been undertaken to solve the co-unit inclusion problem in various systems. Polyethylene copolymers with units containing short linear or alkyl branches have been studied by a combination of thermal, small angle and wide angle x-ray scattering, and mass density measurements (61,62). In these studies, small angle x-ray scattering is used to calculate the mean squared electron density fluctuation, $\overline{\eta^2}$, which can be related to the volume fractions ϕ_C and ϕ_A and densities ρ_C and ρ_A of a two phase system:

$$\overline{\eta^2} = \phi_C \phi_A (\rho_C - \rho_A)^2 \quad (6)$$

where

$$\phi_C + \phi_A = 1. \tag{7}$$

The mass density, $\bar{\rho}$, is related to these variables by:

$$\bar{\rho} = \phi_C \rho_C + \phi_A \rho_A \tag{8}$$

By determining ϕ_C by an independent method such as wide angle x-ray scattering or differential scanning calorimetry it is possible to then solve Equations 6-8 for ρ_C and ρ_A. The crystalline density can then be compared to that calculated from lattice parameters and the amount of inclusion analyzed. Vonk et al. (61) found little disagreement between crystalline density values as calculated from 6, 7, and 8 and values calculated from lattice parameters for copolymers of ethylene and units with short linear or alkyl branches. Systematic differences were observed in the crystal density values for copolymers of ethylene and vinyl acetate and ethylene and acrylic acid. These results were interpreted as indicating exclusion of the branched co-units and partial inclusion of the vinyl acetate and acrylic acid units in the polyethylene crystal lattice.

Roe and Gieniewski (63) studied this problem in chlorinated polyethylene crystallized from the melt. For polymers containing 0.2 to 1.7 chlorine atoms per hundred carbon atoms a decrease in crystallinity from 80 to 60% was observed. An analysis was made using Equations 6-8 and the

additional relation:

$$\rho_a = \rho_a^\circ + \beta W_{Cl} \tag{9}$$

which assumes a linear relation between the amorphous density and weight fraction of chlorine, W_{Cl}, in that phase. This permitted the calculation of the partition coefficient for chlorine:

$$\gamma = (W_c)_{Cl}/(W_a)_{Cl} \tag{10}$$

γ was observed to vary from 0.13 to 0.18 in the above overall copolymer composition range.

An important point in these studies is the subtraction of the diffuse scattering component. Roe and Gieniewski analyzed the tail of the scattering curve using the relation:

$$\tilde{I} = \tilde{K}_S/S^3 + \delta \tag{11}$$

where $\tilde{I}$ is the infinite height slit smeared scattering intensity, $S = 2\sin\theta/\lambda$, and δ represents the scattering component due to density fluctuations within phases. The component δ was then subtracted before an evaluation of $\overline{\eta^2}$ was made. This analysis follows the theory of Ruland (64) for internal density fluctuation scattering as will be described in detail in a later section. Vonk et al. (61,62) used the somewhat less exact procedure of subtracting the observed minimum intensity value from the data as a measure of δ.

Johnson et al. (65) studied the structure of some

ethylene-phosphonic and copolymers by similar techniques. The degree of crystallinity as calculated by WAXS decreased from 54% for a low density polyethylene sample to 33% for a sample containing about 2.8 phosphonic acid samples per hundred carbon atoms. A sample containing about 8 phosphonic acid units per hundred carbon atoms exhibited no WAXS crystalline peaks. SAXS studies showed scattering maxima decreasing from 260 Å to 200 Å and disappearing above a phosphonic acid concentration of 2 units per hundred carbon atoms. The invariant, $\overline{\eta^2}$, was calculated and observed to increase linearly with the concentration of phosphonic acid units. An analysis in terms of Equations 6, 7, and 8 was made. The results showed an increase in ρ_c while ρ_a remained fairly constant. However WAXS measurements of the lattice parameters showed no evidence of crystal lattice expansion. This discrepancy led the authors to conclude that the two phase model was inadequate to describe the system. They advocated the use of a three phase model in which the third phase consists of phosphonic acid and enriched domains. A critical question in the validity of this study is the method of diffuse scattering intensity. The authors state that the level of background was subtracted by assuming the tail of the scattering curve has a θ^{-4} variation for desmeared data. This approach is essentially equivalent to an analysis in terms of Equation 11. However care must be taken that after subtraction a good agreement with θ^{-4} is

achieved over a broad angular range. The linear increase in $\overline{\eta^2}$ with phosphonic acid concentration is a unique result for this type of random copolymer system. Both Roe et al. and Vonk reported substantial systematic decreases in $\overline{\eta^2}$ with increasing amounts of the non-crystallizing co-unit. If an insufficient subtraction of the diffuse scattering component was made by Johnson et al. this could lead to the observed increase in $\overline{\eta^2}$. The published data given are not sufficient to determine the correctness of the diffuse scattering component subtraction.

A general criticism of the experimental studies of crystallizing random copolymers can be made that the independent methods for determining ϕ_C do not observe the same phase volume fractions as seen by the small angle x-ray scattering technique. The use of small angle neutron scattering (SANS) has provided an alternate method that does not suffer from this criticism. Schelten (66) has studied the chlorinated polyethylene system by a combination of SAXS and SANS. SANS may be used to measure the mean squared fluctuation in neutron scattering cross section, $\overline{\chi^2}$. $\overline{\chi^2}$ may be related to the volume fractions and neutron scattering cross section of the two phases through the relation:

$$\overline{\chi^2} = \phi_A \phi_C (\sigma_C - \sigma_A)^2 \qquad (12)$$

The neutron scattering cross section of a phase can be re-

lated to the electron density of the phase by a constant which depends on the chemical composition of that phase. Schelten et al. arrived at essentially similar conclusions to Roe et al. through the use of this approach namely that while most chlorine atoms were present in the amorphous phase some inclusion in the crystal phase did also occur.

C. Small Angle X-ray Scattering

The technique of small angle x-ray scattering (SAXS) is one of a number of current scattering methods. The usefulness of a particular scattering technique for a particular problem depends on the size and nature of the scattering entities. Small angle light scattering results from polarizability fluctuations and is useful in the size range of 5,000 Å and above. Wide angle x-ray scattering (WAXS) utilizes wavelengths in the range of 0.5-3 Å and results from electron density fluctuations on a size level of 10 Å or less. SAXS is useful in the intermediate size range of 10-5000 Å and results from electron density fluctuations. Neutron scattering techniques study fluctuations in neutron scattering cross section which result principally from the type of nuclei present in the sample. The wavelengths used in neutron scattering are generally in the range of 5-10 Å. Thus wide angle and small angle neutron scattering (SANS) study size ranges comparable or slightly larger than WAXS and SAXS. The fact that neutron and x-ray scattering result

from different properties of the scattering entities makes them very complementary. This complementarity is currently being used in a powerful manner in the study of phase separated systems. A recent review of these scattering techniques and current applications to polymers has been written by Stein and Higgins (67).

1. General. The amplitude of x-ray scattering $A(\underset{\sim}{h})$ is given by the Fourier transform of electron density distribution, $\rho(\underset{\sim}{x})$, of the scattering sample (68). This is described by:

$$A(\underset{\sim}{h}) = \int \rho(\underset{\sim}{x}) \exp(-i\underset{\sim}{h}\cdot\underset{\sim}{x}) d\underset{\sim}{x} \tag{13}$$

where

$$\underset{\sim}{h} = (2\pi/\lambda)(\underset{\sim}{S} - \underset{\sim}{S}_o) \tag{14}$$

λ is the incident wavelength and $\underset{\sim}{S}_o$ and $\underset{\sim}{S}$ are unit vectors in the direction of the incident and scattered rays, respectively. The magnitude of the scattering vector, $\underset{\sim}{h}$, is given by:

$$|\underset{\sim}{h}| = \frac{4\pi \sin\theta}{\lambda} \tag{15}$$

where θ is half of scattering angle. The observed intensity of scattering, $I(\underset{\sim}{h})$, is given by the product of A(h) and its complex congregate, $A^*(\underset{\sim}{h})$:

$$I(\underset{\sim}{h}) = AA^*$$

$$= \int\int \rho(\underset{\sim}{x}_a)\rho^*(\underset{\sim}{x}_b)\exp(2\pi i\ \underset{\sim}{r}\cdot\underset{\sim}{h})\,d\underset{\sim}{x}_a\,d\underset{\sim}{x}_b \qquad (16)$$

where a and b denote different parts of the sample and $\underset{\sim}{r}$ is the vector connecting these parts.

The basic problem of scattering techniques is to acquire information about the electron density distribution in the sample from the observed scattering intensity function. As discussed previously this can be done through two approaches. The first involves comparison of the observed intensity function to scattering functions calculated from models for the scattering system. The second involves Fourier inversion of the scattering function. The Fourier inversion represents the scattering information in a more readily interpretable manner but may also include errors involved in the inversion calculation.

2. Classification of scattering systems. Scattering systems may be classified according to the two criteria of concentration and order. These two criteria determine whether interparticle interference effects are important or whether only intraparticle interference is important. In a dilute or low concentration system a large degree of order is necessary for interparticle interference to be important. In a concentrated system the exclusion of volume by the particles themselves can impose some ordering on the system. If the

location of particles is completely random aside from this volume exclusion effect a particle volume fraction of about 30% is required to produce an interference maximum (69). In systems of high order which are thus nearly crystalline interference maxima will be observed at any concentration. A high degree of order must in general reflect the existence of some special interaction potentials in the system.

3. Scattering from dilute systems. The scattering by a single particle without interparticle interference is given by:

$$I(\underset{\sim}{h}) = I_e(\underset{\sim}{h})\ F^2(\underset{\sim}{h}) \tag{17}$$

where $I_e(\underset{\sim}{h})$ is the intensity that would be scattered by a single electron and $F^2(h)$ is the square of the structure factor of the scattering particle (1).

The structure factor of a particle is determined solely by its geometry and electron density structure. These latter factors characterize the shape function of the particle (70). For a sphere of radius R the shape function $S(\underset{\sim}{x})$ is given by:

$$\begin{aligned} S(\underset{\sim}{x}) &= 1 \qquad \text{for } |x| \leq R \\ &= 0 \qquad \text{for all other } x. \end{aligned} \tag{18}$$

The structure factor is the Fourier transform of the shape function:

$$F(\underset{\sim}{h}) = \int_{O}^{\infty} S(\underset{\sim}{x}) \exp(-2\pi i(\underset{\sim}{r}\cdot\underset{\sim}{h}))\, d\underset{\sim}{v}_r \qquad (19)$$

where dv_r denotes a differential volume element. When evaluated this expression leads to:

$$F = 3\cdot V\left[\frac{\sin hR - hR\cos hR}{(hR)^3}\right] \qquad (20)$$

where V is the sphere volume. The structure factors for a wide range of particle geometries including ellipsoids of revolution (68-72), circles (70), rectangles (70), parallelepipeds (70), tetrahedrons (70), rods (73), needles (73), plates (73), and cylinders (69,73), among others.

For a collection of particles the intensity is proportional to the number of particles and the averaged squared structure factor $\overline{F^2}(h)$. To calculate this one must consider distribution in particle size and density and distributions in particle rotation for non-centrosymmetric particles. It should be noted that the averaged squared structure factor, $\overline{F^2}(h)$ is only equal to the squared averaged structure factor $\overline{F(h)}^2$ for centrosymmetric particles. For particles varying in size and/or density but identical in shape the intensity is proportional to the square of the particle volume, V_i, and the square of the density difference $\rho_i - \rho_o$:

$$I(h) = C\,\overline{F^2(h)} \sum_i g_i V_i (\rho_i - \rho_o)^2 \qquad (21)$$

where ρ_o is the density of the medium outside of the particle and g_i is the fraction of particles i.

The analysis of particle size and particle size distribution by SAXS has received much attention (74-76). Guinier (74) has shown that for a dilute monodisperse system in which the particles assume all orientations with equal probability that the scattered intensity can be expressed in terms of the power series:

$$I(s) = I(0)\ (1 - (4\pi^2/3)s^2R^2 + \ldots) \qquad (22)$$

where I(0) is the scattered intensity at zero angle. R is the electronic radius of gyration:

$$R = \left(\frac{\sum_K f_K\ r_K^2}{\sum_K f_K} \right)^{1/2} \qquad (23)$$

where f_K is the scattering factor of the Kth electrons which is a distance r_K from the electronic center of gravity. Equation 23 can be approximated as:

$$\log I(s) = \log I(0) - (4\pi^2/3)s^2R^2 \qquad (24)$$

The form of Equation 24 allows the determination of R from the slope of a plot of $\log I(s)$ versus s^2. Guinier (74) has compared the approximate expression of Equation 23 with exact intensity expressions for spheres and ellipsoids of revolution with the same radius of gyration. The results

show good agreement. They further indicate that particles of very different geometries can have nearly the same scattering curve for the case of random orientation.

For non-centrosymmetric particles with definite rotation this is not the case. Here the scattering pattern is no longer circularly symmetric (77). The approximate exponential function describing the scattered intensity for an orientation defined by the vector $\underset{\sim}{\ell}_o$ is:

$$I(s) = n^2\bar{N} \exp(-4\pi^2 s^2 D^2(\underset{\sim}{\ell}_o)) \qquad (25)$$

Measurements for each orientation of $\underset{\sim}{\ell}_o$ then lead to the determination of an average inertial distance of the particle with respect to the plane perpendicular to $\underset{\sim}{\ell}_o$ and passing through the center of gravity. The principal advantage of the study of oriented particles is that the determination of inertial distances for different orientation gives a rather precise idea of the particle geometry. To obtain the greatest information it is advantageous to direct the incident beam along one of the principal axes of the particle. For example the SAXS pattern from an ellipsoid with the x-ray beam normal to the unequal axis will be an ellipse with its unequal axis perpendicular to that of the scatterer. The ellipsoid may be characterized as having axes a, a, and va. The variation of intensity with angle in the direction parallel to the unequal axis is $e^{-a^2v^2h^2/5}$ and $e^{-a^2h^2/5}$ in

the perpendicular direction. Thus intensity measurements at the two azimuthal angles are sufficient to characterize the parameters a and v which define the ellipsoid.

An important point in particle size analysis is that the expressions 23-25 do not take into account any effects of interparticle interference. Obviously such effects will lead to systematic deviations and will in general prohibit the use of particle size analysis. Only in cases where either the nature of the interparticle interference function is known which is extremely rare or in cases where a portion of the curve exists where interparticle interference is weak can one attempt to use this type of analysis.

The analysis of particle size distributions from SAXS has been much studied but still suffers from many fundamental difficulties. In general a particular form of the distribution function must be assumed which may or may not reflect the existing size distribution. Also particularly troublesome are the ambiguities of effects of distributions in particle size and distributions and uncertainties in particle shape. Hosemann (75) advocates the use of a Maxwellian distribution and describes a method for determining the parameters to characterize the distribution. Roess and Shell (76) have shown in general that it is difficult to uniquely determine distribution statistics for Maxwellian distributions of several particle geometries.

4. Scattering from concentrated systems. The expression for the intensity of scattering may be reformulated (78) to separate intra and interparticle interference effects:

$$I(h) = I_e(h)\bar{N}\left\{\overline{F^2(h)} - \frac{\overline{F(h)}^2}{v_1}\int_0^\infty \frac{\sin hr}{hr}\,[1 - P(r)4\pi r^2 dr]\right\} \tag{26}$$

where v_1 is the average volume available to each particle and P(r) is the interparticle interference function. The function P(r) has the property of having a maximum value at r = 0 and decreasing towards unity as r increases. In a dilute system P(r) is always one.

As the concentration of particles increases v_1 obviously decreases. An initial study of increase in particle concentration on scattering was made by Zernicke and Prins (78). These authors considered only the effect of concentration on v_1 and not on P(r). Subsequently the problem has been treated more generally by Debye (79), Yvon (80), Kirkwood (81), Born and Green (82), and Fournet (83). In general all of these treatments predict the occurrence of one or more scattering maxima with increased particle concentration. The exact predictions for scattering vary according to the assumptions concerning the nature of the interparticle thermodynamic potential and its influence on P(r). The theories have had some success in predicting the scattering from simple fluids such as condensed argon.

Fournet's treatment (82) of the fluid theory of Born and Green (81) gives the scattering relation for spheres:

$$I \sim F^2(hR)[1 + 2vb\Phi(2hR^*)]^{-1} \qquad (27)$$

where v is the number of scattering particles per unit volume and b is the Van der Waals covolume related to the distance of closest approach. Φ denotes the sphere scattering function of Equation 20. As pointed out by Riley and Oster (84) it can be shown that 27 gives a scattering maximum only for particle volume fractions above about 33%.

Hosemann (85) has taken the different view that one can treat scattering from condensed systems without resorting to an analysis of interparticle thermodynamics. His analysis is based upon the idea of the paracrystalline lattice which will be discussed in a later section.

5. Scattering from crystalline and paracrystalline systems. Crystalline and paracrystalline scattering systems are systems where a relatively high degree of ordering is present. The function P(r) in these cases is quite special. For a crystalline system the interference term will be zero everywhere except for special values. Crystal disorder or paracrystallinity will broaden the region for which the interference term is non zero. In general the subject of scattering of x-rays by crystals constitutes the special case of

x-ray diffraction. Pure diffraction is seldom seen in the small angle x-ray scattering region. Disorder in crystals may arise for several reasons. Guinier (86) discusses the effects of substitution and local displacements which give rise to short range disorders. The subject of crystal imperfections destroying long range order has been treated in depth by Hosemann (87) and is also reviewed by Guinier (88). This effect has been termed by Hosemann as paracrystallinity of the second kind. He considers the perturbed crystal to be built from three fundamental vectors, $\underset{\sim}{a}$, $\underset{\sim}{b}$, and $\underset{\sim}{c}$ which fluctuate independently. The interference factor, Z(s), calculated from such a system is:

$$Z(s) = \prod_{i=a,b,c} \frac{1 - p_i^2}{1 + p_i^2 - 2p_i \cos 2\pi u_i} \qquad (28)$$

where $u = sA$ and A is the lattice spacing. The function p characterizes the extent of deviation from the crystal and is given by:

$$p = \exp(-2\pi^2 s^2 D^2) \qquad (29)$$

where D is a coefficient which is characteristic of the distribution width. Figure 3 shows the form of Z(s) versus s in a typical case. As can be seen the function goes through a series of maxima before approaching a constant value at large s. It should be noted that the function is zero in

the region of s prior to the first node.

The equation for scattered intensity for a paracrystalline lattice of infinite size is given by:

$$I(h) = N_p \, \Delta\rho_p^{\,2} \, \overline{F_p^{\,2}}(h) \, Z(h) \qquad (30)$$

where F_p is the structure factor of the N_p particles arranged on the lattice and $\Delta\rho_p^{\,2}$ the density difference between the particles and the matrix. Hosemann has also considered the effect of finite size of the lattice. In this case scattering may also arise from the lattice as a whole. The scattered intensity in this case is given by:

$$I(h) = N_L \, \Delta\rho_L^{\,2} \, \overline{F_L^{\,2}}(h) + N_p \, \Delta\rho_p^{\,2} \, \overline{F_p^{\,2}}(h) \, Z(h) \qquad (31)$$

where F_L is structure factor of the N_L lattices with a density difference $\Delta\rho_L$ from the matrix. The effect of finite size is to give rise to zero order scattering in the region prior to the first interference node.

6. Porod's law and the scattering invariant. The analyses of scattering discussed thus far have concentrated on the zero order scattering region where intraparticle interference terms dominate and the intermediate scattering range where either intra or interparticle effects may be important. Important information can also be obtained in the scattering region at large scattering angles. The theory of SAXS in the infinite s limit was first thoroughly examined

by Porod (89-92). Porod (89) demonstrated that for a large number of scattering systems including dilute collections of spheres, rods, lamellae, etc., as well as for concentrated systems that the scattering intensity obeys the relation:

$$\lim_{s\to\infty} s^4 I(s) = K \tag{31}$$

The constant K is related to the specific inner surface of the scattering system, O_s, through the relation:

$$O_s = \frac{2\pi^2 \phi_2 K}{Q} \tag{32}$$

where ϕ_2 is the volume fraction of the dispersed phase. Q is the total scattering integral:

$$Q = \int_0^\infty s^2 I(s) ds \tag{33}$$

The specific inner surface can be defined as the ratio of the area of the phase interface to the volume occupied by the disperse phase. For a system of known particle shape knowledge of the specific inner surface can be used to calculate particle size (93).

The total integral Q can also be used to calculate the mean squared electron density fluctuation, $\overline{\eta^2}$. This requires that the intensity function in Equation 33 be placed on an absolute level. This procedure is discussed

in detail in a subsequent section. The mean square electron density fluctuation, $\overline{\eta^2}$, is obtained from the relation:

$$\overline{\eta^2} = \frac{4\pi Qa}{T\lambda N_A^2 P_s t_s} \tag{34}$$

where a is the sample to detector distance, N_A is Avogadro's number, P_s is the sample attenuated intensity of the incident beam, and t_s the sample thickness. T is the Thomson scattering factor which is equal to 7.9×10^{-26} if the energy flux is expressed per square centimeter.

$\overline{\eta^2}$ represents the averaged squared deviation of the electron density from the average electron density $\bar{\rho}$:

$$\overline{\eta^2} = \overline{(\rho - \bar{\rho})^2} \tag{35}$$

This quantity is simply related to the phase densities, ρ_1 and ρ_2, and volume fractions, ϕ_1 and ϕ_2, for a two phase system:

$$\overline{\eta^2} = \phi_1\phi_2(\rho_1 - \rho_2)^2 \tag{36}$$

Similarly for a three phase system:

$$\overline{\eta^2} = \phi_1\phi_2(\rho_1 - \rho_2)^2 + \phi_1\phi_3(\rho_1 - \rho_3)^2 + \phi_2\phi_3(\rho_2 - \rho_3)^2 \tag{37}$$

The derivation of Equation 31 relies on the assump-

tion that there is an infinitely sharp transition from one scattering phase to another and that the electron density within phases is strictly invariant (94). In real systems the density transitions between phases cannot be infinitely sharp but should have at least the width produced by the electron distribution of the basic structural elements of the phases. This effect has been treated by several authors including Hosemann (95), Ruland (94), Vonk (96), and Hashimoto (97,98). Hosemann (95) has shown that the effect of a finite transition thickness can be conveniently represented by a convolution of the ideal density distribution $\Delta\rho$ with a "smoothing" function h so that the observed density distribution becomes:

$$\Delta\rho_{obs}(z) = \Delta\rho(z) * h(z) \tag{35}$$

where * denotes the convolution product.

The convolution product of the two functions a(x) and b(x) is defined by:

$$a(x) * b(x) = \int_{-\infty}^{+\infty} b(\eta)a(x - \eta)d\eta \tag{36}$$

where η for scattering is the electron density.

The fundamental scattering equation, 16, may be rewritten as the self convolution of the electron density fluctuation, $\Delta\rho$:

$$I = \mathcal{F}(\Delta\rho^{*2}) \tag{37}$$

where $\mathcal{F}$ denotes the Fourier transform. Combining 35 and 37 leads to:

$$I = \mathcal{F}((\Delta\rho * h)^{**2}) \tag{38}$$

This can be shown to reduce to

$$I = I_{ideal}\, H^2 \tag{39}$$

where I_{ideal} is the intensity function with infinitely sharp boundaries and H is given by:

$$H = \mathcal{F}(h) \tag{40}$$

The smoothing function H has been evaluated for different transition zone geometries. For a linearly varying boundary characterized by:

$$h(z) = \begin{cases} 1/t & 0 \leq z \leq t \\ 0 & z > t \end{cases} \tag{41}$$

H is given by:

$$H = \frac{\sin^2 \pi ES}{(\pi Es)^2} \tag{42}$$

This quantity is shown in Figure 4.

An expansion of the same function followed by trunca-

tion of terms of higher than second order leads to:

$$H = 1 - 2\pi^2 E^2 s^2 \tag{43}$$

which is valid for small σs. One problem with this expansion approximation is that the whole analysis is carried out in the large s region according to the limiting form of Equation 31. In some cases (99) the approximation may be poor.

The intensity for the linear transition zone is thus predicted to be modified according to the relation:

$$I = (K/s^4)(1 - \pi^2 E^2 s^2/3) \tag{44}$$

For the case of an intensity function, $\tilde{I}(s)$, measured with infinitely long and narrow slits it can be shown that:

$$\tilde{I}(s) = \frac{K}{2s^3}\left[1 - \frac{2\ ^2E^2s^2}{3}\right] \tag{45}$$

Using 45 a linear plot of $s^3\tilde{I}(s)$ versus s^2 or $s\tilde{I}(s)$ versus s^{-2} can be used to obtain the transition width, E. Vonk (96) has measured E for various polymeric systems and found values in the range of 4 to 25 Å.

Hashimoto has solved the case of a Gaussian transition zone shown in Figure 5 where:

$$h(z) = 2\pi\sigma^2 \exp(-z^2/2\sigma^2) \tag{46}$$

In this case the intensity is modified according to:

$$I = \left[1 - (4\pi^2\sigma^2)s^2 + \theta(\pi\sigma s)^4\right] \tag{47}$$

He contends that the higher order term θ can be neglected although the previously mentioned objection can again be raised. The transition zone boundary for this case can be shown to produce an equivalent effect to a linear boundary provided that:

$$t = 2\sqrt{3}\,\sigma \tag{48}$$

Density fluctuations within phases lead to excess scattered intensity above the Porod law limit. This is in contrast to the case of a finite transition zone where negative deviations are observed. Provided there is no correlation between the density fluctuation of one phase with that of another the intensity components are simply additive (96). For a two phase system:

$$I = CF(\gamma) + \phi_1\Delta\rho_1\,\overline{F\ell_1} + \phi_2\Delta\rho_2\,\overline{F\ell_2} \tag{49}$$

where C is a constant relating the intensity and $F(\gamma)$ for the case of no internal fluctuations and $\overline{F\ell_1}$ and $\overline{F\ell_2}$ stand for the intensity component of the density fluctuation within phase one and two, respectively. For a three dimensionally homogeneous fluctuation $\overline{F}$ is given by (78):

$$\overline{F\ell} = \frac{\langle N^2\rangle_V - \langle N\rangle_V^2}{\langle N\rangle_V} \tag{50}$$

where N is the number of electrons and the average is taken over a volume, v, which is large compared with the interaction between the atoms and molecules within a given phase. Since SAXS does not distinguish between the time average and space average of the density, amorphous substances with frozen in liquid structures as well as systems with a gas type distribution of foreign atoms or vacancies will show homogeneous density fluctuations. For systems with strongly anisotropic disorder the density fluctuations can become inhomogeneous in which case the fluctuation component is modified. For example if the order is essentially one dimensional and the fluctuation of the density projected onto a straight line parallel to the direction of disorder is $F\ell_1$ one obtains:

$$\overline{F\ell} = \frac{\tau F\ell_1}{2\pi s^2} \tag{51}$$

where τ is the surface density of electrons in the two dimensional entities which participate in the fluctuation.

Internal density fluctuations which are three dimensional and homogeneous modify Porod's law according to:

$$s^4 I = K + s^4 U \tag{52}$$

or

$$s^4 (I - U) = K$$

where U denotes the internal fluctuation component. For a two phase system:

$$U = \phi_1\rho_1 \overline{F\ell_1} + \phi_2\rho_2 \overline{F\ell_2} \qquad (53)$$

Equation 52 predicts that a plot of s^4I versus s^4 should yield a straight line with slope U and intercept K.

Internal density fluctuation scattering has been reported recently in several homopolymer systems (100,101). In these cases the fluctuations present are due to thermal and not compositional changes. As previously mentioned internal density fluctuation scattering has been reported for a number of copolymer and ionomer systems. In these cases the fluctuations arise principally from compositional effects.

The problem of systems exhibiting both finite width transition zones and internal density fluctuations has been treated by Bonart for polyurethanes (102). In this work a plot of $s^3\tilde{I}(s)$ vs. s^2 is made to evaluate U from the slope. The intercept at the ordinate is termed K_∞. A curvature away from a linear relation is observed in some cases at large s by Bonart in these plots but this is neglected. A plot of $\ln[s^3(\tilde{I}(s) - U) - K_\infty]$ is then made to evaluate the transition zone thickness from the slope and a constant K from the intercept. The ratio K_∞/K is interpreted by Bonart to represent the fraction of phase structures present with boundaries. This analysis has been criticized by Koberstein

(99). He points out that it is unreasonable to believe that some phases have perfectly sharp boundaries while all others have some finite boundary thickness. The problem may result from the neglect of the curvature in the initial plot at high s values. This curvature could possibly result from a distribution of transition zone boundaries or in phase structure sizes.

7. Scattering models for semi-crystalline polymers. Several different approaches have been used to describe the SAXS from semi-crystalline polymers. These include the Tsvankin-Buchanan model (103), the Hosemann linear paracrystalline model (104), the Vonk correlation function approach (105, 106), and the recently described interface distribution function approach of Ruland (107). Experimental methods and data treatment have been recently reviewed for these systems (108, 109,110). The Tsvankin-Buchanan model consists of a one-dimensional model of alternating crystalline (high density) and amorphous (low density) regions. Scattering from such an assembly can be calculated from the projection of electron density onto a line. A trapezoidal electron density profile is assumed. An exponential amorphous thickness distribution and a symmetrical rectangular crystal thickness distribution are adopted. Due to the type of distributions chosen, the crystallinity is uniquely related to the position and width of the scattering maximum for a given dispersion of

thickness and boundary layer widths. Calibration curves were proposed which permit the determination of the average crystal and amorphous layer thicknesses from the experimental peak positions and half widths. While this approach is convenient it fails to use all of the information of the entire intensity function. Warner et al. (111) have shown that calculated curves regenerated from the calibration parameters give relatively poor fits to the experimental intensity curves.

The Hosemann approach (104) as extended by Bramer (112,113) and Wenig (114,115) generalizes the Tsvankin-Buchanan model. Here the lattice consists of a finite number of lamellae in which the crystalline and amorphous regions are arranged according to paracrystalline statistics. A finite transition zone between the crystalline and amorphous layers is also included. The final equation for the model becomes:

$$I(s) = \frac{K}{s^2} \mathrm{Re}\left\{ \frac{N(1 - F_a)(1 - F_c)}{(1 - F_d)} + F_c \left[\frac{1 - F_a}{1 - F_d} \right]^2 (1 - F_d^N) \right\} \cdot Z_1(s) \qquad (54)$$

where K is a normalization constant. F_c and F_a are the structure factors for the crystalline and amorphous layers where:

$$F_\alpha = \int_0^\infty H_\alpha(\alpha)\ \exp(-2\pi i s\alpha)\, d\alpha \tag{55}$$

and

$$F_d = F_a - F_c \tag{56}$$

$Z_1(s)$ accounts for the finite transition zone thicknesses and is given by:

$$Z_1(s) = \frac{1}{(2\pi i s)^2 E} \left| 1 - \exp(-2\ isE) \right|^2 \tag{57}$$

where E is the transition zone thickness. N is an explicit parameter which is mean number of parallel lamellae averaged over the clusters in the entire array. Typically Gaussian distribution functions have been adapted for the crystalline and amorphous thicknesses:

$$H_\alpha(\alpha) = \frac{1}{\left[2\pi\overline{(\Delta x_\alpha)^2}\right]}\ \exp\left[\frac{-(x - x_\alpha)^2}{2\overline{(\Delta x_\alpha)^2}}\right] \tag{58}$$

The explicit parameters used to fit the data are the crystal, amorphous, and transition zone thicknesses and crystal and amorphous thickness distribution parameters and N. In several studies (111,114,115) values of N of 2.0 or less have been reported. The physical interpretation of this is not clear. Baczek (110) has suggested that N represents

the equivalent number of exactly parallel lamellae. Other authors (115) have merely viewed N as a parameter describing the degree of angular disorder in the lamella stack.

The correlation function approach to scattering was originally proposed by Debye et al. (116,117) and has been further discussed by Porod (91) and Vonk (105,106). The correlation function is defined as:

$$\gamma(r) = \frac{\langle \Delta\eta_1 \ \Delta\eta_2 \rangle_r}{\langle \Delta\eta^2 \rangle} \tag{59}$$

where $\Delta\eta_i = \rho_i - \bar{\rho}$ as before. Vonk has proposed the following relation for calculation of the correlation function from the experimental intensity function:

$$\gamma(r) = \frac{\int_0^\infty s^2 I(s)_e \cos 2\pi r \cdot s}{\int_0^\infty s^2 I(s)_e \, ds} \tag{60}$$

$\gamma(r)$ is normalized so that:

$$\gamma(0) = 1$$
$$\gamma(\infty) = 0 \tag{61}$$

The position of the first maximum in $\gamma(r)$ corresponds approximately to the average crystal plus amorphous thickness. $\gamma(r)$ as defined by Equation 49 is a one dimensional correla-

tion function. The experimentally calculated correlation function is compared to theoretical correlation functions calculated for a linear two phase model of randomly oriented alternating electron density regions. Various distributions have been used for the crystalline and amorphous thicknesses. The major difference between the Vonk treatment and the Hosemann linear paracrystalline model is the former assumes an infinite one-dimensional array while the latter analyzes finite clusters. Warner (111) has questioned the possibility of infinite stack models in fitting the scattering from systems involving significant amounts of angular lamellar disorder such as polymer blends containing a non-crystallizing component.

The interface distribution approach of Ruland (107) proposes the use of an alternate function which is the correlation function of the first derivative of the density function. Ruland feels that the spacings and thickness distributions can be more easily extracted in this manner. The approach is largely analogous to a sharpened Patterson function used in diffraction analyses. Both the Vonk and Ruland approaches suffer from the problem that errors may be propagated in the Fourier inversion calculation. Initially these approaches involve less a priori assumptions about the scattering system. However if it is necessary to resort to theoretical models of the calculated functions this advantage is lost. In view of the foregoing discussion it has

been decided to use the Hosemann linear paracrystalline model in analysis of semi-crystalline polymers in this work. However the uncertainty regarding the interpretation of the parameter N in that model is noted.

8. Absolute intensity measurements. In order to calculate the SAXS invariant it is necessary to place the scattering intensities on an absolute level. Absolute intensity is defined as the ratio of the scattered intensity to the incident intensity on the sample. To the high intensity of the incident beam it is necessary to attenuate the beam before any measurement is possible. Attenuation can be accomplished by either using calibrated filters or by chopping the beam with a perforated rotating disc. The methods of performing absolute intensity measurements have been discussed by Kratky (116,117) and Hendricks (118). In this work the absolute intensity has been measured through the use of a secondary Lupolen polyethylene sample. The scattered intensity at a particular scattering angle (0.59° 2θ for CuK_α radiation) has been measured for this sample through main beam attenuation. The energy per centimeter length of primary beam after sample attenuation is given by:

$$P_s = \frac{K\ I_s\ a\ A}{F} \qquad (62)$$

where K is the calibration constant, A the sample attenuation factor, F the counting tube slit area and I_s the intensity

of scattering from the standard sample at the calibration angle. The sample attenuation factor may be calculated from the absorption coefficients of the component atoms. However it is recommended to measure it experimentally due to uncertainties in thickness.

9. Collimation and slit desmearing. The theories of SAXS presented in the above sections are derived primarily on the basis of a point-like cross section of the incident beam which can be closely achieved by collimation with small pinholes. In practice the use of such pinholes necessitates very long counting times to accumulate sufficient intensities for statistical accuracy. Two approaches are in principle possible to compare theories with slit collimated intensities. The first is to correct the experimental curves to give the corresponding point-like patterns. This is known as slit desmearing. The second involves including the effects of slit smearing in the theory. In general the effect of slit smearing depends on the particular slit geometry used in the experiment. However in a large number of cases the geometry closely corresponds to the infinite length slit approximation. The approach of smearing of theoretical models has been confined to the case where this approximation is observed to hold. In this work the first approach has been used in most cases since the infinite height approximation was not valid in many cases and since smeared theoreti-

cal expressions were not generally available.

Guinier (119,120) has shown that for slits of arbitrary height (length) but of negligible width the experimental intensity curve, $\tilde{I}(s)$ is related to the equivalent intensity function for point collimation, $I(s)$ by:

$$\tilde{I}(s) = \int_0^\infty W(\phi)\, I\,(s^2 + \phi^2)^{1/2}\, d\phi \qquad (63)$$

where $W(\phi)$ is a weighting function describing the shape of the main beam intensity profile along the length of the slit. $W(\phi)$ is normalized so that:

$$\int_0^\infty W(\phi)\, d\phi = 1 \qquad (64)$$

The nature of $W(\phi)$ depends on both the collimation geometry and the nature of the scattering pattern. The scattering system may be considered to be of infinite height providing:

$$L > 2m + d \qquad (65)$$

where L is the height of the homogeneous part of the beam at the receiving slit, d is the height of that slit, and m is the angular distance measured in the plane of registration. Systems not meeting this criterion are of finite height. For the case of a scattering pattern of one maximum (ring) the beam must have a height equal to the diameter of the ring

for the infinite height assumption to hold. For the case of infinite height $W(\phi)$ is a constant and it no longer satisfies the normalization relationship.

The method of desmearing for infinite height systems has been described by Vonk (121). The inversion of Equation 63 has been shown by Guinier to yield:

$$I(s) = C \int_0^{\infty} \frac{d\tilde{I}(s^2 + u^2)^{1/2}}{d(s^2 + u^2)^{1/2}} \cdot \frac{du}{(s^2 + u^2)^{1/2}} \qquad (66)$$

where C is a constant and u is a variable of integration. The differentiation indicated by Equation 66 can greatly amplify random errors in the intensity function. To avoid this Vonk (121) has smoothed the scattering curve by fitting it with a Fourier series characterized by a variable number of coefficients. The details of the fitting procedure and subsequent integrations are described in an appendix along with a listing of the computer program.

Kratky, Porod, and Kahovec (125) have shown that a Gaussian weighting function is valid for $W(\phi)$ for a wide variety of systems:

$$W(\phi) = 2p\pi^{-1/2} \exp(-p^2\phi^2) \qquad (67)$$

In this case the desmeared intensity is given by:

$$I(h) = \frac{-\exp(p^2h^2)}{p\pi^{1/2}} \int_h^\infty \frac{N'(t)\,dt}{(t^2 - h^2)^{1/2}} \qquad (68)$$

The constant p is determined by the slit height with point collimation corresponding to the limit of infinite p. N'(h) is the first derivative of the intensity function, N(h), where

$$N(h) = \tilde{I}(h)\ \exp(-p^2h^2) \qquad (69)$$

Schmidt (126) has discussed numerical methods for taking the derivative in Equation 68. Procedures are analyzed in terms of propagation of random errors in the input data and introduction of other errors. The recommended analysis involves the numerical differentiation of N(h) which is represented b least squares fitting a cubic polynomial taking six experimental points at a time. The numerical differentiation is carried out using the rearranged equation of Schmidt and Hight (127):

$$I(h) = \frac{-\exp(p^2h^2)}{p\pi^{1/2}} \sum_{i=0}^{\infty} \int_{(j+1)\Delta}^{(j+i+1)\Delta} \frac{ds\,N'(s)}{(s^2 - h^2)^{1/2}} \qquad (70)$$

In this expression i and j are taken to be integers and $h = i\Delta$. The slit desmeared intensity is given as a sum of terms which are the product of the experimental intensity values F_j and constant T_{ij} which depend on the collimation

system:

$$I(j\Delta) = \sum_{i=0}^{\infty} T_{ij} F_{j+i-2} \qquad (71)$$

Hendricks and Schmidt (128) have described the calculation of the weighting function for different collimation geometries. The Beeman four-slit system described by these authors is essentially the same as the geometry used in the Rigaku-Denki camera described in a later section. The Gaussian weighting function form is also assumed to be valid in this work. In this case the constant p in Equation 67 is given by:

$$p = (\pi)^{1/2} W(0) \qquad (72)$$

The exact program for finite height desmearing (SAXSC) is listed in an appendix. The procedure used is identical to that of Baczek (110).

The study of anisotropic scattering systems presents special problems with regard to x-ray collimation. An inherent assumption in all of the slit desmearing procedures is that the scattered intensity depends solely on the scattering angle 2θ and has no azimuthal dependence. Generalizations of slit desmearing to other scattering shapes have been treated by Kranjc (129) and Synecek (130). In Kranjc's treatment the experimental intensity function is expressed as the

convolution of the point intensity function and the intensity distribution on the "trace of the primary beam." In the approach of Synecek accurate integrated intensities must be determined at various azimuthal angles. Both of these approaches remain only theoretical and have not been used in practice. The measurement of SAXS on an anisotropic system followed by desmearing with these approaches would involve extensive angular measurements followed by elaborate computation of the desmearing correction. The large number of angular measurements required would require long times using a conventional x-ray camera with a single detector just to obtain a single pattern. To a large degree the great difficulty in performing such desmearing correction has led to the use of position sensitive detectors. These detectors which are described in Chapter II permit the simultaneous collection of data at different angles. This time savings permits the use of pinhole geometries and the subsequent intensity loss acceptable. The use of pinhole geometry makes the use of any collimation corrections unnecessary in most cases.

C H A P T E R I I

DEFORMATION STUDIES OF AN ETHYLENE-METHACRYLIC ACID IONOMER

A. Introduction

In the review of the first chapter it was noted that other workers (15,29) had reported no change in the 3-4° 2θ SAXS scattering peak for ethylene-methacrylic acid ionomers on stretching. This was found despite the fact that clear evidence for crystalline orientation was present. This observation has been an important consideration in the evaluation of models for ionomer structure. For example the spherical aspect of the shell-core model of MacKnight et al. (28) was adopted in part because rotation of such a structure would lead to no change in scattering, while rotation of non-spherical structures would lead to an azimuthal variation. The absence of any azimuthal dependence of scattering in deformed samples has also been cited as evidence against the Cooper (25) paracrystalline lattice model. Such a homogeneous model would be expected to produce SAXS spacing changes corresponding to the dimensional changes of the sample.

In view of the importance of the deformation studies it was deemed by this author reasonable to repeat these

studies in a more rigorous fashion than in the prior studies. In particular the following aspects of this study are significantly different from prior work.

1. The ionomer studied contains essentially no separate crystallinity of the ethylene units. This was achieved by using a sample of high methacrylic acid content ionized to a high degree and then quenching from the melt. The absence of crystallinity eases the interpretation of scattering since only ionic structures are present. In addition any deformation mechanisms observed can be attributable solely to the ionic structures.

2. The scattering was measured using the ten meter two dimensional position sensitive detector at the Oak Ridge National Laboratories (ORNL). The availability of this excellent system is a vast improvement in sensitivity over the photographic methods used in the previous studies.

3. The scattering was observed for higher deformations than in previous studies. In this work the entire deformation range from 0-300% was explored while for example in the studies of Taggart (29) only deformations less than 70% were studied.

These three aspects must be viewed as the principal explanation why pronounced changes were observed in the ionomer scattering peak on deformation in this study which were not seen by the other authors. To pinpoint which or more of the three factors is in fact the reason is not possible

at the present time. This would require for example studies at lower methacrylic acid contents using the ORNL apparatus. However it can be said that in view of the fact that the system studied in this work contained no separate crystalline structure the results must be viewed as more representative of the behavior of the ionic aggregates than the results of the prior studies.

B. Experimental

1. Sample preparation and characterization. An ethylene-methacrylic acid copolymer containing 6.1 mol % methacrylic acid units was obtained from the DuPont Company. The number average molecular weight has been characterized as 5,400 with a weight average molecular of 25,500. The measurements were determined by gel permeation chromatography using trichlorobenzene as a solvent at 137°C. The melting point has been measured as 93°C by differential scanning calorimetry at a heating rate of 20°C/minute. The copolymer was neutralized by dropwise addition of cesium methoxide to a 1% solution of the copolymer in filtered p-xylene.

The solution of the copolymer was prepared in a four-neck reaction kettle with stirrer and heated to reflux (137°C). Nitrogen gas was bubbled through the solution to prevent oxidation of the polymer. A solution of cesium methoxide in p-xylene was made by reacting about one half gram of cesium metal with methanol (~2 ml) and then adding

~20 ml of p-xylene. This was added to the copolymer solution leading to precipitation of the salt form of the copolymer. This precipitate was removed and added to excess methanol, filtered, digested in methanol overnight to remove excess cesium, and then dried.

Films were compression molded at 110°C with pressure cycled until a level of 10,000 psi was reached. The films were quenched into a mixture of dry ice and isopropanol and then dried in a vacuum oven at room temperature.

The percent ionization of the films was characterized by infrared absorption and x-ray absorption measurements. The infrared determination was made according to the procedure of MacKnight et al. (115) using the equation:

$$\% \text{ ionization} = \left[1 - \frac{\text{integrated absorbance/cm ionized}}{\text{integrated absorbance/cm acid}}\right] \times 100 \qquad (73)$$

The absorbance, A, was measured for the 1700 cm^{-1} carbonyl bond where A is defined as log I_o/I. I_o is the incident and I the transmitted intensity. The infrared scan of one of the partly ionized films is shown in Figure 6. The integrated absorbance per centimeter of the 1700 cm^{-1} carbonyl bond was calculated to be 2700. The integrated absorbance per centimeter of the un-ionized material was measured by Earnest (57) to be 43,000 cm^{-1}. The percent ionization of the copolymer is calculated to be 94% using the two cited

values and Equation 73. The absorbance of the un-ionized material was measured by Earnest at various film thicknesses to confirm Beer's law for these materials. The film thickness of the partly ionized material was 9.4×10^{-3} cm. X-ray absorption was used to characterize the degree of ionization of the exact film to be used for scattering measurements. The x-ray attenuation factor, A, is measured according to the relation:

$$A = I/I_o \tag{74}$$

where I_o is the intensity scattered from a standard scatterer at a particular angle. In this laboratory a styrene-butadiene-styrene (SBS) black copolymer is used which scatters strongly at 0.2° 2θ. I is the scattered intensity at this same angle for the SBS sample with the absorbing sample placed immediately before the detector. A is related to the linear absorption coefficient, μ (cm^{-1}), of the sample (132):

$$\ln A = \exp(-\mu t) \tag{75}$$

where t is the sample thickness. The linear absorption coefficient is related to the mass absorption coefficient μ_m (cm^2/gm):

$$\mu = \mu_m \bar{\rho} \tag{76}$$

where $\bar{\rho}$ is the mass density. The validity of Equation 76 for any sample regardless of the extent of phase separation is

demonstrated in Appendix I. The mass absorption coefficient can be calculated for a sample of known chemical composition. The computer program Ionize listed in the appendix calculates μ_m for various ionomer systems as a function of the percent ionization. The program compares these values to the experimentally determined μ_m to determine the percent ionization. An experimental value of 65.2 cm^{-1} was measured for μ for a sample of 0.036 cm thickness. The mass density measurement was made in a density gradient column containing glycerol and methyl alcohol with a temperature of 23°C regulated to 0.05°C by a jacket with circulating water. The mass density was measured to be 1.12 gm/cm^3. The experimental value of 58.2 for μ_m corresponds to 85% ionization.

WAXS has been measured on the sample in the unstretched state and also after the maximum elongation of 300% was obtained. The percent elongation, X, is defined by:

$$X = \left(\frac{L - L_o}{L_o} \right) \times 100 \qquad (77)$$

WAXS measurements were made on the in-lab built diffractometer using CuK_α radiation with a wavelength of 1.54 Å. The diffractometer uses slit collimation and a scintillation detector with pulse height analysis. The apparatus has been described in detail elsewhere (133).

SAXS has been measured primarily on the ten meter two-dimensional position sensitive camera with rotating anode

generator at ORNL. This apparatus has recently been described by Hendricks (133). A schematic diagram of the camera is shown in Figure 7. The spectrometer uses a 6 Kw Rigaku-Denki rotating anode generator, a graphite crystal monochromator, and a monitor to measure incident beam intensity changes.

The collimation system consists of two pinholes separated by 5 meters. The first is a 1 mm diameter hole in a lead sheet mounted on an x-y positioning stage on the front of the beam line. The second consists of a set of four specially polished tungsten edges mounted to make a 1 mm square hole.

A 125 μm mylar foil tilted at 45° to the beam mounted in a vacuum chamber after the first hole serves to reflect a small portion of the incident beam to a scintillation detector. This beam monitoring system has been shown to be linear over a wide range of incident beam intensity.

The specimen chamber consists of a 30 x 30 x 35 cm vacuum chamber containing externally operated x-y positioning devices for the second slit and specimen holder. Scattered radiation emerges at the end of the flight path through a 30 cm diameter, 0.5 nm thick beryllium window. The entire flight path from the first pinhole to the exit window is evacuated to 20 μm of mercury.

The detector is a Borkowski and Kopp (134) two-dimensional position sensitive proportional counter which

operates on the rise-time method of signal processing. The actual detector elements are high resistance wires. When an x-ray photon strikes a wire signals are generated in two opposite directions. The difference in time required to detect the pulse at two symmetrically placed positions is used to locate the position of initial impingement on the wire. The detector is gas enclosed.

For this study a sample to detector distance of 1.2 meters was used making the total camera dimension 6.2 meters. The 1.2 meter distance is the minimum available at the present time. Despite using this minimum distance it was only possible to obtain scattering data up to an angle of 4° 2θ (70 mrad). Because of this limitation it has not been fully possible to analyze the large angle scattering region. A discussion of ways to obtain the maximum resolution at small angles is given by Hendricks (133). Since this condition was not of particular importance in the current study it will not be discussed here.

The x-ray generator was operated at 40 Kv and 30 ma which is typical. All other conditions were the same as described by Baczek (110).

Data were processed via a Modular Computer System, Modcomp II/220 CP. Results can either be displayed graphically or on hard copy output using this system. A computer program to extract azimuthal cross-section data has been written by Baczek and Carlson (110) and is part of the ORNL

system.

The sample was stretched using the sample stretcher accessory of the Rigaku-Denki SAXS camera at the University of Massachusetts. The original sample length to width ratio was about 4 so that deformation can be expected to be primarily uniaxial. The SAXS scattering pattern, parasitic scattering, and sample attenuation factor were measured at each elongation. Times for scattering runs were typically 3-4 hours. Typical total count values of 200-1000 were obtained in the region of the ionomer scattering peak. These correspond to precisions ranging from 3-7%. The parasitic scattering was measured with no sample in the spectrometer and then normalized according to the sample attenuation factor. These intensity values were subtracted by the computer at each angle.

After each elongation of the sample a time of 3-4 hours was allowed to elapse before a scattering run was made. This was done to avoid measuring time dependent relaxation effects which might be expected to occur for these samples since they are above the glass transition temperature. All scattering measurements were made at room temperature as no other temperature control was available.

C. Results

1. WAXS. WAXS scans over the angular range of 15-30° 2θ are shown for the cesium salt in Figure 8. Figure 8a shows

the data for the unstretched sample. A single peak is observed at an angle of 19.8° 2θ corresponding to the angle of the amorphous halo as reported for polyethylene and these copolymers by numerous workers (2,135). The crystalline 110 and 200 reflection normally seen at 21.4 and 23.7° 2θ are not observed. The absence of WAXS crystalline diffraction does not necessarily mean that no crystallinity is present since very small crystallites in poorly crystallized materials do not give appreciable scattering. However in general the absence of diffraction rings does indicate the overall crystallinity to be less than about 10%. On the basis of previous calorimetric studies by MacKnight (136) and Otocka and Kwei (137) of the crystallinity of salt samples of similar salt co-unit concentration, the crystallinity can be expected to be in the range of 5-6%. For crystallization in this range the contribution of crystal phase structures to SAXS can be expected to be negligible.

Figure 8b contains the WAXS observed from the 300% stretched sample at azimuthal angles of 0° and 90° to the stretching direction. The amount of elongation can also be defined in terms of λ where:

$$\lambda = L/L_o \tag{78}$$

The WAXS scans show only an amorphous halo. Thus no crystallinity is developed on stretching. The scattering pattern shows a weak azimuthal dependence with higher scattering at

90° than 0° azimuthal angle. This is indicative of amorphous orientation in the stretch direction. The azimuthal dependence was confirmed photographically. No attempt was made to quantitatively measure the amount of amorphous orientation from WAXS. In general other techniques such as infrared dichroism and birefringence measurements are more sensitive to amorphous orientation and should be used preferentially to WAXS.

2. SAXS. Figure 9 shows the SAXS contour plots at elongation ratios of 0-300%. The stretching direction is vertical in all plots. The lines in these plots connect points of equal scattered intensity. The plots cover an angular range of about 0.11-4° 2θ (2-70 mrad). The absolute difference between two consecutive contour lines corresponds to about 300 counts. The contour plots are presented here to present a general overview of the data. As can be seen the pattern loses its spherical symmetry in the range of 30-60% deformation. It develops into a two point pattern with strong intensity maxima observed at 90° azimuthal angle for elongation of 100% or higher. The central portion of the pattern becomes elongated in a direction perpendicular to the stretching direction. This would appear to indicate the existence of a rod-like structure oriented with its long direction in the stretching direction. As will be seen in further discussion such a simple interpretation is not pos-

sible in view of the importance of interference effects. The interference effects referred to are the ones leading to the scattering maxima. Even though these effects decrease at smaller angles they may be enough to give the elliptical pattern at small angles. The elliptical pattern in this case would arise since the interference effects only affect the scattering at azimuthal angles about 90°.

The scattering data are plotted in Figures 10-16 in terms of intensity vs. 2θ. Smooth curves have been fit through the data by hand. The data for 9% elongation are not shown since these are negligibly different than for the unstretched case. Intensity functions are shown for azimuthal angles, ψ, of 0° and 90° to the stretching direction for all of the stretched samples.

The scattering pattern for the unstretched sample (Figure 10) represents data which have been circularly averaged over a number of azimuthal angles. The pattern exhibits a maximum at 2.6° 2θ which corresponds to a Bragg spacing of 34 Å as calculated from:

$$d = \frac{\lambda}{2 \sin \theta} \tag{79}$$

A strong zero order scattering component is observed below about 1° 2θ. This pattern is very similar to those previously observed for ionomers. Taggart (29) observed peaks in the range of 2.5-3.5° 2θ for Cs^+ salts of these materials. Long-

worth and Vaughan reported a peak at 3.4° 2θ for a similar material. The discrepancies in peak position probably arise from differences in sample preparation especially thermal treatment. Cooper (138) has shown that the shape and position of the peak can be changed by annealing.

A comparison of the intensity function at 0° and 90° for the stretched samples in Figures 11-16 show several effects:

1. The scattering at $\psi = 0°$ decreases continually with respect to that at $\psi = 90°$.
2. The scattering peak decreases in scattering angle at $\psi = 0°$ up to about 60% elongation and then is no longer observed at higher elongation.
3. The scattering peak at $\psi = 90°$ shifts very little in position but increases in intensity and sharpens with sample elongation.

Figures 17 and 18 compare the intensity functions at several elongations at 0° and 90° azimuthal angles respectively. These figures clearly show the overall decrease in intensity at $\psi = 0°$ and increase at $\psi = 90°$. To calculate these curves intensities were normalized according to sample thickness, t, and attenuation factor, A, according to:

$$I_N = I_o\left(\frac{1}{t}\right)(A) \qquad (80)$$

Normalization for incident beam intensity fluctuations has

already been included since the data has been normalized according to the monitor intensity which is proportional to the incident flux on the sample. Table 1 lists the values of t and A for the various elongation ratios.

The observed spacing changes calculated from the peak position and Equation 79 are plotted in Figure 19 for $\psi = 0°$ and $\psi = 90°$. The error in the spacing was estimated by considering the maximum and minimum peak positions that could be reasonably consistent within the statistical fluctuations in the data. The dashed lines in Figure 19 are those predicted by an affine deformation of the peak spacings. In an affine deformation the spacings at 0° azimuthal angle, $d_{||}$, and at 90° azimuthal angle, $d_{\perp}$, are predicted to change according to the relations:

$$d_{||} = \lambda\, d_o$$
$$d_{\perp} = \lambda^{-1/2}\, d_o \qquad (81)$$

where d_o is the spacing in the undeformed sample. In an affine deformation the microscopic structure changes according to the macroscopic dimensions of the sample. As seen from Figure 19 the deformation in this study is very non-affine especially in that no change is observed for $d_{\perp}$ with elongation.

In view of the fact that data collection was limited to angles less than about 4° 2θ no attempt has been made here

to carefully analyze the tail of the scattering curve according to Porod's law (Equation 31). For this reason the SAXS invariant cannot be obtained.

Based on analysis collected on the Rigaku-Denki camera at the University of Massachusetts it has been determined that it is generally necessary to collect data up to at least 6 or 7° 2θ to accurately evaluate the Porod law parameters for most ionomers. This is clearly not possible with the available ORNL data. This reduces the amount of information which can be obtained concerning the extent of phase separation as a function of elongation. However since the intensity curves have been normalized according to Equation 80, it is possible to analyze relative intensity changes. As will be seen this possibility will be quite powerful in evaluating different proposed models for ionomer structure.

D. Analysis and Discussion

As previously mentioned in the first chapter a number of different models have been proposed for the physical structure of ionomers. In this section these models will be analyzed critically in terms of the experimental data of this study. To carry out this evaluation it was deemed desirable to place each of the models on a quantitative basis so that intensity functions could be generated and compared to the experimental scattering curves. In some cases the models have not been sufficiently defined in the literature

to be unambiguously quantified. In these cases several possibilities are generally considered here which seem to best represent the range of possible physical interpretations. The modeling approach has the disadvantage that even though one model may fit the experimental results one cannot conclude that it is the only model which may do so. However as yet there are no known means for unequivocal deduction of the scattering system geometry from scattering patterns.

1. The paracrystalline lattice model. In this model the ionomer is assumed to consist of ionic aggregates arranged on a disorder lattice. The model is characterized by Equations 28-31 of Chapter I. The principal advocates of this model have been Cooper et al. (25). Other authors (30,31) who have explained the ionomer SAXS peak in terms of a preferred distance between ionic aggregates are also essentially using a paracrystalline lattice interpretation since only for such a lattice does a preferred distance really exist.

As discussed previously Cooper interprets the SAXS maximum as arising from inter-aggregate interference. He has correlated the observed Bragg spacing with the volume per scattering site through the adjustable parameter f^{-1} which corresponds to the number of ionic groups per aggregate. The reported values of f^{-1} of 2-7 correspond to small aggregates expected to have radii of about 3-5 $\mathring{A}$ (12).

It is not completely clear if these authors believe

the paracrystalline lattice to extend throughout the sample (infinite) or just to be present in smaller sections of the sample (finite). In a private communication with Cooper (139) the former was indicated. However it seems that to have a paracrystalline lattice throughout the sample would be stoichiometrically impossible. For example in a 3.6 mol % ethylene-methacrylic acid copolymer ionized 50% with Na^+, Cooper et al. have calculated a volume of $44.8 \times 10^{+2}$ $\mathring{A}^3$ per scattering site. The scattering sites for this sample are said to be trimers. For the whole sample the number of grams of neutralized MAA units per cm^3 can be calculated to be 0.06 on the basis of the stoichiometry and the density of 0.941 gm/cm^3. But by dividing the weight of a trimer aggregate by the volume per scattering site one obtains 0.12 gm/cm^3. Thus to achieve a paracrystalline lattice throughout the sample the Cooper model requires more ions than are present in the system. This difficulty could be avoided by postulating that such a lattice is only present in about half of the sample.

In terms of scattering the paracrystalline lattice can be considered to be infinite or finite. In the infinite lattice which is characterized by Equation 130 there is no zero order scattering from the lattice itself. In the finite case (Equation 31) such scattering does exist depending on the lattice size. Both of these cases will be considered.

a. Infinite paracrystalline lattice. In this sec-

tion only the angular dependence of scattering is being analyzed. For this purpose Equation 30 can be rearranged to give:

$$\frac{I(h)}{N_p \, \Delta\rho_p^{\,2}} = \overline{F_p^{\,2}(h)} \; Z(h) \tag{81}$$

To compare the theoretical scattering from 81 to the experimental curve a normalization factor is calculated so that the sum of the intensity points for the two curves are the same. For this reason the factor $N_p \, \Delta\rho_p^{\,2}$ is not of interest in the comparison. To calculate the theoretical curves the parameters that can be varied are the lattice spacing, A, the disorder parameter, D, and the lattice point structure factor, $\overline{F_p^{\,2}}$. The lattice is assumed to be represented by the sphere structure factor of Equation 20. The only variable necessary to characterize the sphere structure factor is R, the sphere radius. A computer program, PARAC, has been written to calculate the intensities for the paracrystalline lattice models and to compare these with a given experimental scattering curve. The program calculates the relative error, δ, for the theoretical curve according to:

$$\delta = \frac{\sum_i \left| (I_T)_i - (I_e)_i \right|}{\sum_i (I_e)_i} \tag{82}$$

where $(I_T)_i$ are the theoretical intensity values and $(I_e)_i$

the experimental values. The bars indicate the absolute value of the enclosed quantity.

Figure 20 shows a comparison between the calculated curves for the infinite paracrystalline lattice and the experimental data for the undeformed ionomer. A spacing of 34 Å with deviations of 12 Å and 20 Å has been chosen. A point radius of 5 Å has been selected. The deviations, δ, for the curves are 68% for D = 12 Å and 35% for D = 20 Å. These poor fits are chiefly due to the fact that the infinite paracrystalline lattice gives no source of zero order scattering. An important point in this regard is that the zero order scattering observed experimentally for the ionomer is a result of the ionic aggregate structure. In numerous studies (1,25,28) this zero order scattering is reported for salts but not for acid samples. This worker has observed for several ionomer systems that the scattering of the acid sample only approaches that of the salt at angles below about 0.1° 2θ. At that low angle, scattering most probably arises from heterogeneous particle (dirt) scattering that would be expected to be present in both samples. This point will be verified in later chapters.

b. Finite paracrystalline lattice. The finite paracrystalline lattice is characterized by Equation 31. That equation can be rewritten as:

$$\frac{I(h)}{N_L \Delta\rho_L^2} = \overline{F_L^2(h)} + \frac{N_p \Delta\rho_p^2}{N_L \Delta\rho_L^2} \overline{F_p^2(h)}\, Z(h) \qquad (83)$$

To compare the angular variation of scattering with the experimental curve the ratio $N_p \Delta\rho_p^2 / N_L \Delta\rho_L^2$ must be specified but the individual factors need not be known. Values in the range of 1.0 to 3.5 have been considered for $\Delta\rho_p / \Delta\rho_L$. The ratio N_p/N_L is determined once values have been decided for the density ratio and the point and lattice volumes. The computer program PARAC listed in Appendix II calculates intensity curves for this model. The lattice structure factor, F_L, is assumed to be represented by the sphere structure factor which is characterized in this case by the lattice radius, R_L.

It was observed that as the lattice radius was decreased increasingly better fits to the experimental scattering function were obtained. One of the best fits is shown in Figure 21. In this case a lattice radius of 75 Å has been used to achieve a deviation of about 7%. It is seen that the zero order scattering in this case is fit well by the model. But it must be seriously questioned if the paracrystalline lattice statistics are applicable to this small of a lattice which contains only about 10 lattice points.

The overall conclusion that can be drawn from these calculations is that a model which assumes a homogeneous ionic structure throughout an ionomer is unlikely to explain the observed scattering. Only models in which local structural entites with overall dimensions less than 100-150 Å can fit the data. For such local structure models the paracrystalline statistical approach is a poor one. A better

approach is to assume some definite geometry of the ionic aggregate. Such models are considered in subsequent sections.

c. Paracrystalline lattice deformation. A comparison can also be made between the predictions of the paracrystalline lattice model and the observed scattering curves for the stretched sample.

To obtain the expression for scattering it is necessary to evaluate the product $\underset{\sim}{r}\cdot\underset{\sim}{h}$ in Equation 16. The vector $\underset{\sim}{h}$ may be generally expressed as:

$$\underset{\sim}{h} = C\left[(1 - \cos\theta)\underset{\sim}{i} + (\sin\theta\sin\mu)\underset{\sim}{j} + (\sin\theta\cos\mu)\underset{\sim}{k}\right] \qquad (84)$$

where C is a constant, μ is the azimuthal angle, $\underset{\sim}{i}$ is a unit vector parallel to the scattering vector direction and $\underset{\sim}{j}$ and $\underset{\sim}{k}$ are unit vectors perpendicular to $\underset{\sim}{i}$. The vector $\underset{\sim}{j}$ is in the stretching direction. For the purposes of mathematical simplicity the lattice will be considered here to be two dimensional. In this case:

$$\underset{\sim}{r} = \underset{\sim}{A}_1 \sin\mu + \underset{\sim}{A}_2 \cos\mu \qquad (85)$$

where $\underset{\sim}{A}_1$ and $\underset{\sim}{A}_2$ are vectors describing the components of $\underset{\sim}{r}$ in the $\underset{\sim}{j}$ and $\underset{\sim}{k}$ directions. The product is given by:

$$\underset{\sim}{r}\cdot\underset{\sim}{h} = A_1 \sin\theta\left(\sin^2\mu + \frac{A_2}{A_1}\cos^2\mu\right) \qquad (86)$$

This expression can be used to evaluate the lattice interference factor, Z, as in reference 71, page 305. The result is:

$$Z = \left\{ \frac{1 - p_1^2}{1 + p_1^2 - 2p_1 \cos\left[2\pi s A_1 (\sin^2\mu + (A_2/A_1)\cos^2\mu\right]} \right\} \cdot \left\{ \frac{1 - p_2^2}{1 + p_2^2 - 2p_2 \cos\left[2\pi s A_1 (\sin^2\mu + (A_2/A_1)\cos^2\mu\right]} \right\} \tag{87}$$

Here A_1 and A_2 are the magnitudes of $\underset{\sim}{A}_1$ and $\underset{\sim}{A}_2$. The lattice deviations are defined by:

$$p_1 = \exp(-2\pi^2 s^2 D_1^2)$$
$$p_2 = \exp(-2\pi^2 s^2 D_2^2) \tag{88}$$

For an infinite paracrystalline lattice it is expected that the lattice spacings will deform according to the overall dimensions of the sample in which case

$$A_1 = \lambda (A_1)_o$$
$$A_2 = \lambda^{-1/2} (A_2)_o \tag{90}$$

Using Equations 87, 88 and 30 it is possible to calculate scattering patterns for deformed infinite paracrystalline lattices for which the lattice spacing changes are given by Equation 90. This is done by the computer program PARACOR listed in Appendix II. Figure 22 shows the spacing changes calculated from the positions of scattering maxima for such

a model. In this figure, A_o, the undeformed spacing is 34 Å. Values of 0 and 12 Å have been used for the disorder parameter D. As the figure indicates, the predicted changes in Bragg spacings closely follow the affine predictions for both values of the disorder parameter. Thus the deformation of an infinite paracrystalline lattice should produce changes in the Bragg spacings which are quite dissimilar to the experimental values. This also suggests that local structure models should be used to explain the deformation behavior of this system. In local structure models spacing changes can be expected to be quite different than changes in overall sample dimensions. This considers the fact that the mechanical properties in the region around the structure may be very different than the overall mechanical properties of the matrix in which the local structures are encompassed.

2. The spherical shell-core model. On the basis of the observed SAXS scattering curves and the calculated radial distribution functions for ionomers, MacKnight, Taggart, and Stein proposed the spherical shell-core model shown in Figure 2. In this model the central core and the shell constitute regions of excess electron density. The region between the core and shell and the matrix outside of the shell have lower electron densities. In a completely general model each of these regions could be assigned different electron densities. However in this treatment it will be assumed that the

electron density of the region between the ionic core and shell is the same as that of the matrix. This reduces the problem to that of a three phase system.

The structure factor for the sphere-shell model is calculated as follows. The shape function is given by:

$$\begin{aligned} S(r) &= \rho_1' && 0 \le r \le R_1 \\ &= \rho_3' && R_1 < r \le R_2 \\ &= \rho_2' && R_2 < r \le R_3 \\ &= \rho_3' && R_3 < r \end{aligned} \tag{91}$$

This can be simplified for the purposes of calculation by realizing that the scattering from an object depends only on density differences and not on the absolute value of the density. Thus S(r) can be equivalently represented by:

$$\begin{aligned} S(r) &= \rho_1 && 0 \le r \le R_1 \\ &= 0 && R_1 < r \le R_2 \\ &= \rho_2 && R_2 < r \le R_3 \\ &= 0 && R_3 < r \end{aligned} \tag{92}$$

where $\rho_1 = \rho_1' - \rho_3'$ and $\rho_2 = \rho_2' - \rho_3'$. (93)

It should be carefully noted that in the following calcula-

tions ρ_1 and ρ_2 do not denote the actual densities of the shell and core but rather the density differences of Equation 93. To obtain the actual densities ρ_1' and ρ_2' one must know the value of ρ_3' and use Equation 93.

The structure factor is then given by:

$$F = \frac{\int_0^{R_1} 4\pi r^2 \rho_1 (\sin(kr)/kr)\, dr}{\int_0^{R_1} 4\pi r^2 \rho_1\, dr} \qquad (94)$$

$$\frac{\int_{R_2}^{R_3} 4\pi r^2 \rho_2 (\sin(kr)/kr)\, dr}{\int_{R_2}^{R_3} 4\pi r^2 \rho_2\, dr}$$

Evaluating Equation 93 and dividing by ρ_1 gives:

$$F/\rho_1 = \frac{3(\sin(kR_1) - kR_1\cos(kR_1))}{R^3(R_1^3 - A(R_2^3 + R_3^3))}$$

$$+ \frac{3A(\sin(kR_3) - kR_3\cos(kR_3) - \sin(kR_2) + kR_2\cos(kR_2))}{R^3(R_1^3 - A(R_2^3 + R_3^3))} \qquad (95)$$

where $A = \rho_2/\rho_1$. The computer program SHELL2 listed in Appendix II has been written to calculate the angular varia-

tion of intensity from the spherical shell-core model. Input parameters include R_1, R_2, R_3, and A.

Figure 23 shows scattering curves calculated for typical values of R_1, R_2, and R_3 as a function of the parameter A. At high A values two principal peaks are observed. The peak at lower angles corresponds to shell-shell interference while that at higher angles corresponds to shell-core interference. As A is decreased only the shell-core interference peak is seen. At very small values of A this peak begins to turn into a shoulder and disappear. It is observed that for values of A in the range of about 0.04 to 0.10 scattering patterns are seen very similar to those observed experimentally for ionomers. The model not only predicts the scattering maximum but also zero order scattering comparable to experimental results.

A quantitative comparison has been made for this model with the undeformed scattering curve and is shown in Figure 24. For values of $R_1 = 5$ Å, $R_2 = 41$ Å, $R_3 = 46$ Å, and $A = 0.007$ a fit has been obtained with a relative error of 7%. The relatively low value of A for this case as compared to Figure 23 results from the increased value of R_2. It is difficult to precisely define the certainty in the values of the parameters of the model fit since the relative error depends on all of them taken together. To give some indication of the effect of the parameters on δ a few results are listed in Table 2. As can be seen a significant change

in most of the parameters results in poor fits. In fit number 5 a broad distribution of R_1 is considered over the range of 4-14 Å. In fit number 6 it is seen that a decrease in R_3 and simultaneous increase in A can also give a good fit. This is only possible for R_3 values less than about 10 Å. In an examination of a large number of fits with this model it was observed that the mutual compensation effect between R_3 and A gave rise to the largest uncertainties in determining the best fit.

Various mechanisms may be considered for the deformation of the spherical shell-core model. In this section it will be assumed that the local stresses in the region of the ionic aggregates are the same as that for the sample as a whole. However in that case the core-shell distance perpendicular to the stretching direction would decrease leading to a change in the SAXS spacing at 90° azimuthal angle which is not observed. It is quite possible that the local strain pattern in the region of the ionic aggregates is much different from that of the whole sample. In this section a deformation mechanism is assumed which is consistent with the observed changes in SAXS spacings. The changes in intensity of SAXS scattering are then compared to the observed changes to test the validity of the mechanism.

Thus a deformation mechanism will be treated in which the ellipsoid dimensions parallel to the stretching direction change according to:

$$(R_1)_{||} = \nu_1 (R_1)_o \tag{96}$$

and

$$(R_2)_{||} = \nu_2 (R_2)_o \tag{97}$$

$(R_3)_{||}$ is assumed to change according to:

$$(R_3)_{||} = (R_3)_o + (\nu_2 - 1)(R_2)_o \tag{98}$$

The dimensions perpendicular to the stretching direction will be assumed not to change. The excess mass of the core and shell over the matrix should remain constant with stretching so that:

$$A' = A\left(\frac{V_s \; V_c'}{V_s' \; V_c}\right) \tag{99}$$

where V_s and V_c are the shell and core volumes and primed variables denote values after deformation.

The structure factor for ellipsoids, F_e, has been discussed by Barber (140). It has been shown that:

$$F_e = \left[\frac{3}{U^3} (\sin U - U \cos U)\right]^2 \tag{100}$$

where

$$U = \frac{4\pi}{\lambda} a \sin(\theta/2)[\cos^2(\theta/2)\cos^2\psi + (b^2/a^2)(1 - \cos^2(\theta/2)\cos^2\psi]^{1/2} \tag{101}$$

where a and b are the long and short axis respectively. Equation 101 describes the case where the ellipsoid is arranged with its long axis perpendicular to the scattering direction. ψ is the azimuthal angle.

The program SHELLD, listed in Appendix II, has been written to calculate scattering curves for this model. Figure 26 shows scattering curves at $\psi = 0$ and 90° for various values of ν_1 and ν_2 using values for the undeformed dimensions as in Figure 24. In this case only a small deformation of the core is considered relative to that of the shell. The results show that as ν_1 and ν_2 are increased the scattering curve at $\psi = 90°$ is larger in intensity than that at $\psi = 0°$ as is observed experimentally. Figures 27 and 28 show the same data of Figure 26 plotted at constant azimuthal angle. It is seen that the overall intensity at $\psi = 90°$ decreases with increasing ellipticity. This is contrary to the observed intensity increase at this azimuthal angle. Figure 27 shows the intensity at $\psi = 0°$ decreases in agreement with experiment. The maximum is observed to shift to lower angles for $\psi = 0°$ also in agreement with experiment. However the exact way in which the peak shifts relative to the overall intensity decrease is not in agreement with the experimental results. Namely in Figure 17 a peak shift is observed before any large intensity decrease is found, while Figure 27 shows a large intensity decrease simultaneous with the peak shift.

In conclusion the spherical shell-core model gives a good fit of the undeformed data. A simple elliptical deformation of the model can explain some of the aspects of the scattering observed on stretching. However some serious deficiencies are found particularly in that the model predicts a decrease in intensity at $\psi = 90°$ with deformation while an increase is observed experimentally.

One other point should be made with regard to this model. In the deformation it has been assumed that the shell density remains radially uniform. Actually it would be expected that chains would be pulled away from the equatorial region toward the polar region. This would lead to a densification at the poles and decreased density at the equator. Such density changes would produce even less scattering at $\psi = 90°$ with stretching and worsen the discrepancy between the model and experiment.

3. Lamellar models. The occurrence of lamellar or layered structures in lipids suggests that such structures might also be present in ionomers (141). The problem of scattering from such layered structures has been treated by several different authors (142-145). In most of these treatments the layers have lateral dimensions large compared to the interlayer spacing. Hosemann (145) has shown that the factor s^2 can be used to reduce the scattering from a three dimensional layered structure of this kind for comparison with a one

dimensional model. In the case of ionomers the lateral dimension of the layers is likely to be comparable to the interlayer spacing. This conclusion is based on the sizes deduced from the radial distribution function approach and also the radius of gyration determinations. Thus for ionomers the Hosemann s^2 factor cannot be used. Instead it is desirable to use a three dimensional model to generate intensity functions for comparison with the experimental results. In this work only a two dimensional model will be considered. This has been done largely for the purpose of mathematical simplicity. It is felt that most of the physical ideas are adequately represented by the two dimensional model. In addition it will be seen that due to the large number of possible parameters it will not be possible to unambiguously assess the layer model. This ambiguity would be somewhat worse if a three dimensional model had been used.

An initial attempt was made to model the system with a two layered structure. Here the layers were assumed to represent the ionic regions of excess electron density. The derivation of scattering equations for the two layer model will not be given here since it is essentially similar to the derivation for the three layer model which is given in detail later. It was found that the two layer model gave rise to an insufficient interference to fit the ionomer scattering maximum. This result was observed for a range of parameters for the layer thicknesses and layer widths.

In view of this result the three layer model shown in Figure 29 was adopted. The layers here again represent the ionic rich regions. The thicknesses of the central and outer layers are assumed to be the same for simplicity. In a general consideration of this model one could assign different electron densities to the central and outer layers as well as the inter-layer region and the matrix. In this treatment it will be assumed that the matrix and inter-layer regions have the same electron densities. Different phase densities will be allowed for the central and outer layers. This treatment is essentially analogous to the treatment of the spherical shell-core model. Some calculations have been made to justify these assumptions. An attempt was made to fit the experimental results using the same density for the outer and central layers. This failed to give good fits to experiment. The model was then modified to allow a different density for the inter-layer region and the matrix but retaining equal densities for the outer and central layers. This also could not fit the experimental results.

The shape function for the three layer model is given by:

$$S(\underset{\sim}{X}) = 1 \begin{cases} |X_1| \leq L_1/2 \\ |X_2| \leq W/2 \end{cases}$$

$$= A \begin{cases} |X_1| \leq 3L_1/2 + L_2 \\ |X_2| \leq W/2 \end{cases} \qquad (102)$$

$$= 0 \quad \text{all other X}$$

where W is the lamella width and L_1 and L_2 are the layer spacings as in Figure 29.

The structure factor is then given by:

$$F(\underset{\sim}{S}) = \int_{-(W/2)}^{W/2} \int_{-(L_1/2)}^{L_1/2} \exp(-2\pi i(S_1X_1 + S_2X_2))dX_1dX_2$$

$$+ \int_{-(W/2)}^{W/2} \int_{L_1/2 + L_2}^{3L_1/2 + L_2} A \exp(-2\pi i(S_1X_1 + S_2X_2))dX_1dX_2$$

$$+ \int_{-(W/2)}^{W/2} \int_{-(3L_1/2 + L_2)}^{-(L_1/2 + L_2)} A \exp(-2\pi i(S_1X_1 + S_2X_2))dX_1dX_2 \qquad (103)$$

where $\underset{\sim}{S}_1$ and $\underset{\sim}{S}_2$ are the components of $\underset{\sim}{S}$ in the X_1 and X_2 directions. Evaluation of Equation 103 using the shape function of 102 gives:

$$F(S) = \left[\frac{\sin(\pi S_1 L_1)}{\pi S_1 L_1} + A\left(\frac{\sin(2\pi s_1(3L_1/2 + L_2))}{\pi s_1}\right.\right.$$

$$\left.\left. - \frac{\sin(\pi s_1(L_1 + 2L_2))}{\pi s_1}\right)\right] \cdot \sin\left(\frac{\pi s_2 W}{s_2}\right) \qquad (104)$$

Actually due to the finite width of the layers Equations 102-104 only apply to a limited range of the angle μ as shown in Figure 30. For $\mu < \mu_1$ the structure acts only as a single layer in which case the structure factor is:

$$F(S) = \frac{\sin(\pi S_1 L_1)}{\pi S_1} \cdot \frac{\sin(\pi S_2 W)}{\pi S_2} \qquad \mu < \mu_1 \qquad (105)$$

For μ greater than μ_1 but less than μ_2 the structure factor is:

$$F(S) = \left[\frac{\sin(\pi S_1 L_1)}{\pi S_1} + A\left(\frac{\sin(\pi S_1 X')}{\pi S_1} - \frac{\sin(\pi S_1(L_1 + 2L_2))}{\pi S_1}\right)\right]$$

$$\cdot \sin\left(\frac{\pi S_2 W}{\pi S_2}\right) \qquad (106)$$

where

$$X' = (W/2)\tan\mu - L_1/2 - L_2 \qquad (107)$$

The computer program MICELLE listed in Appendix II has been written to calculate scattering curves from this model and compare them to experimental curves. Figure 31 shows curves

calculated for this model as a function of the outer to central layer density ratio, A, for random layer orientation. The curves show that a range of A values exist which gives scattering curves essentially similar to those for ionomers.

Figure 32 shows a fit of the model to the experimental data for the undeformed sample. In this fit only single values of the layer spacings and width are considered. In the real system a distribution of widths is certainly present. But it is felt that due to uncertainties in distribution types and the fact that only a two dimensional model is used, it is not reasonable to try to analyze the size distribution. The larger value of A found for the lamella model as compared to the spherical shell-core model reflects the relatively smaller volume of the outer layers in the lamella model in comparison to the shell of the other model.

In the deformation of the lamella model both rotation and stretching are possible. Here a deformation mechanism incorporating only rotation will be considered initially. The possibility of stretching resulting in changes in L_2 will be subsequently treated.

The structure factor for an individual layered structure depends on the Bragg scattering angle, θ, and the azimuthal angle, μ, for that structure:

$$\underset{\sim}{S} = \underset{\sim}{S}(\mu,\theta) \tag{108}$$

The angle μ is related to the macroscopic azimuthal angle

relative to the stretching direction, ψ, and the angle between the stretching direction and the direction perpendicular to the layers (tilt angle), ω:

$$\mu = \psi - \omega \tag{109}$$

The magnitude of the components of the vector, S, are related to μ through the relations:

$$|\underset{\sim}{S}_1| = S_1 \sin \mu \tag{110}$$

$$|\underset{\sim}{S}_2| = S_2 \cos \mu \tag{111}$$

The distribution of tilt angles will be assumed to be Gaussian:

$$g(\omega) = C \exp\left(-(\omega - \omega_o)^2/\beta^2\right) \tag{112}$$

where β characterizes the width of the distribution and C is a normalization constant. The convention will be used that $\omega_o = 90°$ describes the tilt angle for the case of the layers lying perpendicular to the stretching direction. In the undeformed state the distribution of layers should be random which corresponds to the case of large β. With elongation the layers may orient. To attempt to fit the experimental curves for the deformed samples it is necessary to assume that the layers rotate so that the layer direction becomes parallel to the stretching direction (ω =

90°). Thus β must decrease with orientation to produce the desired rotations. The orientation distribution may also be characterized by the second order orientation function:

$$f(\omega) = 2\overline{\cos^2\omega} - 1 \qquad (113)$$

where $\overline{\cos^2\omega}$ is the average value of $\cos^2\omega$. For random orientation $f(\omega)$ is 0. For all of the layers lying parallel to the stretching direction $f(\omega)$ is 1.

The computer program MICELLD listed in Appendix II calculates scattering curves for the lamella model as a function of $f(\omega)$. Scattering curves may be obtained at any azimuthal angle.

Figure 33 shows calculated scattering curves at $\psi = 0°$ for various values of $f(\omega)$. The model predicts a decrease in intensity with increased layer orientation. A peak shift is also predicted to lower 2θ. As with the spherical shell-core model the peak shift occurs at a slower rate than the intensity decrease. This is contrary to the experimental results.

Figure 34 shows the scattering curves for $\psi = 90°$. The model predicts increased intensities with a constant peak position in agreement with the experimental curves.

The fact that simple rotation fails to fit all of the data suggests stretching may also be involved. This would presumably involve an increase in L_2 for lamella with

$\omega = 0°$ and a decrease in L_2 for lamella with $\omega = 90°$. Since no peak shift is observed at $\psi = 90°$, it is necessary that the net effects of elongation, compression and lamellar rotation be mutually compensating for that azimuthal angle.

Ellipsoidal shell-core models may also be considered in which the undeformed sample consists of randomly oriented ellipsoids. Deformation of such structures might involve rotation and or stretching. It is clear that it is impossible to unambiguously select one of these models on the basis of the present data.

The arrangement of the polymer molecules within these structural models is a problem of interest. In the case of the spherical and lamellar core-shell structures it would be desirable to know the extent of connection between the shell and core regions. For the case of a highly oriented sample it is likely that structural orientation occurs to align molecules parallel to the draw direction. This implies that molecules lie principally parallel to the layer direction. Studies of infrared dichroism for deformed ionomers have shown that the carboxylate ion bond at 1560 cm^{-1} shows perpendicular dichroism (54,147). Thus the carboxylate groups orient perpendicular to the chain direction and would lie perpendicular to the layer directions. The dichroism measurements of Read and Stein (147) and Uemura et al. (54) indicate that the three dimensional orientation function is only about 0.1-0.2 for the carboxylate

ion at elongation ratios of 2. This implies that these groups are still fairly random. The SAXS data indicate that the layers would have achieved a much greater orientation at comparable elongation. This implies that the orientation of carboxylate groups with respect to the layer direction is preferentially perpendicular but with a large average deviation.

Since no scattering maximum is observed at high elongations at $\psi = 0°$, it is possible to carry out a size distribution analysis. As discussed in the first chapter, this will determine the size of the dimension parallel to the layer direction. In terms of the lamella model this corresponds to an average of W and the direction perpendicular to W and parallel to the layers. The Guinier approximation of Equation 25 is assumed. Initially a Gaussian distribution of particle size was used but this resulted in relatively poor fits of the data at 300% elongation. A good fit was obtained using a Lorentzian distribution with a relative error of 5% as shown in Figure 36. The Lorentzian distribution is characterized by:

$$g(R) = \frac{C}{1 + (2(R - R_o)/\beta)^2} \qquad (114)$$

where x_o is the most probable value of x, C is a normalization constant, and β characterizes the distribution width. The size distribution used to calculate Figure 36 is shown

in Figure 37. The distribution indicates a most probable size of 40 Å with significant fractions present for sizes in the range of 10-70 Å. These calculations have been carried out using the computer program SIZE listed in Appendix II.

4. Conclusions. The scattering curves from the cesium salt of an ethylene-methacrylic acid ionomer have been obtained in the undeformed state and also at various percent elongations. The absence of any crystallinity of the hydrocarbon units has allowed an interpretation of scattering solely in terms of ionic structural aggregates. It has only been possible to explain the undeformed scattering data by models involving local structure. An infinite paracrystalline lattice model fails to explain the data since it contains no source for zero order scattering.

The scattering pattern becomes strongly azimuthally dependent with elongation. The Bragg spacings at azimuthal angles parallel and perpendicular to the stretching direction vary in a manner which is very dissimilar to the affine prediction. This means that the effective ionic structural dimensions are changing very differently than the dimensions of the sample as a whole. Such a discrepancy is only expected for local structure models.

Scattering curves have been calculated for a spherical shell-core model in which stretching of the spheres to

ellipsoids occurs. The model correctly predicts an intensity decrease at $\psi = 0°$ but fails to predict an increase in intensity at $\psi = 90°$. The relative rates of intensity decrease and peak shift at $\psi = 0°$ are also incorrectly predicted.

A model involving rotation of lamellar structures correctly predicts decreased intensities at $\psi = 0°$ and increased intensities at $\psi = 90°$, but fails to predict the relative rates of peak shift and intensity decrease at $\psi = 0°$. This discrepancy could presumably be resolved by incorporating stretching. Other ellipsoidal models involving combinations of rotation and stretching could also presumably fit the data. The present extent of information does not allow an unambiguous discrimination between such models. It is probable that a rotational mechanism must play a major role in any correct explanation of the deformation behavior.

C H A P T E R I I I

STUDIES OF STYRENE-METHACRYLIC ACID IONOMERS

A. Introduction

Ionomers prepared from styrene-methacrylic acid and copolymers have been studied in detail by Eisenberg (43-46A, 49) as previously mentioned. These studies have indicated that the manner of ion aggregation is different for this system than the ethylene-methacrylic acid ionomers. Eisenberg has proposed that in the styrene system at low ion concentration the ionic groups are present in very small aggregates termed multiplets. At high concentrations, above about 6 mol %, changes in mechanical, dielectric, and other properties are observed. Eisenberg has proposed that these changes reflect an increased concentration of larger aggregates which are termed clusters. In contrast in the ethylene-methacrylic acid ionomers, evidence exists that ions tend to aggregate in "clusters" even at low ion concentrations of 2-3 mol %.

The technique of SAXS is appropriate for the study of this proposed change in aggregation behavior. In principle SAXS has the ability to determine changes in aggregate size and also to investigate possible inter-aggregate and intra-aggregate structures. The styrene-methacrylic acid ionomer

system is also a good system for study in that the styrene units do not form a crystalline phase which can complicate the interpretation of SAXS and which may also affect the manner of ion aggregation.

A preliminary study of the SAXS from styrene-methacrylic acid ionomers was conducted by Eisenberg and Navratil (76). These workers made photographic measurements primarily on lithium and cesium salts and also on some unneutralized copolymers. From these studies scattering peak positions were determined as a function of ion concentration. Cesium salts were found to exhibit a peak corresponding to a Bragg spacing of 45-60 Å as well as a second peak corresponding to a spacing of 5-10 Å. Lithium salts showed spacings in the range 5-25 Å but not larger. Unneutralized samples showed the same pattern as polystyrene for which 6 and 11 Å spacings were observed. No attempt was made to measure the complete angular dependence of x-ray scattering.

The study of Eisenberg and Navratil does indicate that there are structural differences between, for example, the cesium salts and the unneutralized copolymers. However beyond that little can be said. The interpretation of a scattering maximum in terms of an average distance or an average volume is in general invalid. A particularly good discussion of this point is given by Guinier and Fournet (148). It has also been seen in the second chapter of this work that models assuming that the scattering peak corre-

sponds to the lattice spacing of a paracrystalline lattice are probably incorrect for ionomers. Thus to obtain information about the physical structure of ionomers it is really necessary to measure the entire scattering curve. In this work this has been done for a series of cesium salts and unneutralized styrene-methacrylic acid copolymers in the range of 2-10 mol % co-unit concentration. The observed SAXS has been interpreted in terms of the various theories outlined in the first chapter. Emphasis has been placed on determining (1) the extent of aggregation as determined through (a) an analysis of the SAXS invariant and (b) the amount of internal density fluctuation scattering, and (2) the geometrical arrangement of ions within aggregates as analyzed in terms of the angular dependence of scattering.

B. Experimental

1. Sample Preparation. A number of samples were obtained directly from Eisenberg. The procedures for the free radical copolymerization and neutralization used for these have been described (44). Table 3 lists the co-unit concentrations and molecular weights of these samples. A few copolymer samples were prepared in this laboratory using the procedures described by Eisenberg to produce molecular weights in the range of 60,000. Table 3 lists the initiator concentrations, polymerization times, and temperatures used. The chemical composition was analyzed by infrared spectroscopy.

Typical spectra for some unneutralized samples are shown in Figure 38. The spectra show the characteristic 1605 cm^{-1} phenyl bond and the carbonyl stretching bonds at 1700 cm^{-1} and 1745 cm^{-1}. These two bonds have been assigned to carbonyl groups attached to dimerized and free hydroxyl groups by Longworth and Morawetz (149).

Figure 39 shows typical infrared spectra for neutralized cesium salts. The carbonyl stretching bonds at 1700 cm^{-1} and 1745 cm^{-1} observed for acid samples are absent for salts. Instead a band appears at 1560 cm^{-1} which corresponds to the carboxylate ion asymmetric stretching mode. IR scans were not obtained for salts with concentrations above 6 mol %. The absence of the 1700 cm^{-1} and 1745 cm^{-1} bands indicates the films were highly ionized. It was not possible to obtain films thin enough for IR measurements for salts above about 6 mol % ion concentration.

The degree of ionization of the films used for x-ray measurements was determined by x-ray absorption. Table 4 lists the experimentally measured linear absorption coefficients, sample thicknesses, densities, and degree of ionization values for the salts and unneutralized copolymers. The degree of ionization for the salts was calculated using the computer program Ionize as described in the first chapter. Density measurements were made in the thermally stabilized density gradient described in Chapter I.

Films were prepared for study by drying for several

days in a vacuum oven at about 75°C followed by compression molding at about 20°C above the glass transition temperature at 10,000 psi and slow cooling. Films were stored *in vacuo* until just prior to scattering measurements. The film of the ethylene-methacrylic acid cesium salt was prepared as in Chapter II, followed by annealing at 80°C for one week in a vacuum oven.

2. SAXS measurements.

a. Camera geometry and data collection. A Rigaku-Denki Small Angle X-Ray Diffractometer (Catalog No. 2202) utilizing slit geometry and a scintillation counter detector with pulse height analyzer was used in the measurement of SAXS. The camera geometry is shown in Figure 40. Slits S_1 and S_2 collimate the x-rays prior to impingement on the sample. Slit S_3 removes parasitic scattering arising from S_2. The sample is located just after S_3. Scattered x-rays from the sample pass through an evacuated chamber and then through slits S_4 and S_5 before hitting the detector. Slit widths used in measurements were chosen according to the recommendations of the manual and are listed in Table 4.

CuK x-rays were generated at 40 killivolts and 11.5 milliamps with a General Electric CA8-F fine focus tube and XRD-6 generator. CuK_β radiation was removed by a nickel filter located prior to S_1. A Harshaw Chemical Company NaI (Tl) scintillation counter (type K968SHG32K) including a NB-18A

preamplifier was used to detect scattered radiation in conjunction with a Digital Automation Company Model 200 Spectrometer. Settings for pulse height analysis were determined using the procedures of Taggart (29). Table 6 lists the determined values.

Alignment of the camera was carried out following procedures in the manual. These procedures have been described in greater detail in a recently written working manual for the camera.

Angular step and pre-set count values for the scattering runs were chosen to reduce run times to a minimum while still maintaining sufficient angular and counting accuracy. A preset count greater than 1000 was used in nearly all cases. Generally two readings were taken at each angle of measurement.

Background scans were taken with the sample taped in position on the detector following the procedure of Warner. In this way parasitic scattering from the slits is most accurately attenuated by the sample (150).

Scattering for a sample immersed in water was carried out by placing the sample inside a cell in the sample position. The cell consisted of two aluminum plates with circular holes which were covered by thin sheets of Mylar attached by epoxy resin. For background measurements the cell was placed between the first and second slits on a cell holder. This was done since positioning of the cell

before the detector would have been difficult.

Temperature runs were made using a heated cell obtained from P.H. Geil of Case Western Reserve University in conjunction with a constantin temperature detector. The latter was calibrated using ice water and boiling water to set 0°C and 100°C. No background runs were made at higher temperatures.

A PDP-8 minicomputer was used to control the scanning and counting operations. Data output was obtained on paper tape through a teletype. The data was then read from these tapes onto files in the CDC Cyber 70 computing system. The computer program TRANF2 listed in Appendix II was written to convert the data output into intensity values in counts per second at each angle. The computer program SMOOTHS written by J. Koberstein and listed in Appendix II was then used to fit a smooth line through the computed intensity values. It was found that SMOOTHS gave comparable but more reproducible results than the hand smoothing procedures used previously (151). An exception to this was the case of background curves where SMOOTHS was often unable to fit the initial step fall-off in intensity. For this reason background curves were smoothed by hand prior to subtraction from scattering data.

b. Slit desmearing. The theory of corrections for slit smearing has been described in Chapter I. As previously discussed it is generally necessary to determine the

validity of the infinite height assumption for a particular scattering system. To assess this assumption a comparison was made between results from finite height desmearing using SAXSC and infinite height desmearing using the Vonk program. The smeared and desmeared curves for the critical case of a 7.7 mol % Cs^+ salt are shown in Figure 41. The small but significant differences in the desmeared curves show that the infinite height assumption may not hold in this system. For systems where the finite height assumption was deemed valid essentially no differences were found in the desmeared curves using SAXSC and the Vonk program (110). For this reason the program SAXSC was chosen for desmearing of all curves for the styrene-methacrylic acid ionomer system. The program assumes a Gaussian weighting function as in Equation 67. The parameter p was calculated to be 12.6 following the method of Hendricks and Schmidt (128). Data was inputed in 0.1° angular increments for most scans.

To assess the validity of the desmearing procedure a comparison was made between pinhole data taken at the Oak Ridge National Laboratories and slit desmeared data taken on the Rigaku-Denki camera. Unfortunately the exact sample used in the ORNL studies was not studied at the University of Massachusetts. However data has been taken on a sample taken from the same batch of ionized material and prepared in an otherwise identical manner. Figure 42 shows SAXS curves for the pinhole and slit desmeared data using SAXSC as described

above. The curve obtained using pinholes shows a somewhat sharper maxima than the slit desmeared data. The relative error between the two curves is of the order of 3-4%. Baczek (110) obtained the opposite result for pinhole and slit desmeared data on undeformed low density polyethylene, namely that desmearing over-corrected giving a sharper peak. However the nature of the scattering function for semi-crystalline polyethylene is very different than that for ionomers. The use of two different ionomer samples may also be a source of discrepancy in the comparison of this study.

C. Results and Discussion

1. Observed scattering curves. The observed desmeared scattering curves for the unneutralized acid samples are shown in Figure 42. The curves show an initial falloff at low scattering angles followed by a nearly constant intensity region and then a slow upturn at large scattering angles. None of the curves exhibits a scattering maximum. This angular dependence of scattering is consistent with SAXS results for amorphous polymers found by Uhlmann (152) and for polymer melts found by Vonk et al. (61). According to these authors the falloff at low scattering angles can be largely attributed to foreign heterogeneities, i.e., dirt. The source of scattering in the intermediate regions for homopolymers is thermal density fluctuation scattering. For copolymers with heteroatoms such as oxygen local composi-

tional variations can also be expected to give rise to a constant scattering component. The increased level of scattering observed with increasing methacrylic acid co-units is consistent with increased compositional fluctuations. At large angles an additional scattering component is found that is the initial portion of the wide angle amorphous halo.

Desmeared scattering curves for cesium salt samples are shown in Figure 43. Curves for the 2.5, 3.8, and 5.5 mol % samples are basically similar to those for the acid samples in terms of the angular dependence of scattering. The scattering curves for the 7.7 and 9.7 mol % samples exhibit maxima corresponding to Bragg spacings of about 30 Å. An increase in the overall level of scattering is observed with increasing salt concentration.

2. Extent of ionic aggregation. To obtain information about the extent of ionic aggregation it is desirable to calculate the SAXS invariant. This requires an analysis of the Porod region of the scattering curves. Plots of $s^4 I$ vs. s^4 are shown in Figure 44 for the cesium salt samples. The plots exhibit straight line portions at large s with slopes which increase with increasing ion concentration. The slope of the plot is equal to U, the internal fluctuation scattering component, according to Equation 52. The intercept is equal to the Porod law constant K. The values obtained for U are plotted in Figure 45.

After U is subtracted from the observed scattering intensities it is possible to carry out the integration of Equation 33 and to calculate $\overline{\eta^2}$ from Equation 34. The results of these calculations are plotted in Figure 46. The mean squared electron density fluctuation is observed to increase slowly with ion concentration up to about 6 mol % and then to increase sharply.

The mean squared electron density fluctuation is related to the phase densities and volume fractions of a two phase system through Equation 36. For such a system it is also true that:

$$\overline{\rho_e} = \phi_1\rho_1 + \phi_2\rho_2 \qquad (115)$$

where $\overline{\rho_e}$ is the average electron density and

$$\phi_1 + \phi_2 = 1 \qquad (116)$$

The three Equations 36, 115, and 116 involve four unknowns and thus cannot be uniquely solved. It is possible to estimate ρ_1 which will denote the ionic phase density and then to calculate values for the other variables based on this estimate. Eisenberg (12) estimates that about 5 ion pairs occupy 100 $\mathring{A}^3$ in ionic structures. This gives a value of 2.5-3 mole-el/cm^3 for ρ_1. In terms of the spherical core-shell and lamellar models this would be expected to correspond to the core or inner layer densities. An average value

of ρ_1 for these models would be close to about 0.8 mole-el/cm^3. A value of ρ_1 of about 1 mole-el/cm^3 has been reported by Pineri (33). Table 5 lists values for ρ_2, ϕ_1, and ϕ_2 calculated from ρ_1 values of 2.5 and 0.8 mole-el/cm^3. The results indicate that the value of ϕ_2 is fairly small generally of the order of a few percent with the possible exception of the 7.7 and 9.7 mol % samples which may have ϕ_2 values of 0.10-0.20. These values are much less than the Fournet theoretical volume fraction of 30-35% required to produce a SAXS maximum (84). Thus the maxima must arise from effects other than the volume exclusion and ordinary thermodynamic potential considerations of Fournet. These effects might include some special ordering of the interparticle distances as in the Cooper model or intraparticle order as in the local structure models discussed in Chapter II. In view of the other results of Chapter II the local structure models must be considered to be the more probable explanation.

The calculated values for ρ_2 in Table 5 are larger than the literature value of 0.56 mole-el/cm^3 for pure polystyrene (152). If this excess density is attributed to the presence of ions in phase two, it is possible to calculate the fraction F of ions in phase two:

$$F = \frac{\phi_2(\rho_2 - \rho_2^{o})}{\bar{\rho}\ R} \qquad (117)$$

where R is the fraction of ionic electrons in the entire system and ρ_2^o is electron density of pure polystyrene. In these calculations all of the electrons of the methacrylic acid units are considered to be ionic. The calculated values of F are also listed in Table 7. It is seen that a significant fraction of ions is excluded from the ionic phase based on either estimate for ρ_1. The calculated values for F based on ρ_1 = 0.8 mole-el/cm^3 tend to indicate an increased efficiency of aggregation with ion concentration. Values of F based on ρ_1 = 2.5 mole-el/cm^3 indicate that the efficiency is essentially constant. The F values are based on values for $\overline{\eta^2}$ which contain errors of 10-15% and also on assumptions for ρ_1 and implicit assumptions involved in Equation 117 and the two phase model. Therefore these values are not exact in any way. Nevertheless it is interesting to compare these with values obtained by Eisenberg and Hodge (49) from dielectric measurements. These authors have estimated the relative numbers of ions contained in multiplets and clusters based on the relative magnitudes of dielectric loss peaks assigned to these structures. They estimate that the fraction of ions in multiplets ranges from about 65% for a 2 mol % sodium salt to about 20-30% for a 9 mol % sodium salt. The fraction of ions in multiplets might be identified with the fraction seen by SAXS as non-phase separated. In this case Eisenberg's values are in fair agreement with the SAXS values considering the large uncertainties in the

two methods of determination. The use of different metal salts might also be a source of discrepancy.

A comparison can be made of the extent of ionic aggregation for the styrene-methacrylic acid and ethylene-methacrylic acid ionomers. Taggart (29) has measured relative values of $\overline{\eta^2}$ for cesium salts of the latter. To place these values on an absolute level SAXS was observed for an 85% ionized 6.1 mol % annealed sample and calibrated with the Kratky standard. The observed scattering curve is shown in Figure 48. A value of 5.7×10^{-3} $(\text{mole-el/cm}^3)^2$ was obtained for $\overline{\eta^2}$ for this sample. This value has been used to obtain the results of Figure 65. The value of $\overline{\eta^2}$ for the ethylene-methacrylic acid ionomers is observed to increase rapidly at low ion concentrations in contrast to the styrene-methacrylic acid system.

The values for U for the two systems are also plotted in Figure 65. At low ion concentrations this component is much smaller for the ethylene-methacrylic acid system. The interpretation of U for a two phase system follows from Equation 46. For ionomers internal fluctuations may in principle be present in either phase. However since the volume fraction of the ionic phase is very small the fluctuation component for that phase will be small as follows from Equation 49. This is true even though the density difference for the ionic phase is larger. Thus the source of internal density fluctuation scattering in ionomers will result prin-

cipally from the presence of ions in the ion poor phase.

The dependencies of $\overline{\eta^2}$ and U on ion concentration are mutually consistent. Ions which are present in the phase separated aggregates do not contribute to U. Thus Figure 65 indicates that the fraction of phase separated ions is greater for the ethylene-methacrylic acid ionomers at low ion concentrations than for the styrene-methacrylic acid ionomers. At higher ion concentrations the extent of ionic aggregation becomes comparable in the two different systems.

3. Size and structure of ionic aggregates. Information about the size and geometric structures of ionic aggregates is obtainable from analysis of the angular dependence of the intensity function. In this section the zero order scattering portion of the curves will be analyzed in terms of the Guinier approximation of Equation 22 allowing also for the possibility of a particle size distribution. This analysis is more likely to be valid for the low ion concentration salts where intensity maxima are not observed. Subsequently the entire angular dependence of scattering will be analyzed in terms of the local structure models discussed in Chapter II. It will be seen that these two approaches indicate comparable aggregate sizes.

The intensity functions of the cesium salts have been fit over the angular range of .001132-.001698 $\mathring{A}^{-1}$ in S using the computer program SIZE. Since these are three dimensional

intensity functions Equation 22 has been used. Lorentzian size distributions described by Equation 114 have been used. This distribution allows for an asymmetric particle size distribution. Such a distribution might be expected since there is an effective lower limit of particle size of a few Å but essentially no upper limit. Symmetrical Gaussian distributions gave poorer fits. Table 8 lists the calculated values for the most probable radius of gyration $(R_g)_o$, the size distribution width β, and the relative error between the computer fit and experiment δ. The most probable radii of gyration determined for this system range from 12-20 Å This is somewhat larger than the 7-10 Å values determined by MacKnight et al. (28) for cesium salts of the ethylene-methacrylic acid system. One possible source of the discrepancy lies in the fact that MacKnight et al. carried out their size analysis at larger scattering angles beyond the scattering maximum. Such an analysis weights the scattering from smaller particles to a greater extent than the size distribution analysis performed in this study.

The full angular dependence of scattering can be analyzed in terms of the models for ionomer structure discussed in Chapter II. The observed scattering curves have been fit with the spherical core-shell model over the angular range of 0.4-4.8° 2θ. Table 9 lists the parameters and relative error δ of these fits. The fits indicate a relatively constant core radius of 6-8 Å and also relatively

constant values of the core-shell separation distance and shell thickness. The parameter A is also fairly independent of ion concentration. The width β of the distribution of R_2 values changes greatly. This parameter can be interpreted in two ways. First it may represent an actual distribution of R_2 values present in different aggregates. Secondly it may be that the shell ions are not included in a narrow region of uniform electron density but are rather distributed over the space outside the core. In this case R_2 would represent the radius of greatest shell ion density. These two possibilities can clearly give rise to the same scattering pattern. For the latter possibility it would be more correct to assume some shape for the shell ion density geometry. However this would be difficult mathematically. The relatively large values of δ may reflect the incorrectness of the assumption of a uniform shell density. It must also be pointed out that the model fits for the 2.5 and 3.8 mol % samples are not completely unique. Fits with similar relative errors could be obtained for values of the parameters differing by up to about 20-30% from those reported in Table 9.

The particle size found from the Guinier particle size analysis in the low angle region is fairly consistent with the size values found from the spherical shell-core model analysis. The radius of gyration of the sphere core-shell model is given by:

$$R_g = \frac{3(R_1^5 + A(R_3^5 - R_2^5))}{5(R_1^3 + A(R_3^3 - R_2^3))} \qquad (117)$$

This expression assumes a single value of R_2. Using the parameters of Table 9 gives values of 20-30 Å for R_g as calculated from Equation 117.

The scattering data can also be analyzed in terms of the lamellar model discussed in Chapter II. Attempts were made to fit the data over the angular range of 0.4-4.8° 2θ using the computer program MICELLE. In the fits a range of L_2 values was used as described by the Lorentzian size distribution as in Equation 114. It was found that several combinations of model parameters could give fits with relative errors of about 20%. In view of this ambiguity and the fact that only a two dimensional model was used no attempt was made to exactly determine the best model fits. In general the best fits were obtained for models with L_1 of about 4-8 Å, L_2 of about 30-40 Å, W of about 30-40 Å, and with values of A of about 0.8. These sizes are comparable with the particle sizes found from the Guinier analysis.

The analysis of the angular dependence of scattering for the cesium salts indicates that particles are present with radii of gyration predominately in the range of 10-30 Å. This size is comparable with the sizes found previously for cesium salts of the ethylene-methacrylic acid ionomers and also with particle size studies by Pineri et al. (20,33) on

other similar systems. The local structure models discussed in Chapter II have been found to be capable of producing scattering curves very similar to those observed experimentally. It is not possible to unambiguously choose the best parameters or even the best overall aggregate geometry based on the data for undeformed samples. The models do however indicate aggregate sizes comparable to those found from the Guinier analysis. There is some indication from the spherical shell-core model fits that the occurrence of the scattering maximum at high ion concentrations reflects either a narrowing in the size distribution or a sharpening of the electron density profile in the region of the ionic shell.

The effect of exposure to water was investigated for the 9.7 mol % cesium salt. Figure 49 shows scattering curves for the dry sample and the same sample after exposure to water for 300 hours. The curves have been normalized to the same intensity level. The scattering maximum is observed to essentially disappear although a small shoulder is seen in the curve at about 1.5° 2θ for the wet sample. It is not generally possible to compare the values of $\overline{\eta^2}$ or U for these samples since the presence of water changes the phase densities in an unknown way. It is possible to analyze the angular dependence of scattering for the wet sample in terms of the Guinier size distribution analysis. A fit of the data over the angular range of 0.2 to 1.0° 2θ indicates a most probable radius of gyration of about 20 Å with a dis-

tribution width of 0.15 for a Lorentzian particle size distribution. These values are essentially the same as for the dry sample. Taggart (29) has similarly observed that the particle radius of gyration is largely unchanged on saturation with water in studies of ethylene-methacrylic acid ionomers.

The effect of temperature on SAXS was studied for the 7.7 mol % cesium salt. Scattering runs at 60°C and 80°C showed the same angular dependence and absolute level of scattering as seen for the run at room temperature. A slight increase in the SAXS was observed at 120°C. However since the sample was visibly darkened during the experiment and hence degraded no importance can be attached to this latter run.

D. Conclusion

SAXS has been measured for a series of styrene-methacrylic acid copolymers and their cesium salts in the range of 2-10 mol % methacrylic acid co-unit concentration. Scattering from the unneutralized copolymer has been explained as arising almost entirely from short range electron density fluctuations. The size of the fluctuation component can be determined from a plot of $s^4 I(s)$ vs. s^4. For the cesium salts an additional intensity component attributed to phase separated ionic domains was observed and used to calculate the mean square electron density fluctuations $\overline{\eta^2}$. $\overline{\eta^2}$

increased slowly with ion concentration up to 6 mol % and rose sharply thereafter. Values of U for the cesium salts have been observed to increase rapidly at concentrations below 6 mol % and then to level off for higher ion concentrations. Values of $\overline{\eta^2}$ have been combined with mass density measurements and interpreted in terms of a two phase model. The analysis shows that the electron density of the ion poor phase is higher than that expected for pure polystyrene. A significant fraction of the ionic groups must be excluded from the ionic phase to account for the excess electron density. The exact amount of exclusion cannot be calculated with great accuracy due to uncertainties in the value of the ionic phase electron density. However it is shown that reasonable estimates for this density lead to exclusion fractions which are fairly consistent with similar exclusion calculations based on dielectric studies made on this system by Eisenberg.

The angular dependence of scattering has been analyzed in terms of a Guinier size distribution analysis and in terms of local structure models. These two approaches give similar results for size of ionic aggregates generally indicating most probable radii of gyration in the range of 10-30 Å. Either the spherical core-shell model or the lamellar model is capable of explaining the angular dependence of scattering over the whole SAXS region.

The scattering medium for the 9.7 mol % cesium salt

was observed to largely disappear on prolonged exposure to water. This observation is consistent with results previously obtained on the ethylene-methacrylic acid ionomers.

CHAPTER IV

STUDIES OF POLYPENTENAMER BASED IONOMERS CONTAINING PHOSPHONATE SIDE GROUPS

A. Introduction

The ethylene-methacrylic acid and styrene-methacrylic acid copolymers discussed in Chapters II and III are prepared by free-radical polymerization reactions at high pressure. As a result it is difficult to maintain control over alkyl chain branching, molecular weight distribution, and the distribution of acid groups as a function of composition. Recently many workers have investigated the effect of the incorporation of pendant carboxylic acid groups into preformed homopolymers. This work has included the incorporation of hydrogen bond forming groups other than carboxylic acid groups. For example Phillips et al. (40,154) studied polyethylene into which phosphonic acid side groups had been introduced. These polymers were also studied by Johnson et al. (65) as previously mentioned. Sanui et al. (155) have described the preparation of polypentenamers with pendant ionic groups. In the original investigation thioglycolate groups ($-SCH_2COOR$) were incorporated where R groups included ester and metal salt groups. The polypentenamer contains

unsaturated moieties which can be used to attach side groups or which may be saturated in a subsequent hydrogenation reaction. This latter possibility was also studied by Sanui et al. Recently the incorporation of phosphonic acid side groups into polypentenamers has been described by Azuma et al. (156). Samples prepared by Azuma have been used in the morphological studies of this work. The original polypentenamer was provided by the Goodyear Tire and Rubber Company. It contains 82% trans and 17% cis double bonds with 1% of vinyl side groups. The number average molecular weight was characterized as 94,000 with a weight average molecular weight of 172,000. The general reaction scheme used in the preparation of the polymers for study is given in Table 10. The products studied include unhydrogenated phosphonic acid, ester, and cesium salt samples as well as the analogous hydrogenated samples. The concentration of phosphonic acid units has been determined from an analysis of the infrared spectroscopy results and results of elemental analysis. For the unhydrogenated polymers samples with concentrations of 6.5 and 11.1 mol % side groups have been studied. These have been referred to in previous work as the 5% and 10% samples. This nomenclature will also be used here. Samples containing 6.7 and 11.1 mol % side groups have been studied for the hydrogenated samples. These will also be referred to as the 5% and 10% samples. All concentrations refer to the percentage of pentenamer units. In

terms of the number of side groups per carbon atom along the chain, these concentrations are effectively 2.5 times less than those cited in the previous chapters for the ethylene-methacrylic acid or styrene-methacrylic acid systems.

The thermal properties of the polymers have also been characterized by Azuma et al. (156). A melting point of 131°C was determined for a Hy-PP sample by differential scanning calorimetry at 20°C/minute. This is the same value reported by Sanui et al. (155). This value is in the lower range of values reported for the T_m of linear polyethylene. For example Mandelkern (157) reports a value of 137.5°C. The melting point is observed to decrease nearly linearly with side group concentration independently of side group type. For a side group concentration of 6.7 mol % a T_m of 107-109°C is reported. The observed T_m's for a concentration of 11.1 mol % side groups range from 93-95°C. The glass transition of the unhydrogenated polypentenamer was measured to be -98°C. This value increases to (-70)-(-74)°C for a 6.5 mol % side group concentration and to (-53)-(-55)°C for an 11.1 mol % side group concentration. The concentrations referred to here denote the actual values.

B. Experimental

1. Sample preparation. Films of the unhydrogenated materials were prepared by compression molding at 40°C and 10,000

psi followed by slow cooling to room temperature and then drying in vacuum until the time of scattering measurements. Films of the hydrogenated materials were prepared by compression molding at temperatures 20°C above the melting point at 10,000 psi and then quenching in dry ice and isopropanol. Some films were then annealed at 80°C in a vacuum oven for three days. All films were maintained under vacuum until prior to scattering measurements.

2. WAXS studies. WAXS measurements were made on the in-lab built diffractometer using CuK_α radiation with a wavelength of 1.54 Å described in Chapter II. Scans for crystallinity measurements were conducted over the range of 10-30° 2θ with angular increments chosen to permit the desired level of peak resolution. The output data was converted to intensities and corrected for background, incoherent scattering, and polarization effects according to the relation:

$$I = (I_{exp} - I_B \exp(-\mu d \sec\theta)) \cdot (2/(1 + \cos^2 2\theta)) \cdot (\exp(\mu d \sec\theta)/\sec\theta) - I_{INC} \quad (118)$$

where I_{exp} is the observed intensity with the sample in the scattering position, I_B is the observed intensity with no sample, I_{INC} the incoherent intensity, μ is the linear absorption coefficient, and d the sample thickness. The incoherent intensity is approximated by the observed intensity

at 60° 2θ. The program to convert input intensities and apply the corrections of Equation 118 is entitled WCORR and has been previously listed (166).

3. SAXS studies. SAXS measurements were made according to the procedures described in Chapter III. For the hydrogenated acid and ester samples data was collected over 0.05 to ~3° 2θ at angular increments of 0.0167° 2θ up to 1° 2θ and then in increments of 0.0333° 2θ. Data for these samples was desmeared according to the Vonk infinite height program listed in Appendix II. Since any scattering maxima for these samples occur at low angles (~0.5° 2θ) compared to the maximum angle of data collection the infinite height criterion should apply. The Vonk program initially fits the scattering curve with a Fourier series prior to differentiation. A required input parameter is the number of Fourier coefficients. It was found that good fits of the Fourier series to the observed scattering curve were obtained for 20-40 coefficients.

Procedures for background subtraction and absolute intensity measurements were performed as described in Chapter III. Table 11 lists the observed values for sample thicknesses, attenuation factors, and Lupolen standard sample intensity values for all samples.

C. Results and Discussion

1. Hydrogenated polymers. The observed WAXS curves for

these samples are listed in Figures 50-52. The curves for the hydrogenated polypentenamer (Hy-PP) show the 110 and 200 crystalline reflections of the orthorhombic polyethylene unit cell in addition to the amorphous halo. The relative intensity of the crystalline to amorphous peak intensities is observed to decrease with increasing side group concentration. The observed intensity profiles have been used to calculate the degree of crystallinity of the samples following the method of Mathews et al. (158). This method is less general than the procedure of Ruland (159). Ruland's method involves division of the scattering curve into several segments and an extrapolation of the crystalline to amorphous area ratios evaluated in the segments to determine the disorder parameter K. The disorder parameter corrects for thermal vibrations which may cause atoms in the crystalline lattice to scatter as if they were in the amorphous region. In the method of Mathews et al. the disorder parameter is effectively assumed to be one. MacKnight et al. (160) have successfully applied the method of Mathews et al. in studies of ethylene-methacrylic acid and acrylic acid copolymers. The degree of crystallinity X_C is given by the relation:

$$X_C = (I_{110} + I_{200})/(I_A + I_{110} + I_{200}) \qquad (119)$$

where I_A, I_{100}, and I_{200} are the integrated intensities of the resolved amorphous halo, and the 110 and 200 crystal planes, respectively. The resolution of the peaks is based

on the following assumptions:

1. The intensities for the scattering maxima are symmetric about the scattering maxima.
2. The peak of the amorphous halo occurs at 19.8° 2θ, the 110 reflection occurs at 21.4° 2θ, and the 200 reflection occurs at 23.7° 2θ.

The degrees of crystallinity calculated from this method are listed in Table 11. The calculated value of 0.45 for the Hy-PP sample is less than the values of 0.6-0.85 usually observed in high density polyethylenes. The value is comparable to typical crystallinities of 40-50% reported for low density polyethylene. The difference in melting point and degree of crystallinity between the Hy-PP sample and high density polyethylene seems to indicate the presence of some defects in the Hy-PP structure which decrease its ability to crystallize to the same extent. As noted previously the WAXS method is capable of evaluating crystallinities above about 0.10. The 10% Hy-PP-PO(OCs)$_2$ sample shows no detectable WAXS crystallinity but might have a crystalline fraction of about 0.10 or less. A degree of crystallinity of this order was observed by Azuma (164) by DSC on this material.

The mass densities observed for the hydrogenated polypentenamers are also listed in Table 13. The value of 0.940 gm/cm^3 reported for the annealed Hy-PP sample is higher than values of 0.92 usually reported for low density

polyethylene but less than typical values of 0.95 commonly observed for high density polyethylene samples. An increase in density is observed with increasing concentration of phosphonate side groups as expected.

The observed SAXS curves are shown in Figures 53-55. All curves have been corrected for slit smearing effects using the procedures described in a previous section. The hydrogenated polypentenamer and the 5% substituted samples exhibit distinct SAXS maxima. No such maxima are observed for the 10% substituted samples.

The Porod region of the scattering curves for the hydrogenated polypentenamer and the 5% substituted samples are shown in Figures 56-58. The plots of $s^3\tilde{I}(s)$ versus s^2 have been made to analyze the data in terms of Equation 45. The transition thickness, E, has been evaluated from the slope m according to the relation:

$$E = \left[\frac{3(-m)}{2\pi^2}\right]^{1/2} \qquad (120)$$

Values of 23 Å, 28 Å, and 45 Å were determined for the hydrogenated polypentenamer and the 5% Hy-PP-PO$(OCH_3)_2$, and 5% Hy-PP-PO$(OH)_2$ samples, respectively.

The size of the transition zone boundary has been interpreted in terms of the nature of the crystal fold surface (161,162). Values of 4-13 Å have been reported for E for bulk crystallized high density polyethylene depending on

crystallization conditions (96). Based on surface energy calculations the 4 Å value was thought to be indicative of a relatively tight fold surface. Values of E of 20 Å or more were thought to be indicative of loose fold surfaces of the switchboard type proposed by Flory (163). Values of E in the range of 10-20 Å might be consistent with an intermediate type of fold surface. On this basis the values reported in this study indicate irregular fold surfaces. The considerably larger value found for E for the acid sample may reflect the tendency of the acid groups to form hydrogen bonds. This would be expected to place additional constraints on the chain configuration near the fold surface region, making a sharp transition from crystalline to amorphous polymer more difficult.

The scattered intensities $\tilde{I}(s)$ were corrected to yield the scattering from an identical system with sharp phase boundaries according to the equation:

$$\tilde{I}(s)_{corr} = \frac{\tilde{I}(s)}{1 - \frac{2\pi^2 E^2 s^2}{3}} \qquad (121)$$

The scattering curves for the 10% acid and ester samples exhibited positive deviations from Porod's law at large angles. The deviations were analyzed to determine the internal density fluctuation component U which was then subtracted from all of the intensity points. For these samples U was evaluated from the smeared data for which case a

plot of $s^3\tilde{I}$ versus s^3 is used. The slope of the plot is equal to U. Plots are shown in Figure 59.

After correcting the scattering curves for deviations from Porod's law the mean squared electron density fluctuation $\overline{\eta^2}$ was calculated. It should be noted that the Vonk program (H109) calculates $\overline{\eta^2}$ from the smeared total integral $\tilde{Q}$ where:

$$\tilde{Q} = \int_0^\infty s\tilde{I}(s)\, ds \tag{122}$$

This is related to the desmeared total integral Q through:

$$\tilde{Q} = 2Q \tag{123}$$

The calculated values for $\overline{\eta^2}$ are listed in Table 13. A decrease in $\overline{\eta^2}$ is observed with increasing side group concentration. This is consistent with the results of Roe and Gieniewski (63) on chlorinated polyethylene as well as results of Vonk et al. (61) on other random copolymers. The results appear to be inconsistent with the values reported by Johnson et al. (65). The polymers used in this study and that are different in terms of branch content and side group distribution. This presumably could give rise to different extents of phase separation.

The values for $\overline{\eta^2}$ have been interpreted in terms of the two phase model according to Equations 36, 115, and 116

where the phases in this case are crystalline and amorphous. WAXS crystallinity values are weight fraction crystallinities. These have been converted to volume fraction crystallinities according to the relation:

$$\phi_c = W_c(\bar{\rho}/\rho_c)$$

The value of 1.002 has been used for ρ_c, the crystal density. Actually the results of the calculations indicate a value of ρ_c somewhat different from this. However, this secondary correction was deemed negligible. Values calculated for ρ_c and ρ_a are listed in Table 13. The values for ρ_c are relatively constant independent of side group concentration or type. The value of ρ_a increases with increasing side group concentration. This is consistent with exclusion of the phosphonate side groups from the crystal lattice. Johnson et al. have estimated that the phosphonate group occupies a volume at least equal to that of a tetrahedron 2.9 Å on a side. This is based on the bond lengths of 1.54 Å for the P-O group and 1.07 Å for the O-H group. Thus the phosphonic acid group cannot become an integral part of the regular crystalline lattice. Thus exclusion of the phosphonic acid and ester groups from the crystal lattice is not surprising.

The SAXS curves for the hydrogenated polypentenamer and the samples with 5% side groups have been analyzed in terms of the Hosemann paracrystalline lattice model. The

pertinent equations for this model were given in Chapter I. The data analyzed here have not been corrected for deviations from Porod's law. All of the data have been multiplied by s^2 for comparison with the one dimensional model for reasons explained in Chapter I. Figures 60-62 show the experimental curves and model fits. Table 14 lists the parameters used in obtaining the model fits. The crystal spacing C decreases from a value of 150 Å to ~45-60 Å for the polymers with 5% side groups. Johnson et al. reported a crystal spacing of 93 Å for low density polyethylene and a spacing of 56 Å for a sample with a phosphonic acid concentration of 1.8 mol %. This concentration is close to that of the 5% samples of the current study. The amorphous spacing increases from 80 Å to ~120 Å with the incorporation of 5% side groups which is consistent with a reduction in the chain length available for inclusion in the crystal. A linear crystallinity ℓ_c may be defined by the relation:

$$\ell_c = C/(C + A) \tag{124}$$

Linear crystallinities of 0.65, 0.27, and 0.32 are obtained for the Hy-PP, 5% Hy-PP-PO$(OCH_3)_2$, and 5% Hy-PP-PO$(OH)_2$ samples, respectively. The value for the Hy-PP sample is larger than the WAXS crystallinity of 0.45. This may indicate the presence of amorphous regions outside of the lamella stack. Such regions are detected by the WAXS technique but would not

be seen by the SAXS method. In this respect the agreement between WAXS and SAXS crystallinities for the acid and ester samples is somewhat surprising. The arrangement of lamella in these samples is not well known. Small angle light scattering studies showed a typical (165) four-lobed light scattering pattern with cross polaroids (H_V) indicative of a spherulitic morphology for the Hy-PP sample. The ester and acid samples showed only an H_V light scattering pattern with a continuous decrease in intensity from a central spot. Optical microscopic investigation showed birefringence which was present over the entire field of view. These results would indicate a sample consisting of crystal and amorphous layers arranged randomly throughout the sample with no crystal superstructure.

The transition zone values evaluated from the Hosemann model analysis are in reasonable agreement with those found from the direct analysis of the Porod region. The parameter N decreases dramatically from 100 to around 2 on incorporation of 5 mol % side groups. As discussed previously the interpretation of N is uncertain. However it can be said that such a large decrease in N is indicative of less parallel lamella stacking. This is consistent with the interpretation of a transition from a spherulitic to random layer morphology given to the light scattering studies.

The SAXS curves observed for the 5 and 10 mol % cesium salts are shown in Figure 65. The scattering curves

both show a region of zero order scattering and a subsequent scattering maximum. The Bragg spacing increases from about 34 Å for the 5% Hy-PP-PO$\{$OCs$)_2$ sample to 48 Å for the 10% Hy-PP-PO$\{$OCs$)_2$ sample.

The Porod region of the scattering curves for these samples is analyzed in Figure 64. Positive deviations from Porod's law are observed at large angles in the plots of $s^4 I(s)$ versus s^4. These have been used to evaluate the internal density fluctuation component U as before. After subtracting U from the intensity points, a calculation of $\overline{\eta^2}$ was made. The resulting values are compared in Figure 65 to those for the ethylene-methacrylic acid and styrene-methacrylic acid cesium salts. Figure 65 also makes such a comparison of values of U. The dependence of $\overline{\eta^2}$ and U on ion concentration for this system is more similar to the cesium salts of the styrene-methacrylic acid copolymers than to the salts of the ethylene-methacrylic acid copolymers.

The effect of water was studied for the 5% Hy-PP-PO$\{$OCs$)_2$ sample. Scattering curves are shown in Figure 68 for the dry sample and the same sample after 48 hours of soaking in water. The scattering maximum is observed to disappear. It had been determined by weighing that this material is almost completely saturated with water in 48 hours and that almost no additional weight gain will be observed after that time. The observed disappearance of the SAXS maximum is similar to the behavior found for other water saturated

ionomers and offers additional evidence that the maximum results from the presence of ionic aggregates.

2. Unhydrogenated polymers. WAXS and SAXS was investigated for unhydrogenated polypentenamers. A single amorphous halo at about 19.5° 2θ was seen by WAXS for all samples in runs at room temperature. These runs were conducted above the reported (166) melting temperature of the unhydrogenated polypentenamer.

SAXS curves obtained for 5 and 10% ester and acid samples were typical of those previously discussed for amorphous polymers. No scattering maxima were observed. Desmeared SAXS curves for the cesium salts are shown in Figure 68. The curve for the 5% sample shows a broad shoulder. The 10% sample exhibits a scattering maximum corresponding to a spacing of 42 Å. The Porod region of the scattering curves is analyzed in Figure 67 to determine values for U which were subtracted from the intensity points. Values for $\overline{\eta^2}$ were then calculated and plotted in Figure 65 along with the values for U. The values for $\overline{\eta^2}$ and U are again found to be fairly similar to those for the styrene-methacrylic acid ionomers. Figure 65 indicates that the increase in phase separation with ion concentration for both polypentenamer systems is fairly similar to that of the styrene-methacrylic acid ionomers but relatively different than the ethylene-methacrylic acid ionomers. This indicates that the

manner of phase separation is not simply affected by crystallinity of the hydrocarbon units but depends more on other factors. The distribution of co-units along the polymer chain is not particularly well characterized in any of these systems. However there is some evidence that the ethylene-methacrylic acid distribution is more blocky (50) than for the other systems. Such blockiness might lead to an earlier onset of phase separation than would be found in a system with a more random distribution of co-units.

D. Conclusions

The morphology of a series of polypentenamers substituted with phosphonic acid, ester, and cesium salt groups has been investigated. Samples have included materials with unhydrogenated and hydrogenated backbones. A hydrogenated polypentenamer with no side grwups exhibits a morphology which is semi-crystalline and spherulitic. The SAXS pattern exhibits a definitie lamellar spacing with long range parallelness of lamellae as analyzed in terms of the Hosemann paracrystalline lattice model. Incorporation of side groups leads to a loss of the spherulitic superstructure, a decrease in the overall crystallinity and the SAXS crystal spacing, while the SAXS amorphous spacing increases. An analysis of the SAXS mean squared electron density fluctuation $\overline{\eta^2}$ and mass density values indicates the crystal density is essentially constant but the amorphous density increases. This

pattern is consistent with exclusion of the phosphonate units from the crystal lattice. SAXS curves for the cesium salt samples show maxima. Values for $\overline{\eta^2}$ are comparable to those observed for other ionomers.

Unhydrogenated samples are amorphous according to WAXS at room temperature. SAXS curves for acid and ester substituted samples of these polymers were also typical of those for amorphous polymers. Cesium salt samples showed additional scattering components. Values for $\overline{\eta^2}$ were indicative of partial phase separation of the ionic groups comparable to the hydrogenated polymers and the styrene-methacrylic acid ionomers discussed in Chapter III.

SUGGESTIONS FOR FUTURE WORK

1. Deformation studies of other ionomers. It is of interest to determine if other ionomers besides the ethylene-methacrylic acid ones examined in this study also exhibit azimuthally dependent SAXS patterns. Systems which would seem to be of most interest would be non-crystalline ionomers with high salt contents.

2. Deformation studies as a function of temperature. An examination of the SAXS pattern at small deformations as a function of temperature should reveal detailed information about the structural causes of relaxation mechanisms.

3. Small angle neutron scattering studies. The complementarity of SANS and SAXS has been noted in the text. A combination of the SANS invariant with the SAXS invariant and mass density is sufficient to determine the volume fractions and phase densities for a two phase system. This would also allow a fairly exact calculation of the fraction of ions which are phase separated. In this case the SANS studies would rely solely on the presence of metal ions and density variations for scattering contrast. Studies of this type are currently being planned. In subsequent studies the sensitivity of SANS to isotopic variations could be exploited.

This could be done in two ways. Firstly deuterated or partially deuterated chains could be mixed with hydrogenated material. Possible changes in the radius of gyration resulting from ion clustering could thus be measured for the deuterated chains. Secondly samples with different isotopes of the metal cations could be compared. Such a study could reveal information about the extent of aggregation and the geometry of aggregates.

4. Further study of the internal fluctuation scattering component. A study of the styrene-methacrylic acid copolymers as a function of temperature would be made by SAXS and infrared spectroscopic techniques. The IR spectra could be used to evaluate the relative numbers of monomer and dimer acid groups present. This could be used along with models for such groups to compute the expected level of SAXS internal fluctuation scattering. The calculated value could then be compared with the experimentally observed scattering.

REFERENCES

1. E.P. Otocka, J. Macrom. Sci., Rev. Macrom. Chem., 5, 275 (1971).

2. L. Holliday, "Ionic Polymers," Applied Science, N.Y., N.Y. (1975).

3. A. Eisenberg and M. King, "Ion Containing Polymers--Physical Properties and Structure," Academic Press, N.Y., N.Y. (1977).

4. A. Eisenberg, J. Pol. Sci., Symp., 45, 99 (1974).

5. M.F. Hoover, Jour. Macr. Sci., A4, 1327 (1970).

6. M.F. Hoover, J. Pol. Sci., Pol. Symp., 45, 1 (1974).

7. V. Luzzati and D. Skoulios, Acta. Cryst., 14, 278 (1961).

8. V. Luzzati, in "Biological Membranes," D. Chapmen, ed., p. 71 (1968).

9. W. Philippoff, Disc. of Faraday Soc., 11, 96 (1951).

10. V. Luzzati and A. Tardieu, Ann. Rev. Phys. Chem., v. 25, p. 79-94 (1974).

11. V. Luzzati et al., Acta. Cryst., 13, 660&668 (1960).

12. A. Eisenberg, Macromolecules, 3, 147 (1970).

13. O.A. Ponomarev and I.A. Ionova, USSR Polymer Science, 1181 (1974).

14. W. Kuhn and F. Grün, Kolloid Z., 101, 248 (1942).

15. R. Longworth and D.J. Vaughan, Nature (London), 2:18, 85 (1968); Polymer Prepr. ACS, 9, 525 (1968).

16. Reference 2, Ch. 2.

17. W.J. MacKnight and H.K. Plummer, unpublished results.

18. C. Marx, J. Koutsky, and S. Cooper, Polymer Letters, 9, 167 (1971).

19. M. Pineri, C. Meyer, and A. Bourret, J. Pol. Sci., Pol. Phys., 13, 1881 (1975).

20. C. Meyer, Ph.D. Thesis, University of Grenoble (1977).

21. F.C. Wilson, R. Longworth, and D.J. Vaughan, Polym. Prepr. ACS, 9, 505 (1968).

22. B.W. Delf and W.M. MacKnight, Macromolecules, 1, 510 (1968).

23. W.J. MacKnight, W.P. Taggart, and L. McKenna, J. Pol. Sci., Pol. Symp. 46, 83 (1974).

24. F.L. Binsbergen and G.F. Kroon, Macromolecules, 6, 145 (1973).

25. C.L. Marx, D.F. Caulfield, and S.L. Cooper, Macromolecules, 6:3, 344 (1973).

26. R.J. Roe, J. Phys. Chem., 76, 1311 (1972).

27. J. Kao et al., Macromolecules, 7:1, 95 (1974).

28. W.J. MacKnight, W.P. Taggart, and R.S. Stein, J. Pol. Sci., Symp. 45, 113 (1974).

29. W.P. Taggart, Ph.D. Thesis, University of Massachusetts (1973).

30. A. Eisenberg and M. Novratil, Macromolecules, 7, 90 (1974).

31. M. Pineri, C. Meyer, C. Levelut, and M. Lombert, J. Pol. Sci., Pol. Phys., 12, 15 (1974).

32. A. Moudden, M. Levelut, and M. Pineri, Jour. Pol. Sci., Pol. Phys., 15, 1707 (1977).

33. C.T. Meyer and M. Pineri, J. Pol. Sci., Pol. Phys., 16, 569 (1978).

34. E.P. Otocka and D.D. Davis, Macromolecules, 2, 437 (1969).

35. Reference 2, p. 128.

36. Reference 31, p. 1708.

37. C.T. Meyer, Journal de Physique, C6, 12, 37, 777 (1976).

38. W.J. MacKnight, L.W. McKenna, and B.E. Read, J. Appl. Phys., 38, 4208 (1967).

39. E.P. Otocka and F.R. Eirich, J. Pol. Sci., A2, 6, 921&933 (1970).

40. P.J. Phillips and W.J. MacKnight, J. Pol. Sci., A2, 8, 727 (1970).

41. B.E. Read, E.A. Carter, T.M. Connor, and W.J. MacKnight, Br. Polym. Jour., 1, 123 (1969).

42. W.J. MacKnight and F.A. Emerson, in "Dielectric Properties of Polymers," F.E. Korasz, ed., Plenum, N.Y., N.Y.

43. A. Eisenberg and M. Navratil, Polym. Letters, 10, 537 (1972).

44. A. Eisenberg and M. Navratil, Macromolecules, 6, 604 (1974).

45. A. Eisenberg and M. Navratil, Macromolecules, 7, 84 (1974).

46. A. Eisenberg and M. Navratil, Macromolecules, 7, 90 (1974); A. Eisenberg and E. Shohamy, Pol. Phys., 14, 1211 (1976).

47. N. Erdi and H. Morowetz, J. Colloid Sci., 19, 708 (1964).

48. W.E. Fitzgerald and L.E. Nielsen, Proc. Royal Soc. London, A, a282, 137 (1964).

49. W.J. MacKnight, Am. Chem. Soc. Polym. Preprints, 11, 504 (1970).

50. R.E. Prud'homme and R.S. Stein, Macromolecules, 4, 668 (1971).

51. R.E. Prud'homme and R.S. Stein, Pol. Phys., 11, 1347 (1973).

52. T. Kajiyama, T. Oda, R.S. Stein, and W.J. MacKnight, Macromolecules, 4, 198 (1971).

53. Reference 13, p. 1183.

54. Y. Uemura, R.S. Stein, and W.J. MacKnight, Macromolecules, 4, 490 (1971).

55. T. Kajiyama, R.S. Stein, and W.J. MacKnight, J. Appl. Phys., 41, 4361 (1970).

56. K. Sakomoto, W.J. MacKnight, and R.S. Porter, J. Pol. Sci., A2, 277 (1970).

57. T. Earnest, Ph.D. Thesis, University of Massachusetts (1978).

58. P.J. Flory, J. Chem. Phys., 15, 684 (1947).

59. I. Sanchez and R. Eby, Macromolecules, 8:5, 638 (1975).

60. E.W. Fischer, H.J. Sterzel, and G. Wegner, Kolloid Z., Z. Polym., 251, 980 (1973).

61. G. Kortleve, C. Tuijnom, and C.G. Vonk, J. Pol. Sci., A2, 10, 123 (1972).

62. C.G. Vonk, J. Pol. Sci., C, 38, 429 (1972).

63. R.J. Roe and C. Gieniewski, Macromolecules, 6:2, 212 (1973).

64. W. Ruland, J. Appl. Cryst., 4, 70 (1971).

65. R. Johnson, B. Delf, and W.J. MacKnight, J. Pol. Sci., Pol. Phys., 11, 571 (1973).

66. J. Schelten, Unpublished results presented at SANS conference, APS meeting, Washington, D.C., April 1978.

67. R.S. Stein and J.S. Higgins, Review of SANS, SALS, SAXS, applications to polymers, 1978.

68. A. Guinier and G. Fournet, "Small Angle Scattering of X-Rays," Wiley, N.Y., N.Y. (1955).

69. D. Riley and G. Oster, Disc. of Faraday Soc., 11, 107 (1951).

70. R. Hosemann and S.N. Bagchi, "Direct Analysis of Diffraction by Matter," North Holland Publishing Co., Amsterdam (1962), Ch. 3.

71. A. Guinier, "X-ray Diffraction in Crystals, Imperfect Crystals, and Amorphous Bodies," W.H. Freeman, San Francisco, Calif. (1963).

72. P.W. Barber and D. Wang, Applied Optics, 17:5, 797 (1978).

73. G. Porod, Acta Phys. Austriaca, 2, 255 (1948).

74. Reference 68, Ch. 2, 4.

75. Reference 70, Ch. 3.

76. C.G. Shull and L.C. Ross, J. Appl. Phys., 18, 295 (1947).

77. Reference 68, p. 134.

78. F. Zernicke and J. Prins, Z. Physik., 41, 184 (1927).

79. P. Debye, J. Math. Phys., 4, 133 (1925).

80. M. Yvon, J. Phys. Radium, 7, 201 (1946).

81. J. Kirkwood, J. Chem. Phys., 18, 1040 (1950).

82. M. Born and H.S. Green, Proc. Royal Soc. London, A-188, 10 (1946).

83. G. Fournet, Compt. Rend., 228, 1421 (1949).

84. D. Riley and G. Oster, Acta Cryst., 5, 1 (1952).

85. Reference 70, Ch. 18.

86. Reference 71, Ch. 8.

87. Reference 70, Ch. 9.

88. Reference 71, Ch. 9.

89. G. Porod, Kolloid Z., 124, 83 (1951).

90. G. Porod, Acta Physica Austriaca, 2, 255 (1948).

91. G. Porod, Kolloid Z., 125, 51 (1952).

92. G. Porod, Kolloid Z., 125, 109 (1952).

93. D.S. Brown, F.P. Warner, and R.E. Wetton, Polymer, 13:12, 575 (1972).

94. W. Ruland, J. Appl. Cryst., 4, 70 (1971).

95. Reference 70, Ch. 18, p. 628.

96. C. Vonk, J. Appl. Cryst., 6, 8 (1973).

97. T. Hashimoto et al., Macromolecules, 7, 364 (1974).

98. T. Hashimoto et al., Macromolecules, 10, 377 (1977).

99. J. Koberstein, unpublished results.

100. J. Rathje and W. Ruland, Colloid and Polym. Sci., 254, 358 (1976).

101. J. Wendorff and E. Fischer, Kolloid Z. Polym., 251, 876 (1973).

102. G. Bonart, J. Macro. Sci., Phys., 10:1, 177 (1974); J. Macro. Sci., Phys., 10:2, 345 (1974).

103. D. Buchanan, J. Pol. Sci., A2, 9, 645 (1971).

104. Reference 70, p. 408.

105. C. Vonk and G. Kortleve, Kolloid Z. Z. Polym., 220, 19 (1967).

106. C. Vonk and G. Kortleve, Kolloid Z. Z. Polym., 124, 225 (1968).

107. W. Ruland, Colloid and Polym. Science, 255, 5, 29 (1977).

108. D.S. Brown, Polymer, 14, 379 (1973).

109. B. Crist and N. Morasoff, Jour. Pol. Sci., Pol. Phys., 11, 1023 (1973).

110. S. Baczek, Ph.D. Thesis, University of Massachusetts (1977).

111. F.P. Warner, W.J. MacKnight, and R.S. Stein, Jour. Pol. Sci., Pol. Phys., 15, 12 (1977).

112. R. Bramer, Ph.D. Thesis, University of Ulm (1973).

113. R. Bramer, Colloid and Polym. Sci., 252, 504 (1973).

114. W. Wenig, Ph.D. Thesis, University of Ulm (1973).

115. W. Wenig, F.E. Karasz, and W.J. MacKnight, J. Appl. Phys., 46, 4194 (1975).

116. O. Kratky, Makrom. Chemie, 35A, 12 (1960).

117. O. Kratky, J. Pilz, and P.J. Schmitz, J. Colloid and Interf. Science, 21, 24 (1966).

118. R.W. Hendricks, J. Appl. Cryst., 5, 315 (1972).

119. Reference 68, Ch. 3.

120. A. Guinier and G. Fournet, Nature, 160, 501 (1947).

121. A. Dijkstra, G. Kortleve, and C. Vonk, Colloid and Polymer Science, 210, 121 (1966).

122. P.N. Schmidt, Acta Cryst., 19, 938 (1965).

123. R.W. Hendricks and P.W. Schmidt, Acta Physica Austriaca, 26:2, 97 (1967).

124. P.W. Schmidt, J. Appl. Cryst., 3, 137 (1970).

125. O. Kratky, G. Porod, and L. Kohovec, Z. Elektrochem., 55:1, 53 (1951).

126. P.W. Schmidt, Acta Cryst., 19, 938 (1965).

127. P.W. Schmidt and R. Hight, Acta Cryst., 13, 480 (1960).

128. R.W. Hendricks and P.W. Schmidt, Acta Physica Austriaca, 26:2, 97 (1967).

129. K. Kranjc, Acta Cryst., 7, 709 (1954).

130. V. Synecek, Acta Cryst., 15, 642 (1962).

131. W.J. MacKnight, L.W. McKenna, B.E. Read, and R.S. Stein, J. Phys. Chem., 72, 1122 (1968).

132. L.E. Alexander, "X-ray Diffraction Methods in Polymer Science," Wiley, N.Y., N.Y. (1969).

133. R.W. Hendricks, J. Appl. Cryst., 11, 15 (1978).

134. C.J. Borkowski and M. Kopp, IEEE Transactions, Nucl. Sci., NS-17, p. 340 (1970); NS-19, 161 (1972).

135. S. Krimm and A.V. Tobolsky, Textile Research J., 21, 805 (1951).

136. W.J. MacKnight, T. Kajiyama, and L.W. McKenna, Polym. Eng. Sci., 8, 267 (1968).

137. E.P. Otocka and T.K. Kwei, Macromolecules, 1, 244 (1968).

138. C.L. Marx and S.L. Cooper, Makro. Chem., 168, 339 (1973).

139. S. Cooper, personal communication, APS Meeting, Washington, D.C., April 1978.

140. Reference 72, p. 800.

141. W.J. MacKnight, Pol. Prepr. ACS, 11, 504 (1970).

142. G. Porod, Z. Naturf., A4, 401 (1949).

143. Reference 70, p. 508.

144. O. Krotky and G. Porod, J. Colloid Science, 4, 35 (1970).

145. Reference 70, Ch. 12.

146. B.E. Read and R.S. Stein, Macromolecules, 1:2, 116 (1968).

147. E. Andreeva, V. Nikitin and Y. Boyartchuk, Macromolecules, 9:2, 238 (1976).

148. Reference 68, p. 140.

149. R. Longworth and H. Morawetz, J. Pol. Sci., 29, 310 (1958).

150. F.P. Warner, Ph.D. Thesis, Loughbourough University of Technology (1975).

151. Reference 110, p. 70.

152. D.R. Uhlmann et al., J. Macrom. Sci., Physics, B12:2, 153 (1976.

153. G. Natta, J. Pol. Sci., 16, 143 (1955).

154. P.J. Phillips, F.A. Emerson, and W.J. MacKnight, Macromolecules, 3, 767 (1970).

155. K. Sanui, R.W. Lenz, and W.J. MacKnight, J. Pol. Sci., Pol. Chem., 12, 1965 (1974).

156. C. Azuma and W.J. MacKnight, J. Pol. Sci., Pol. Chem., 15, 547 (1977).

157. L. Mandelkern, Rubber Chem. Tech., 32, 1392 (1959).

158. J.L. Mathews, H.S. Peisser, and R.S. Richards, Acta Cryst., 2, 85 (1949).

159. W. Ruland, Acta Cryst., 14, 1180 (1961).

160. W.J. MacKnight, W.P. Taggart, and L. McKenna, J. Pol. Sci., Polym. Symp., 46, 83 (1974).

161. J.D. Hoffmann and J.I. Lauritzen, J. Res. NBS, 65A, 297 (1961).

162. Reference 150, p. 155.

163. D. Yoon and P.J. Flory, Nature (March 1978).

164. C. Azuma, laboratory report, University of Massachusetts (1976).

165. R.S. Stein and M.B. Rhodes, J. Appl. Physics, 31, 1873 (1960).

166. R. Cembrola, Ph.D. Thesis, University of Massachusetts (1978).

TABLES

14. Parameters used in fits of Hosemann linear paracrystalline model for hydrogenated polypentenamer samples.

TABLE 1

Elongation (%)	t (cm)	I/I_o	P (relative)
0	0.038	0.035	1.00
9	0.036	0.047	0.87
30	0.033	0.059	0.96
35	0.033	0.059	1.41
45	0.032	0.065	1.33
60	0.300	0.083	1.52
100	0.027	0.114	1.51
300	0.019	0.181	2.85

TABLE 2

	R_1 (Å)	R_2 (Å)	R_3 (Å)	A	δ (%)
1.	5	35	8	0.001	3.5
2.	5	35	8	0.005	38
3.	5	35	5	0.005	19
4.	8	35	8	0.001	25
5.	4-14	35	8	0.001	45
6.	5	35	5	0.002	5

TABLE 3

Sample	Mol % MAA	M_n	Neutralization
1[a]	2.5	700,000[c]	Cs^+
2[a]	3.8	660,000[c]	Cs^+
3[a]	5.5	~60,000[d]	Cs^+
4[a]	7.7	75,000[c]	Cs^+
5[a]	9.7	500,000[c]	Cs^+
6[a]	4.6	~400,000[d]	Unneutralized
7[a]	8.6	~400,000[d]	Unneutralized
8[b]	2.5	~60,000[d]	Unneutralized
9[b]	4.6	~60,000[d]	Unneutralized
10[b]	6.7	~60,000[d]	Unneutralized

[a]Samples provided by Eisenberg.

[b]Samples synthesized at University of Massachusetts using following conditions:

Sample	$[BzO_2]$ wt %	Temp (°C)	Time (hr)
8	0.44	80	2
9	0.44	80	2
10	0.44	80	2

[c]Determined by membrane osmometry in toluene.

[d]Estimated from monomer concentrations and polymerization times and from measurements on other samples.

TABLE 4

Sample	μ (cm^{-1})	t (cm)	$\bar{\rho}$ (gm/cm^3)	N
1	14.5	0.061	1.08	91
2	19.1	0.046	1.10	89
3	23.2	0.041	1.12	82
4	33.0	0.060	1.18	85
5	40.3	0.042	1.20	84
6	4.1	0.040	--	--
7	4.4	0.031	--	--
8	4.2	0.096	--	--
9	4.2	0.085	--	--
10	4.3	0.090	--	--

N = % neutralization as determined by x-ray absorption.

TABLE 5

	Position (mm)	Slit Width (mm)	Slit Length (mm)
X-ray Source	0	----	----
Slit 1	5	0.10	10
Slit 2	195	0.10	10
Slit 3	250	0.18	----
Sample	270	----	----
Slit 4	540	0.10	10
Slit 5	580	0.05	10
Detector	585	----	----

TABLE 6

Differential Mode

High Voltage	= 1100	Volts (dial)
Baseline	= 100	Volts (dial)
Window	= 700	Volts (dial)
Time Constant	= 0.5	
Coarse Gain	= 16	Volts
Fine Gain	= 2	Volts

TABLE 7

Ion Conc (mol %)	ρ_1	ρ_2	ϕ_1	F	ρ_1	ρ_2	ϕ_1	F
2.5	2.5	0.58	0.002	0.60	0.80	0.58	0.015	0.54
3.8	2.5	0.59	0.002	0.62	0.80	0.59	0.015	0.68
5.5	2.5	0.60	0.004	0.58	0.80	0.60	0.025	0.61
7.7	2.5	0.62	0,012	0.62	0.80	0.61	0.110	0.51
9.7	2.5	0.64	0.024	0.64	0.80	0.61	0.190	0.34

ρ_1 = density (mole-el/cm^3) of ion rich phase

ρ_2 = density (mole-el/cm^3) of ion poor phase

ϕ_1 = volume fraction of ion rich phase

ϕ_2 = volume fraction of ion poor phase

F = fraction of ions in phase 2

TABLE 8

Ion Concentration (mol %)	$(Rg)_o$ (Å)	β	δ (%)
2.5	15	3.0	17
3.8	15	1.5	12
5.5	12	0.5	20
7.7	15	2.0	24
9.7	20	2.0	17

$(Rg)_o$ = most probable value of radius of gyration

β = width of Lorentzian size distribution

δ = error between calculated scattering curve and experimental

TABLE 9

Ion Concentration (mol %)	R_1 (Å)	$\overline{R_2}$ (Å)	β (R_2)	R_3 (Å)	A	δ (%)
2.5	8	40	100	5	0.035	10
3.8	6	40	100	5	0.050	12
5.5	8	40	60	5	0.030	9
7.7	7	40	40	5	0.020	15
9.7	7	35	40	4	0.030	15

$$R_2 = \overline{R_2} \exp\left(\frac{-(R_2 - \overline{R_2})^2}{\beta \overline{R_2}}\right)$$

TABLE 10

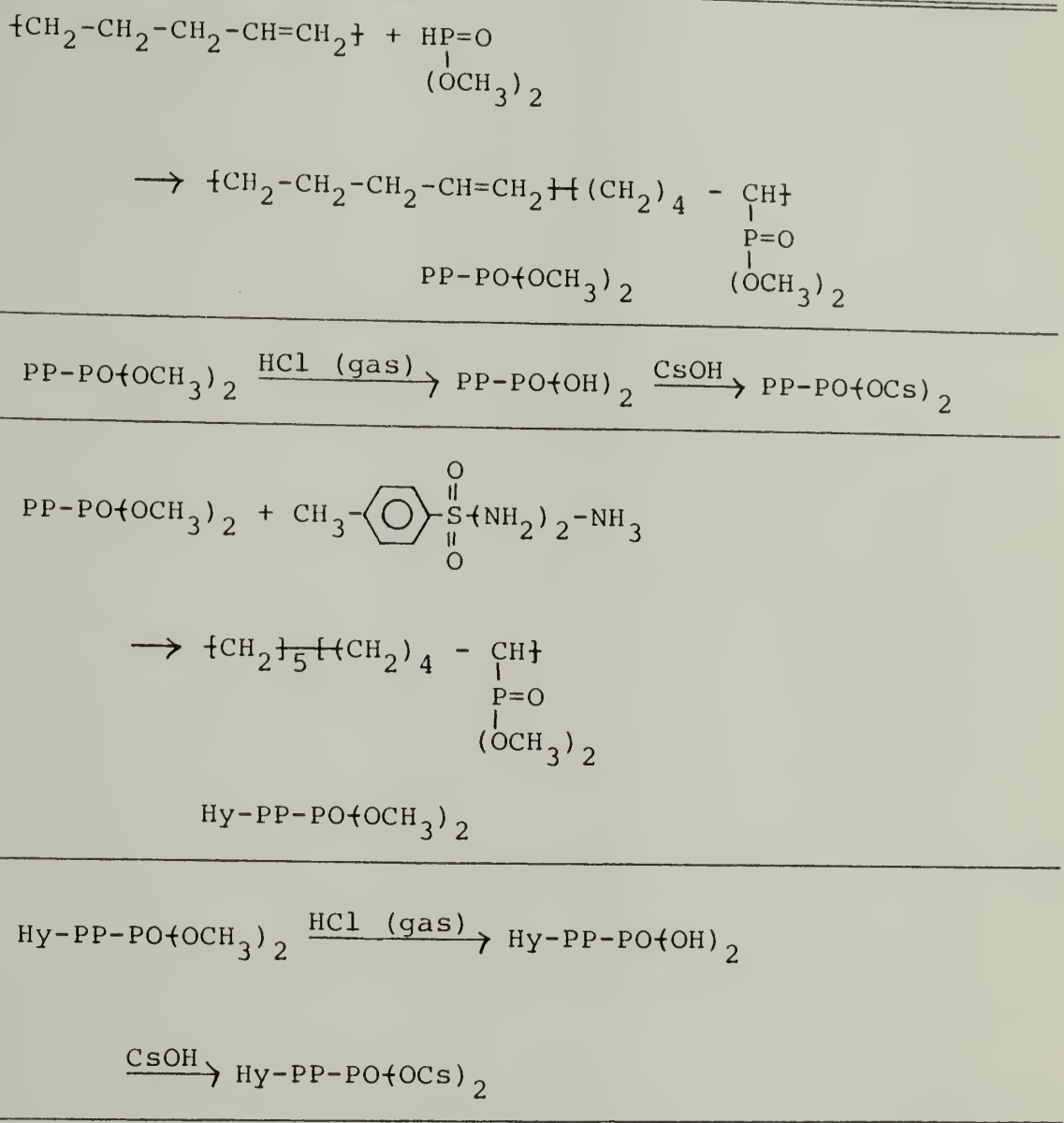

TABLE 11

Sample	t (cm)	I/I_o	I_L (cps)
Hy-PP	0.058	0.772	25.0
5% Hy-PP-PO$(OCH_3)_2$	0.063	0.805	13.3
5% Hy-PP-PO$(OH)_2$	0.049	0.859	12.8
5% Hy-PP-PO$(OCs)_2$	0.052	0.370	13.2
10% Hy-PP-PO$(OCH_3)_2$	0.051	0.745	13.1
10% Hy-PP-PO$(OH)_2$	0.036	0.830	11.7
10% Hy-PP-PO$(OCs)_2$	0.041	0.315	13.1
5% PP-PO$(OCs)_2$	0.051	0.351	6.65
10% PP-PO$(OCs)_2$	0.028	0.550	5.97
5% Hy-PP-PO$(OCs)_2/H_2O$	0.051	0.400*	6.10

t = sample thickness

I/I_o = sample attenuation factor

I_L = Lupolen standard sample intensity in counts per second

*Calculated to exclude cell walls and water surrounding sample.

TABLE 12

Sample	X_c (WAXS)	$\bar{\rho}$ (gm/cm^3)
Hy-PP	0.45	0.940
5% Hy-PP-PO$(OCH_3)_2$	0.30	0.975
10% Hy-PP-PO$(OCH_3)_2$	0.10	0.980
5% Hy-PP-PO$(OH)_2$	0.26	0.970
10% Hy-PP-PO$(OH)_2$	0.12	0.990
5% Hy-PP-PO$(OCs)_2$	0.25	1.020
10% Hy-PP-PO$(OCs)_2$	----	1.085

TABLE 13

Sample	$\overline{\eta^2}$ $\left(\frac{\text{mole-el}}{\text{cm}^3}\right)^2$	$\left(\frac{\text{mole-el}}{\text{cm}^3}\right)$		
		$\rho_c - \rho_a$	ρ_c	ρ_a
Hy-PP	1.33×10^{-3}	0.073	0.590	0.517
5% Hy-PP-PO$(OCH_3)_2$	5.34×10^{-4}	0.050	0.588	0.538
10% Hy-PP-PO$(OCH_3)_2$	1.20×10^{-4}		0.586	0.549
5% Hy-PP-PO$(OH)_2$	3.81×10^{-4}	0.044	0.582	0.538
10% Hy-PP-PO$(OH)_2$	1.86×10^{-4}	0.042	0.595	0.543

TABLE 14

Sample	C (Å)	A (Å)	E	N	δ (%)
Hy-PP	150	80	30	100	10.0
5% Hy-PP-PO(OCH$_3$)$_2$	45	125	30	2	4.5
5% Hy-PP-PO(OH)$_2$	57	120	40	1.8	4.1

FIGURES

FIGURE 1

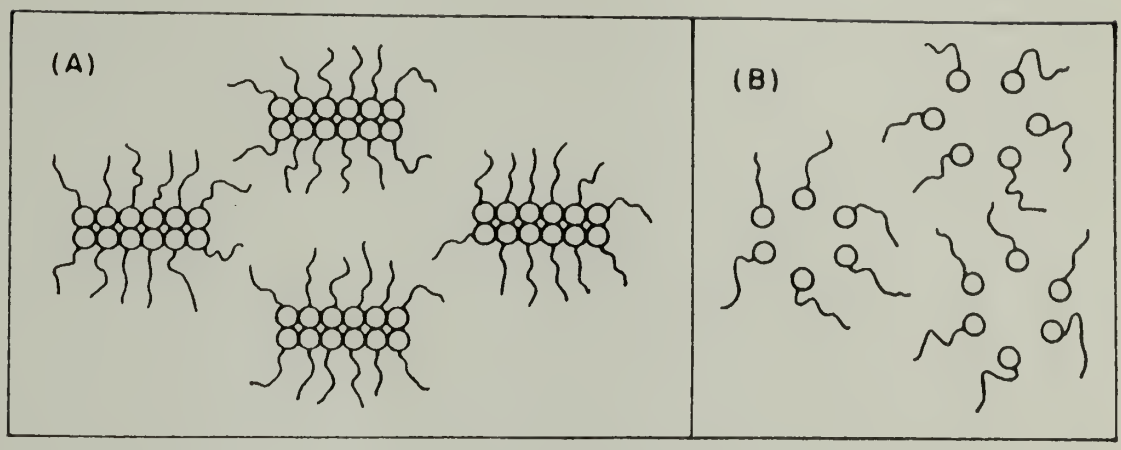

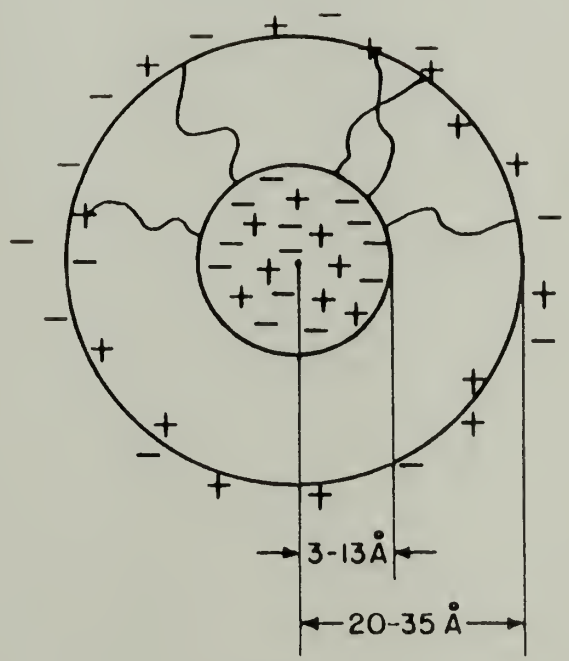

FIGURE 2

FIGURE 3

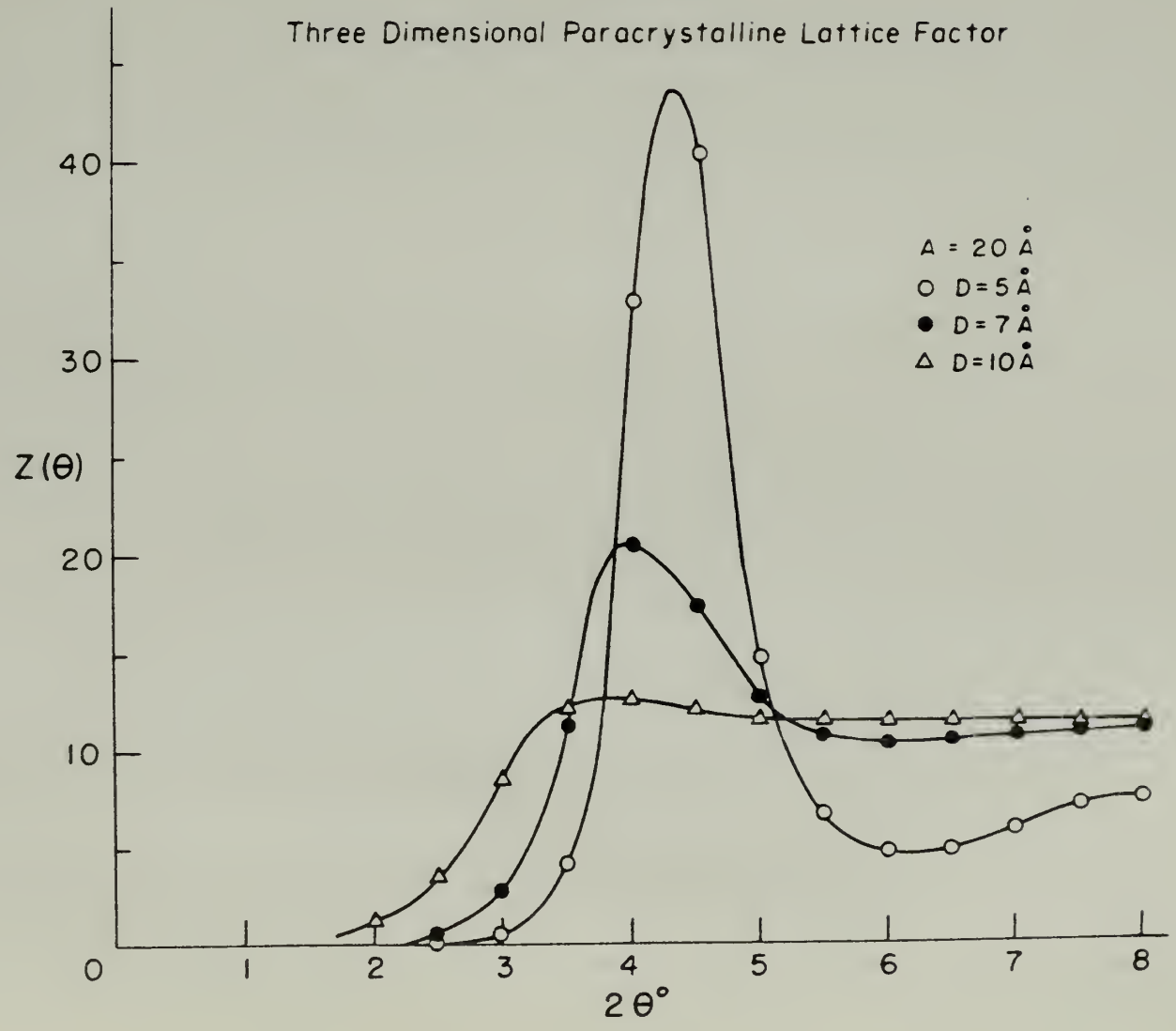
Three Dimensional Paracrystalline Lattice Factor
A = 20 Å
D = 5 Å
D = 7 Å
D = 10 Å
Z(θ)
40
30
20
10
0
1
2
3
4
5
6
7
8
2θ°

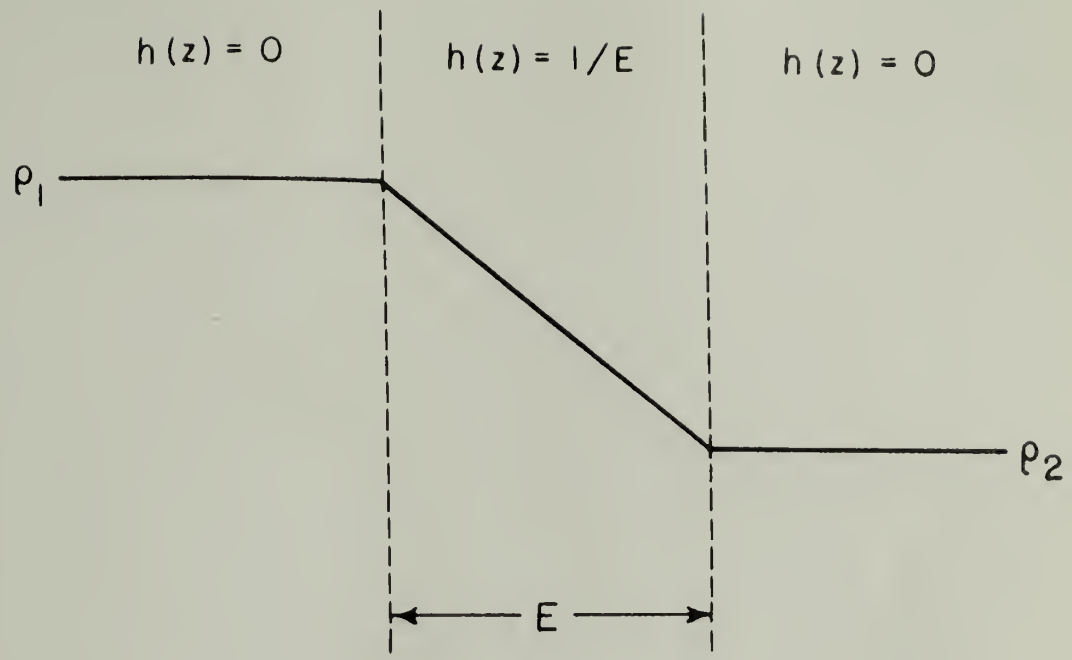

FIGURE 4

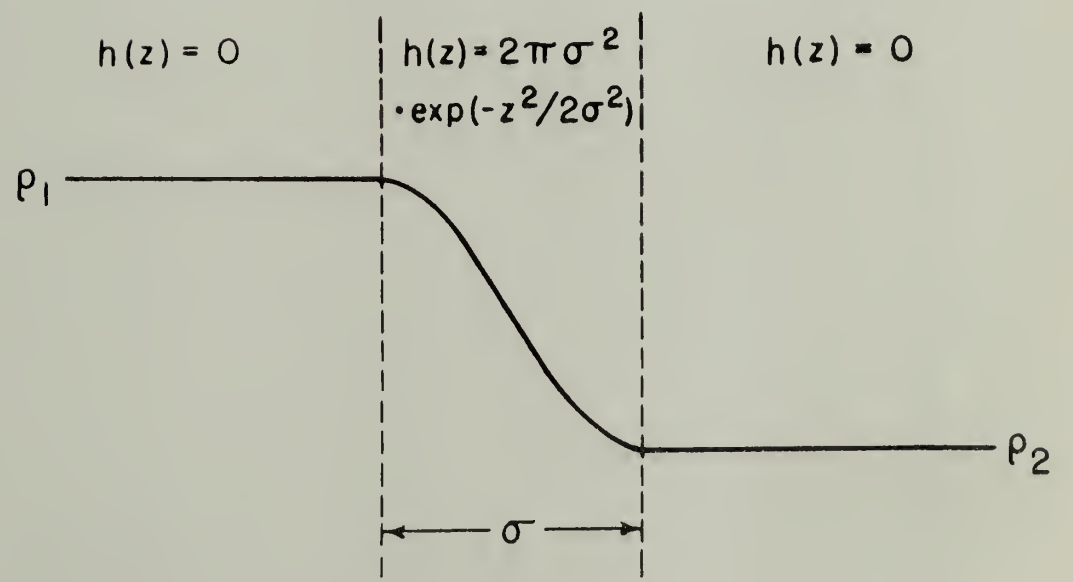

FIGURE 5

FIGURE 6

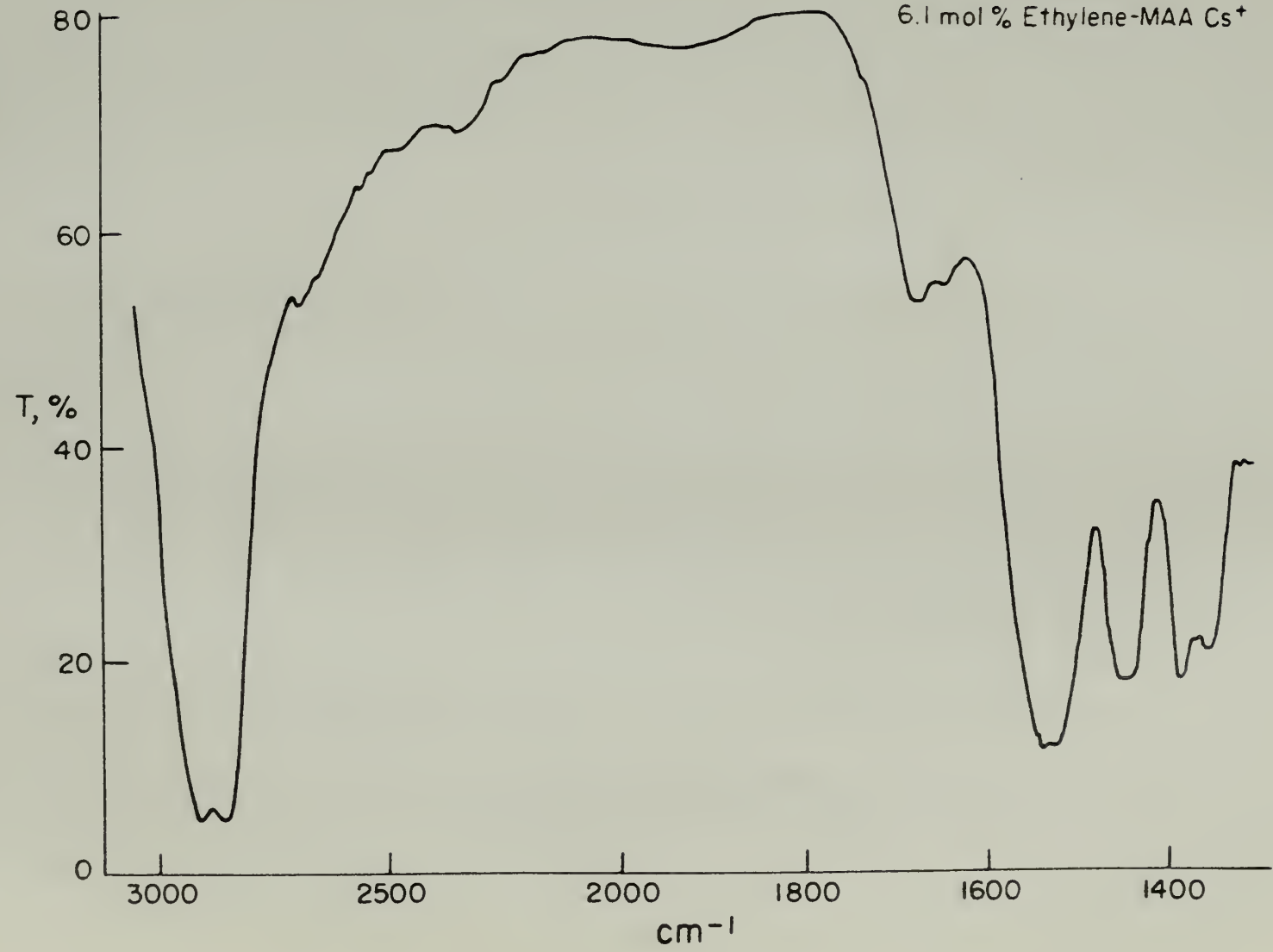
6.1 mol % Ethylene-MAA Cs+
80
60
40
20
0
T, %
3000
2500
2000
1800
1600
1400
cm-1

FIGURE 7

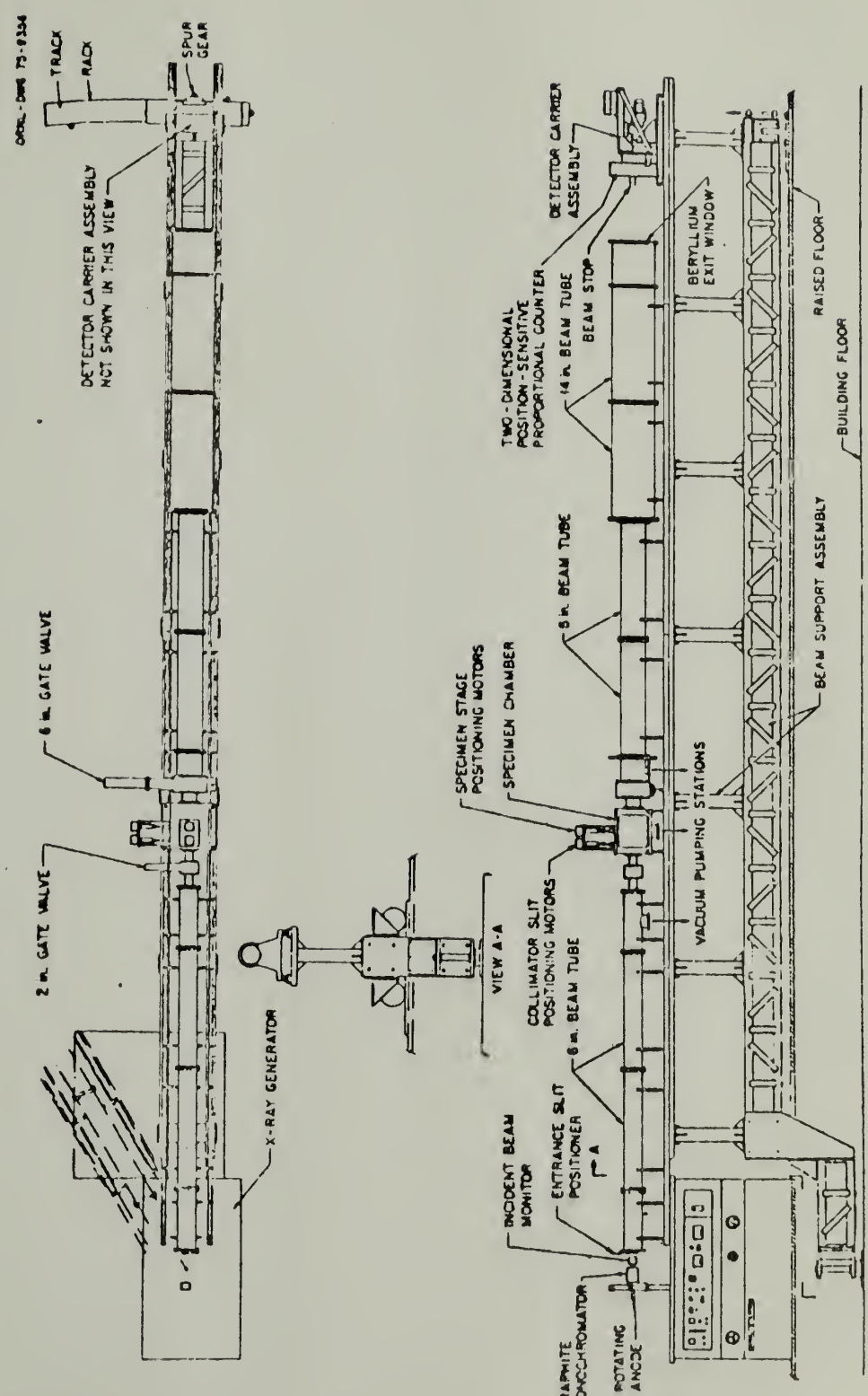
TRACK
RACK
SPUR GEAR
DETECTOR CARRIER ASSEMBLY NOT SHOWN IN THIS VIEW
6 in. GATE VALVE
2 in. GATE VALVE
X-RAY GENERATOR
VIEW A-A
SPECIMEN STAGE POSITIONING MOTORS
SPECIMEN CHAMBER
COLLIMATOR SLIT POSITIONING MOTORS
6 in. BEAM TUBE
INCIDENT BEAM MONITOR
ENTRANCE SLIT POSITIONER
GRAPHITE MONOCHROMATOR
ROTATING ANODE
5 in. BEAM TUBE
VACUUM PUMPING STATIONS
TWO-DIMENSIONAL POSITION-SENSITIVE PROPORTIONAL COUNTER
14 in. BEAM TUBE
BEAM STOP
DETECTOR CARRIER ASSEMBLY
BERYLLIUM EXIT WINDOW
BEAM SUPPORT ASSEMBLY
RAISED FLOOR
BUILDING FLOOR

FIGURE 8

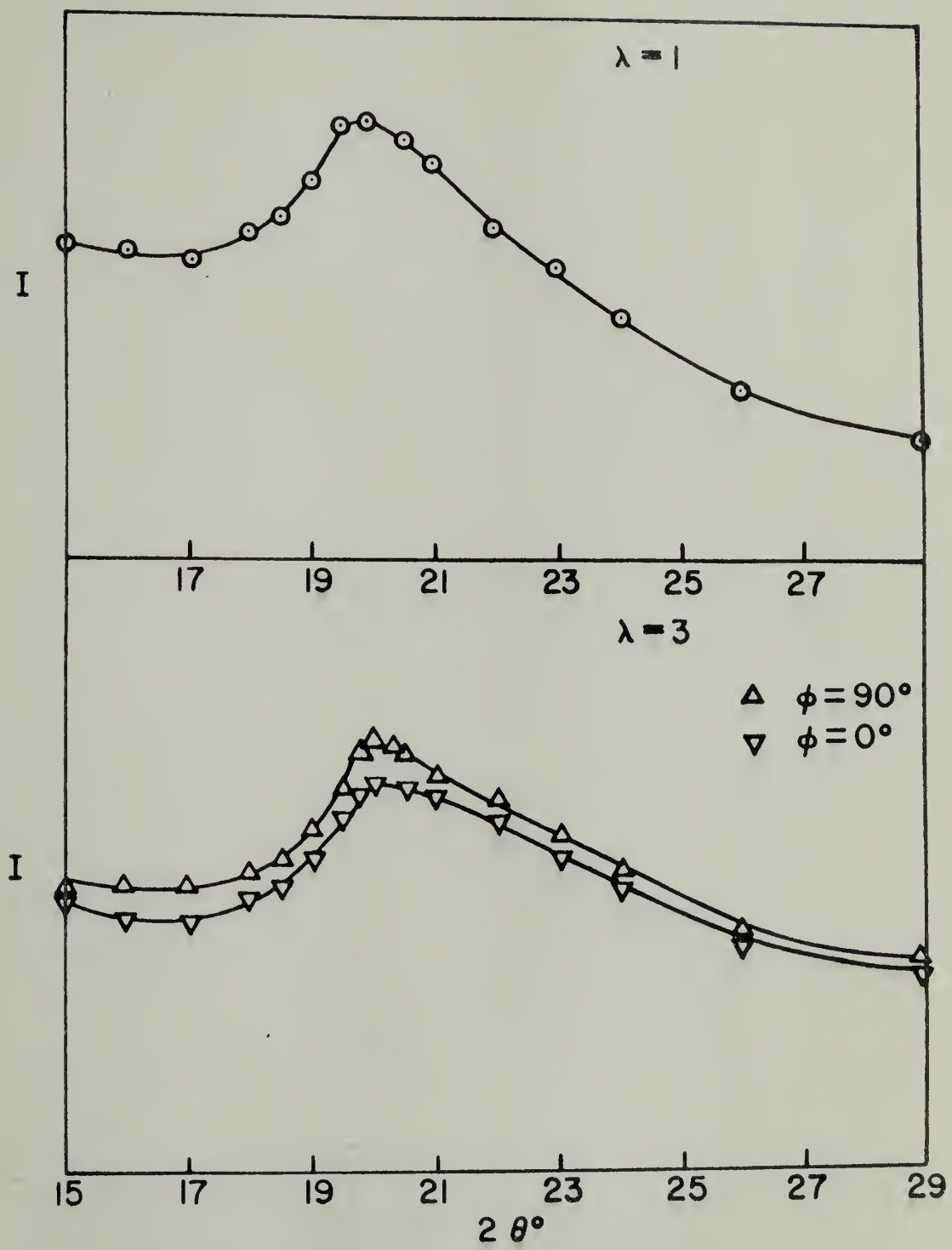

FIGURE 9

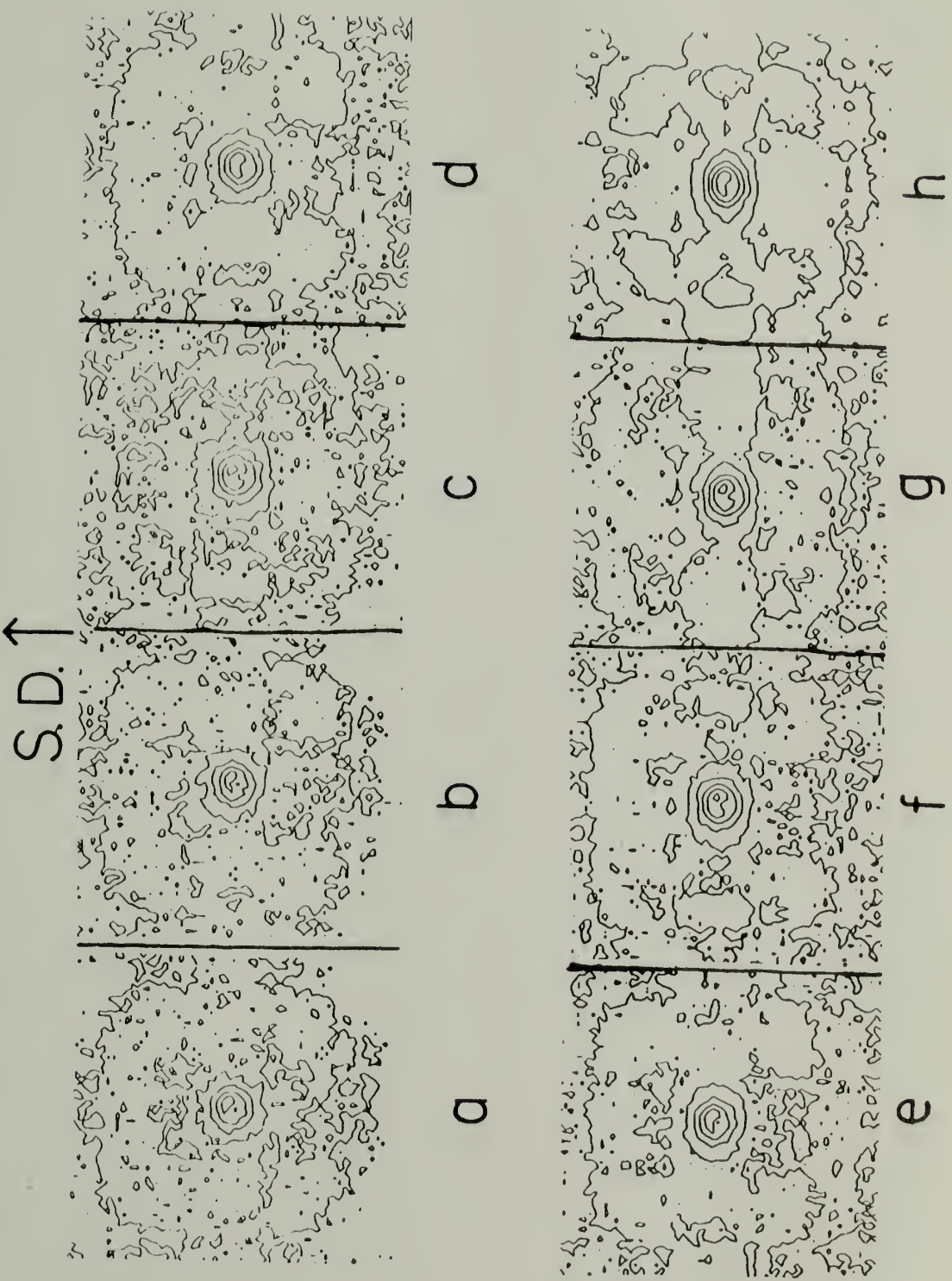

FIGURE 10

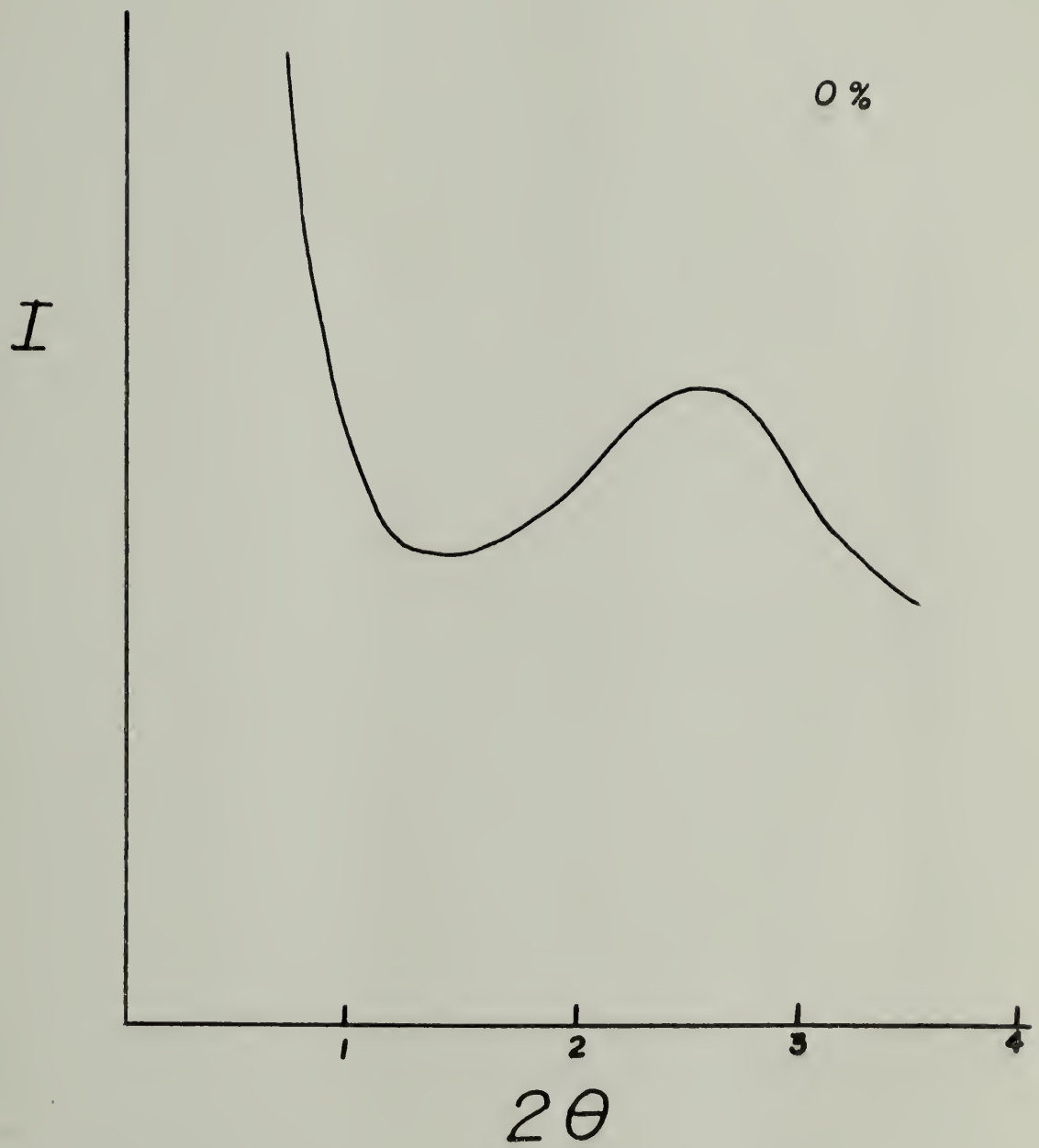

FIGURE 11

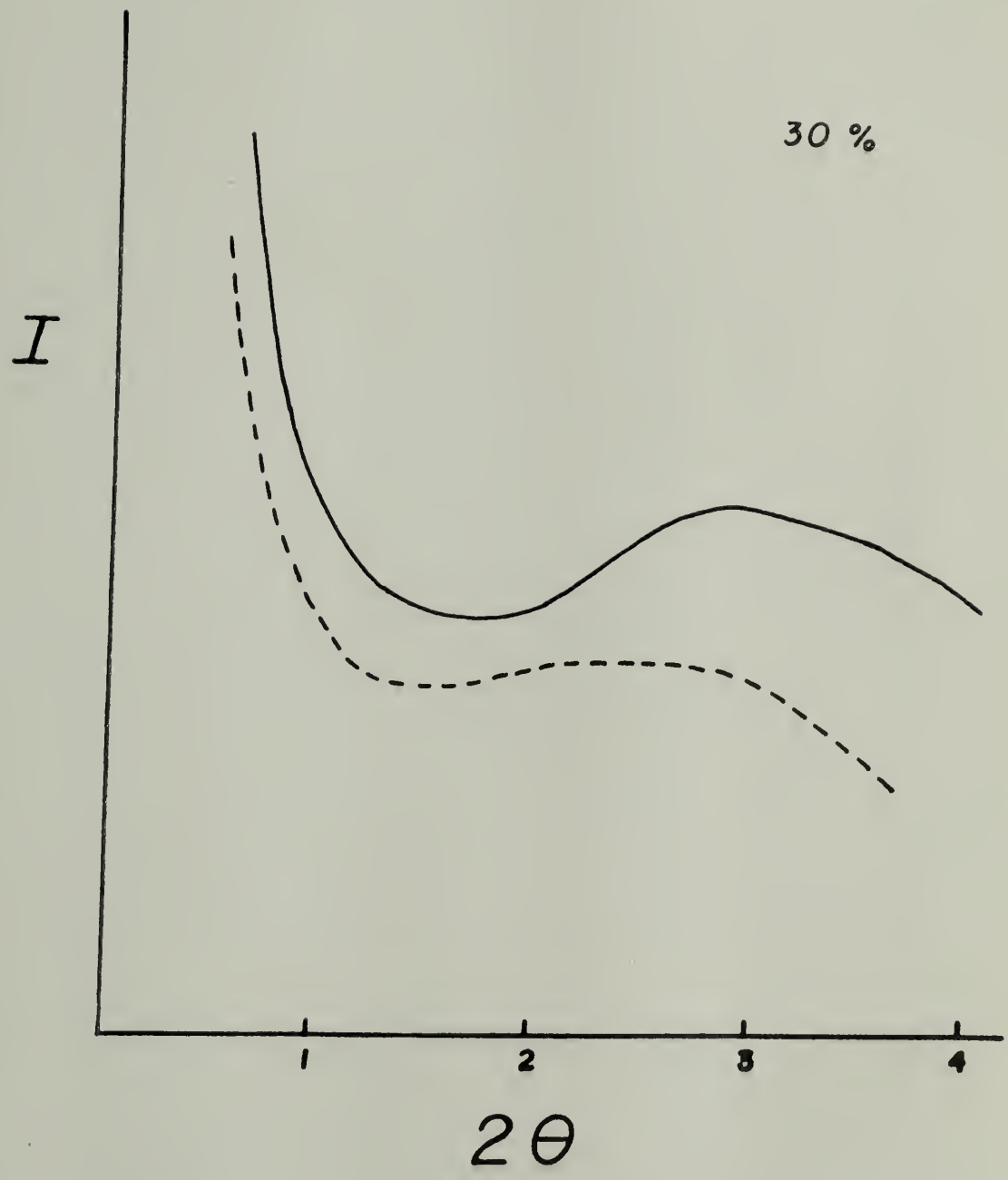

FIGURE 12

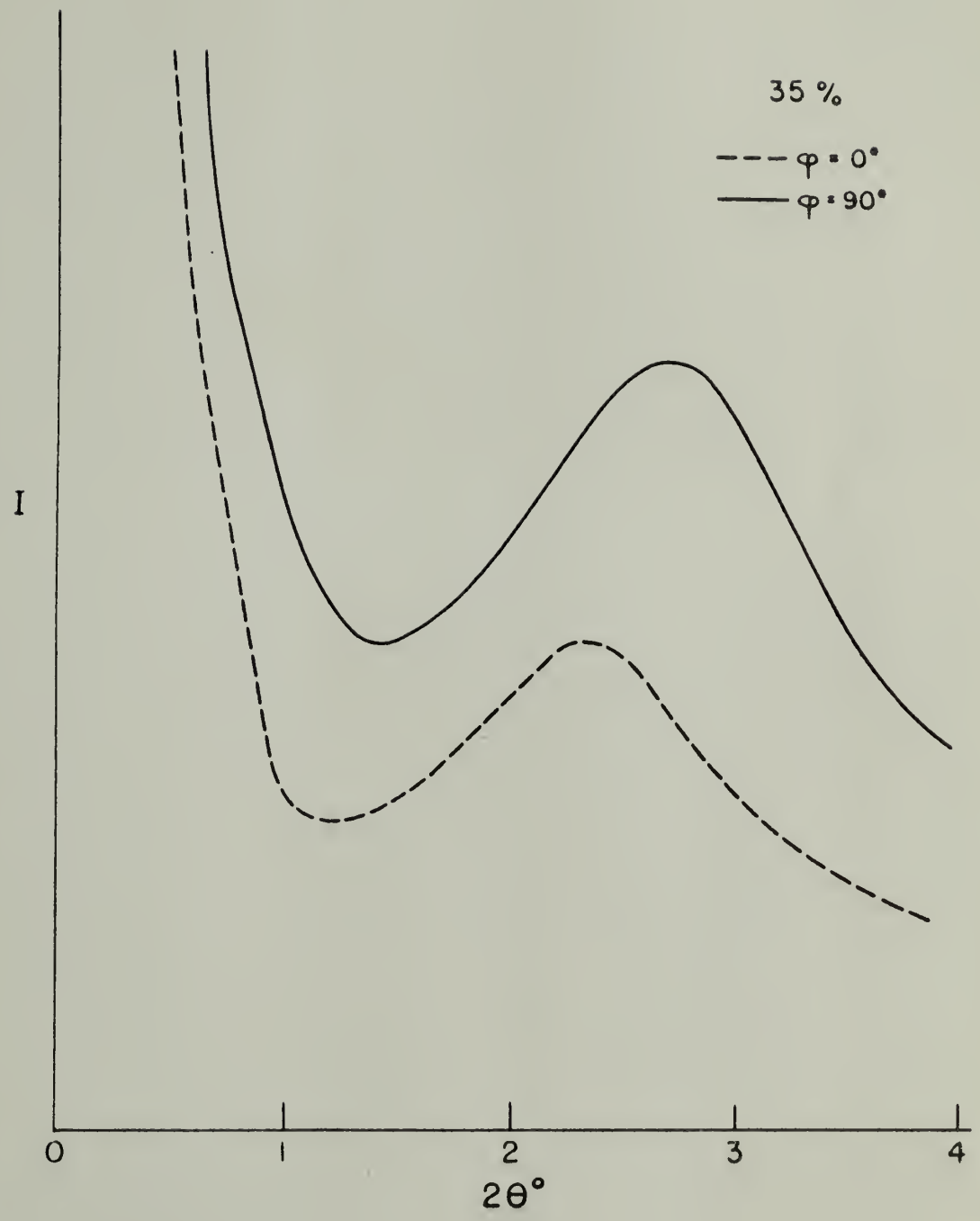

FIGURE 13

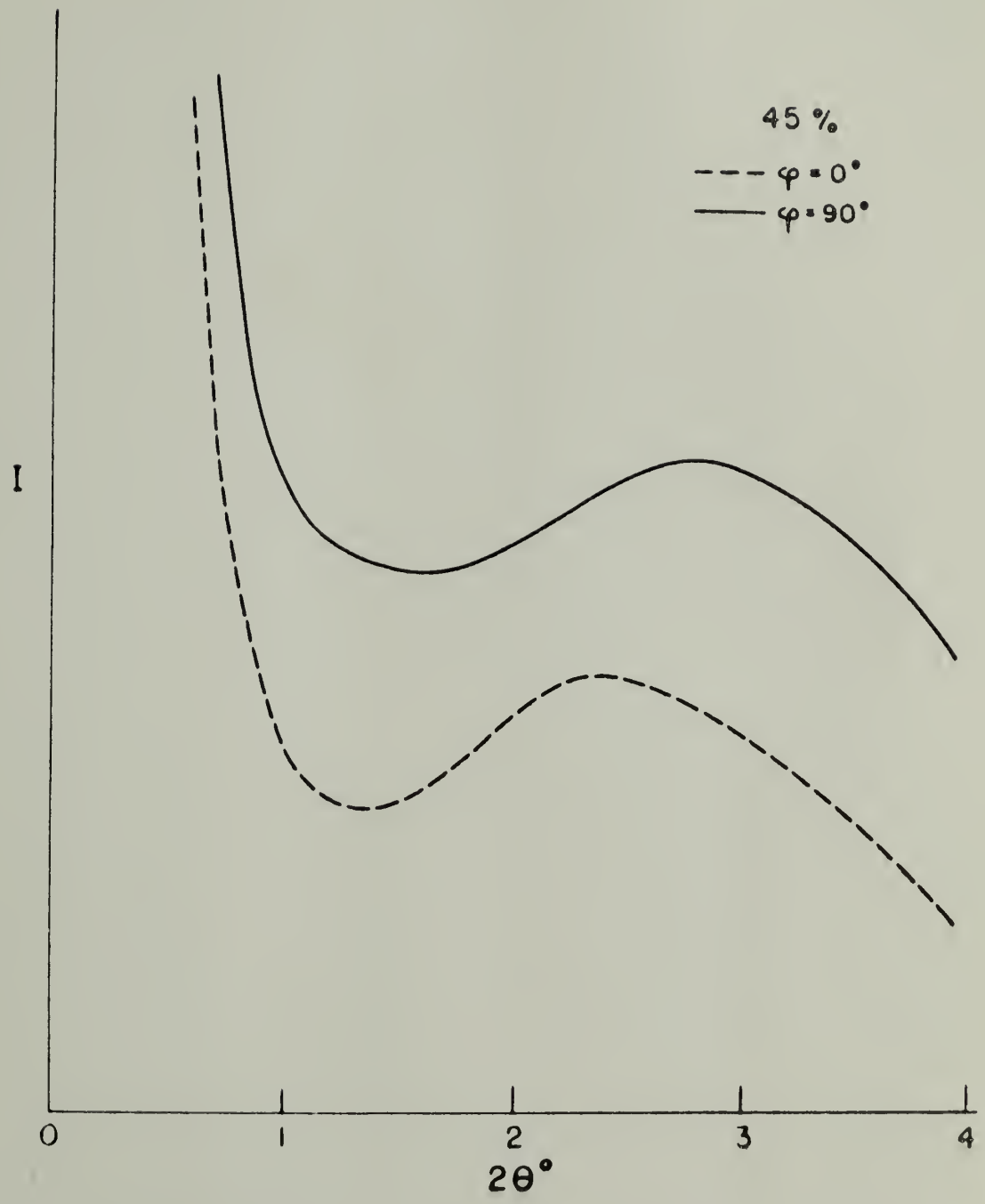

FIGURE 14

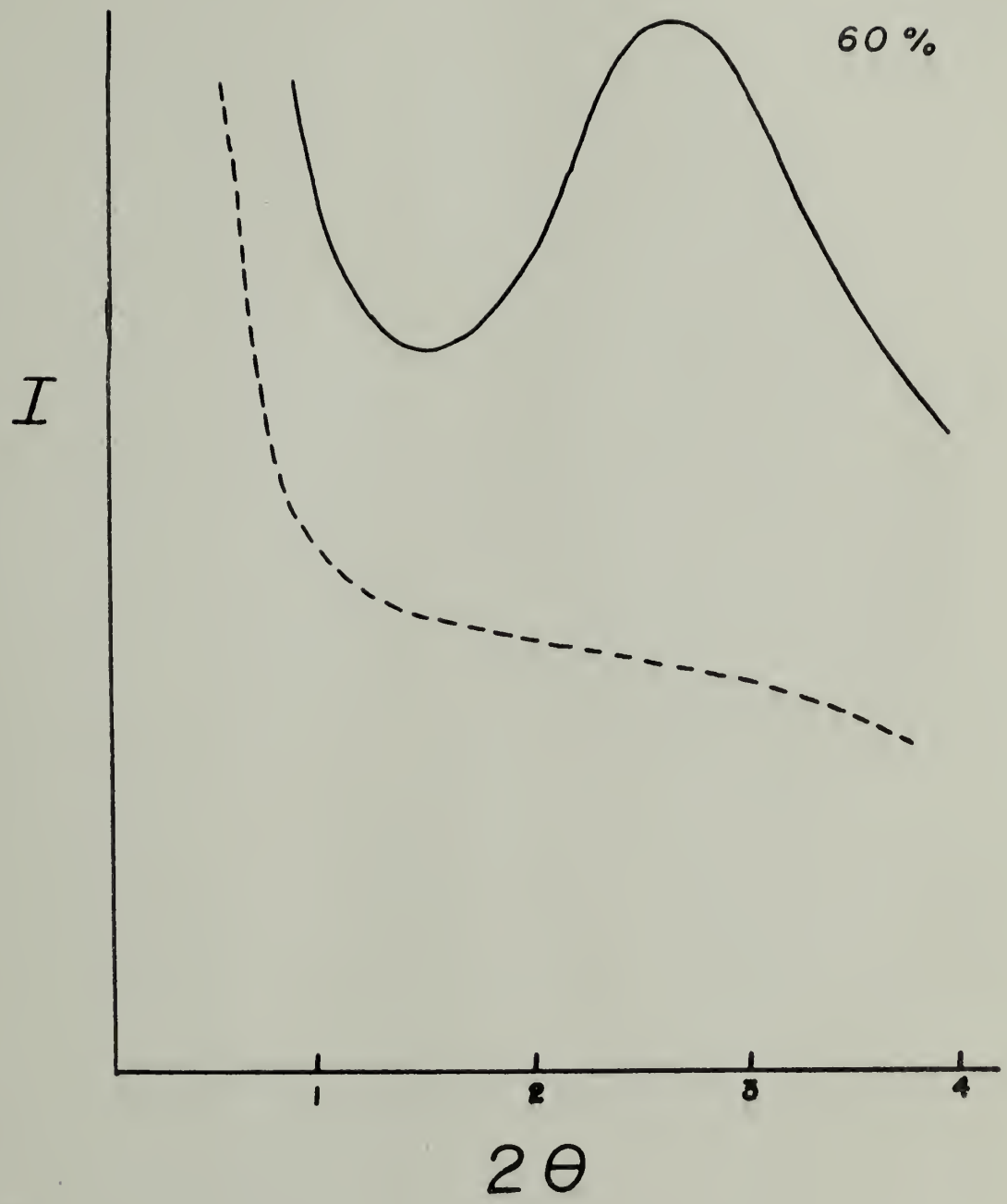

FIGURE 15

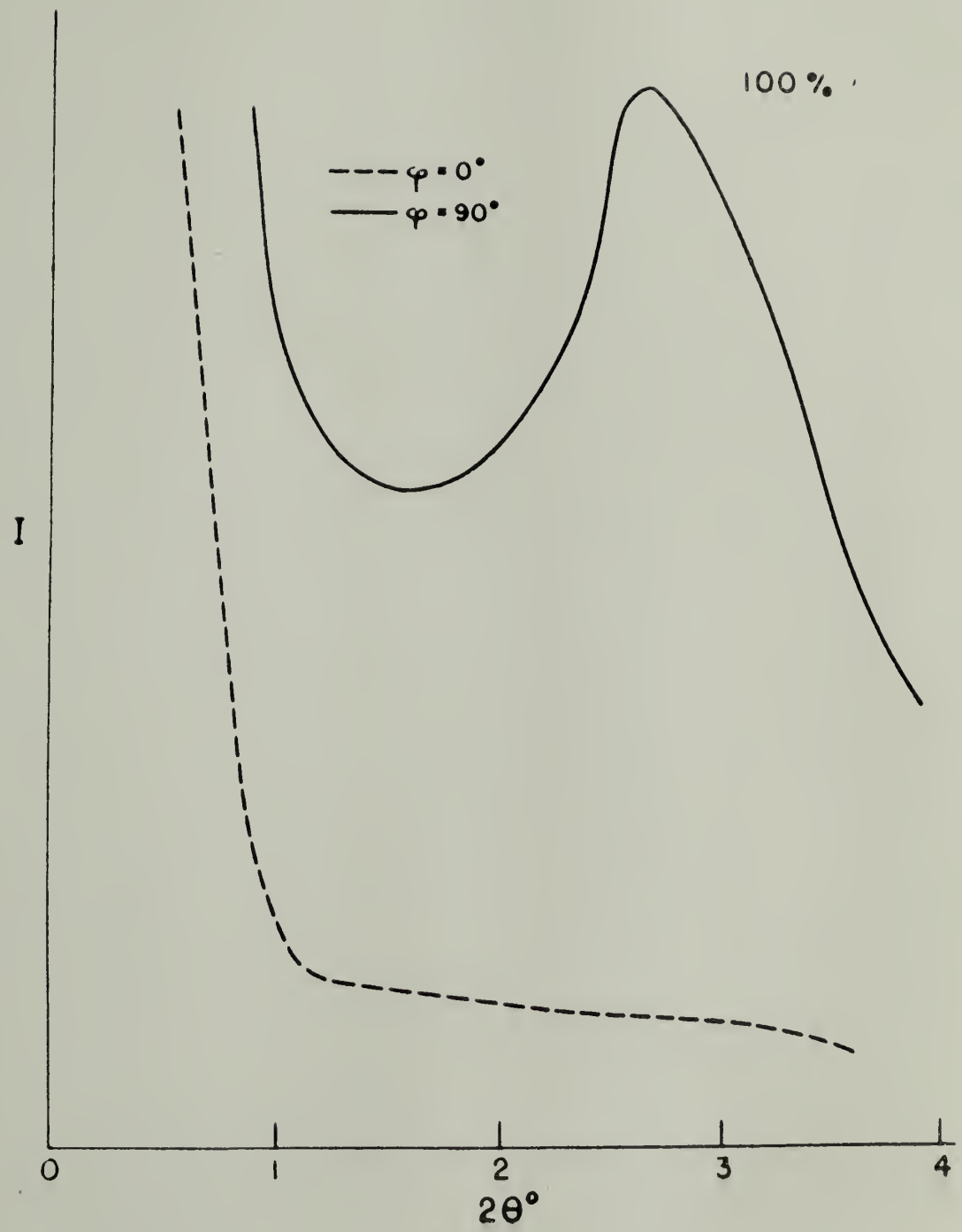

FIGURE 16

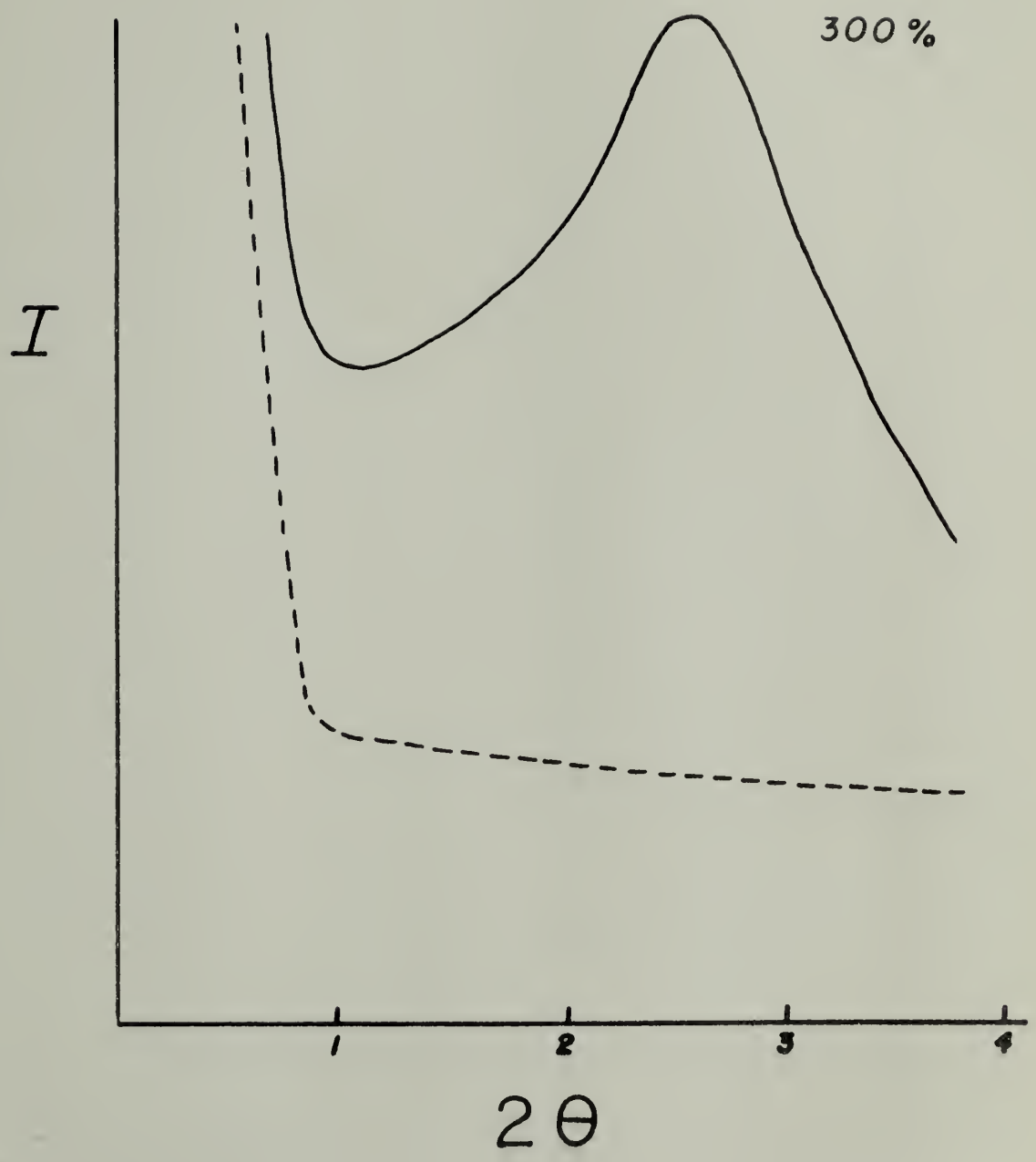

FIGURE 17

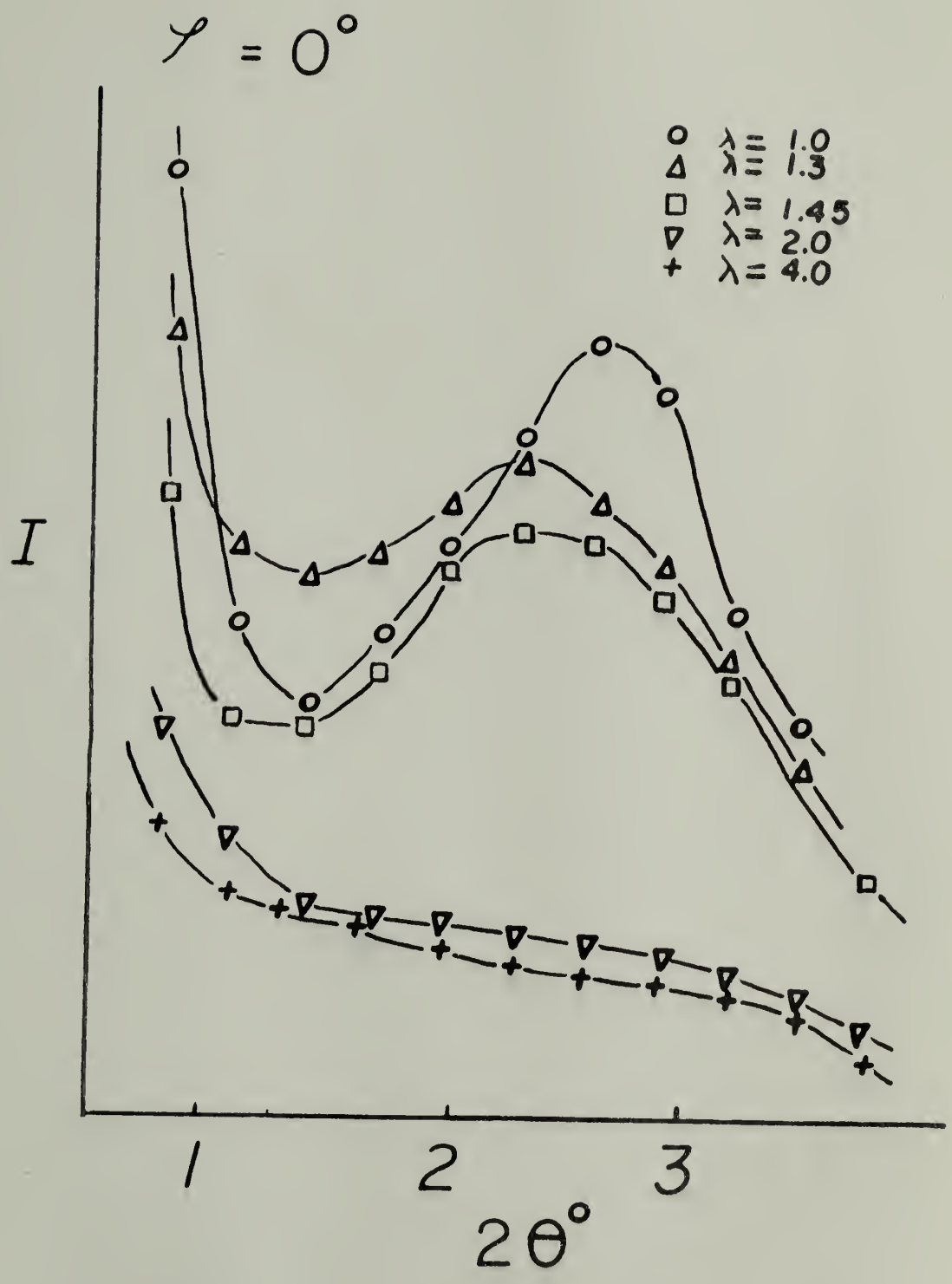

FIGURE 18

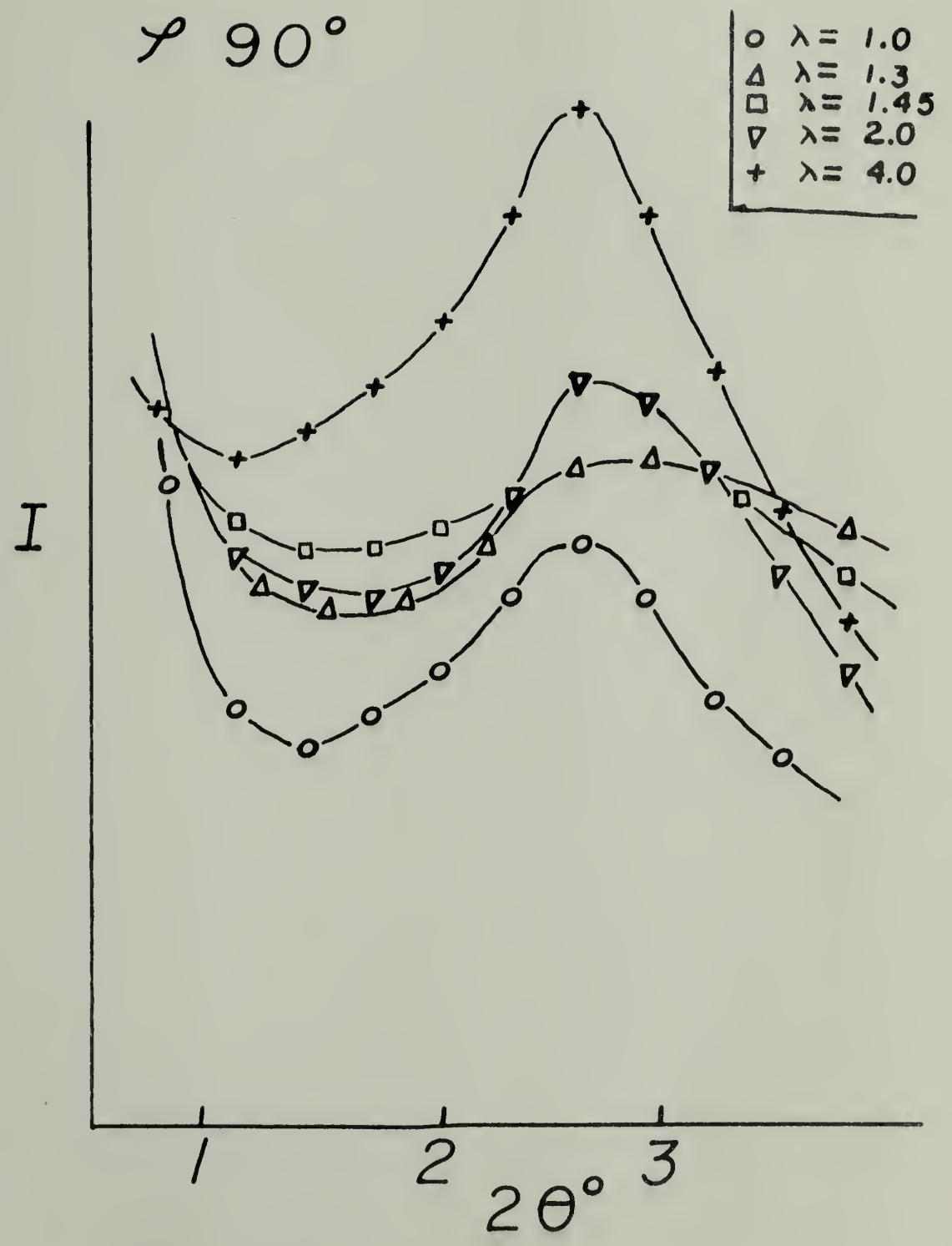

FIGURE 19

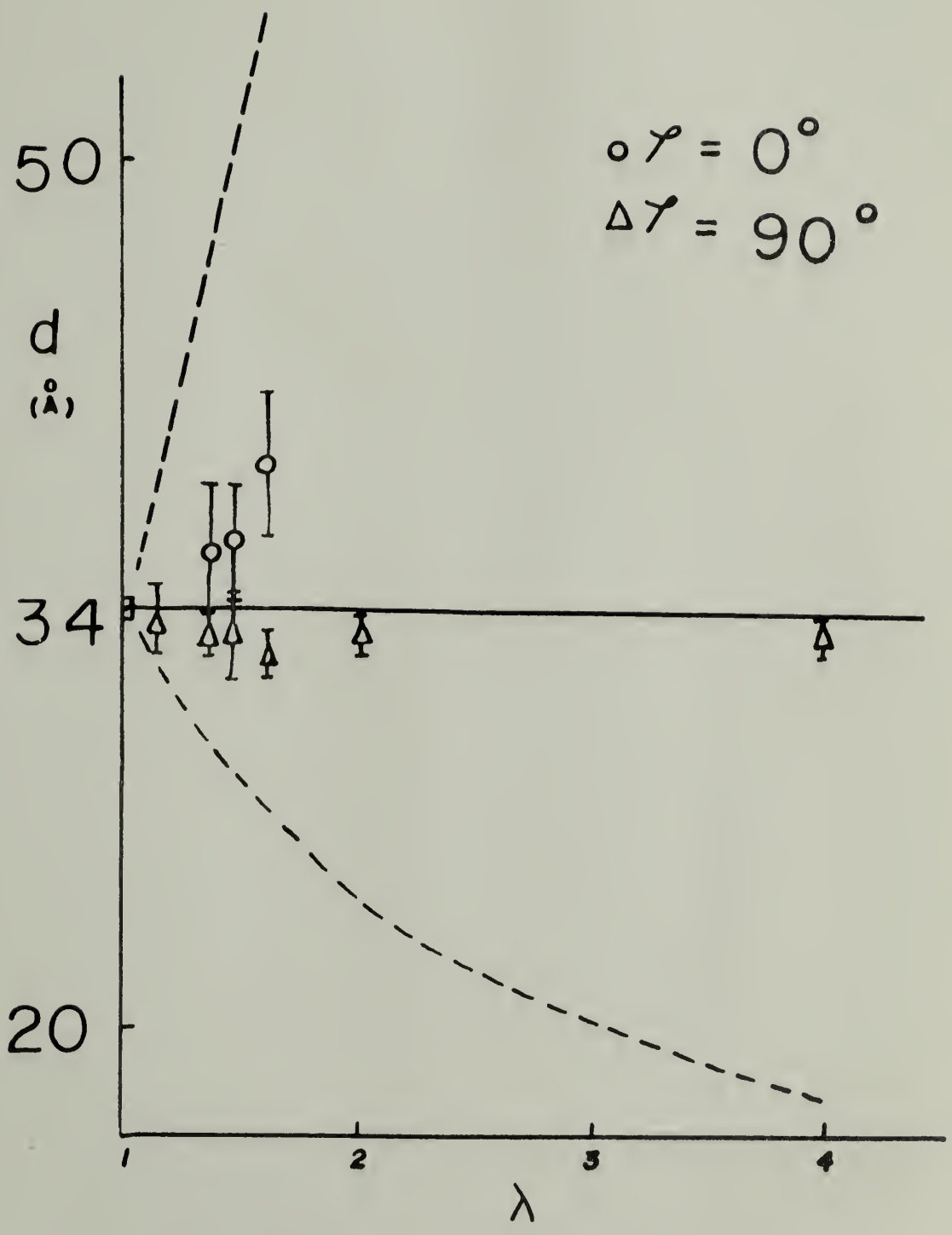

FIGURE 20

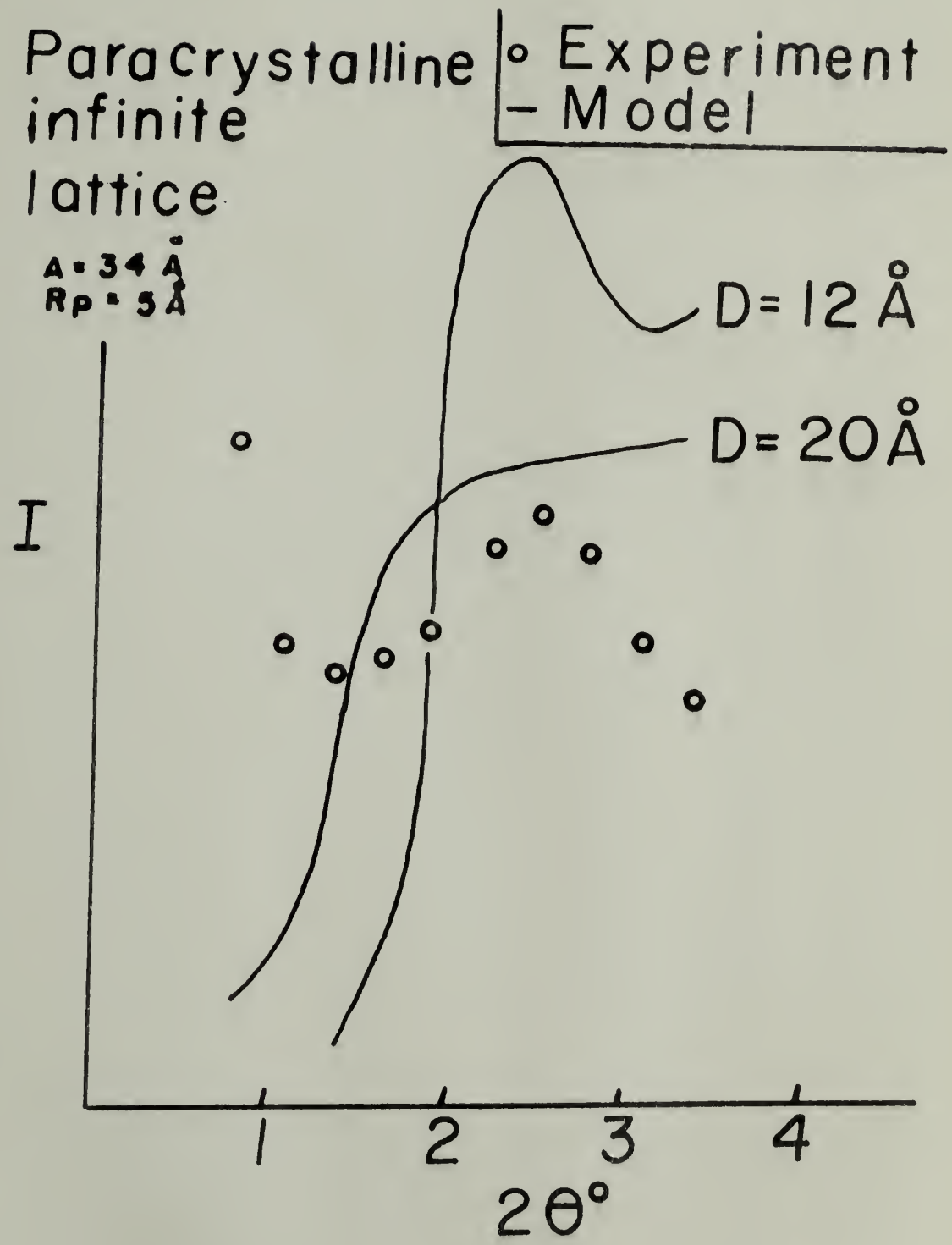
Paracrystalline infinite lattice
A = 34 Å
Rp = 5 Å
° Experiment
– Model
D = 12 Å
D = 20 Å
I
1
2
3
4
2θ°

FIGURE 21

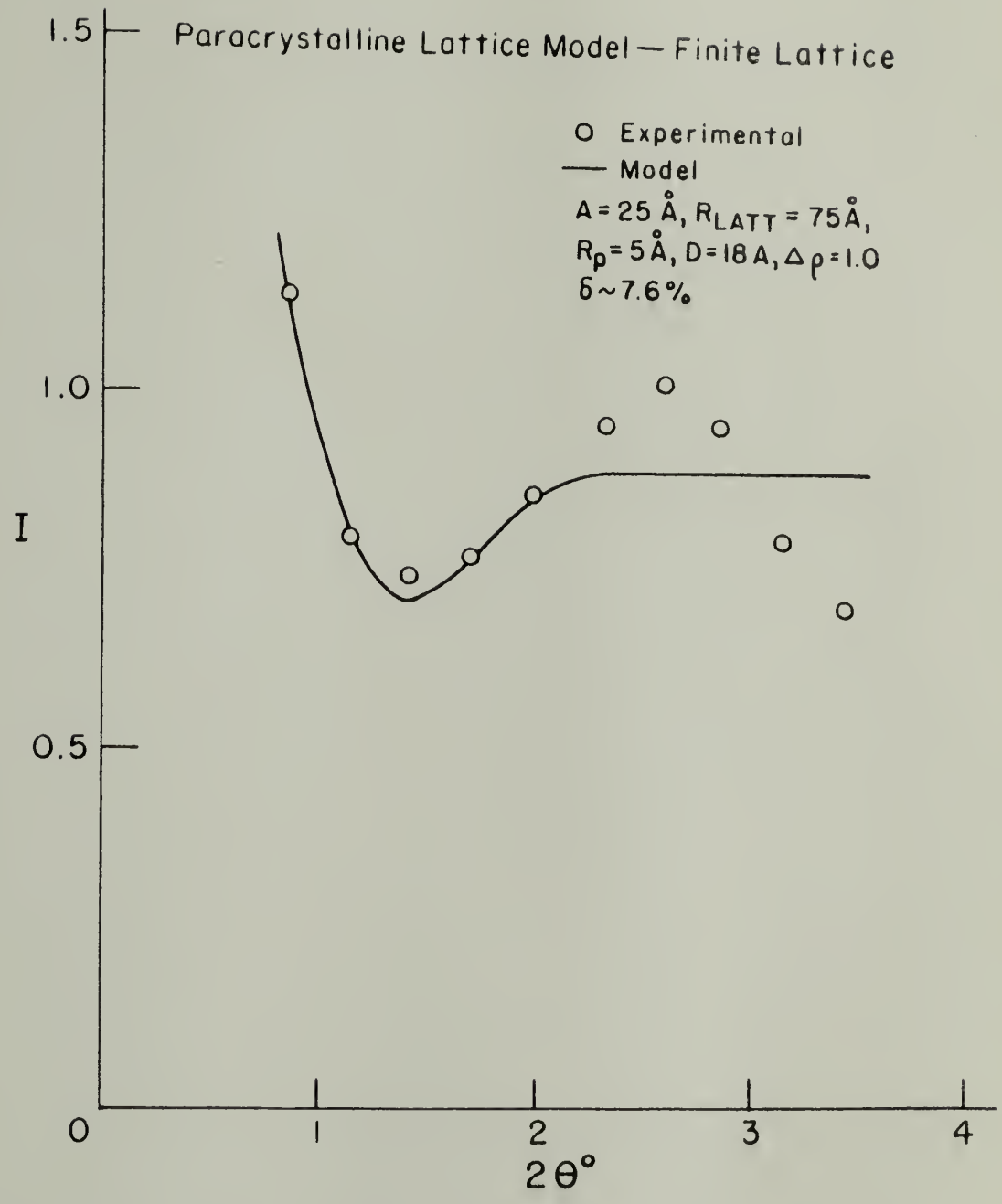
Paracrystalline Lattice Model — Finite Lattice
O Experimental
— Model
A = 25 Å, R_{LATT} = 75Å,
R_p = 5Å, D = 18 A, Δρ = 1.0
δ ~ 7.6%
1.5
1.0
0.5
0
I
1
2
3
4
2θ°

FIGURE 22

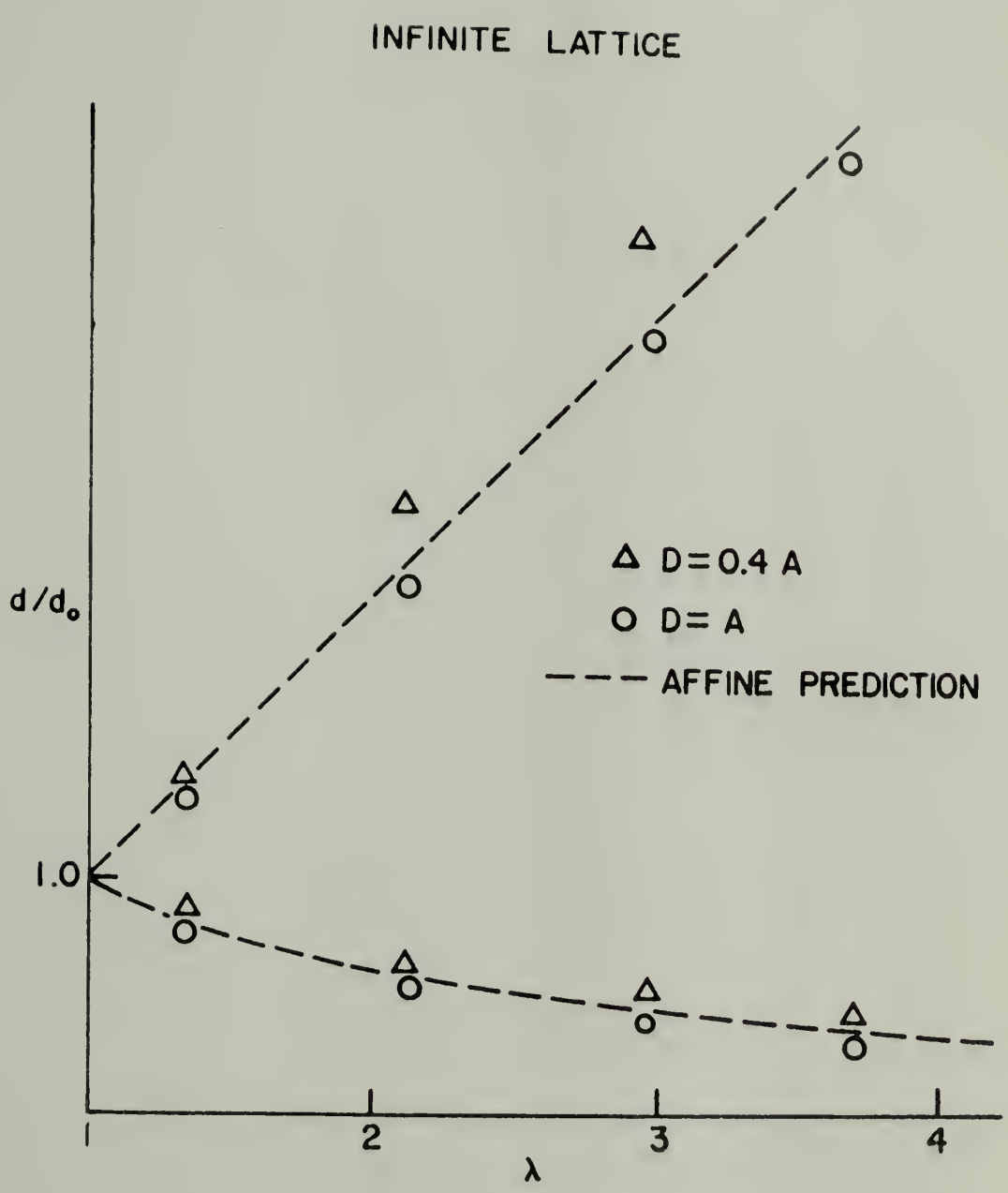

FIGURE 23

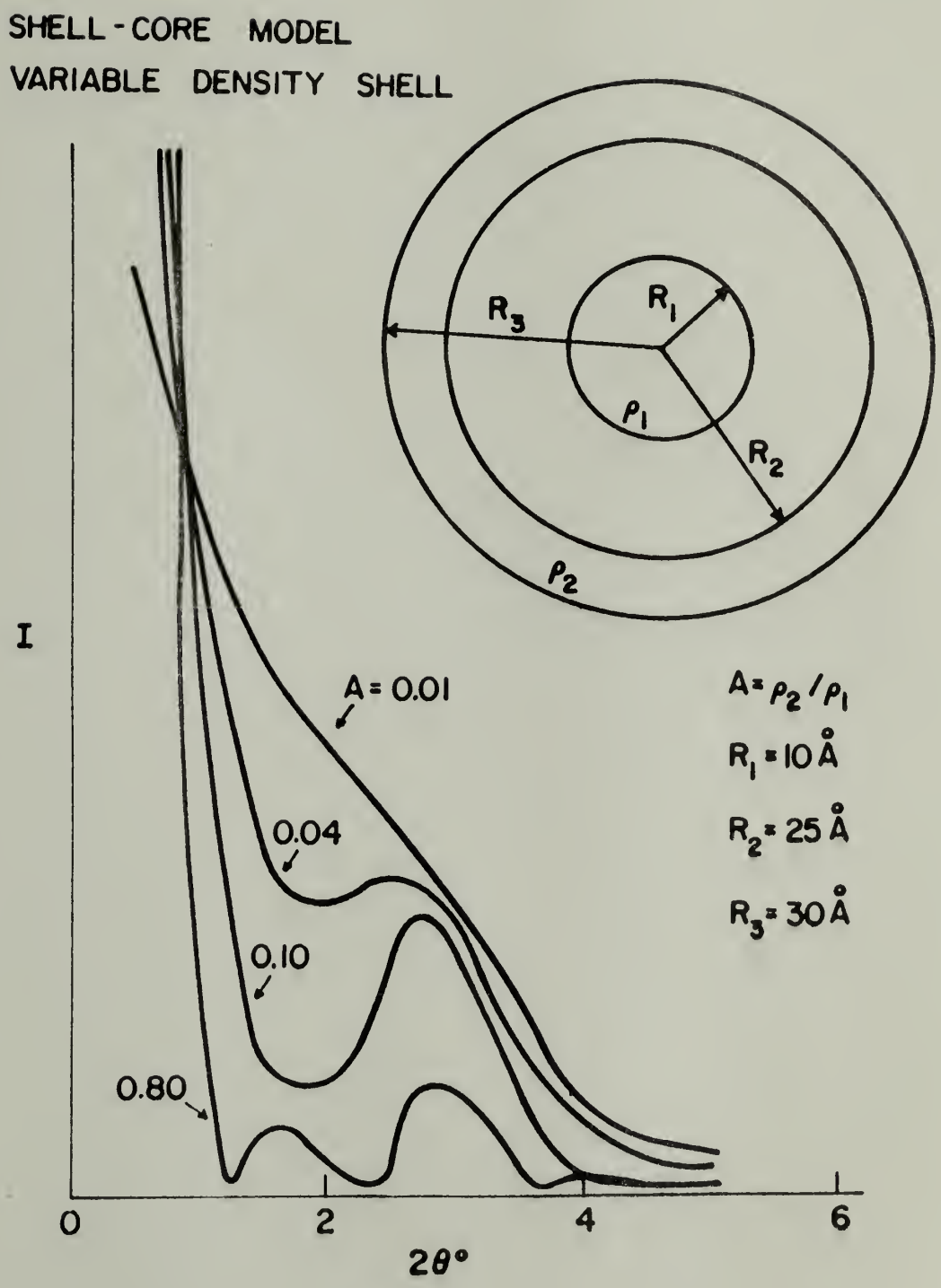
SHELL - CORE MODEL
VARIABLE DENSITY SHELL
R3
R1
ρ1
R2
ρ2
I
A = 0.01
0.04
0.10
0.80
A = ρ2 / ρ1
R1 = 10 Å
R2 = 25 Å
R3 = 30 Å
0
2
4
6
2θ°

FIGURE 24

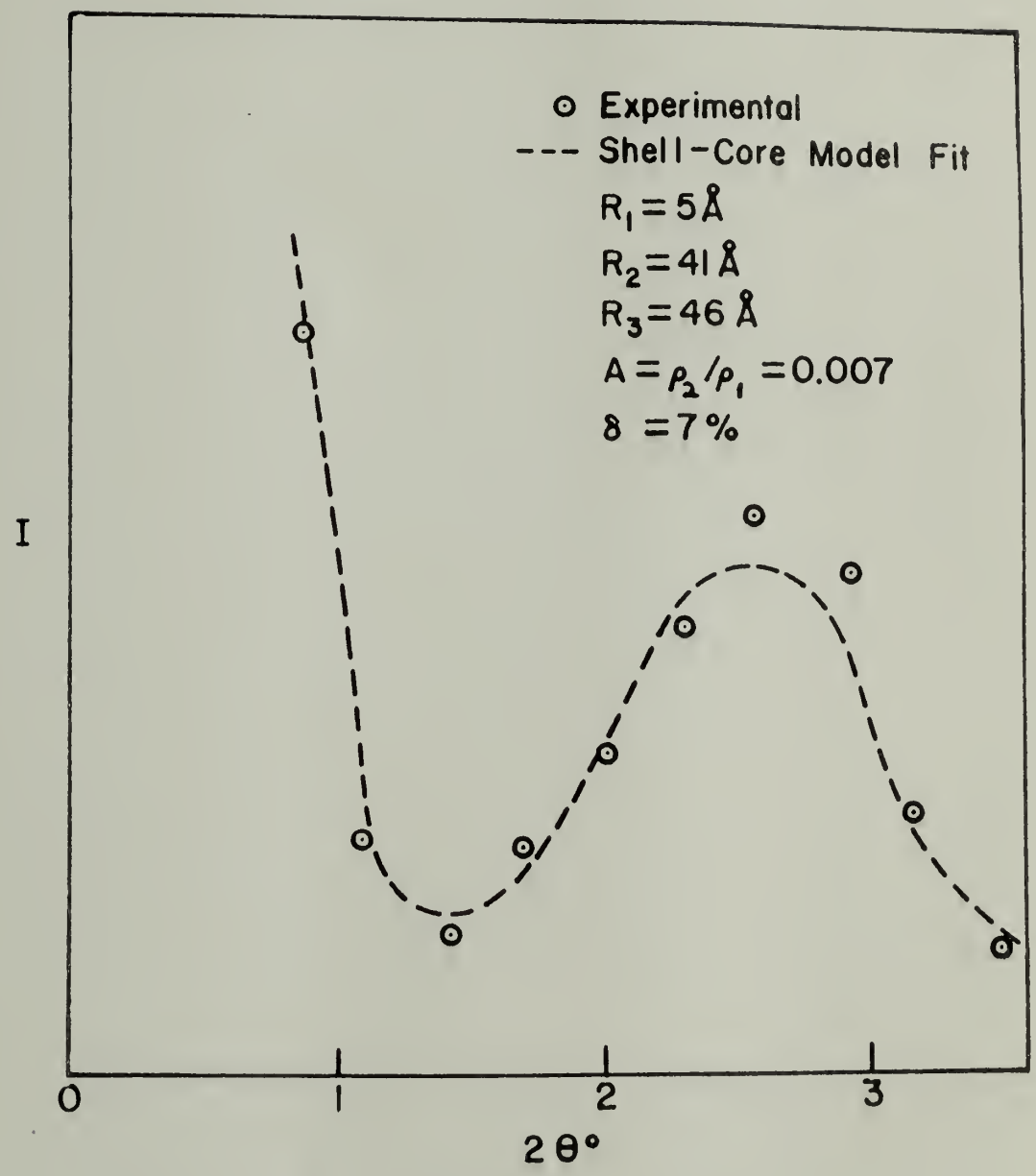
Experimental
Shell-Core Model Fit
$R_1 = 5$ Å
$R_2 = 41$ Å
$R_3 = 46$ Å
$A = \rho_2/\rho_1 = 0.007$
$\delta = 7\%$
I
0
1
2
3
2θ°

FIGURE 25

SHELL-CORE MODEL DEFORMATION

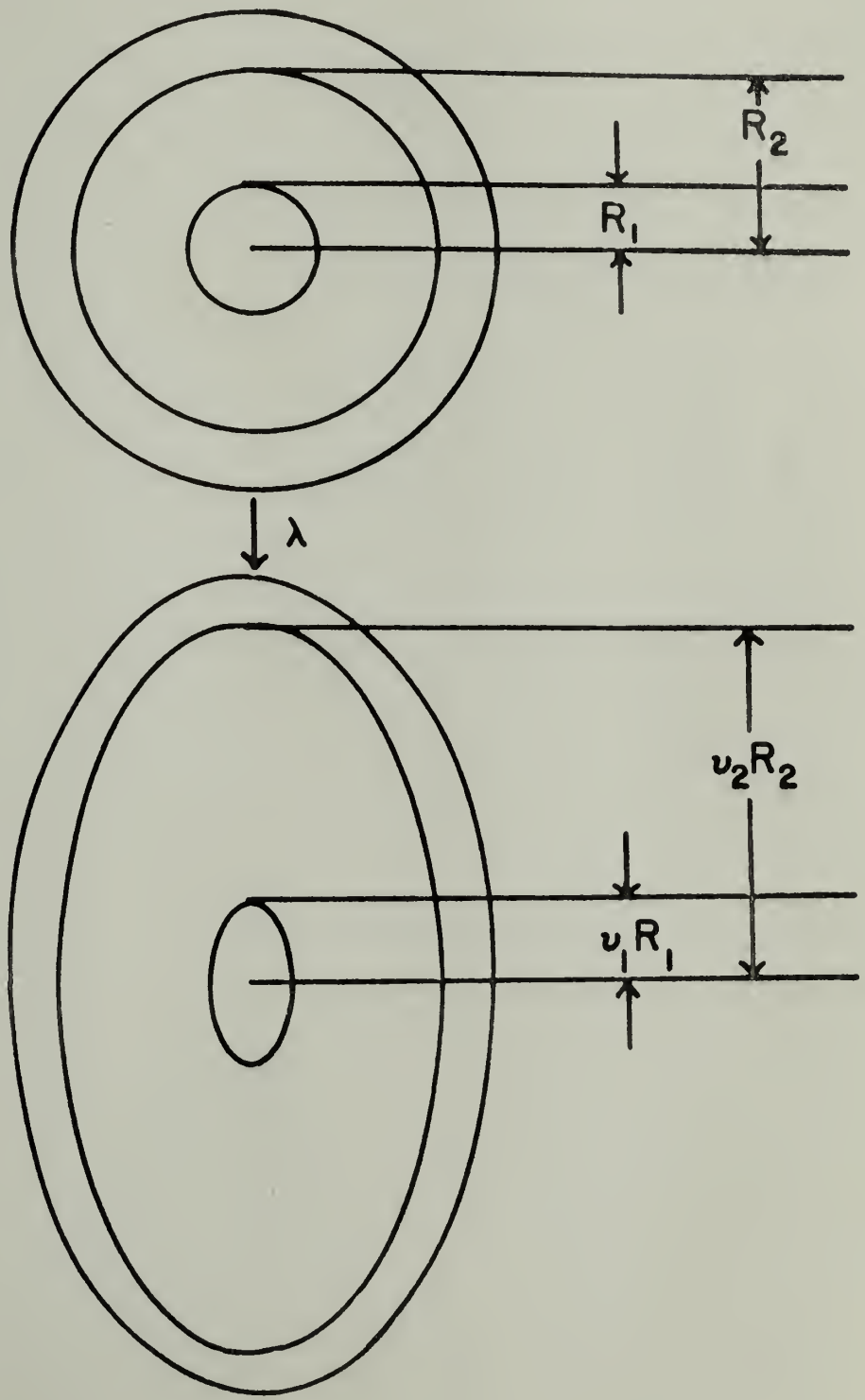

FIGURE 26

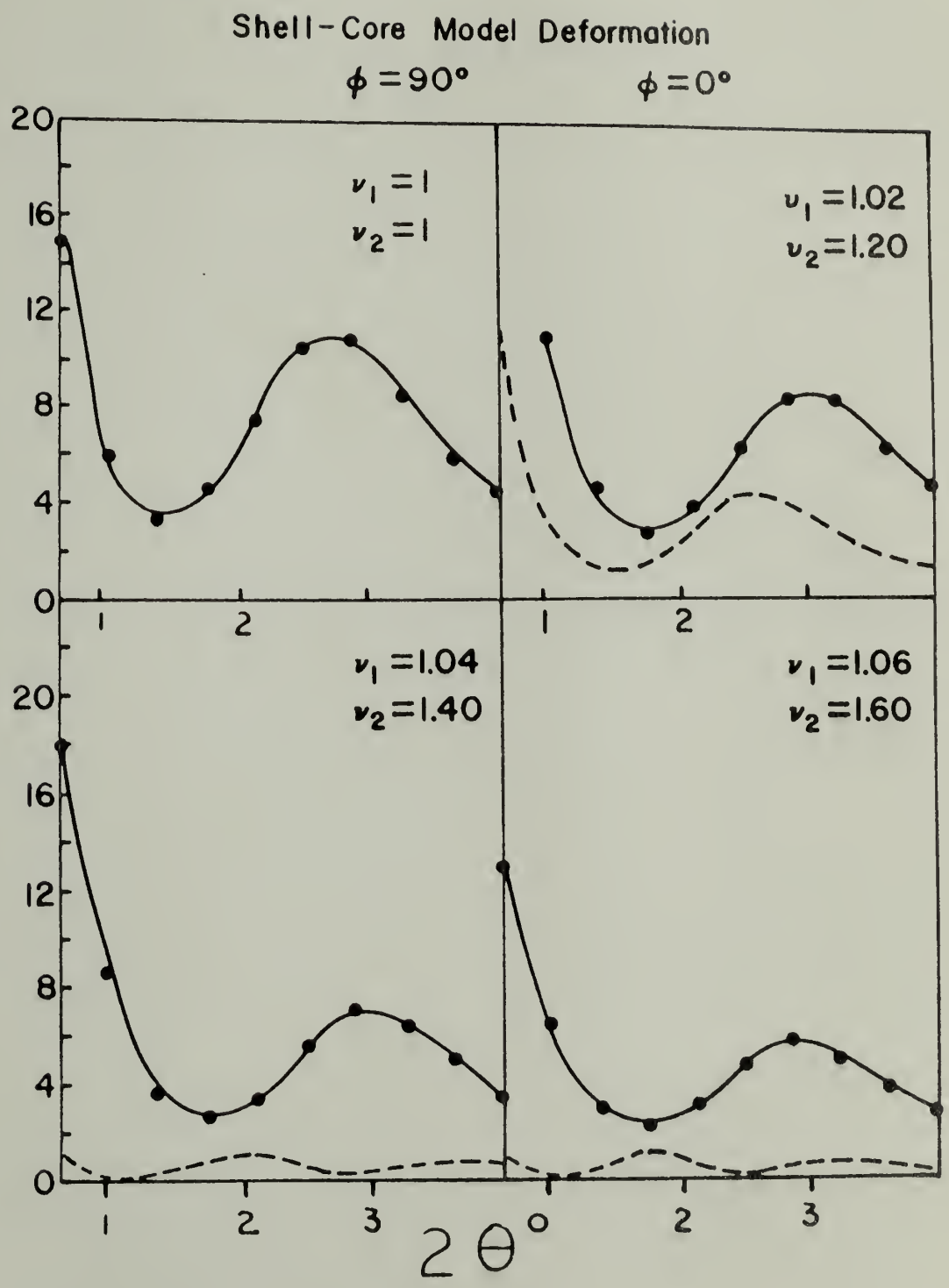
Shell-Core Model Deformation
$\phi = 90°$
$\phi = 0°$
$\nu_1 = 1$
$\nu_2 = 1$
$\nu_1 = 1.02$
$\nu_2 = 1.20$
$\nu_1 = 1.04$
$\nu_2 = 1.40$
$\nu_1 = 1.06$
$\nu_2 = 1.60$
0
4
8
12
16
20
1
2
3
$2\theta°$

FIGURE 27

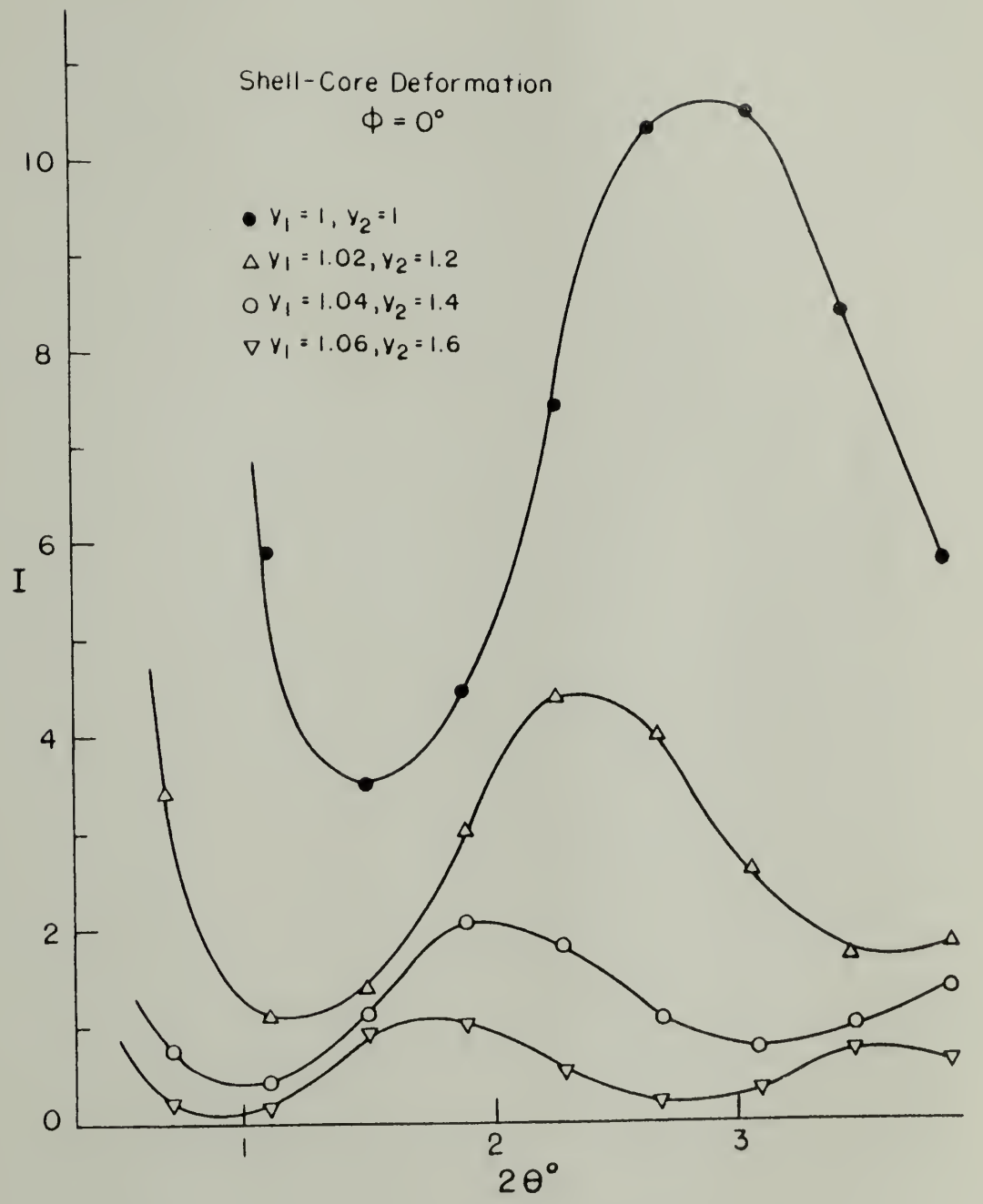
Shell-Core Deformation
Φ = 0°
● $\nu_1 = 1, \nu_2 = 1$
△ $\nu_1 = 1.02, \nu_2 = 1.2$
○ $\nu_1 = 1.04, \nu_2 = 1.4$
▽ $\nu_1 = 1.06, \nu_2 = 1.6$
I
0
2
4
6
8
10
1
2
3
2θ°

FIGURE 28

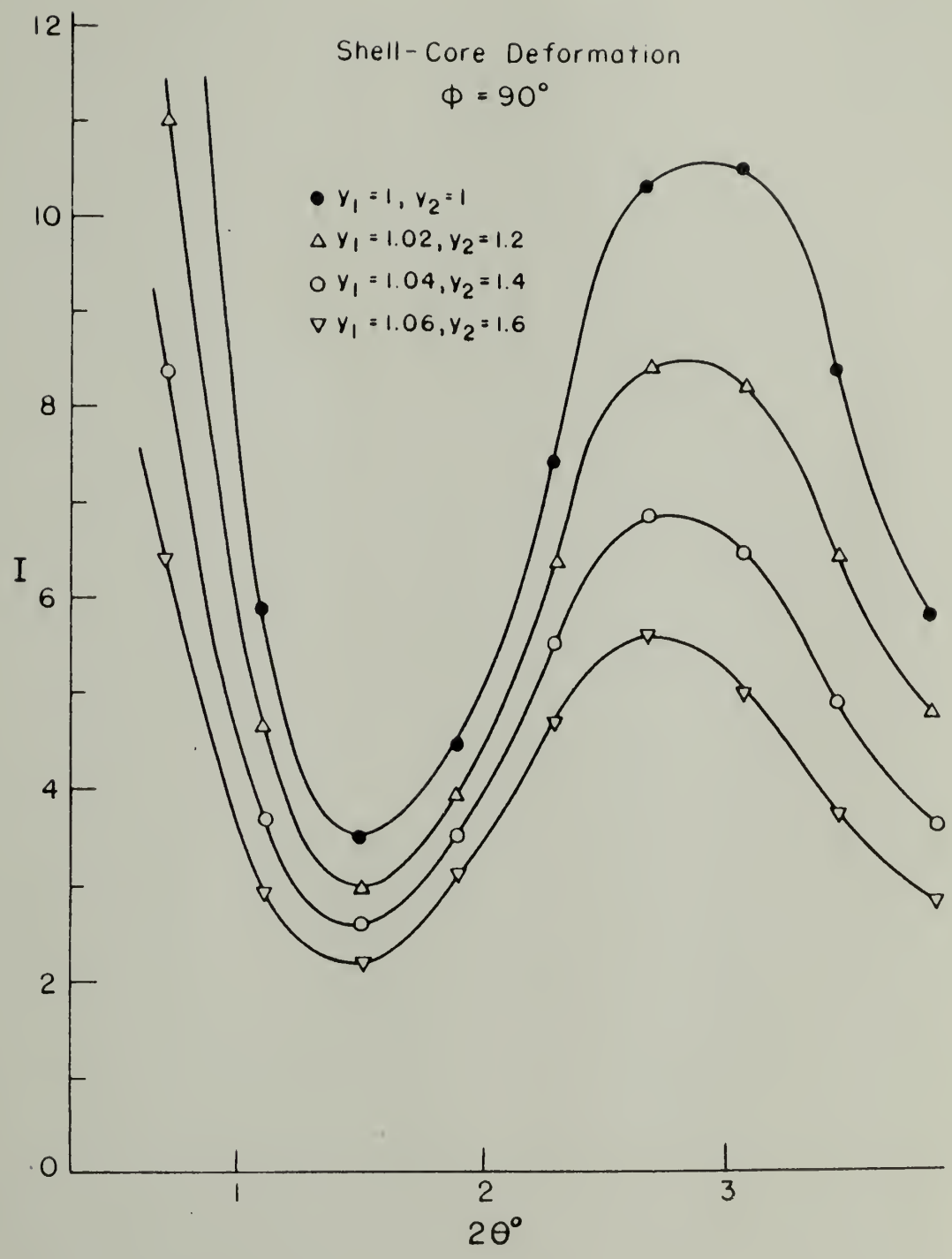
Shell-Core Deformation
Φ = 90°
● $y_1 = 1, y_2 = 1$
△ $y_1 = 1.02, y_2 = 1.2$
○ $y_1 = 1.04, y_2 = 1.4$
▽ $y_1 = 1.06, y_2 = 1.6$
I
12
10
8
6
4
2
0
1
2
3
2θ°

FIGURE 29

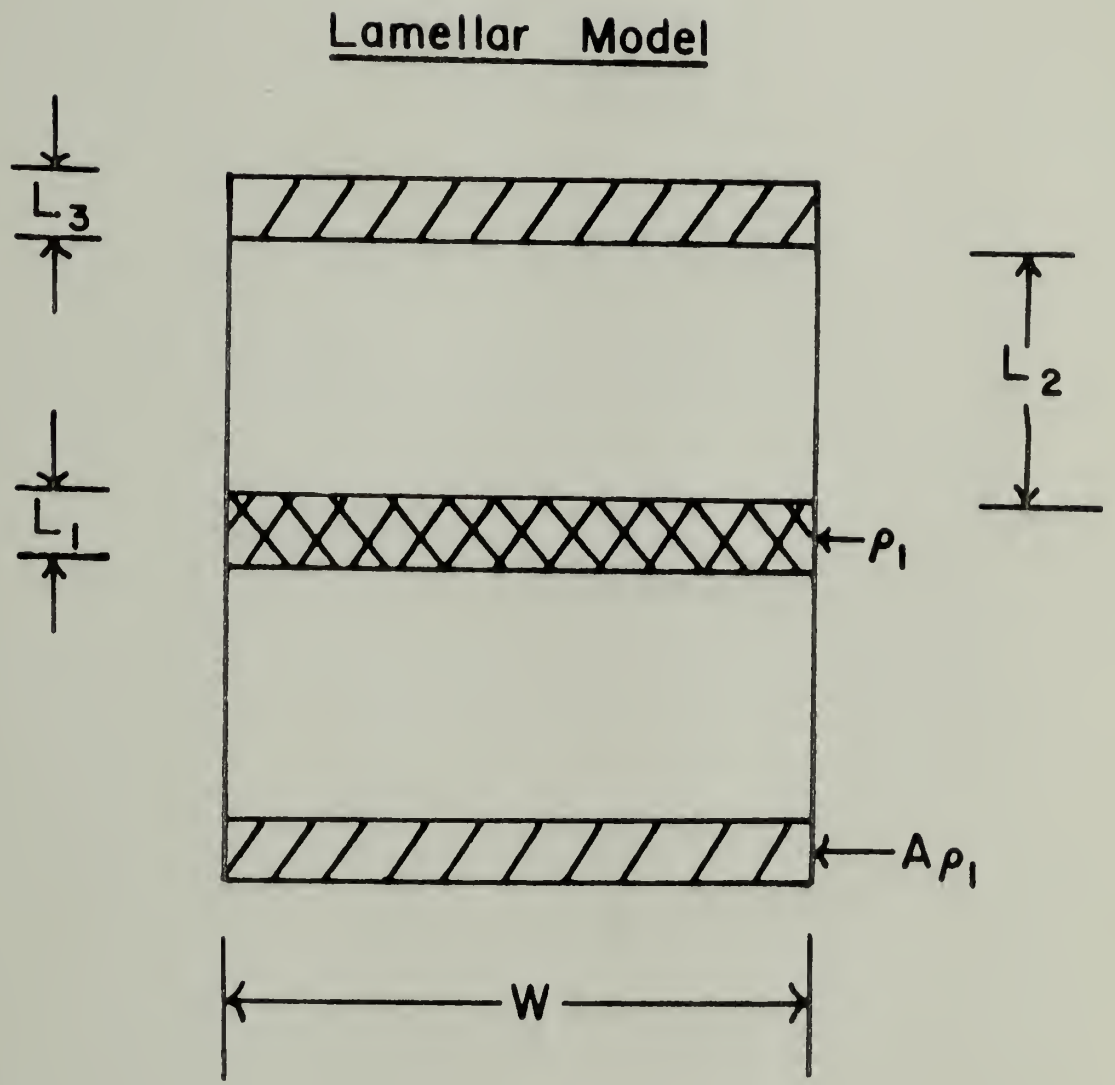

FIGURE 30

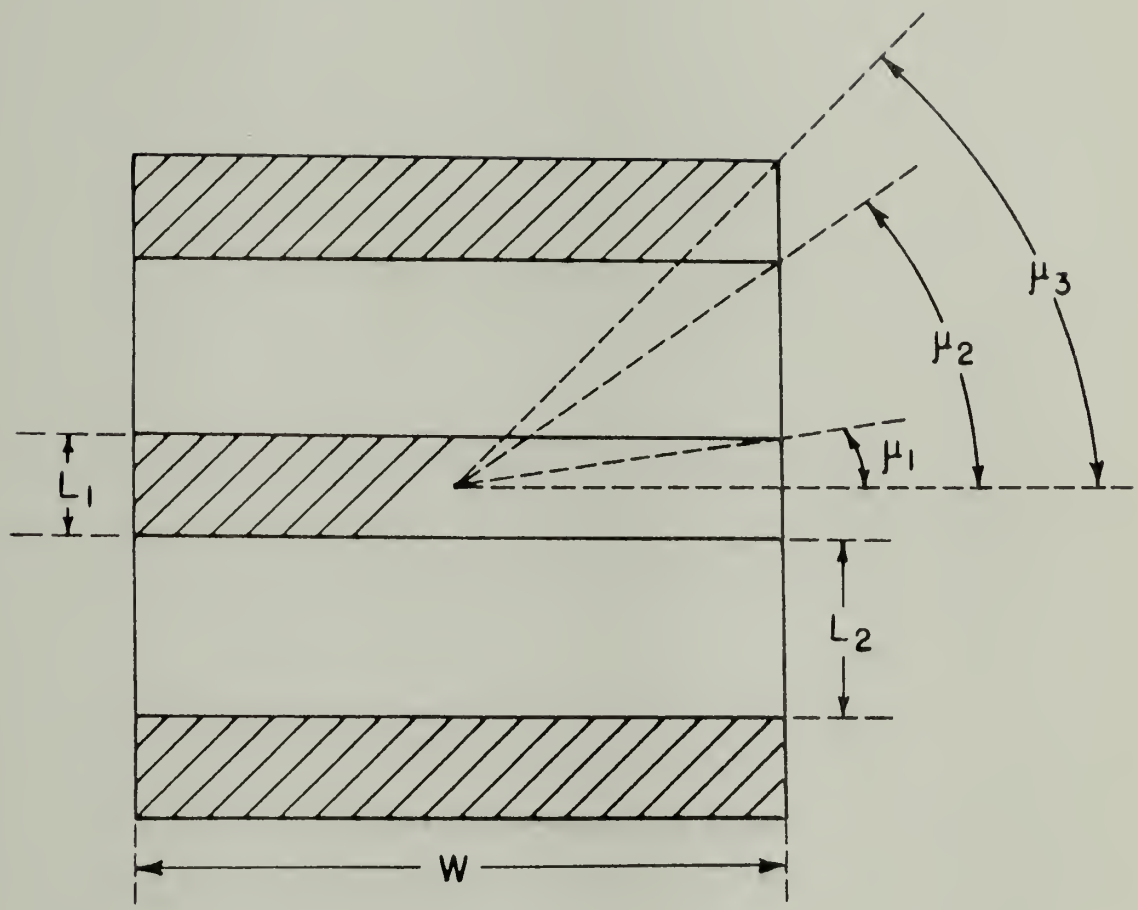

$$\mu_1 = \arctan(L_1 / W)$$

$$\mu_2 = \arctan((L_1 + L_2)/W)$$

$$\mu_3 = \arctan((2L_1 + L_2)/W)$$

FIGURE 31

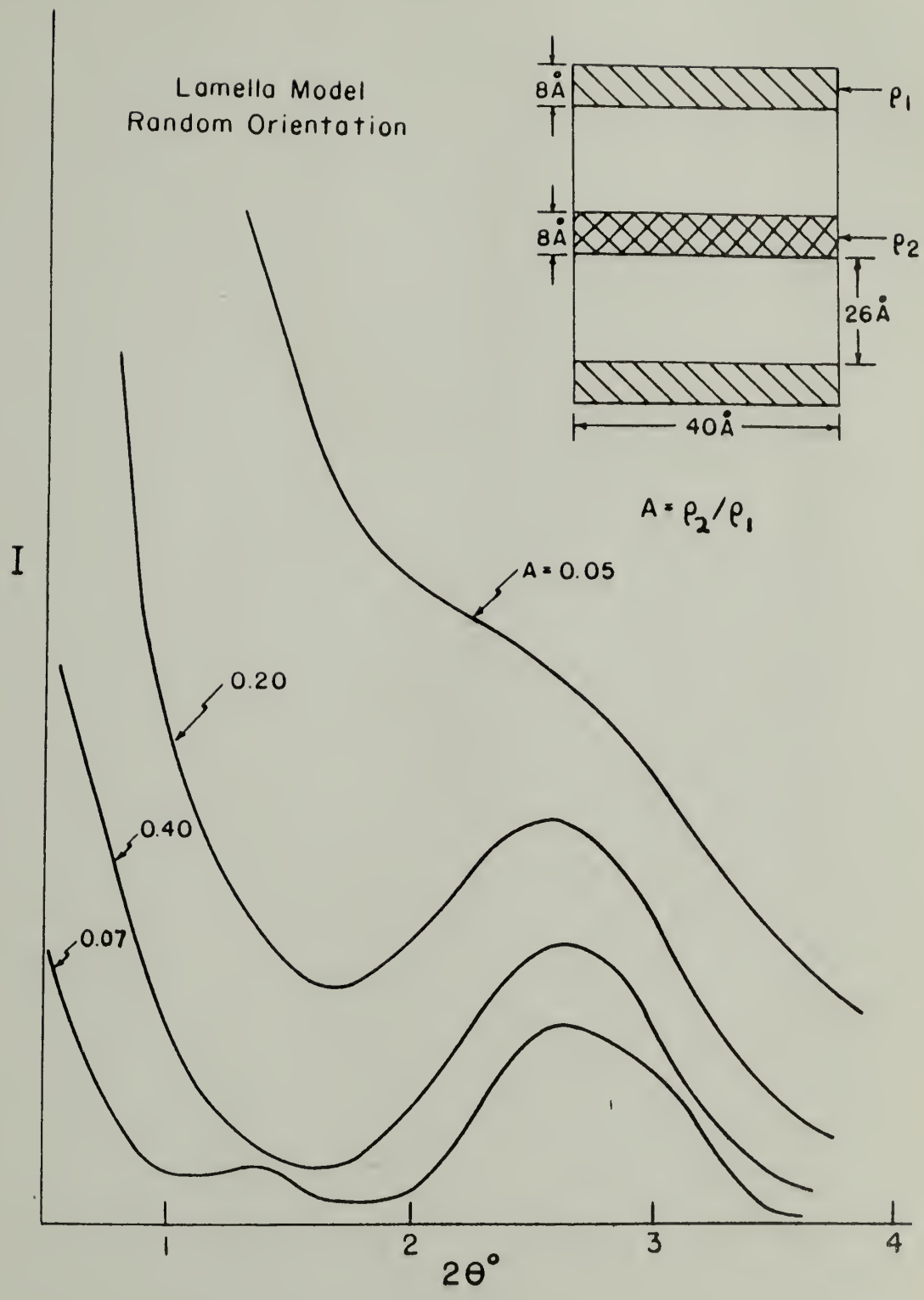
Lamella Model
Random Orientation
8Å
8Å
ρ1
ρ2
26Å
40Å
A = ρ2/ρ1
I
A = 0.05
0.20
0.40
0.07
1
2
3
4
2θ°

FIGURE 32

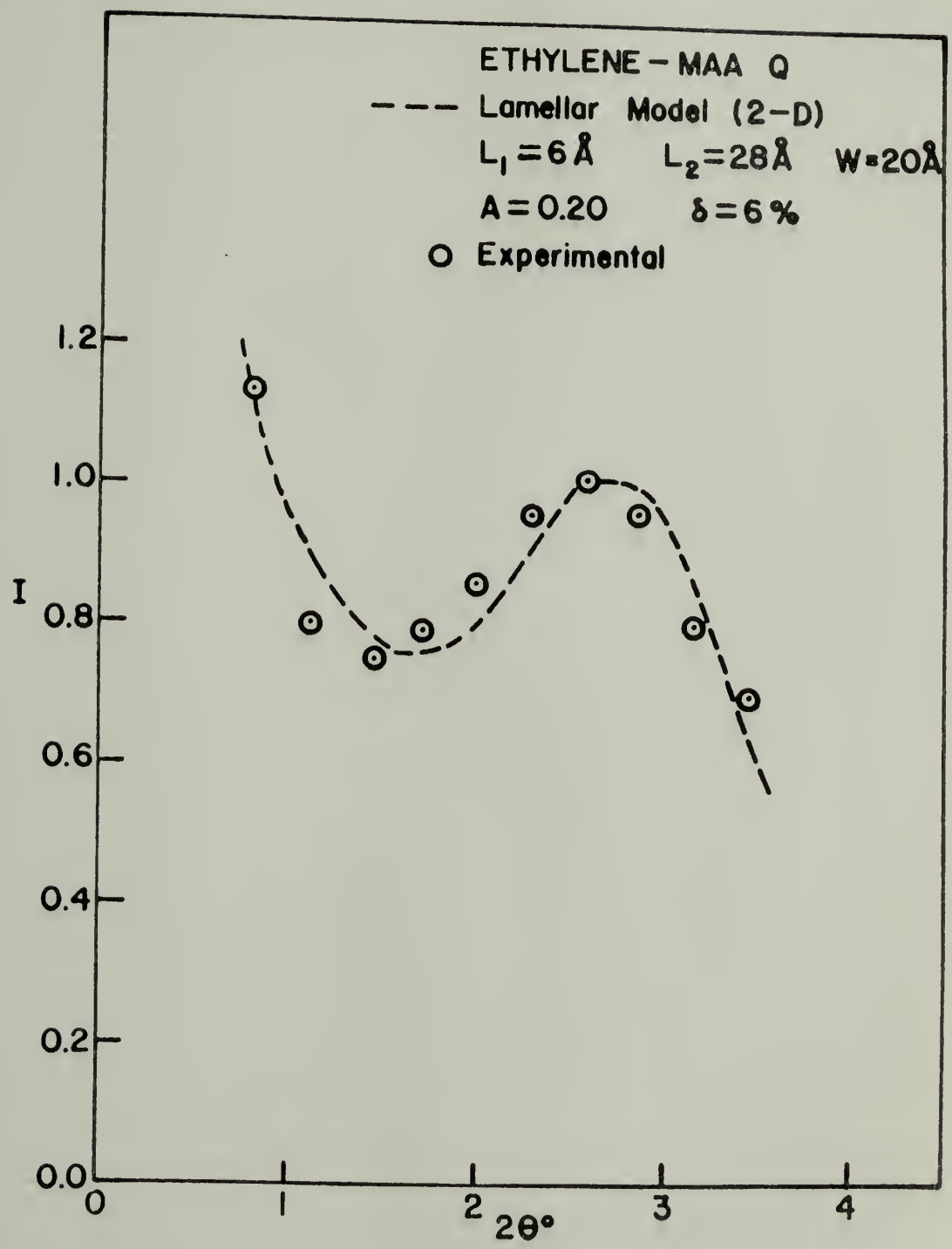
ETHYLENE – MAA Q
Lamellar Model (2-D)
L_1 = 6 Å L_2 = 28 Å W = 20 Å
A = 0.20 δ = 6 %
Experimental
I
1.2
1.0
0.8
0.6
0.4
0.2
0.0
0
1
2
3
4
2θ°

FIGURE 33

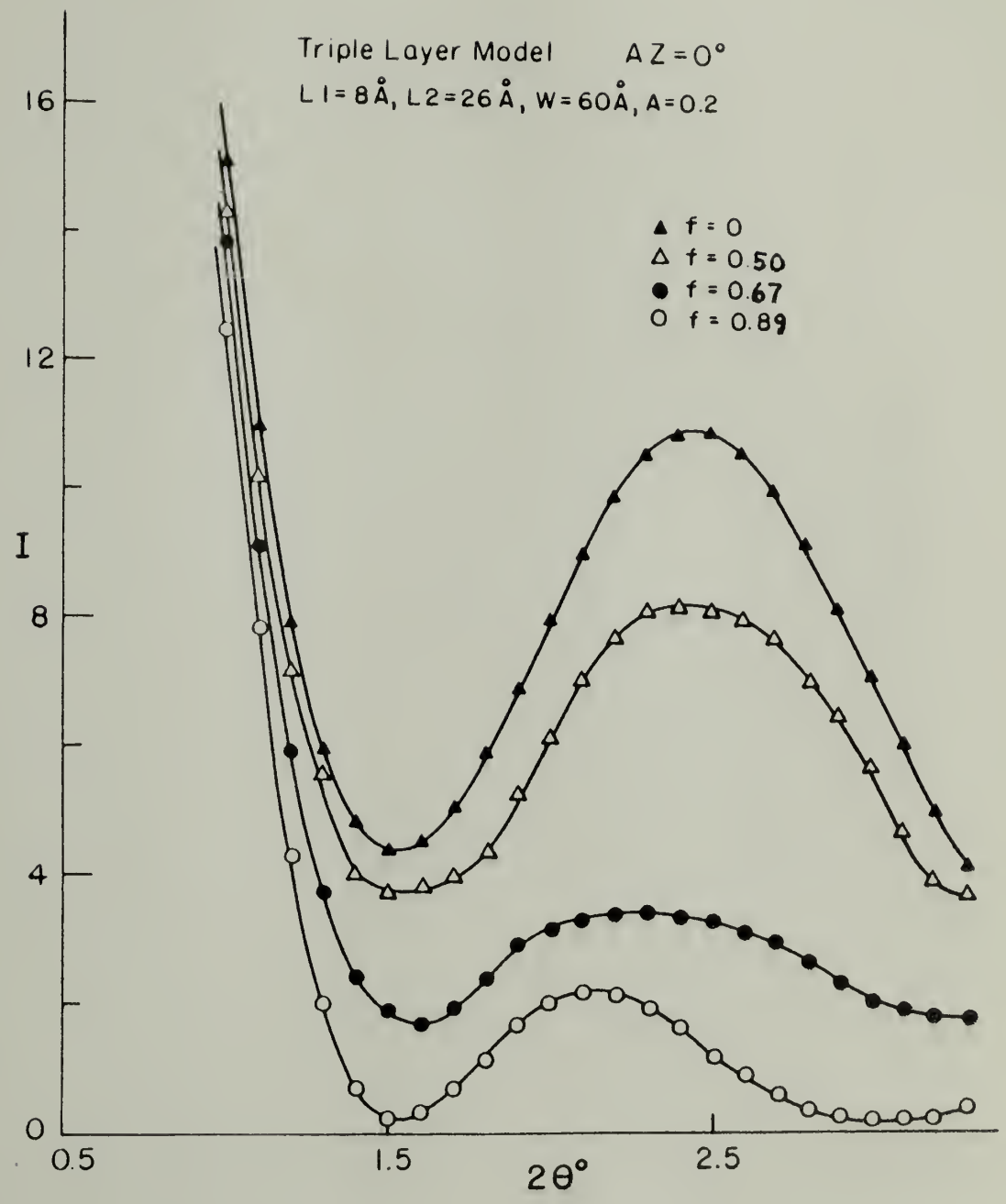
Triple Layer Model
AZ = 0°
L1 = 8Å, L2 = 26 Å, W = 60Å, A = 0.2
▲ f = 0
△ f = 0.50
● f = 0.67
○ f = 0.89
16
12
8
4
0
I
0.5
1.5
2.5
2θ°

FIGURE 34

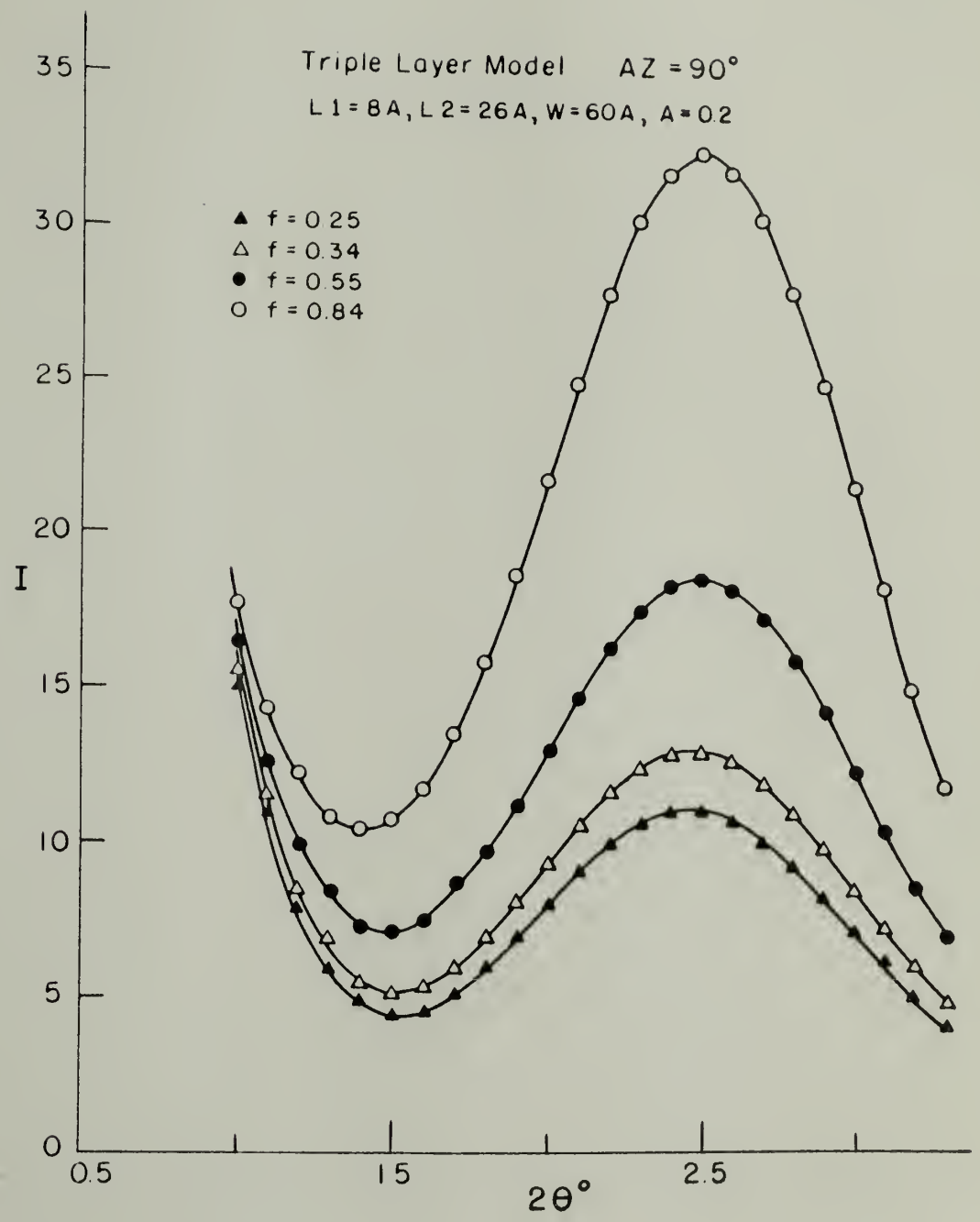
Triple Layer Model AZ = 90°
L1 = 8A, L2 = 26A, W = 60A, A = 0.2
f = 0.25
f = 0.34
f = 0.55
f = 0.84
I
2θ°
0
5
10
15
20
25
30
35
0.5
1.5
2.5

FIGURE 35

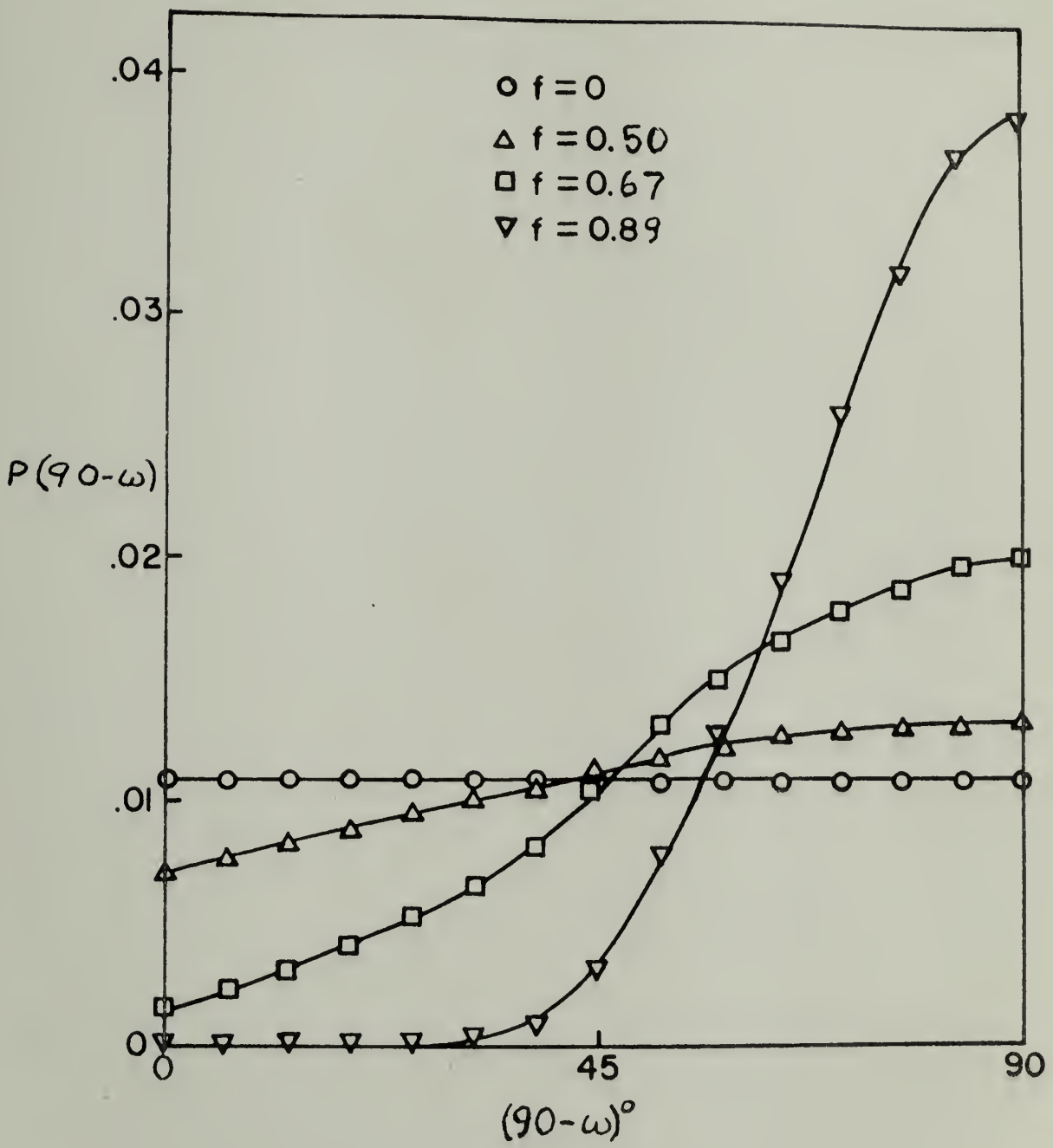

FIGURE 36

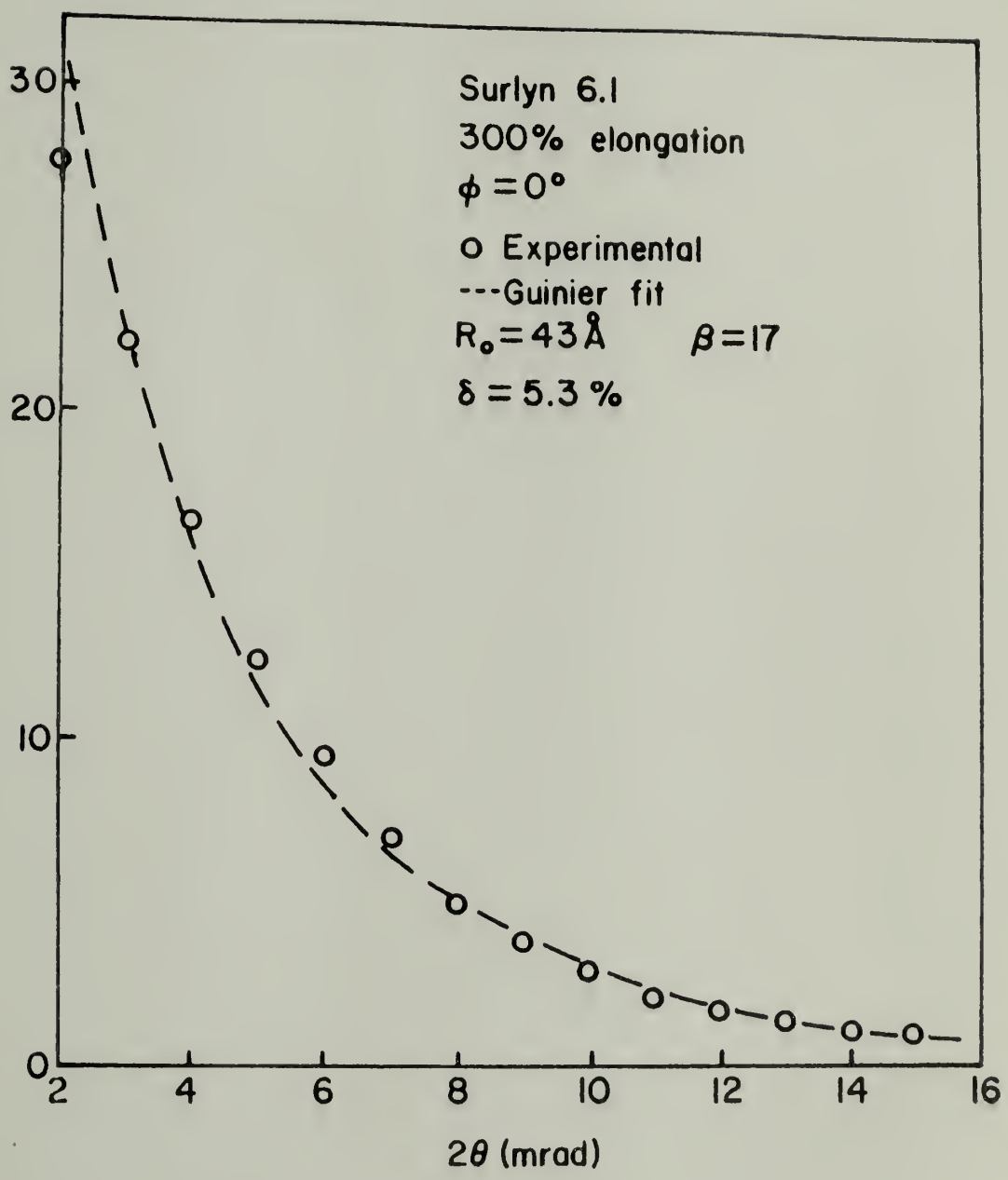
Surlyn 6.1
300% elongation
$\phi = 0°$
o Experimental
---Guinier fit
$R_o = 43$ Å
$\beta = 17$
$\delta = 5.3\%$
30
20
10
0
2
4
6
8
10
12
14
16
2θ (mrad)

FIGURE 37

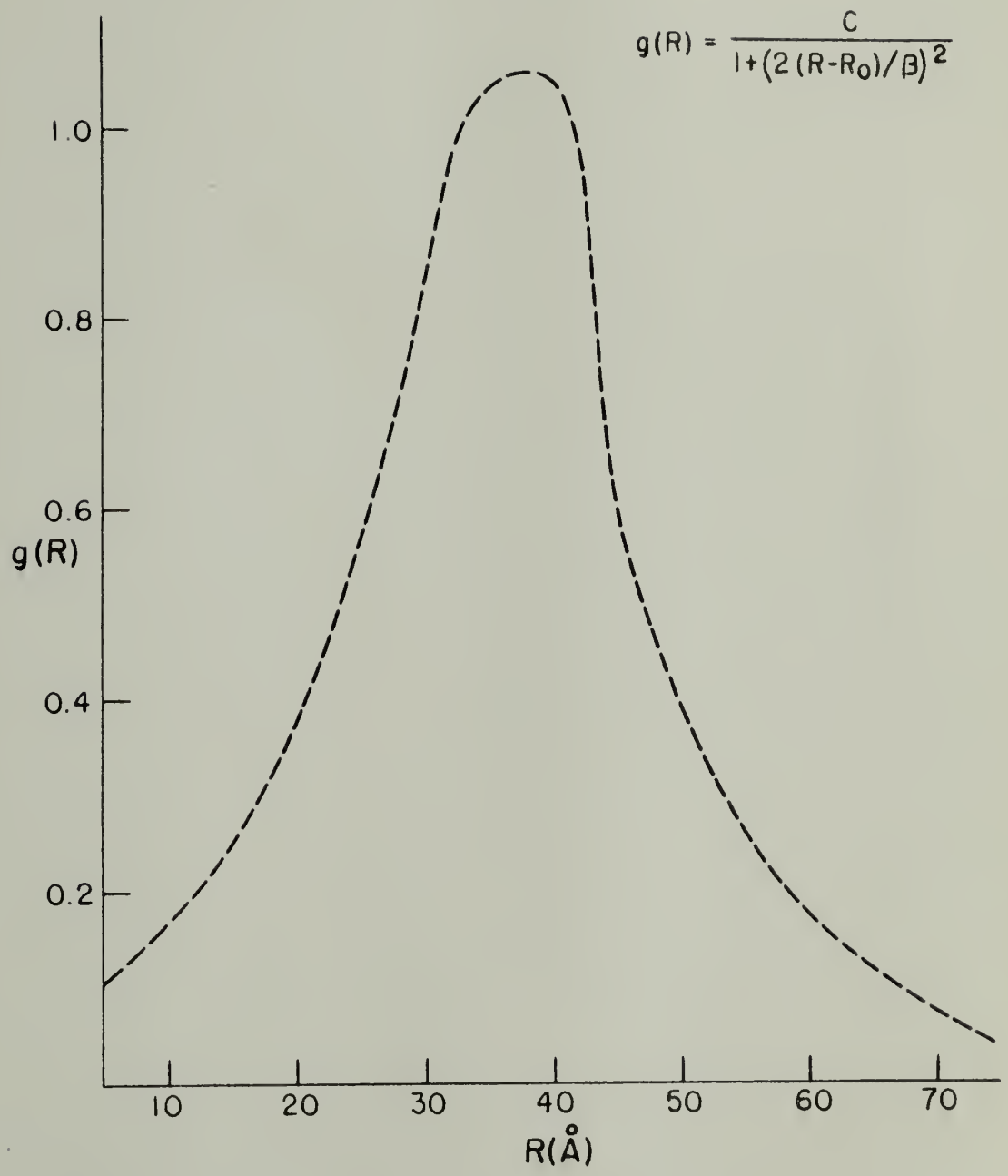

FIGURE 38

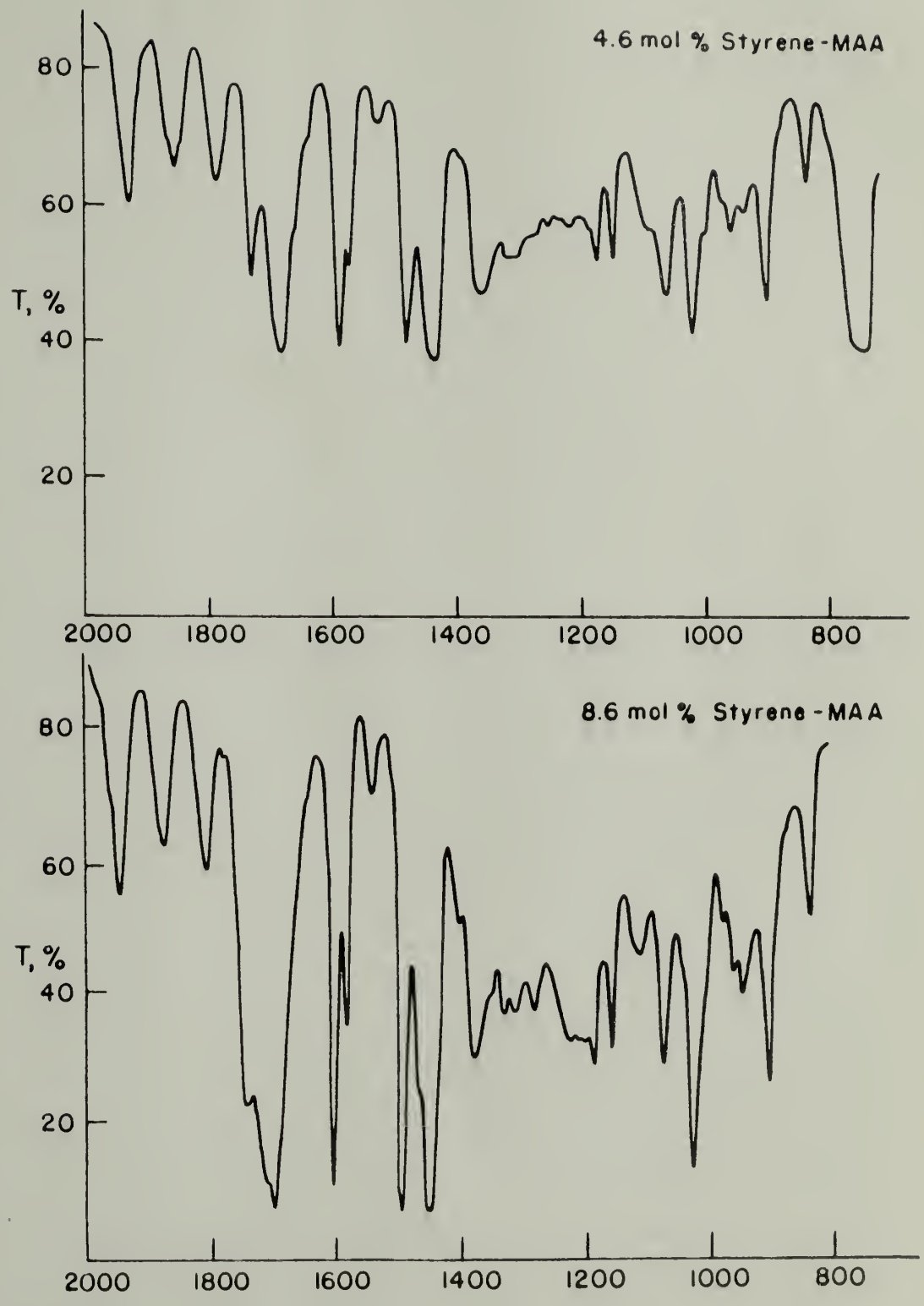
4.6 mol % Styrene-MAA
80
60
T, %
40
20
2000
1800
1600
1400
1200
1000
800
8.6 mol % Styrene-MAA
80
60
T, %
40
20
2000
1800
1600
1400
1200
1000
800

FIGURE 39

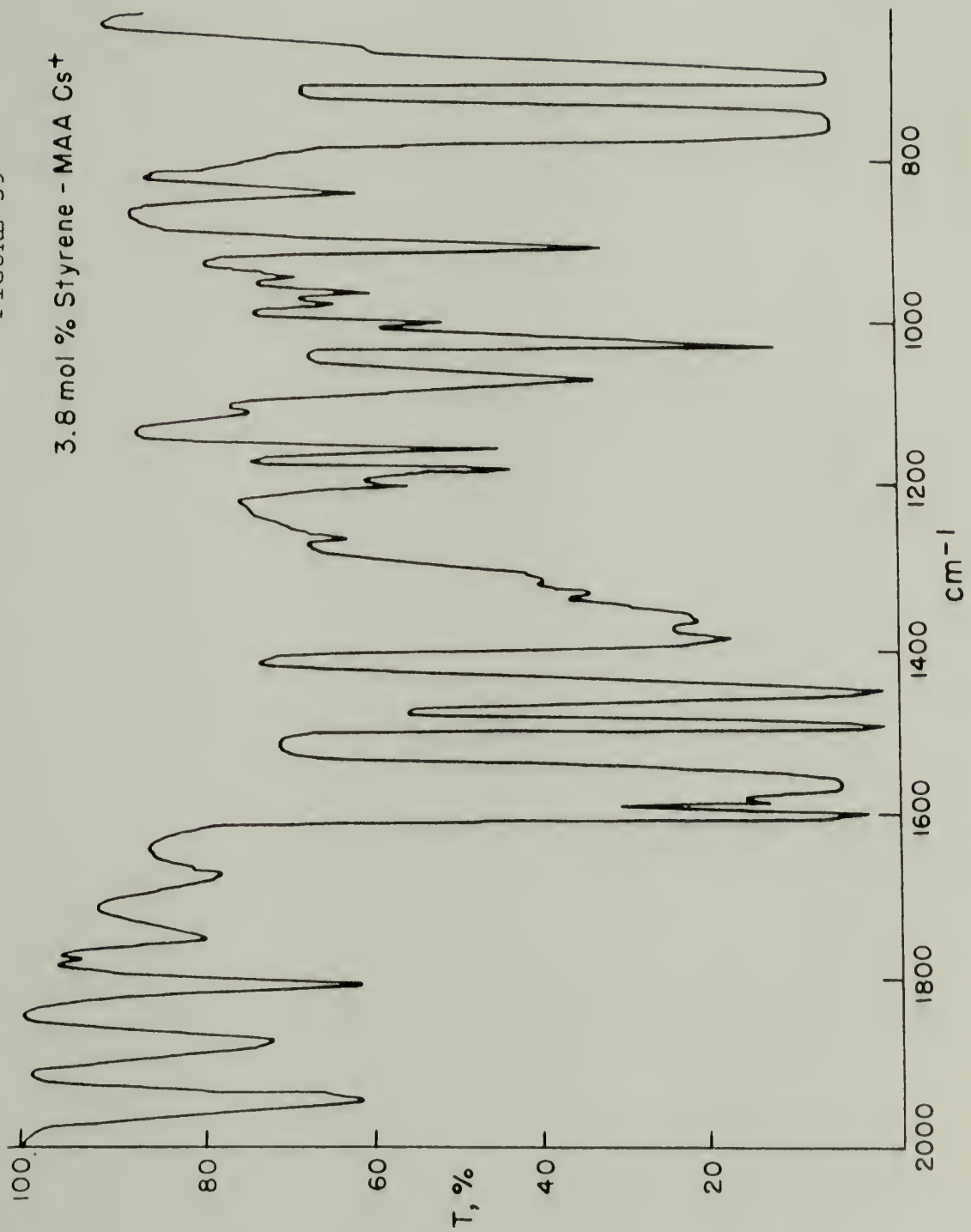
3.8 mol % Styrene - MAA Cs+
100
80
60
40
20
T, %
2000
1800
1600
1400
1200
1000
800
cm-1

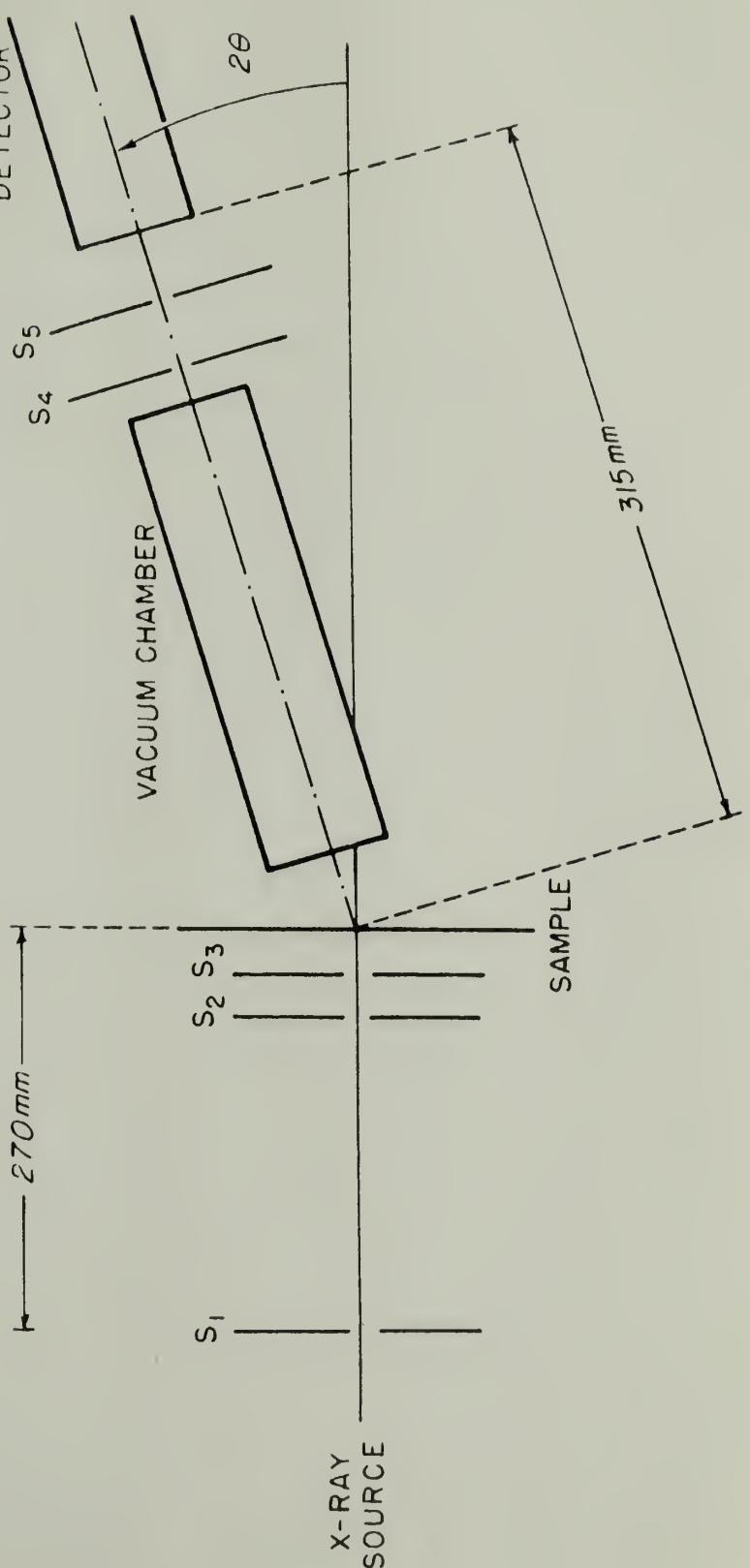

FIGURE 40

Rigaku-Denki SAXS Camera

FIGURE 41

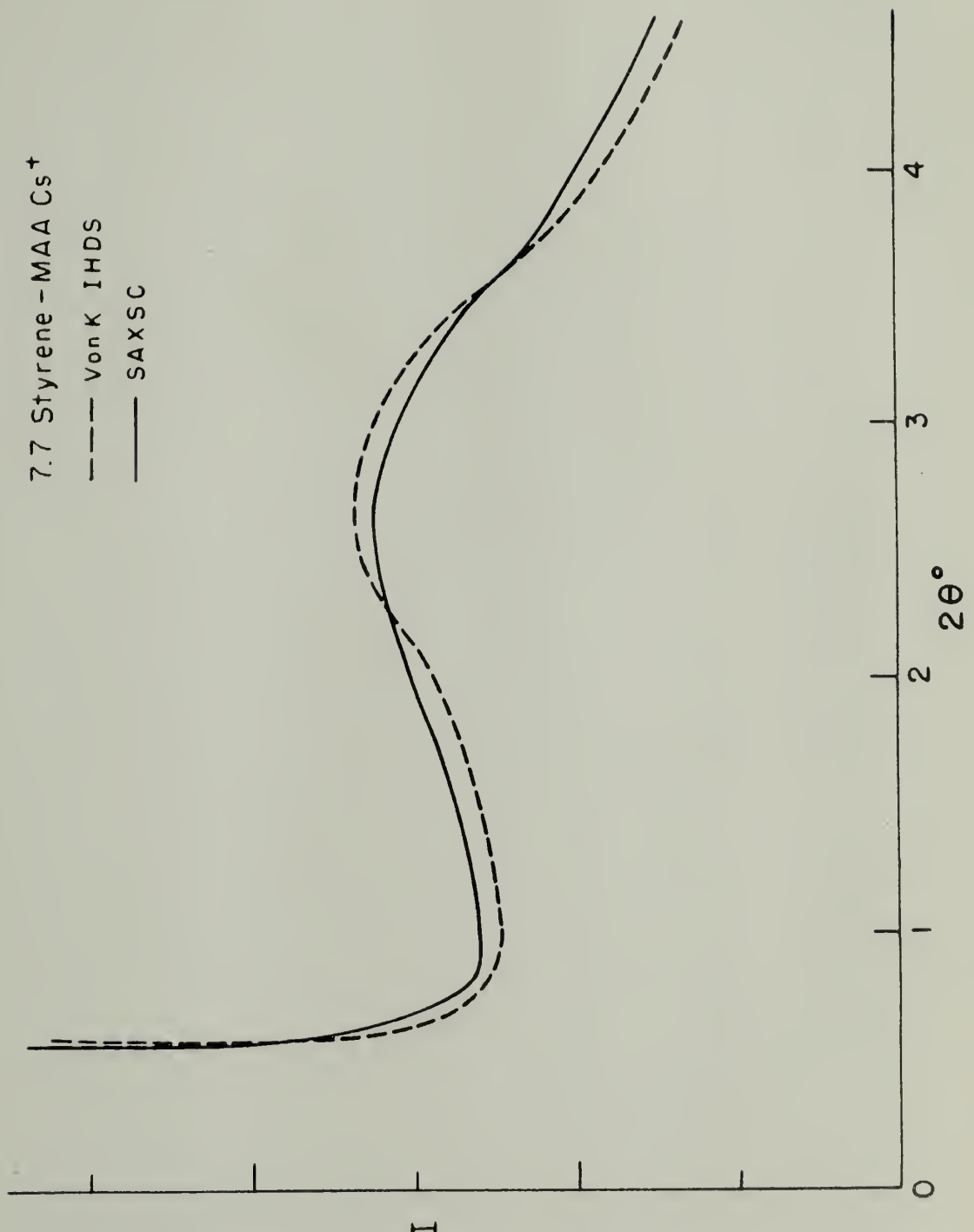

FIGURE 42

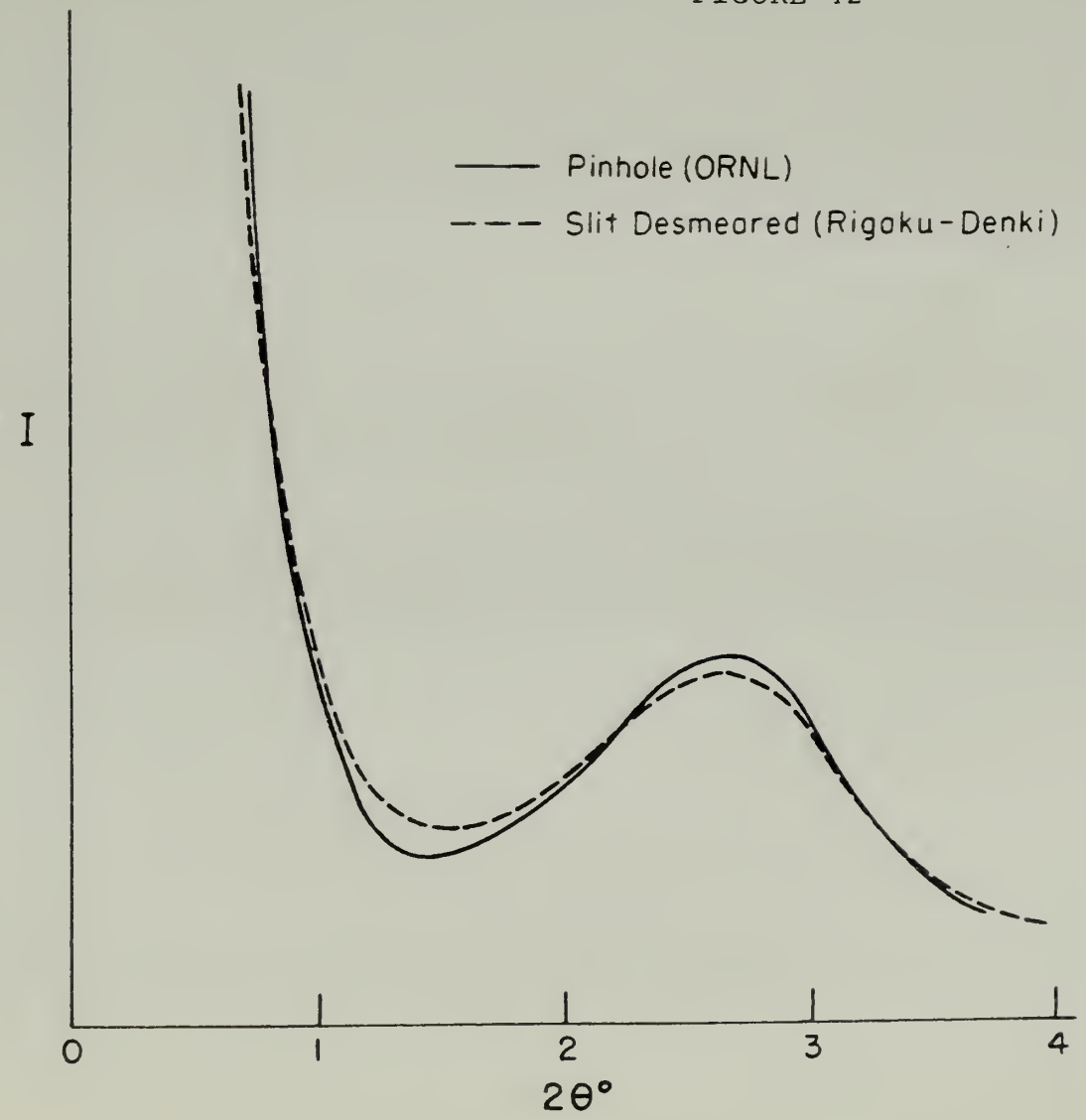

FIGURE 43

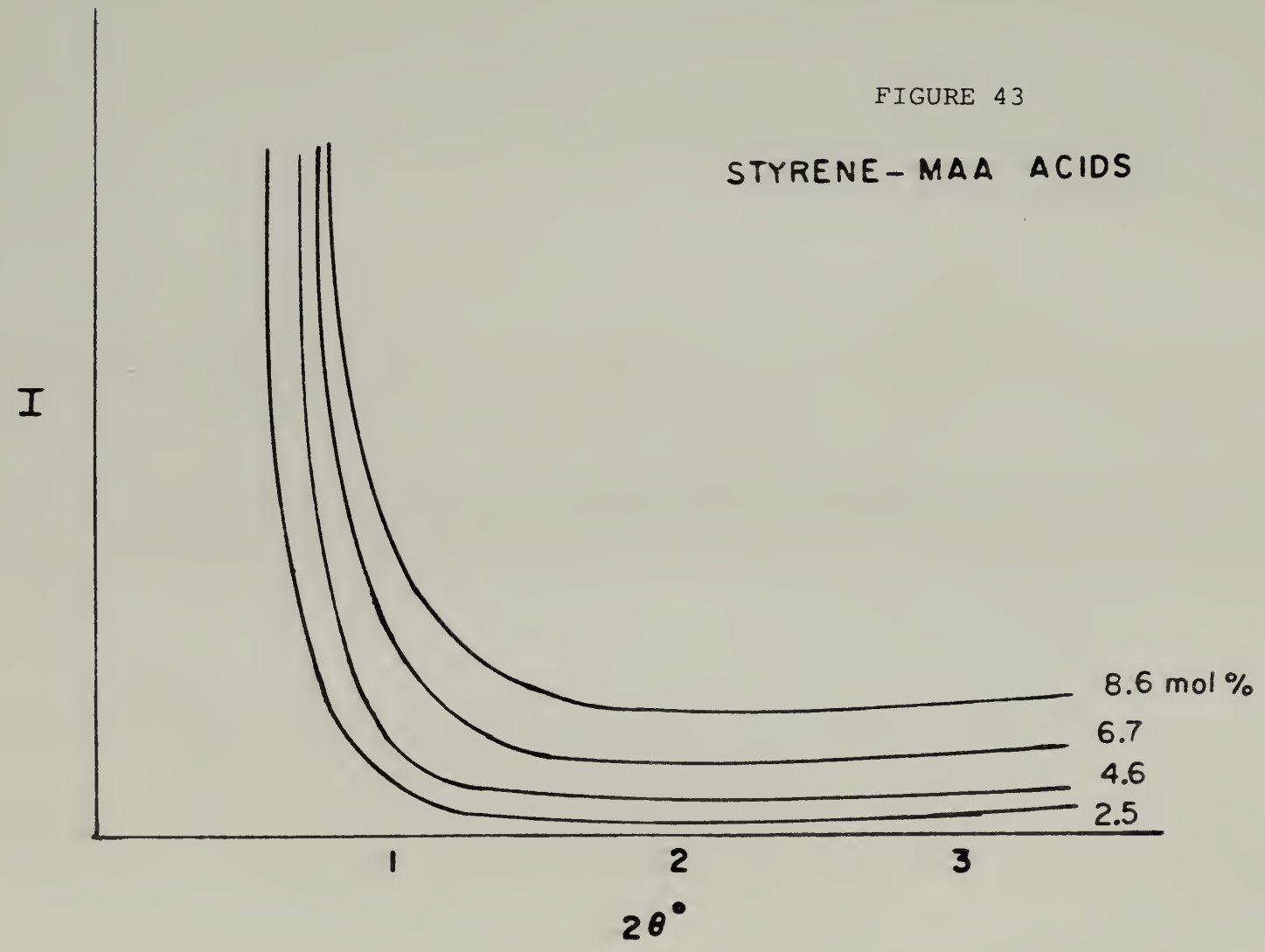

FIGURE 44

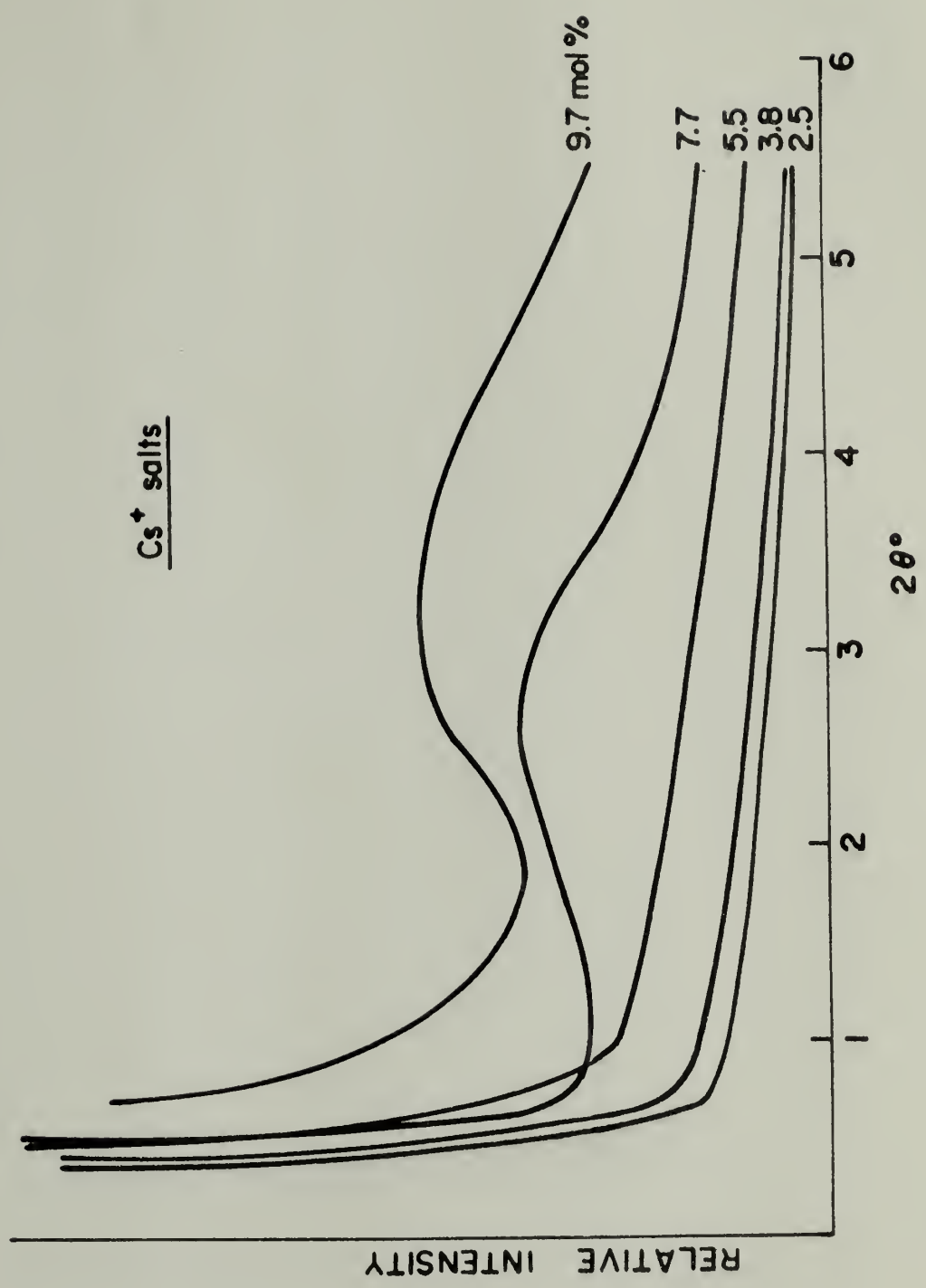


9.7 mol %
7.7
5.5
3.8
2.5
Cs⁺ salts
S⁴I x 10⁵
S⁴ x 10⁵
16
14
12
10
8
6
4
2
0
1
2
3
4
5
6
7
8
9

FIGURE 45

FIGURE 46

NORMALIZED

INTERNAL FLUCTUATION SCATTERING

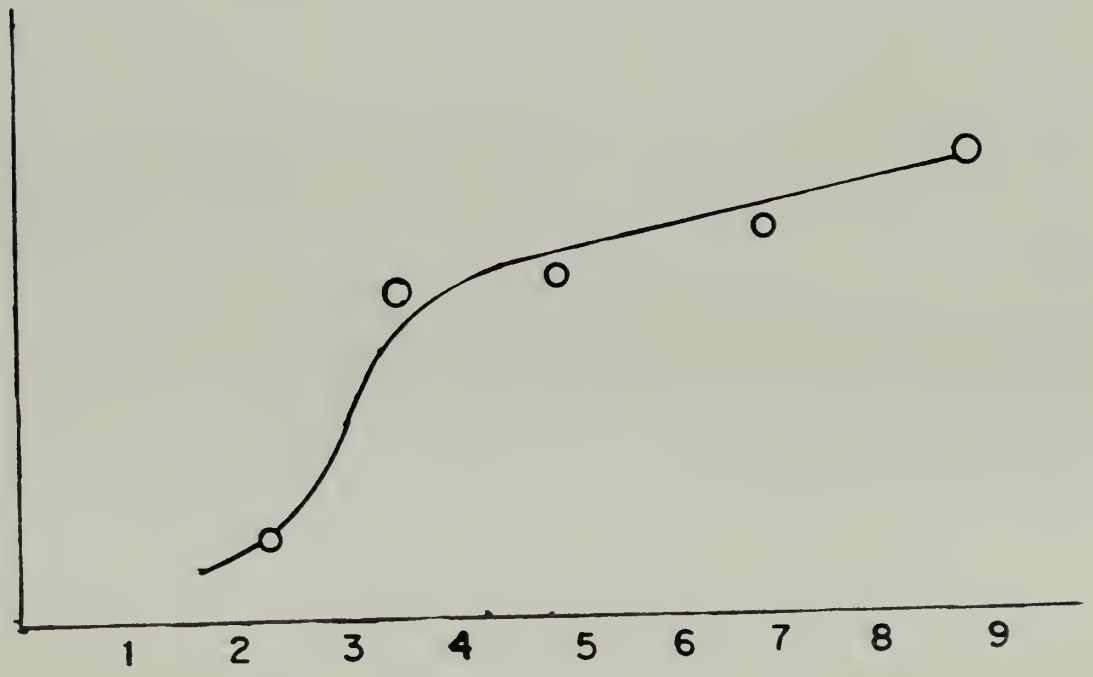

FIGURE 47

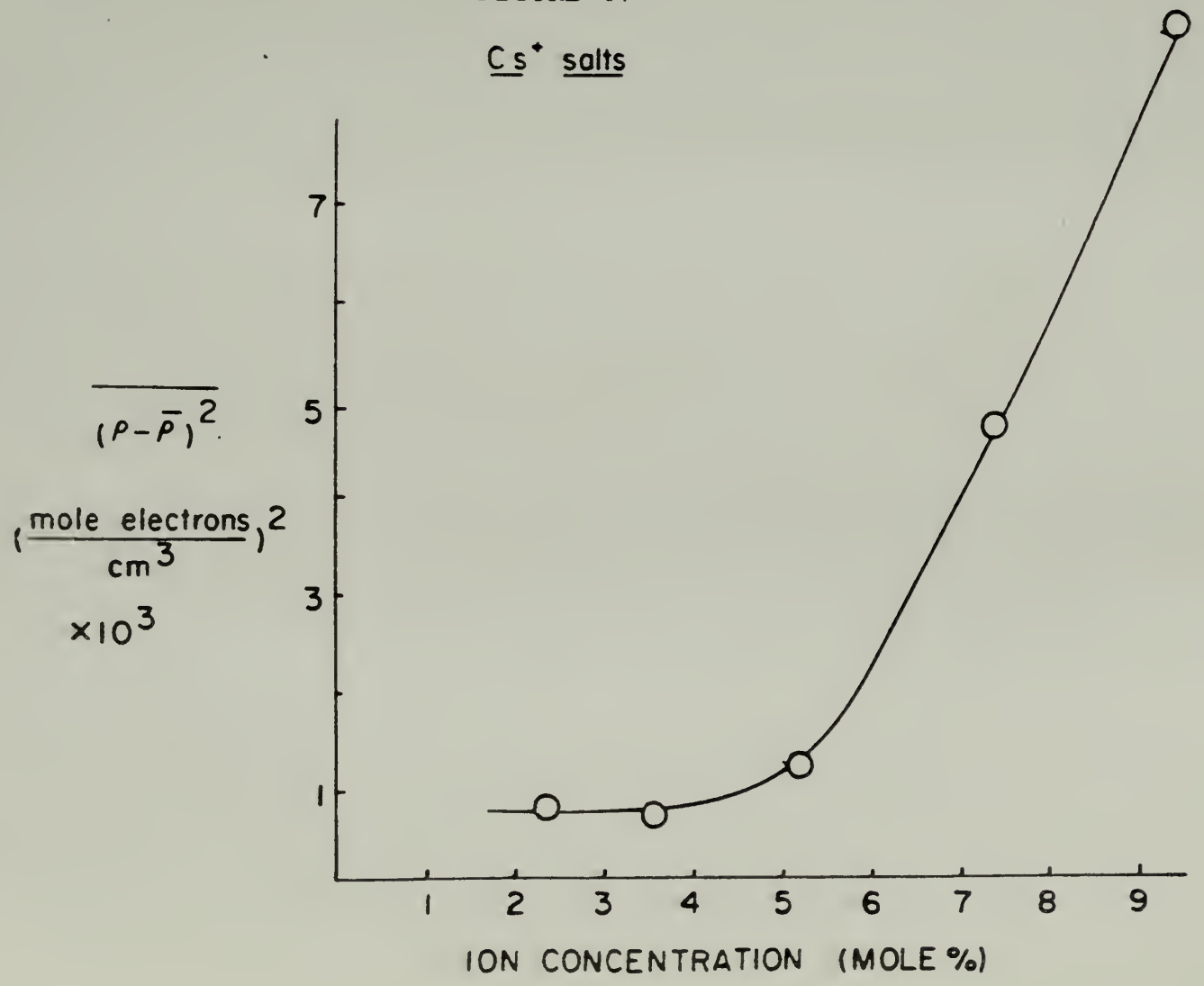
Cs+ salts
$\overline{(\rho-\bar{\rho})^2}$
$(\frac{\text{mole electrons}}{\text{cm}^3})^2$
$\times 10^3$
7
5
3
1
1
2
3
4
5
6
7
8
9
ION CONCENTRATION (MOLE %)

FIGURE 48

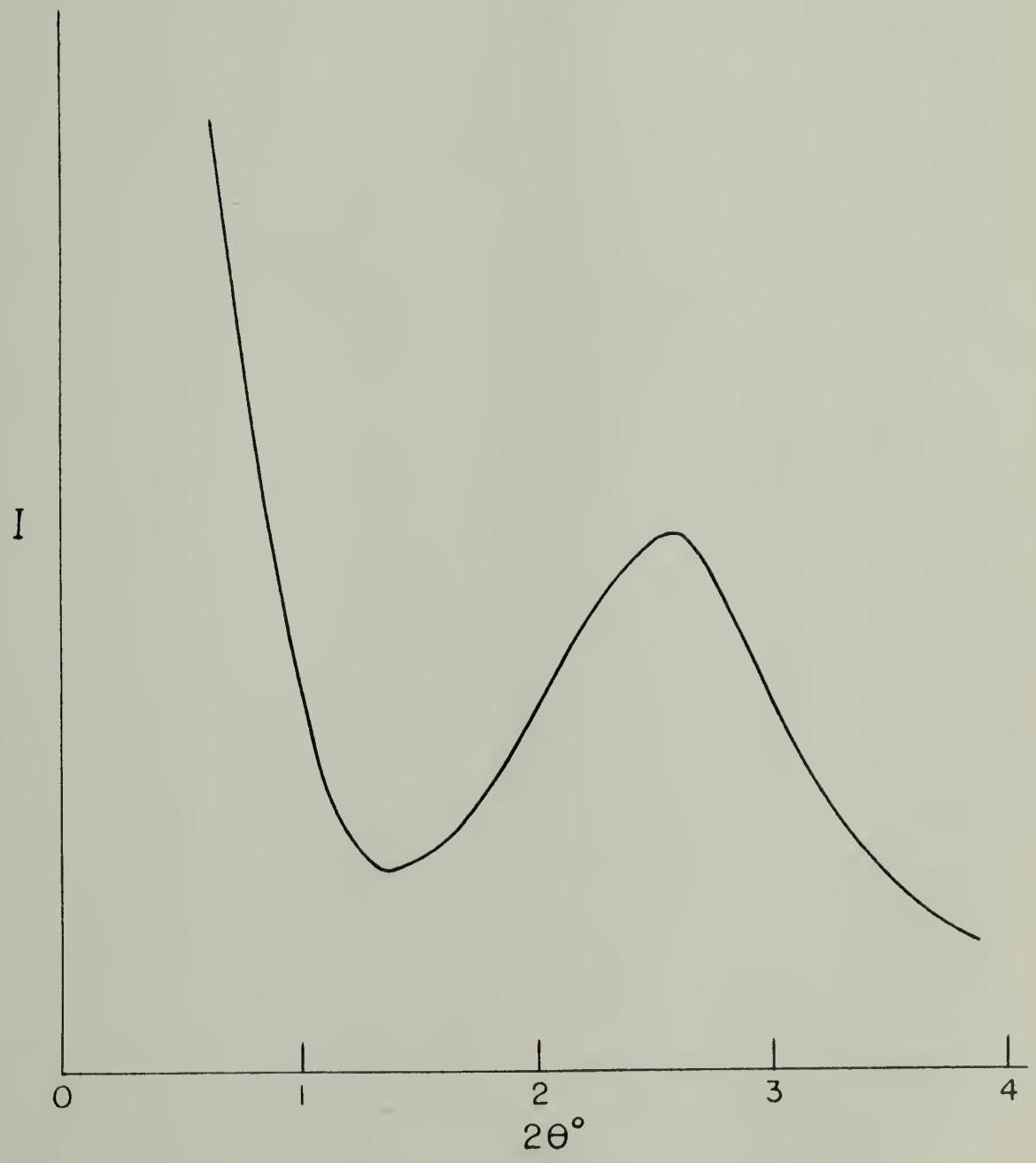

FIGURE 49

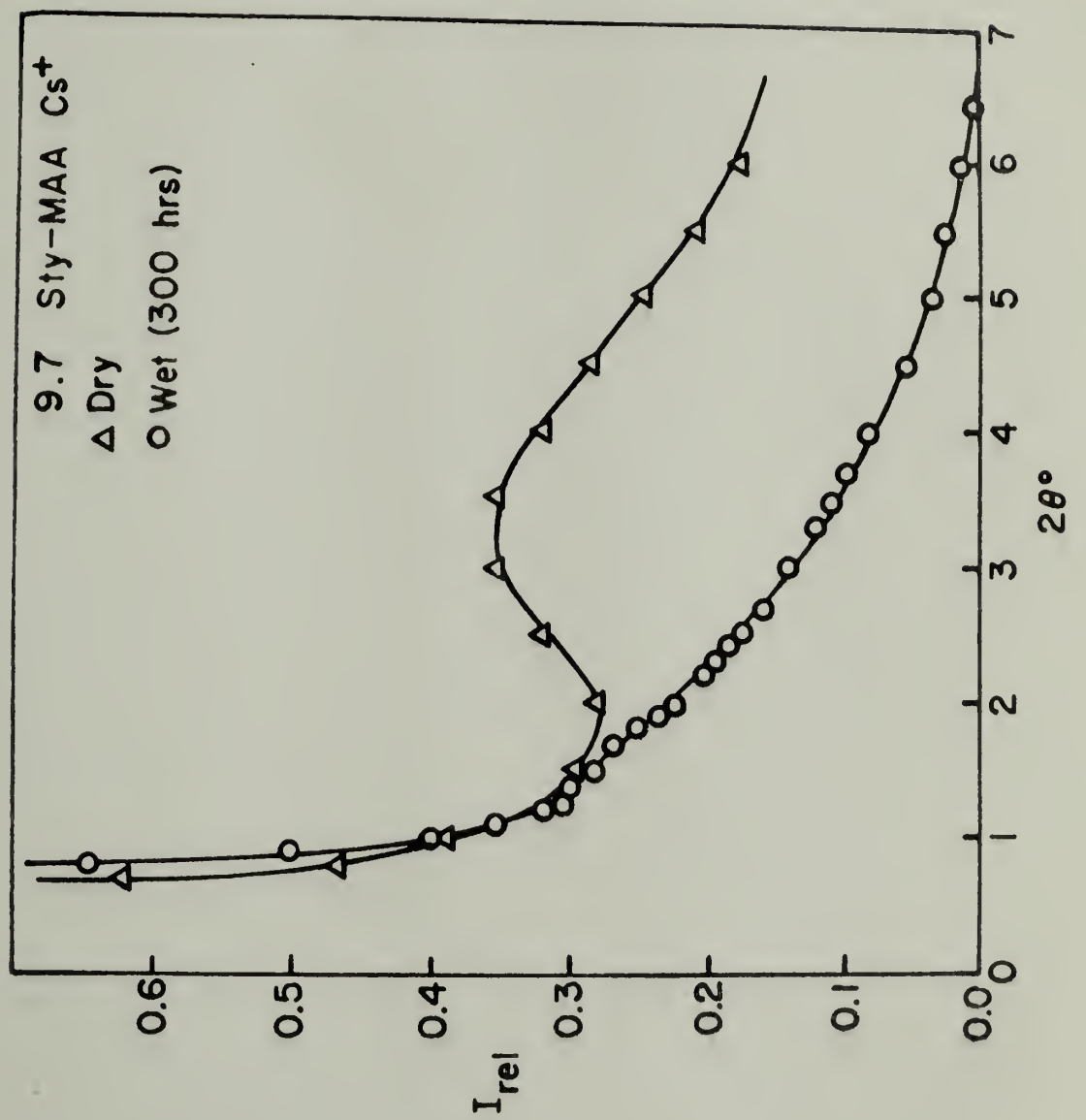
9.7 Sty-MAA Cs+
Δ Dry
O Wet (300 hrs)
0.6
0.5
0.4
0.3
0.2
0.1
0.0
I rel
0
1
2
3
4
5
6
7
2θ°

FIGURE 50

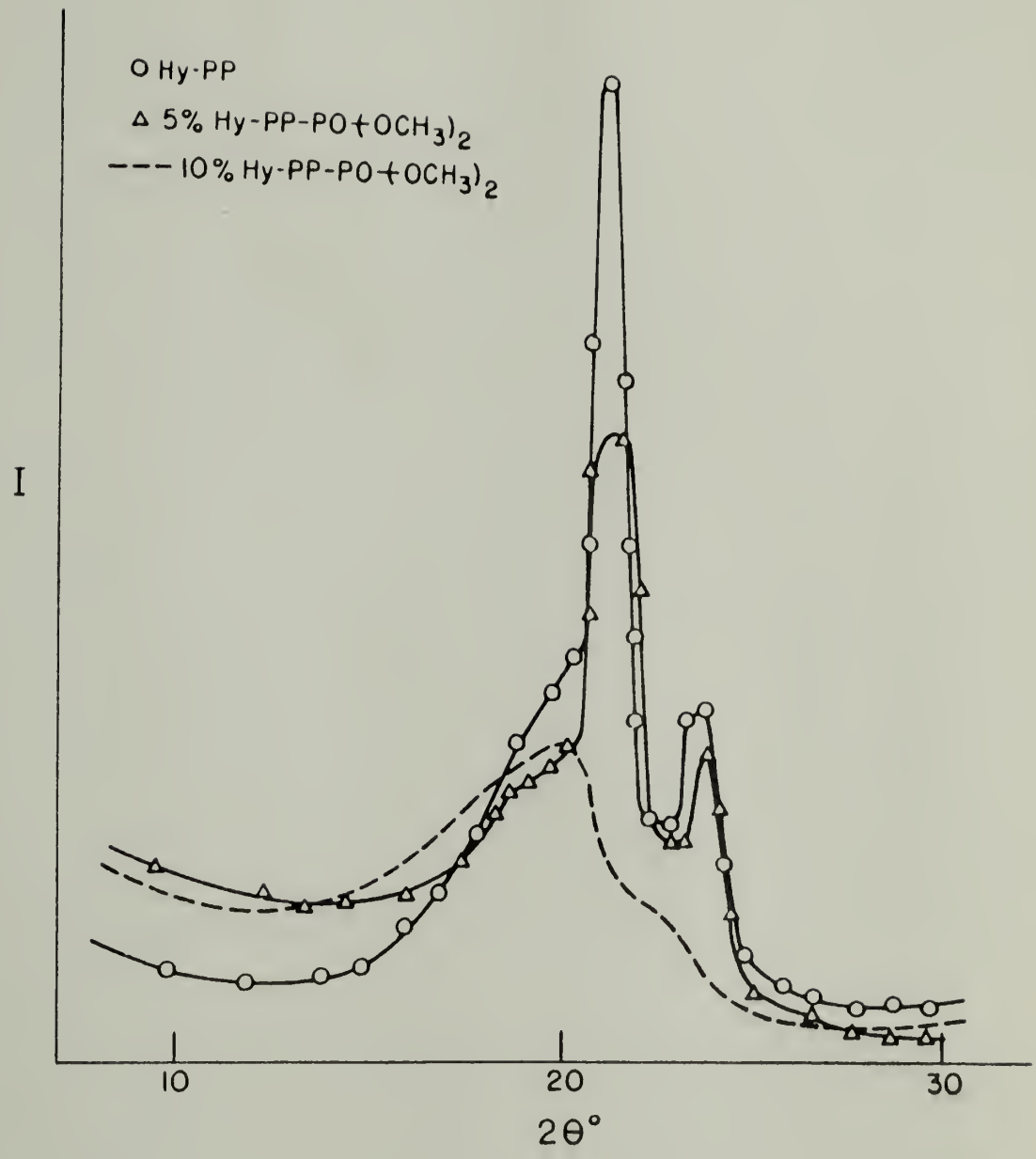

FIGURE 51

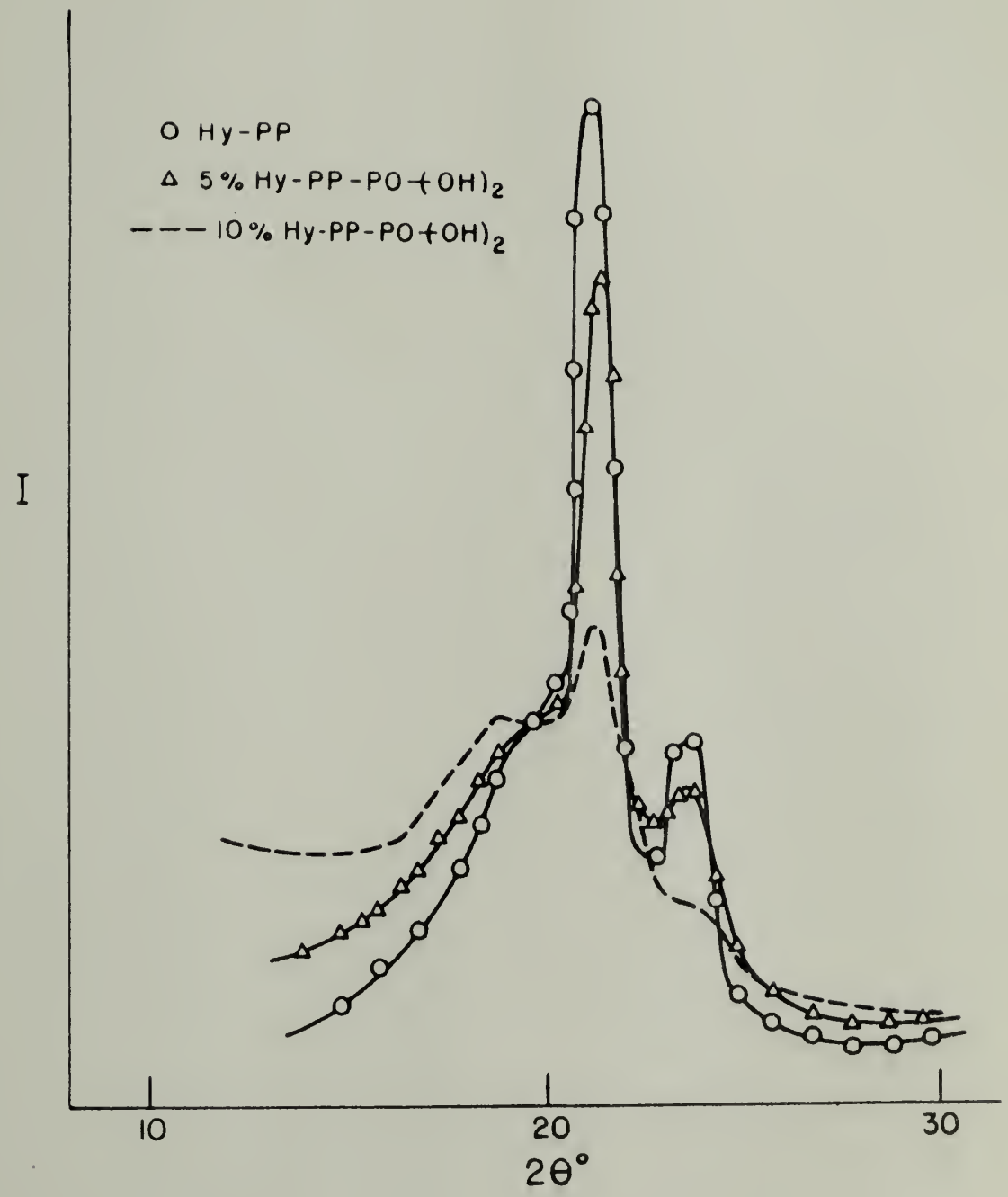

FIGURE 52

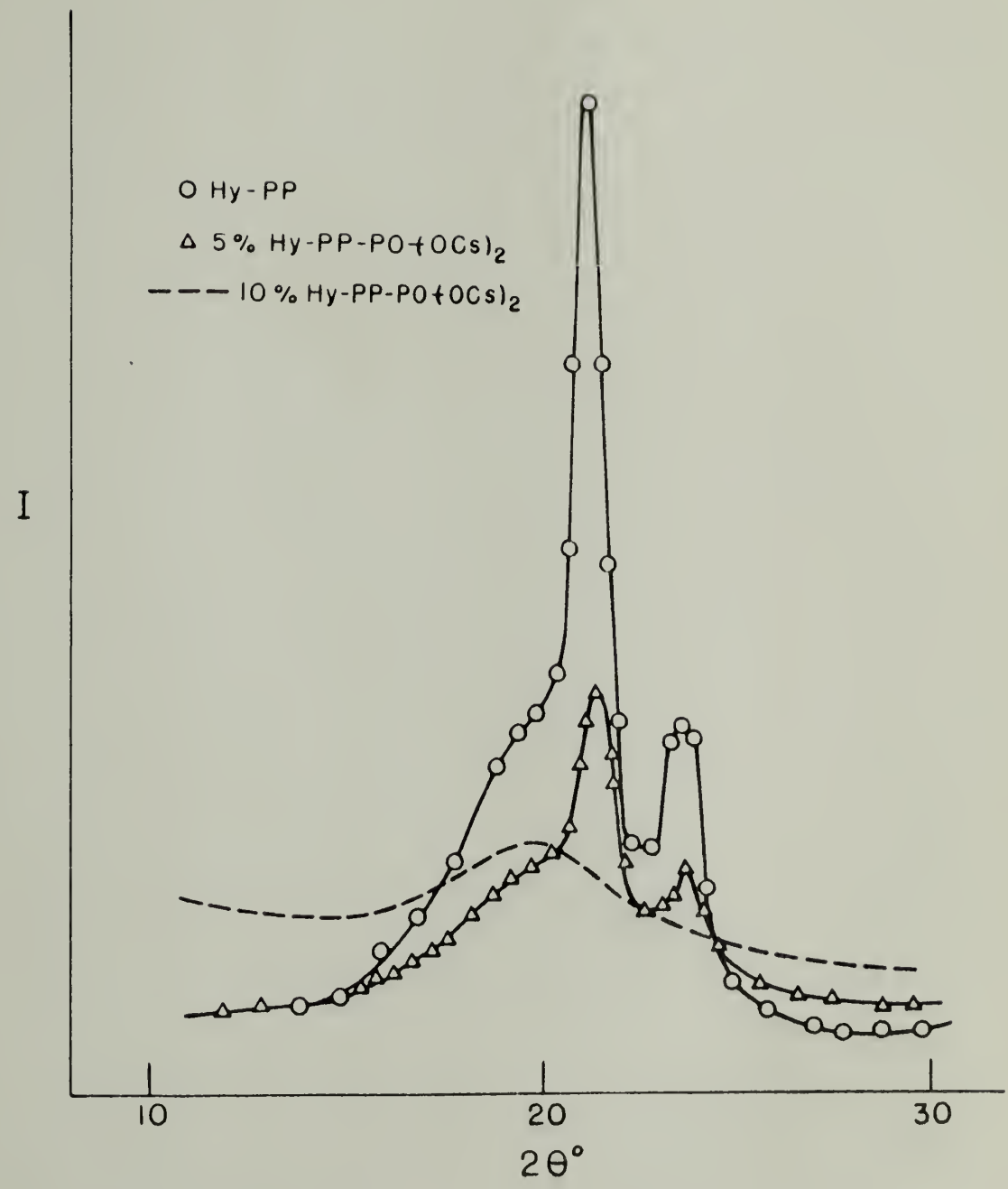

FIGURE 53

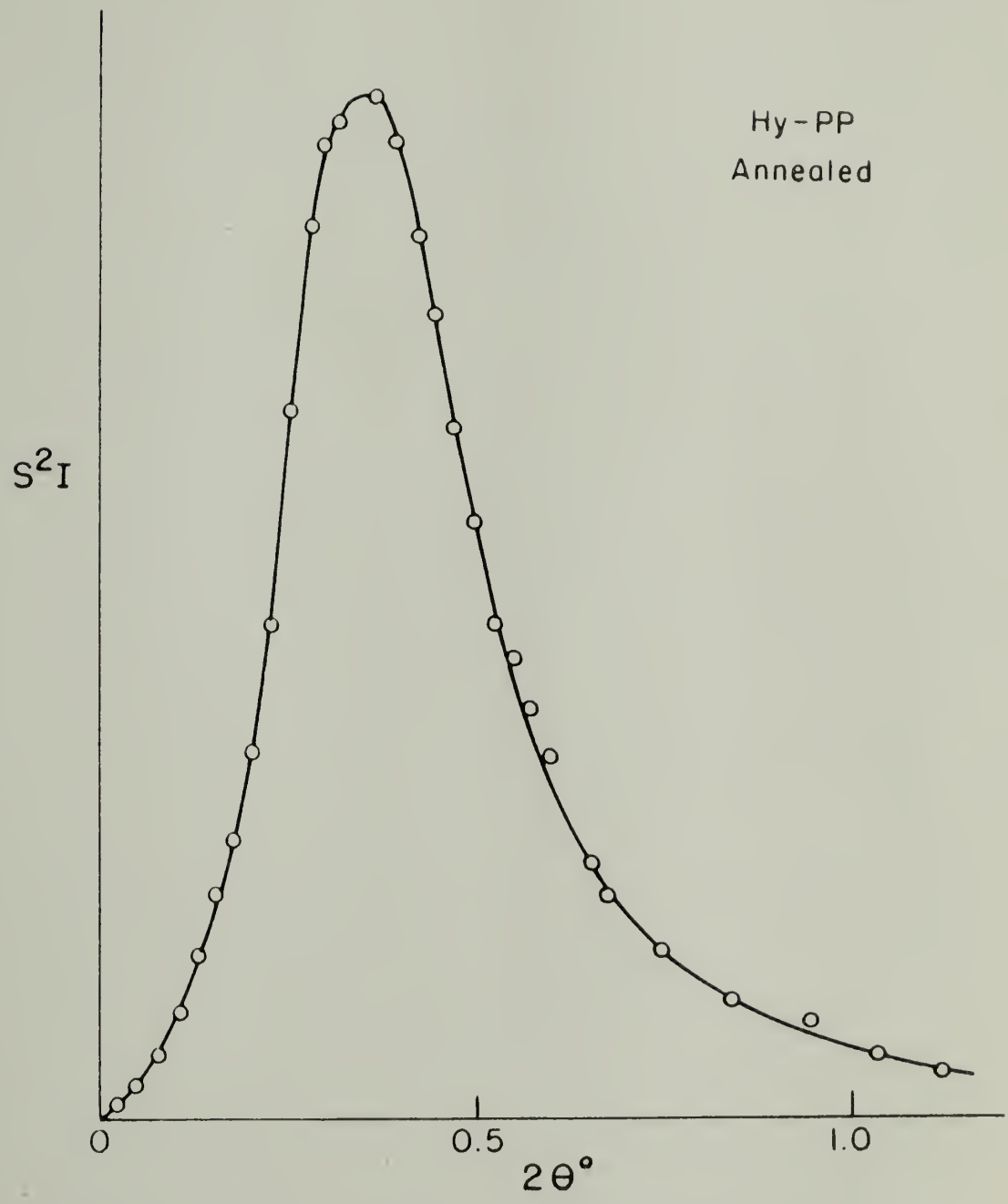

FIGURE 54

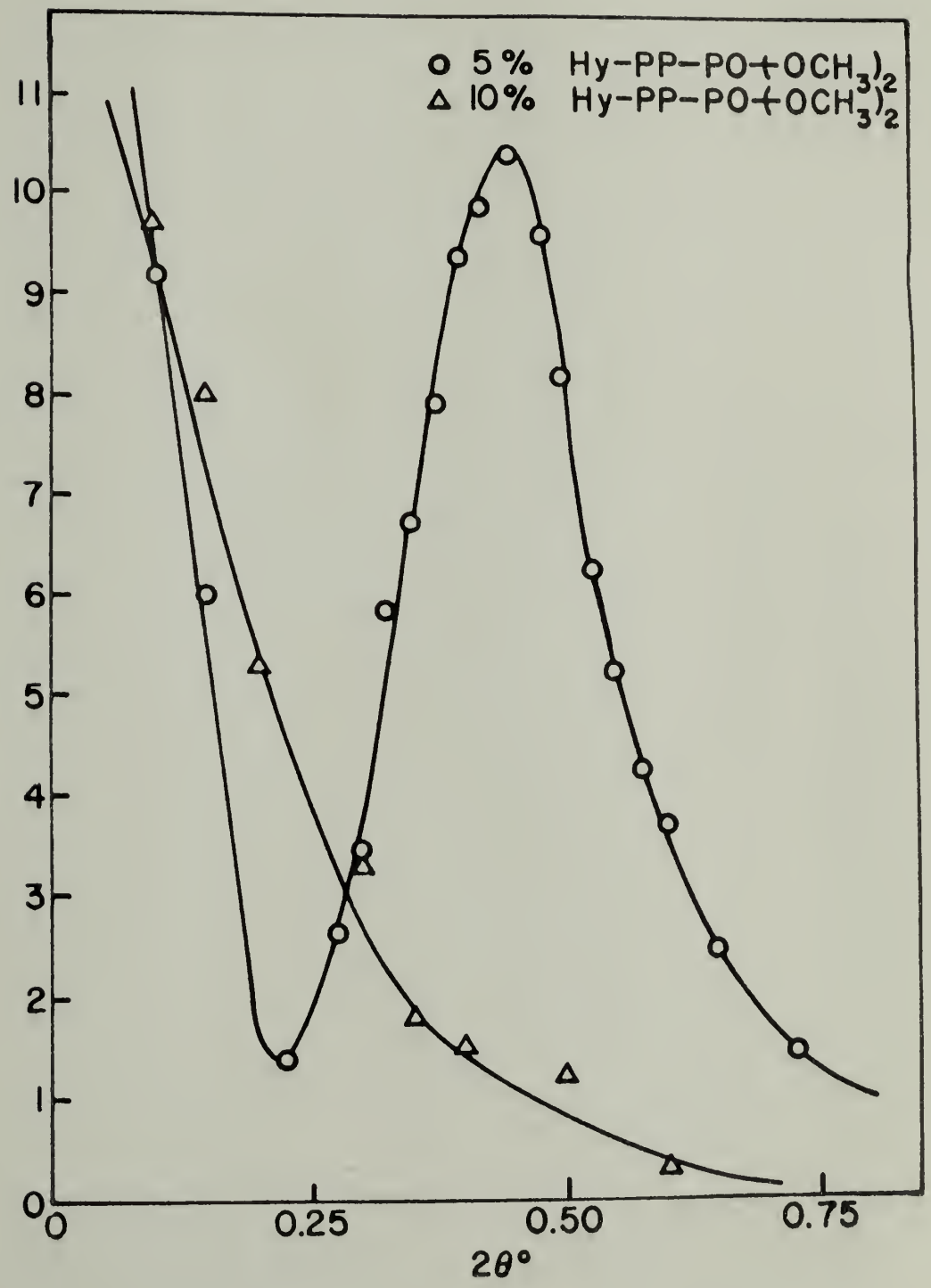
○ 5% Hy-PP-PO+OCH3)2
△ 10% Hy-PP-PO+OCH3)2
11
10
9
8
7
6
5
4
3
2
1
0
0
0.25
0.50
0.75
2θ°

FIGURE 55

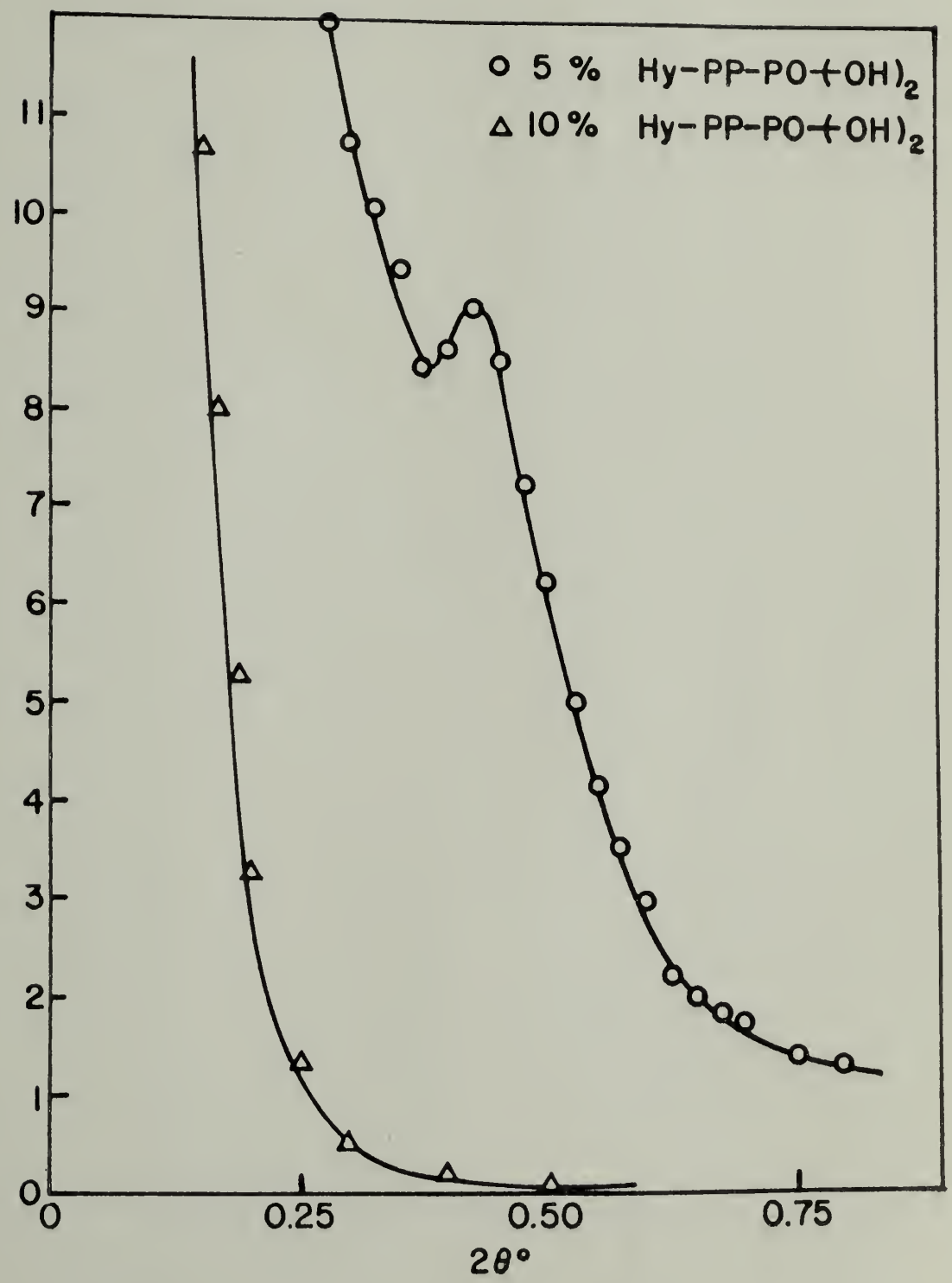

FIGURE 56

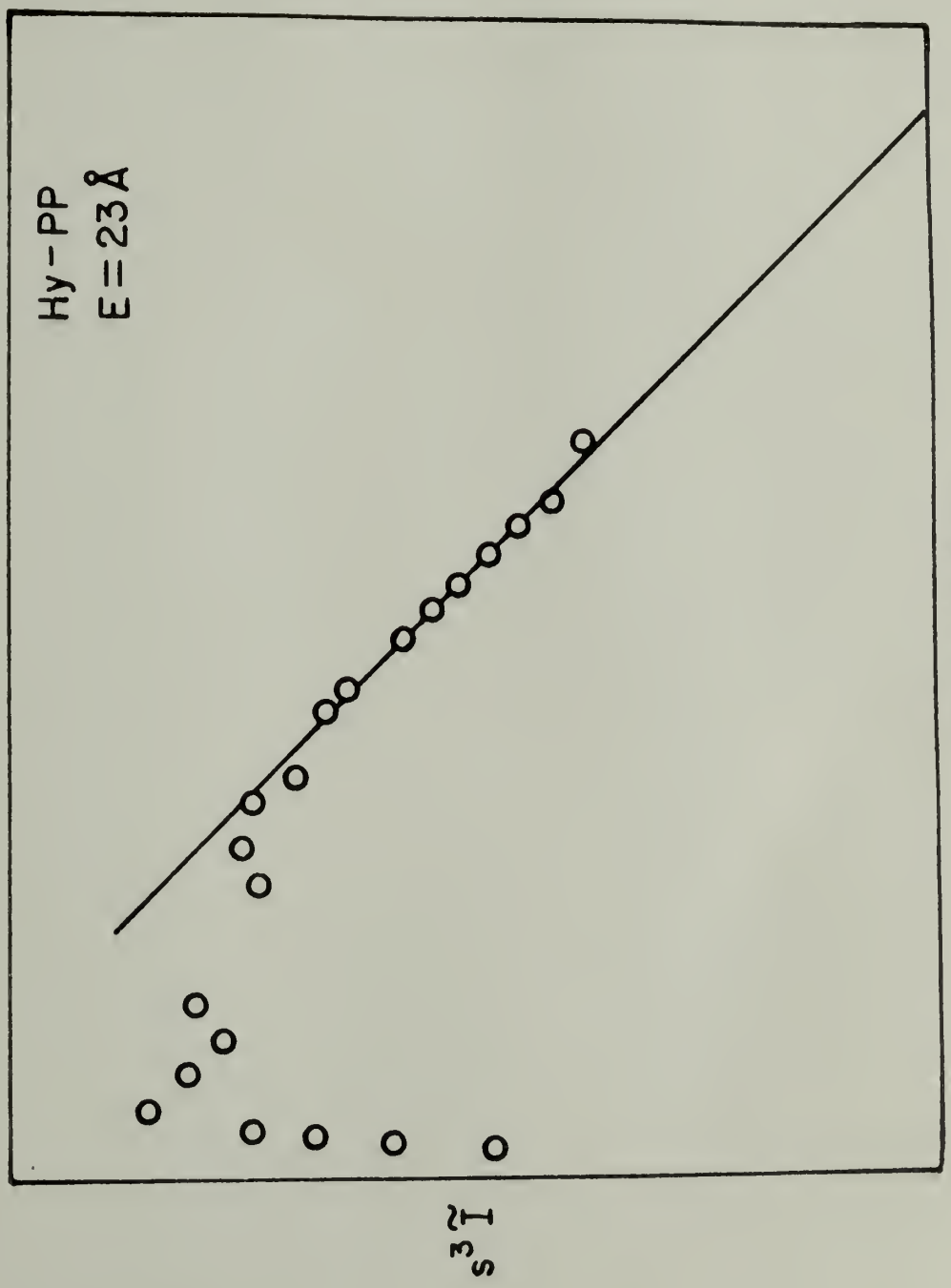

FIGURE 57

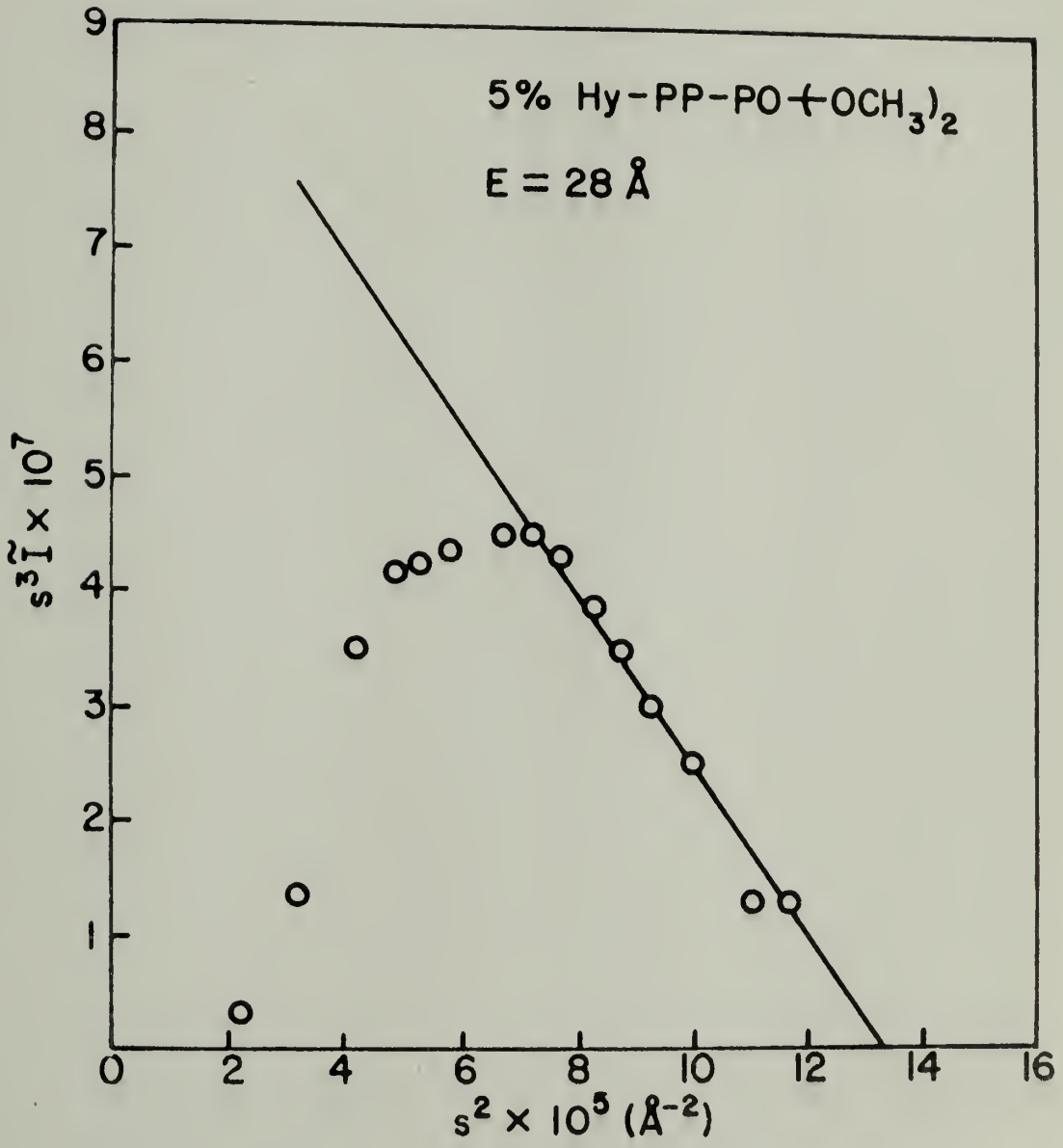
5% Hy-PP-PO(-OCH3)2
E = 28 Å
s³Ĩ × 10⁷
s² × 10⁵ (Å⁻²)
0
2
4
6
8
10
12
14
16
1
2
3
4
5
6
7
8
9

FIGURE 58

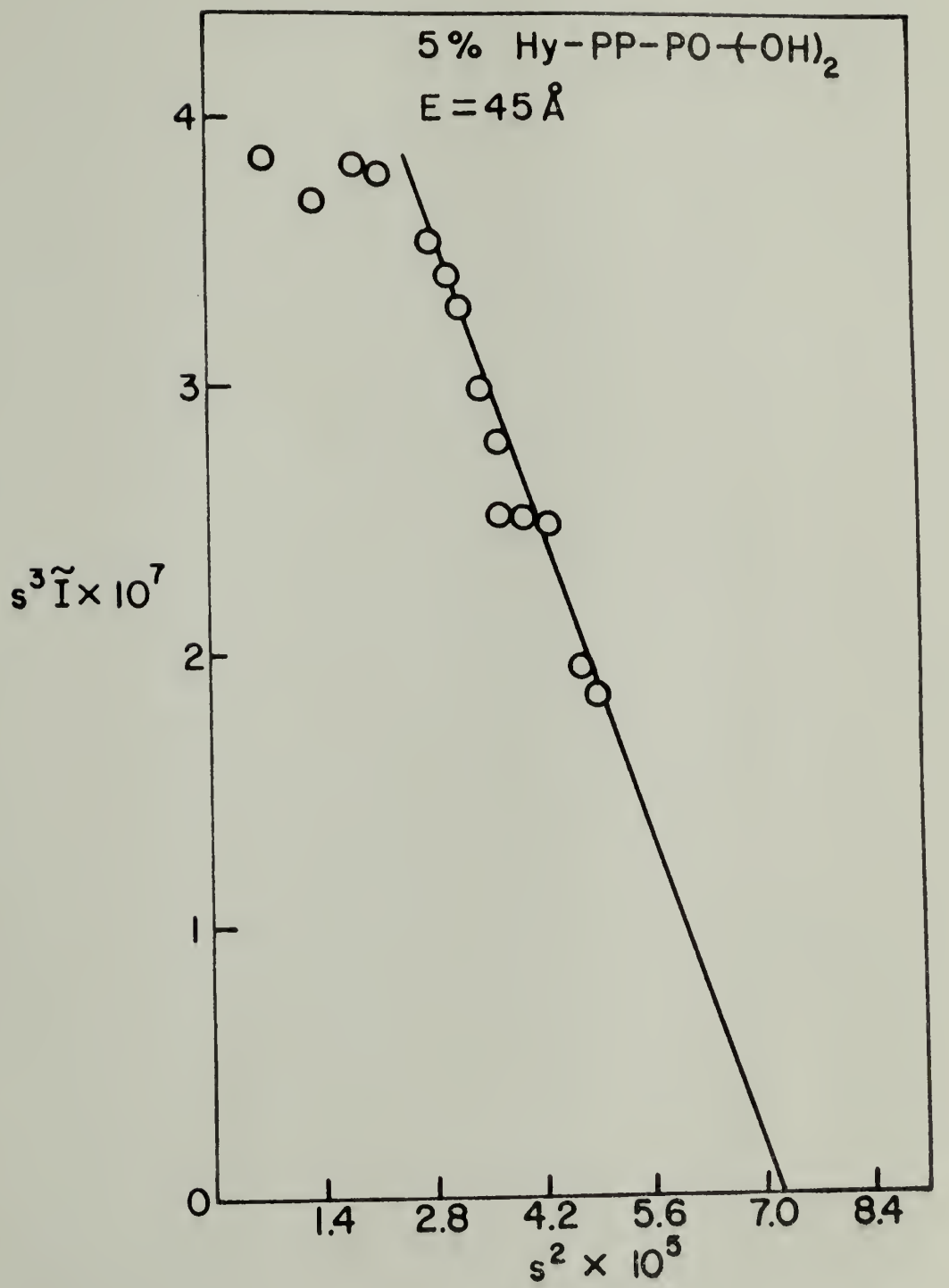

FIGURE 59

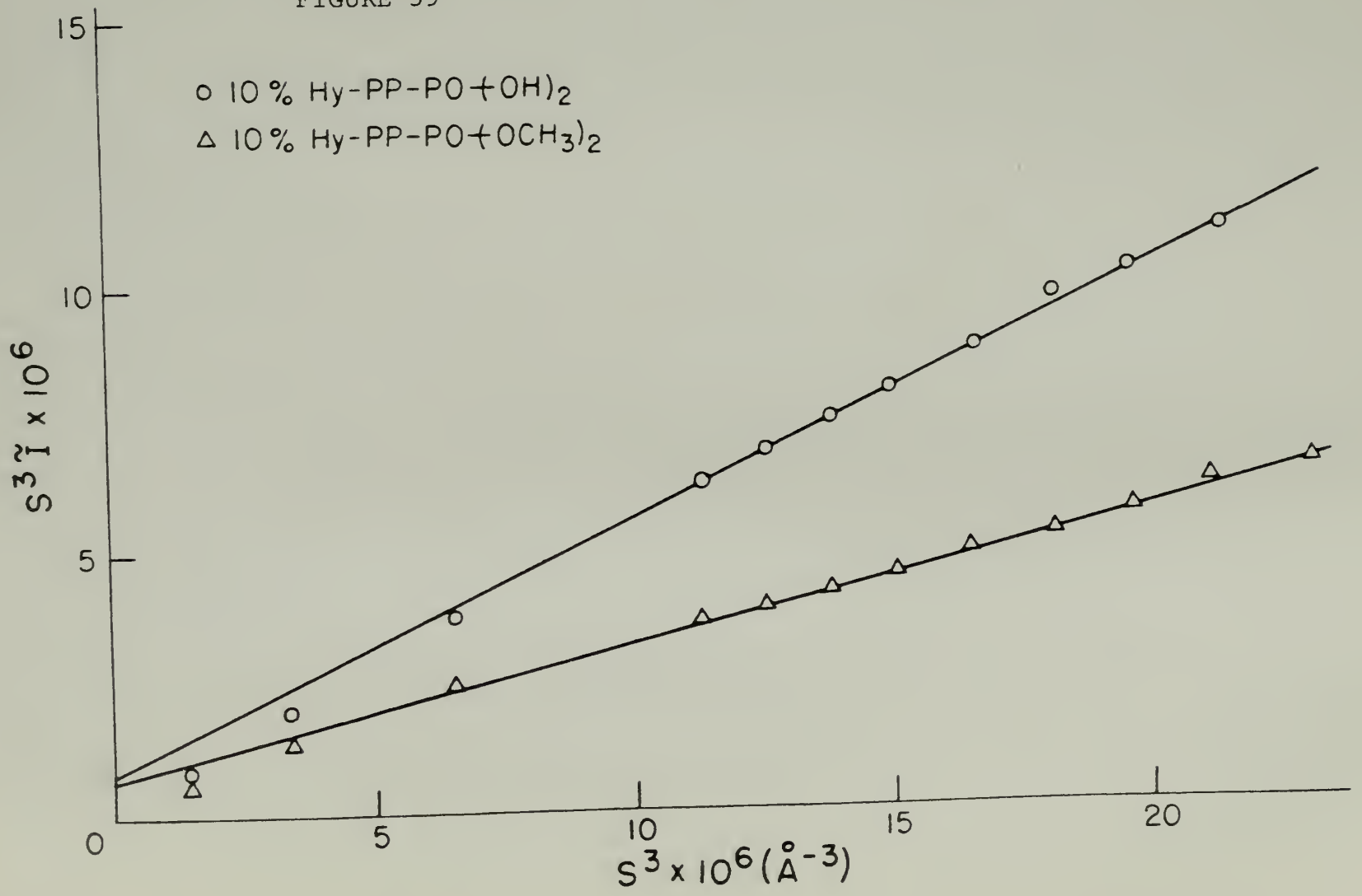
o 10 % Hy-PP-PO(OH)2
Δ 10 % Hy-PP-PO(OCH3)2
15
10
5
0
5
10
15
20
S3Ĩ x 10^6
S^3 x 10^6 (Å^-3)

FIGURE 60

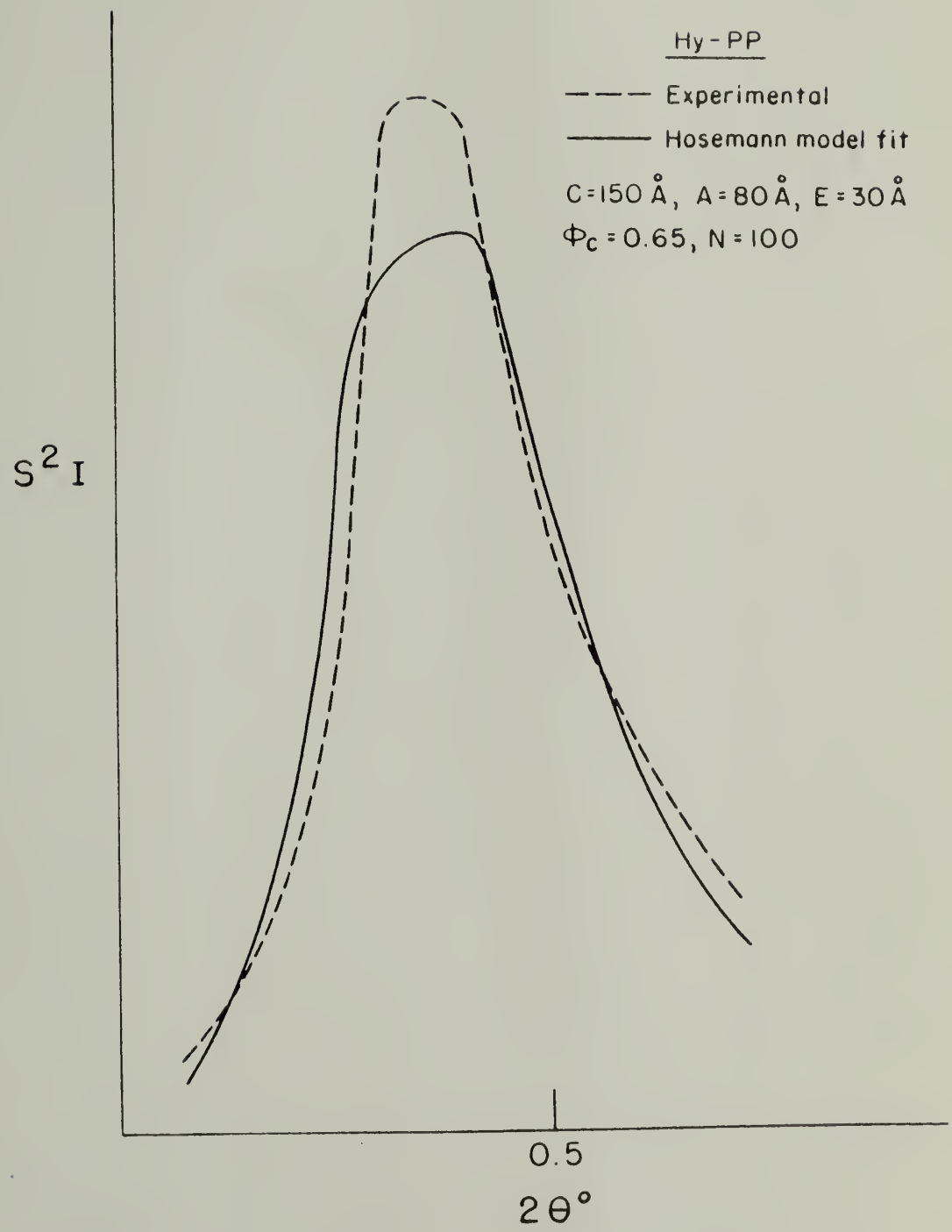
Hy - PP
Experimental
Hosemann model fit
C = 150 Å, A = 80 Å, E = 30 Å
Φ_c = 0.65, N = 100
$S^2 I$
0.5
2θ°

FIGURE 61

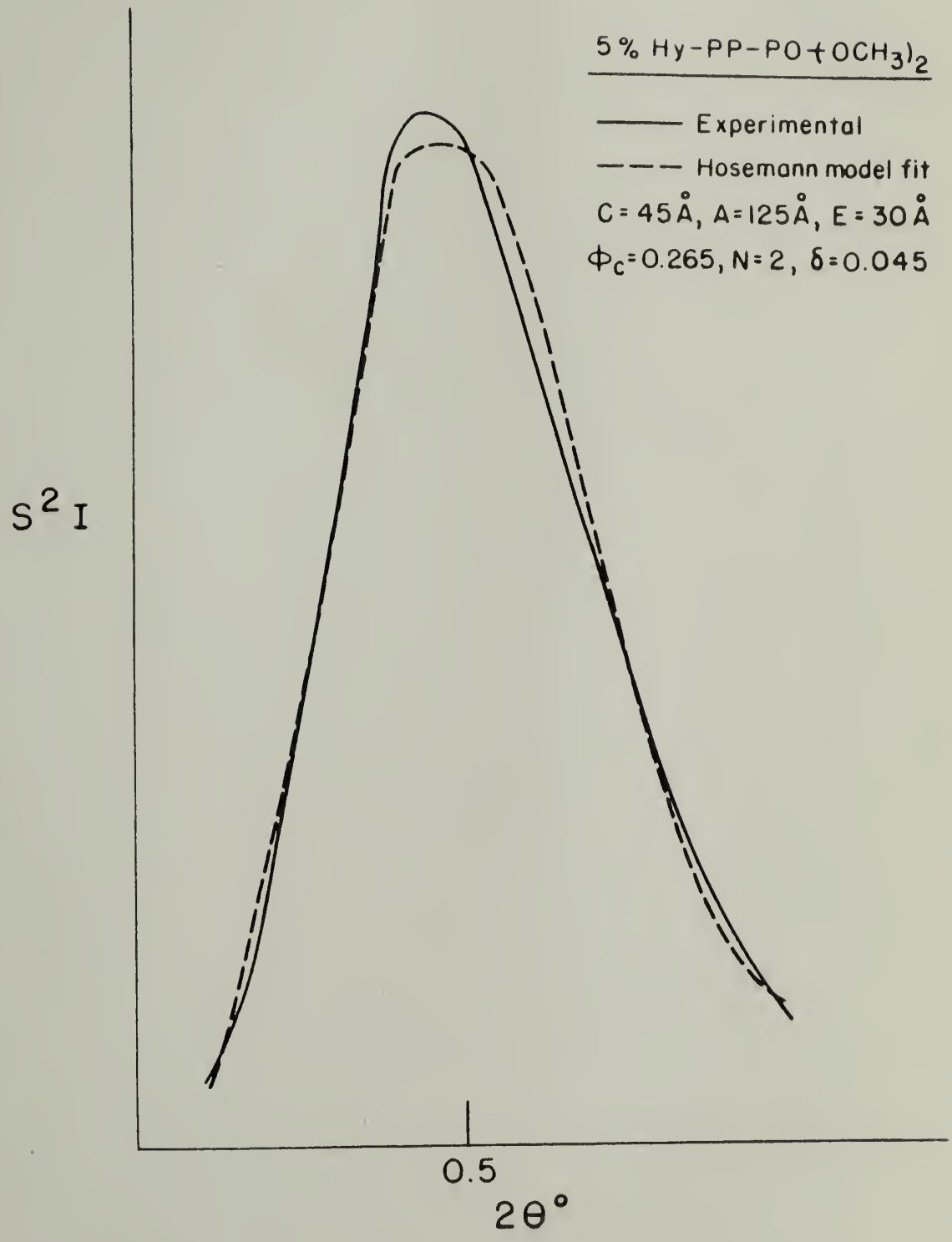
5% Hy-PP-PO(OCH3)2
Experimental
Hosemann model fit
C = 45Å, A = 125Å, E = 30Å
Φc = 0.265, N = 2, δ = 0.045
S2I
0.5
2θ°

FIGURE 62

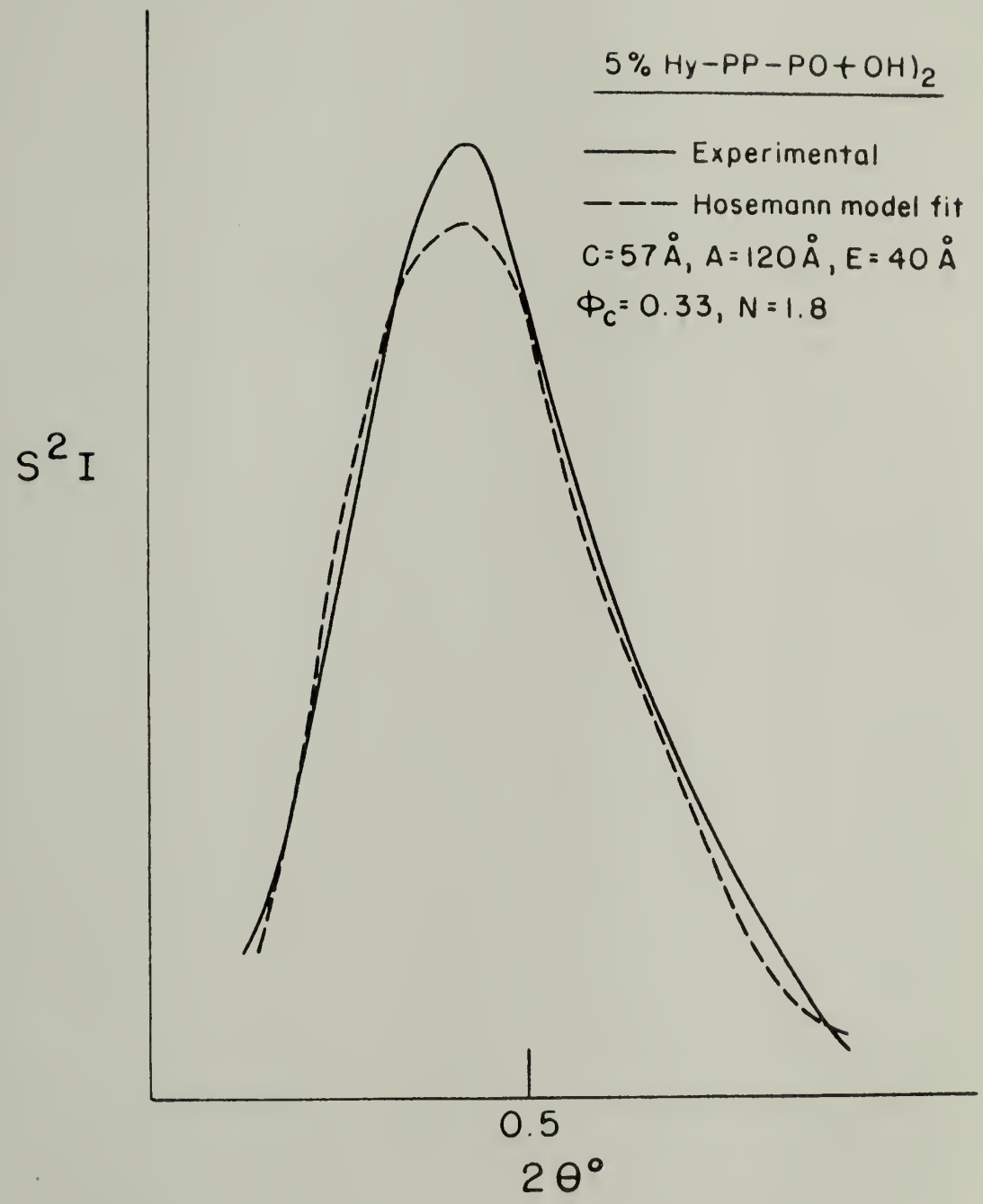
5% Hy-PP-PO(OH)2
Experimental
Hosemann model fit
C=57Å, A=120Å, E=40 Å
Φc=0.33, N=1.8
S2I
0.5
2θ°

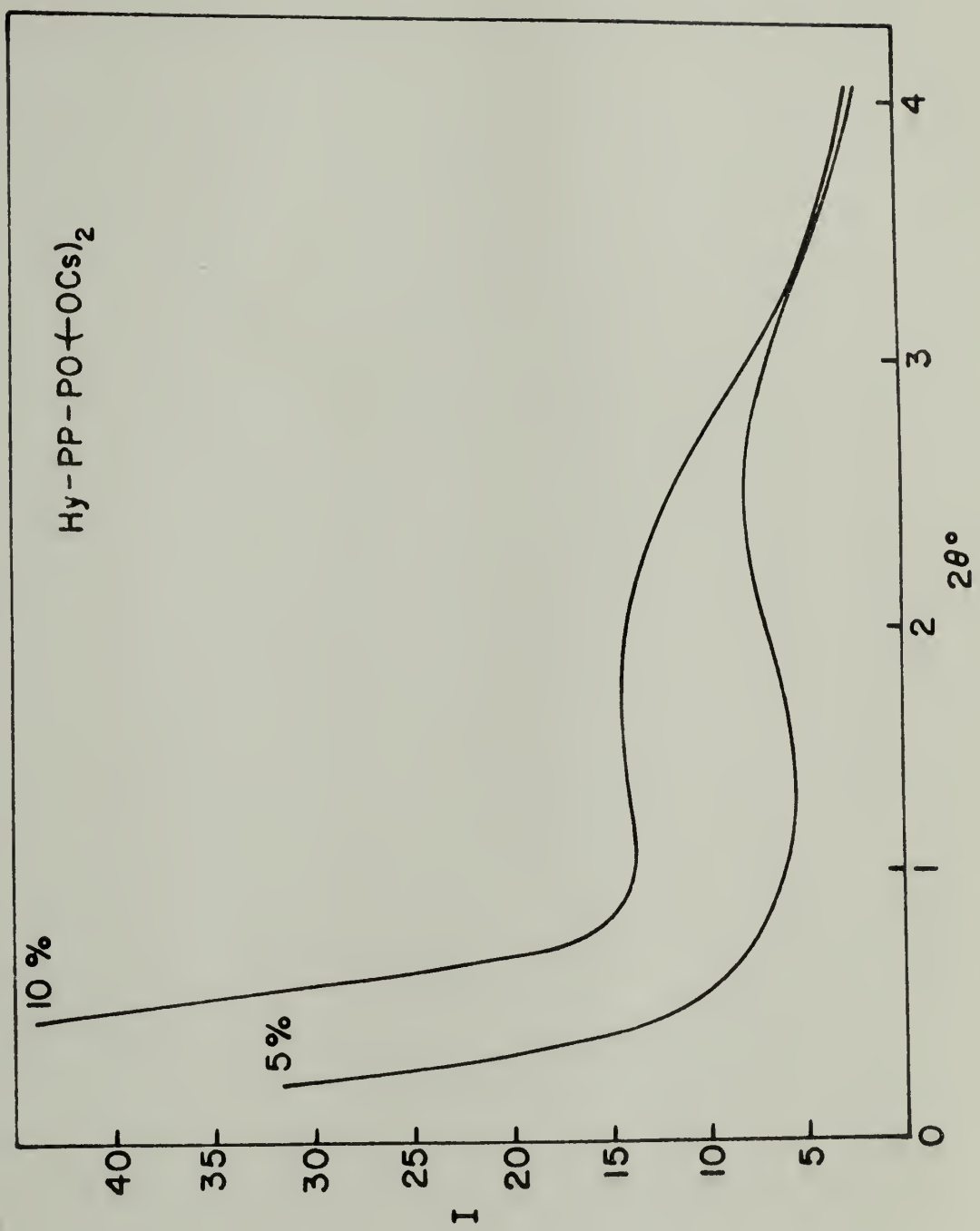

FIGURE 63

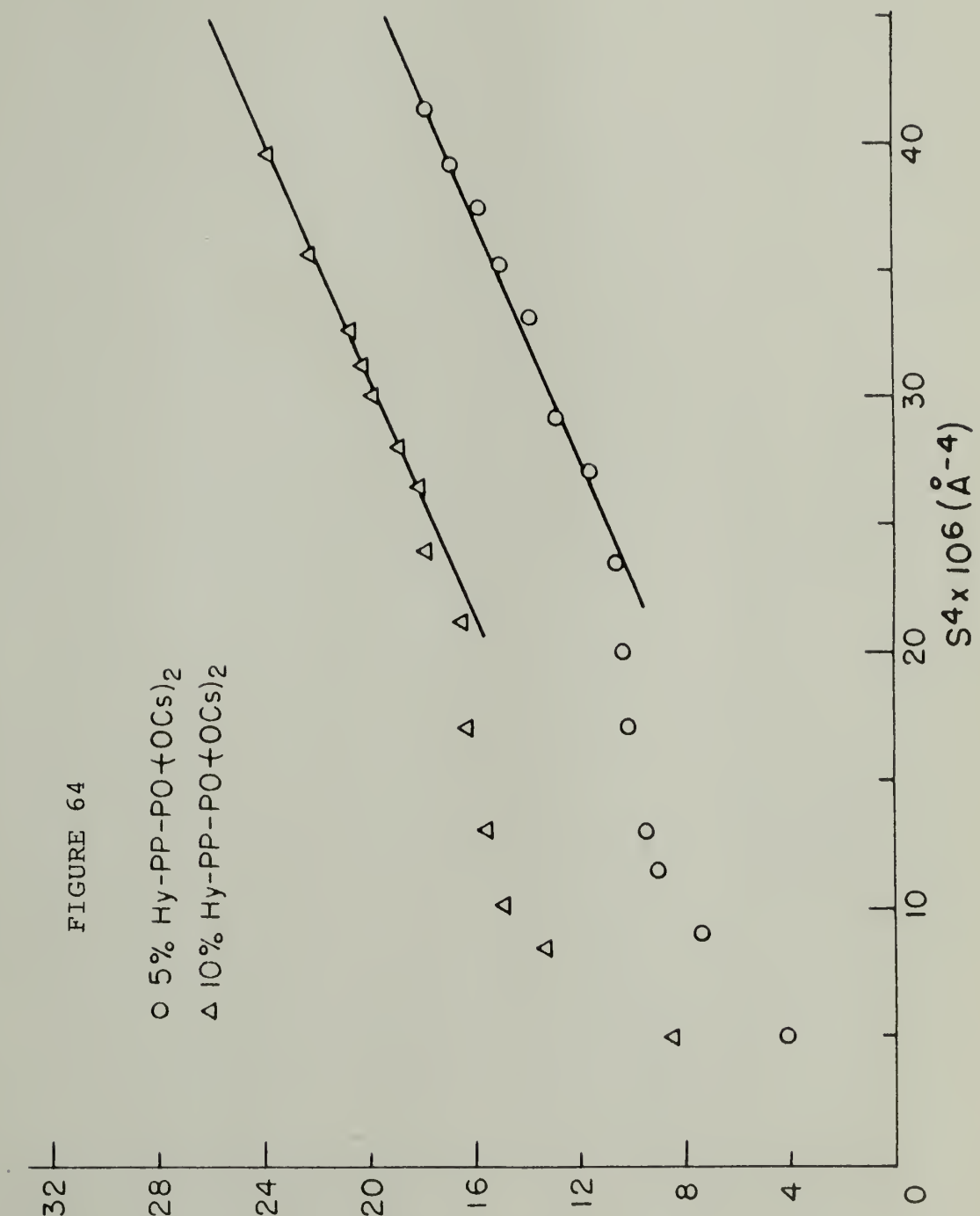
FIGURE 64
○ 5% Hy-PP-PO+OCs)2
△ 10% Hy-PP-PO+OCs)2
S4I x 10^7
S4 x 106 (Å-4)
0
4
8
12
16
20
24
28
32
10
20
30
40

FIGURE 65

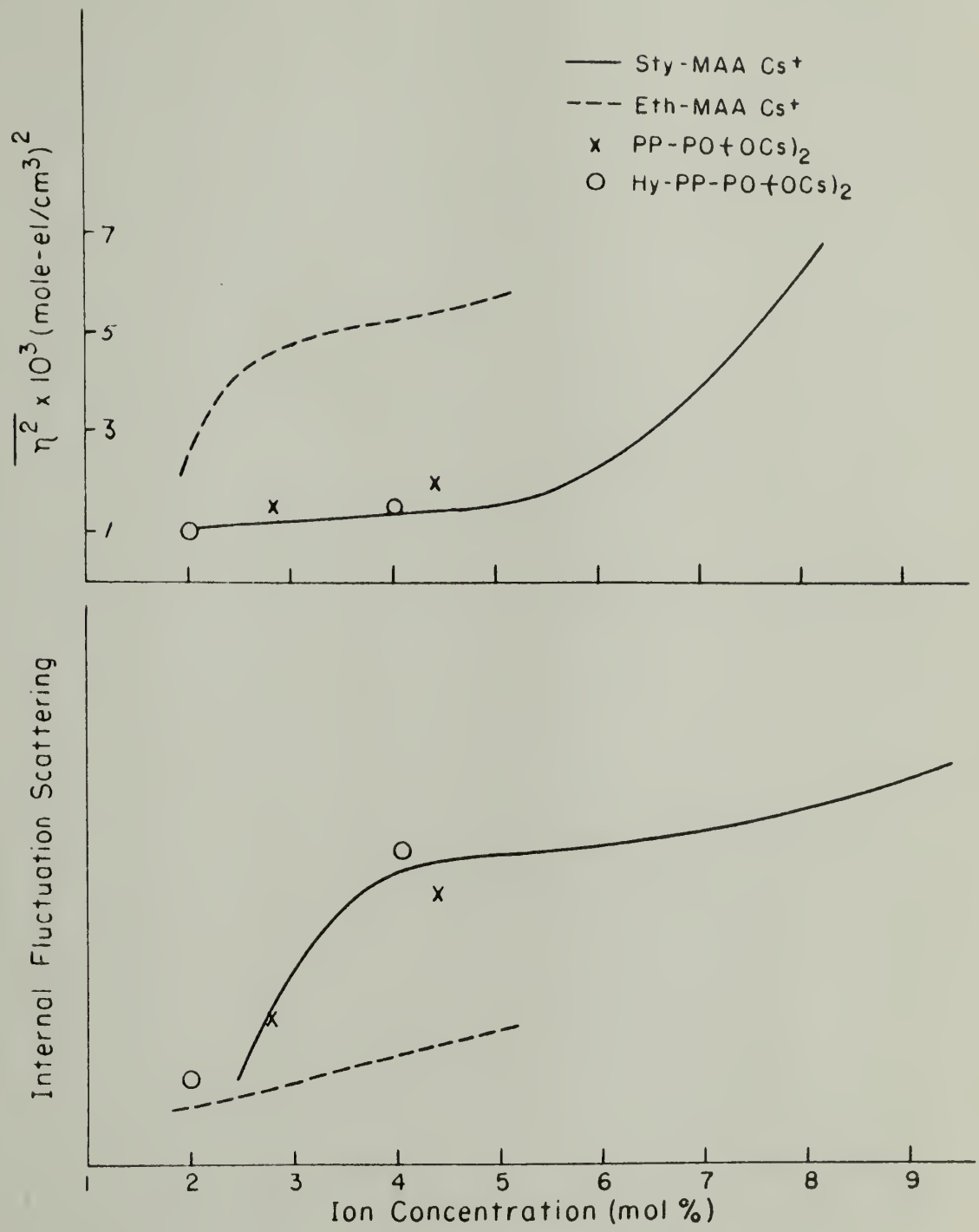
Sty-MAA Cs+
Eth-MAA Cs+
PP-PO+OCs)2
Hy-PP-PO+OCs)2
$\overline{\eta^2} \times 10^3$ (mole-el/cm^3)^2
7
5
3
1
Internal Fluctuation Scattering
1
2
3
4
5
6
7
8
9
Ion Concentration (mol %)

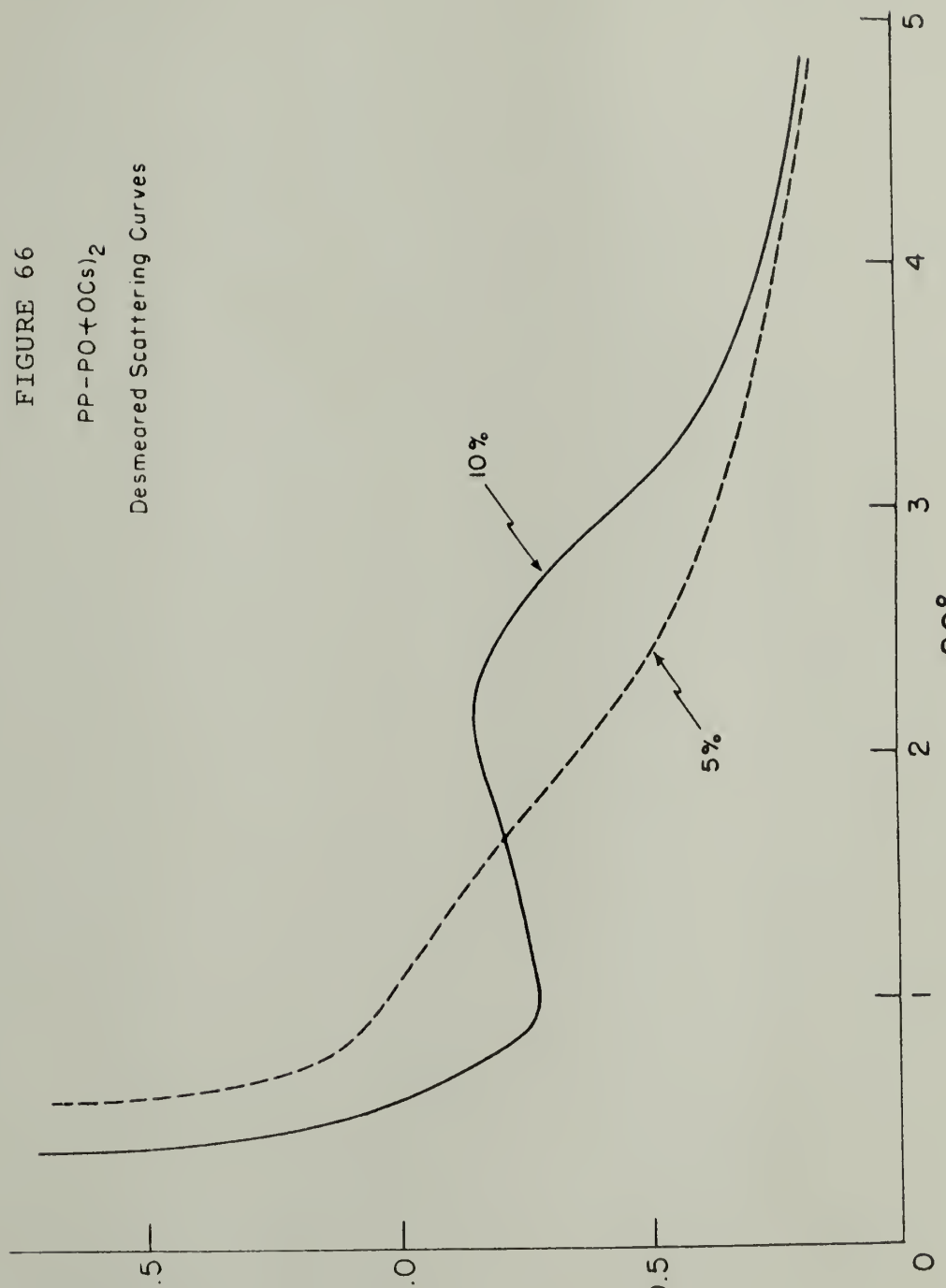

FIGURE 66

$PP-PO+OCs)_2$

Desmeared Scattering Curves

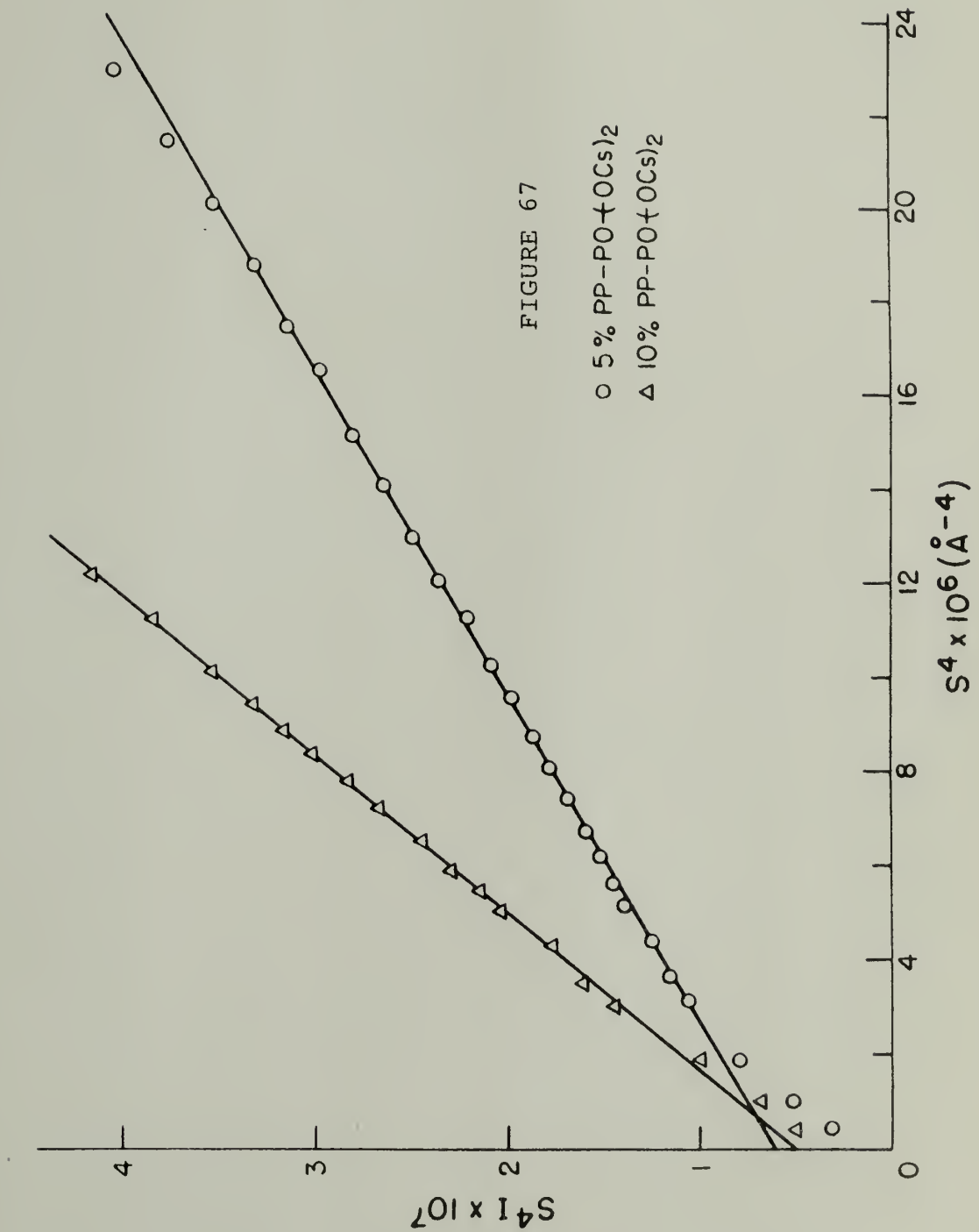
FIGURE 67
○ 5% PP-PO+OCs)2
△ 10% PP-PO+OCs)2
S4I x 10^7
S4 x 10^6 (Å-4)
0
1
2
3
4
4
8
12
16
20
24

FIGURE 68

5% Hy-PP-PO+OCs)$_2$

Desmeared Scattering Curves

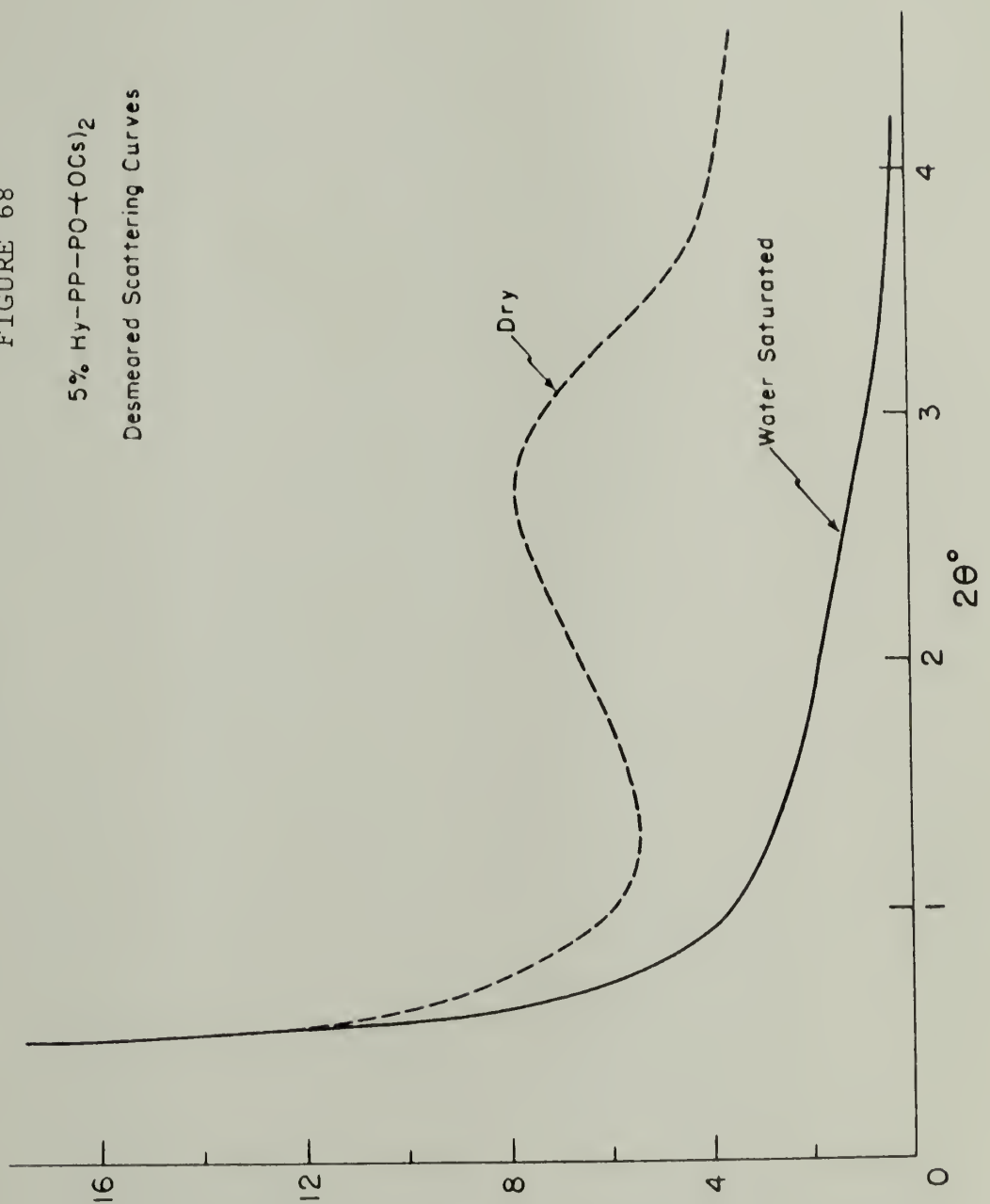

A P P E N D I X I

MASS ABSORPTION COEFFICIENT FOR CHEMICALLY HETEROGENEOUS MULTIPHASE SYSTEMS

The mass absorption coefficient for a multiphase system with N phases is given by:

$$\mu = \sum_{i=1}^{N} \mu_i \, \phi_i \, \rho_i \tag{1}$$

The absorption coefficient of a single phase i is:

$$\mu_i = \frac{\sum_{j=1}^{M} \mu_j W_{ji}}{\sum_{j=1}^{M} W_{ji}} = \sum_{j=1}^{M} \mu_j \, f_{ji} \tag{2}$$

for j phases. W denotes the weight and f the fractional weight of a given component in a phase. Combining Equations 1 and 2 gives:

$$\mu = \sum_{i=1}^{N} \sum_{j=1}^{M} \mu_j \, f_{ji} \, \phi_i \, \rho_i \tag{3}$$

The overall weight fraction of element j is given by:

$$f_j = \frac{\sum_{i=1}^{N} \sum_{j=1}^{M} f_{ji} \, \phi_i \, \rho_i}{\overline{\rho}} \tag{4}$$

Expressions 3 and 4 combine to give:

$$\mu = \sum_{j=1}^{N} f_j \, \bar{\rho} \, \mu_j = \bar{\rho} \sum_{j=1}^{N} f_j \, \mu_j \qquad (5)$$

The linear absorption coefficient is given by:

$$\mu_\ell = \sum_{j=1}^{N} f_j \, \mu_j \qquad (6)$$

Thus the relation:

$$\mu = \mu_\ell \, \bar{\rho}$$

is valid for a chemically heterogeneous multiphase system.

A P P E N D I X I I

COMPUTER PROGRAMS

```
00100 PROGRAM PARAC(INPUT,OUTPUT,TAPE14)
00110C * CALCULATES Z(S,L,A) FOR 3-L CRYSTAL
00120C * ASSUMING POINT LIKE SCATTERERS, SAME STAT.
00130C * PARAMETER IN ALL 3-D. COMPARES TO EXPT
00140 DIMENSION ZE(20),Z(20),ZL(20),TT(20)
00145 CALL GET(6HTAPE14,6HTAPE14,0,0)
00147 4 FORMAT(6X,F5.2)
00150 PRINT 11
00160 11 FORMAT(*TYPE TTMIN,TTMAX,TTLEL IN DEGR,3(F4.2,2X)*)
00170 READ 1,TTMIN,TTMAX,TTLEL
00180 1 FORMAT(3(F4.2,2X))
00190 NTT=1+(TTMAX-TTMIN)/TTLEL
00200 PRINT,NTT
00210 PRINT 21
00220 21 FORMAT(*TYPE A IN ANG. F5.2*)
00230 READ 2,A
00240 2 FORMAT(F5.2)
00245 PRINT 22
00250 22 FORMAT(*TYPE RPMIN,RPMAX,RPLEL IN ANG. 3(F5.2,2X)*)
00260 READ 312,RPMIN,RPMAX,RPLEL
00270 312 FORMAT(3(F5.2,2X))
00272 NR=(RPMAX-RPMIN)/RPLEL
00275 PRINT 24
00280 24 FORMAT(*TYPE FLATT IN ANG. F8.1*)
00290 READ 411,FLATT
00300 411 FORMAT(F8.1)
00310 PRINT 31
00320 31 FORMAT(*TYPE LMIN,LMAX,LLEL IN ANG. 3(F5.2,2X)*)
00330 READ 3,LMIN,LMAX,LLEL
00340 3 FORMAT(3(F5.2,2X))
00350 NL=1+(LMAX-LMIN)/LLEL
00360 PI=3.14159
00370 READ(14,4)(ZE(I),I=1,NTT)
00410 DO 5 I=1,NTT
00420 TOT=TOT+ZE(I)
00430 5 CONTINUE
00440 50 TZ=0
00441 IF(FLATT.NE.0) GO TO 53
00442 FLATT=0.0
00443 PTS=1.0
00444 GO TO 52
00445 53 VLATT=(4/3)*PI*(FLATT**3)
00447 PTS=VLATT/(A**3)
00450 52 DIFFB=1000000.
00452 DO 118 JJ=1,7
00454 BR=1.0+0.5*(JJ-1)
00460 DO 8 J=1,NL
00470 L=LMIN+((J-1)*LLEL)
00480 DO 7 I=1,NTT
00490 TT(I)=TTMIN+(I-1)*TTLEL
00500 TTR=TT(I)*2*PI/360.0
00510 S=2*SIN(TTR/2)/1.542
00520 P=EXP(-2*(PI*S*L)**2)
00530 Z(I)=(1-(P**2))/(1+(P**2)-2*P*COS(2*PI*S*A))
00531 DO 56 K=1,NR
00532 RP=RPMIN+(NR-1)*RPLEL
00533 VR=(RP**3)
00540 U=(S*PI*RP)
00550 F=(3/(U**3))*(SIN(U)-U*COS(U))
00552 F=(F*VR)**2
00560 56 PF=PF+F
```

```
00530 Z(I)=(1-(I**2))/(1+(I**2)-2*I*COS(2*PI*S/R))
00531 DO 56 K=1,NN
00532 RP=RPMIN+(NN-1)*INCR
00533 VR=(II**3)
00540 U=(S*PI*RP)
00550 F=(3/(U**3))*(SIN(U)-U*COS(U))
00552 F=(F*VR)**2
00565 IF(RLATT.NE.0)GO TO 66
00567 RLATT=0
00569 GO TO 660
00570 66 U=S*PI*RLATT
00580 RLATT=3/(U**3)*(SIN(U)-U*COS(U))
00590 RLATT=(RLATT*VLATT)**2
00600 660 Z(I)=Z(I)*FF*(PTS**2)*(LF**2)+RLATT
00620 TZ=TZ+Z(I)
00630 7 CONTINUE
00640 C=TOT/TZ
00650 DIFF=0
00660 DO 9 I=1,NTT
00670 Z(I)=Z(I)*C
00680 DIFF=DIFF+ABS(ZE(I)-Z(I))/ZE(I)
00690 9 CONTINUE
00700 IF(DIFF.GT.DIFFE)GO TO 92
00710 DIFFE=DIFF
00720 DB=D
00725 DRB=DR
00730 DO 10 IC=1,NTT
00740 ZB(IC)=Z(IC)
00750 10 CONTINUE
00760 92 TZ=0
00770 8 CONTINUE
00775 118 CONTINUE
00780 PRINT 101,DB,DRB
00790 101 FORMAT(*DB=*,F5.2,5X,*DFB=*,3X,F4.2)
00792 PRINT 62,RLATT,RPMIN,RPMAX,RFEL
00794 62 FORMAT(*RLATT=*,F8.1,3X,*RP*,F5.2,2X,F5.2,2X,F5.2)
00800 PRINT 20
00810 20 FORMAT(*TT*,4X*ZEXP*,6X,*ZCALC*)
00820 DO 61 I=1,NTT
00830 PRINT 30,TT(I),ZE(I),Z(I)
00840 30 FORMAT(F4.2,2X,F6.2,5X,F5.2)
00850 61 CONTINUE
00860 PRINT 40,DIFFB
00870 40 FORMAT(*REL ERROR=*,2X,F5.3)
00872 PRINT 511
00874 511 FORMAT(*NEW PARAMETERS?, Y=1 N=2*)
00875 READ,JL
00876 IF(JL.NE.1)GO TO 151
00877 PRINT 514
00878 514 FORMAT(*TYPE RLATT F5.2*)
00879 READ,RLATT
00880 PRINT 51
00890 51 FORMAT(*TYPE A*)
00945 READ,A
00946 PRINT 94
00947 94 FORMAT(*TYPE RPMIN,RPMAX,RFEEL 3(F5.2,2X)*)
00948 READ 312,RPMIN,RPMAX,RFEEL
00950 GO TO 50
00960 151 PRINT 152
00970 152 FORMAT(*END*)
00982 STOP
00990 END
READY.
```

```
RAM H109          74/74   OPT=0 TRACE                              FTN  .6+460
      PROGRAM H109 (INPUT,OUTPUT,TAPE1=INPUT,TAPE2=OUTPUT)
C     TOTAL  INTEGRAL  PROGRAM
      DIMENSION N(10,500),A(13),IW(18),N2(500),SA(100),B(300),Q(500)
      READ (1,1) NO
   14 FORMAT (20I4)
    1 FORMAT (I2)
      DO 83 NPLN=1,NO
      MGB=0
      LI=0
      READ (1,2) A
    2 FORMAT (13A6)
      WRITE (2,3) A
    3 FORMAT (1H1,13A6)
      WRITE (2,4)
    4 FORMAT (// H  OPNAME,23X,1HI,7X,6HAANTAL/42H  SERIE  AMIN  AMAX
     1NUI   ONDERGR.        I  ,/)
      DO 6 I=1,10
      DO 5 K=1,500
    5 N(I,K)=0
    6 CONTINUE
      READ (1,*) D,TM,NAX,FK,DR,RMAX,MN,KK
      READ(1,*) TB,TC,DELM,AA,FLA
    8 LI=LI+1
      READ (1,*) LAK,LAG,LAN1,LAN2,ION
      IF ((LAK+LAG).EQ.0) GO TO 13
      IF (LT.EQ.TC) FS=LAN1
      MK=LAK-LAN1
      MG=LAG-LAN1
      IF (MG.GT.MGB) MGB=MG
      DG=LAN2*0.01
      AN=LAN1+DG
      N3=MG-MK+1
      WRITE (2,10) LI,LAK,LAG,AN,ION,N3
   10 FORMAT (4X,I2,2X,2I6,F6.1,I8,6X,I4)
      READ (1,*) (N2(I),I=1,N3)
      READ(1,*) DC,YC,AC,DQ,YQ,AQ,QF,QL,SL
      DO 108 I=1,N3
      N(2,I)=N2(I)-SL
  108 CONTINUE
      IF (DC.EQ.0.0) GO TO 106
      READ(1,*) (N(3,I),I=1,N3)
      DO 101 I=1,N3
      N(4,I)=((N(3,I)-QL)*DC*YC*AC)/(DQ*YQ*AQ)
      N(5,I)=N(2,I)-N(4,I)
      IF (N(5,I).LT.0.0) N(5,I)=0.0
  101 CONTINUE
      READ (1,*) (N(8,I),I=1,10)
      IF(N(8,1).EQ.0.0) GO TO 121
      DO 120 I=1,10
  120 N(9,I)=N(8,I)
      DO 130 I=11,N3
  130 N(9,I)=N(5,I)
  121 CONTINUE
  106 DO 100 I=1,N3
      IF (N(6,1).NE. .0) GO TO 125
      N(9,I)=N(5,I)
  125 SIF=FLOAT(I*I)
```

```
H H109        74/74   OPT=1 TRACE                                FTN 4.0+466
      PC=1.0/(1.0-SIF/KK)
      IF (ICC.NE.1) GO TO 102
      SFF=FLOAT(N(2,I))
      GO TO 103
  102 SFF=FLOAT(N(9,I))
  103 SFC=SFF*PC
      N(10,I)=INT(SFC+0.5)
  100 CONTINUE
      N3=N3-1
      DO 12 I=1,N3
      K=MR+I-1
   12 N(LT,K)=N2(I)-INT(0.5+CG*(N2(I)-N2(I+1)))-ION
      GO TO 8
C  WRITING OF INTERPOLATED INTENSITIES
   13 DO 15 I=1,MGB
      WRITE (2,14) I,(N(I1,I),I1=1,10)
   14 FORMAT (5X,11I9)
      N(1,I)=N(10,I)
   15 CONTINUE
C  ITITIALISATION
      K3B=10
      TM=TM-TS
      ITM=TM
      DO 16 I=1,500
   16 N2(I)=0
      DO 17 I=1,100
   17 SA(I)=0.0
   18 READ (1,19) ICC,K1,K2,K3,IMIN,IMAX,IGR
   19 FORMAT (4I2,3I4)
      ICO=ICC+1
      GO TO (32,23,20), ICO
   20 K3B=K3
      WRITE (2,21) K2,K1,K3
   21 FORMAT (//20H AFTREKKEN   KOLOM,I3,2X,3HVAN,I4,22H  RESULTAAT N
     1AR KOLOM,I4)
      DO 22 I=1,MGB
   22 N(K3,I)=N(K1,I)-N(K2,I)
      GO TO 18
   23 K3B=K3
      WRITE (2,24) K1,K2,K3,IMIN,IMAX,IGR
   24 FORMAT (19H1INSPELEN VAN KOLOM,I3,2X,3HOP ,I3,22H  RESULTAAT NAAR
     1KOLOM,I4//8H IMIN = ,I6,8H  IMAX = ,I6,11H  IGR=NS = ,I6//5X,1HM,
     2X,2HIA,6X,2HIB,5X,3HFAB,/)
      ISA=0
      ISB=0
      DO 26 I=1,MGB
      IF (N(K1,I).LE.IMIN.OR.N(K1,I).GT.IMAX.OR.N(K2,I).LE.IMIN.OR.N(K2
     1I).GT.IMAX) GO TO 26
      ISA=ISA+N(K1,I)
      ISB=ISB+N(K2,I)
      FAB=FLOAT(N(K2,I))/FLOAT(N(K1,I))
      WRITE (2,25) I,N(K1,I),N(K2,I),FAB
   25 FORMAT (2X,3I8,F8.2)
   26 CONTINUE
      IF (ISA.EQ.0) GO TO 27
      FABG=FLOAT(ISB)/FLOAT(ISA)
      GO TO 28
```

```
RAM H109        24/7%   OPT=1 TRACE                                FTN  4.0+460

      27 FABC=0.0
      28 WRITE (2,29) FABC
      29 FORMAT (/40X,6HFAB = ,F10.4)
         DO 31 I=1,MGB
         IF (N(K2,I).LE.IGR.AND.N(K2,1).NE.0) GO TO 30
         N(K3,I)=FABC*N(K1,I)
         GO TO 31
      30 N(K3,I)=N(K2,I)
      31 CONTINUE
         GO TO 18
      32 JT=0
         IGR=0
         TSA=0.0
         DO 35 I=1,MGB
         Q(I)=0.0
         IF(N(K3B,I).NE.0)Q(I)=FLOAT(N(K3B,I))**(-2.0/3.0)
         IF (I.GE.ITM) GO TO 33
         N2(I)=I*N(K3B,I)
         IGR=IGR+N2(I)
         GO TO 35
      33 JT=JT+1
         WRITE (2,34) I,K3B,N(K3B,I)

      34 FORMAT (1X,2(5X,I4),5X,I7)
         SA(JT)=FLOAT(N(K3B,I))*FLOAT(I**3)
         TSA=TSA+SA(JT)
      35 CONTINUE
         TSA=TSA/JT
         GR4=ISA/ITM
         WRITE (2,36)
      36 FORMAT (1H1)
         DO 37 I=1,MGB,10
         I1=I+9
         WRITE (2,38) I,I1,(N(K3B,I2),I2=I,I1)
      37 CONTINUE

      38 FORMAT (5H M  , ,I4,2H -,I5,5X,10I6)
         WRITE (2,39)
      39 FORMAT (31H1PRODUCT OF M TIMES INTENSITY ,,/)
         DO 40 I=1,MGB,10
         I1=I+9
         WRITE (2,41) I,I1,(N2(I2),I2=I,I1)
      40 CONTINUE
      41 FORMAT (1X,6HM*IM ,,5H M    ,I4,2H -,I5,3X,10(2X,I7))
         WRITE (2,42)
      42 FORMAT (42H1BEREKENING A,S T.B.V. STAART V/D KROMM  .,//31H PRODUC
        1T OF I TIMES (M CUBED) .,//)
         DO 44 I=1,MGB,10
         I1=I+ITM-1
         I2=I1+9

         IF (I1.GT.MGB) GO TO 45
         I3=I+9
         WRITE (2,44) I1,I2,(SA(I4),I4=I,I3)
      43 CONTINUE
      44 FORMAT (1X,4H M ,,I4,2H -,I4,2X,10F10.0)
      45 GR=IGR-0.5*(N2(1)+N2(ITM-1))
         WRITE (2,46) TSA,GR,GR4
```

```
9         74/74   OPT=0 TRACE                                FTN 4.6+460        77/07/23.

6  FORMAT (1H1,20H AVERAGE OF ABOVE ,E14.6//20H AREA UNDER CURVE = ,E
   1 14.6,//20H PROD INTEGRAL = ,E14.6)
   QGR=(GR+GRA)/(D*TB)
   WRITE (2,47) QGR,D
7  FORMAT (//20H TOTAL  INTEGRAL  = ,E14.6,/20H SAMPLE THICKNES MM= ,F
   1 8.4)
   WRITE (2,48)
8  FORMAT (1H1,1X,24HI(M) TO THE POWER -2/3 .,//)
   DO 49 I=1,M68,10
   I1=I+9
   WRITE (2,50) I,I1,(Q(I2),I2=I,I1)
9  CONTINUE
0  FORMAT (1X,5H M  ,I4,2H -,I5,3X,10F10.5)
DESMEARING  PROGRAM
   IF (NAX.EQ.0) STOP
1  READ (1,11) MVAN,MTOT,(IW(I),I=1,18)
   IF (MVAN.EQ.0) GO TO 53
   IF (MTOT.EQ.0) MTOT=MVAN
   I1=1
   DO 52 I=MVAN,MTOT
   N(K3B,I)=IW(II)
2  II=II+1
   GO TO 51
3  MIN=0
   MAX=0
   DO 54 I=1,200
   IF (MIN.EQ.0.AND.N(K3B,I).NE.0) MIN=I
   IF (N(K3B,I).EQ.0) GO TO 54
   MAX=I
   NNN=I-MIN+1
   N(K3B,NNN)=N(K3B,I)
4  CONTINUE
   MAAN=MAX-MIN+1
   WRITE (2,3) A
   WRITE (2,55) MIN,MAX,NAX,DELM
5  FORMAT (//30H COMMENCE DESMEARING PROGRAM .,//17H SPECIFICATIONS .
   1,//17X,6HMIN = ,I5,/17X,6HMAX = ,I5,/17X,6HNAX = ,I5,/16X,6HDELM =,
   2F7.2,//24H FOURIER COEFFICIENTS . ,/)
   NAX1=NAX+1
   AMAX=MAX-MIN
   DO 57 IN=1,NAX1
   SA(IN)=0.5*N(K3B,1)
   AN=(IN-1)*3.141592/AMAX
   DO 56 IM=2,MAAN
   AM=IM-1
6  SA(IN)=SA(IN)+N(K3B,IM)*COS(AN*AM)
   SA(IN)=2.0*SA(IN)/AMAX
7  CONTINUE
   WRITE (2,58) (SA(I),I=1,NAX1)
9  FORMAT (1X,8E15.5)
   WRITE (2,59)
9  FORMAT (///)
   AM=0.5*DELM
   CAM=MIN+AM
   DO 60 I=1,500
0  Q(I)=0.0
1  REK=3.141592*AM/AMAX
```

```
FAM*H10Q                    24/7.    OPT=0 TRACE                    FTN 4.6+462
      DO 62 IN=2,NAX1
      AIN=IN-1
      ACO=COS(REK*AIN)
      ASI=SIN(REK*AIN)
      Q(201)=Q(201)-SA(IN)*ASI*AIN
      Q(202)=Q(202)-SA(IN)*ACO*AIN**2
   62 Q(203)=Q(203)+SA(IN)*ASI*AIN**2
      VV=3.141592/AMAX
      Q(201)=Q(201)*VV
      Q(202)=Q(202)*VV**2
      Q(203)=Q(203)*VV**3
      HPH=DAM+0.5*DELM
      HMH=HPH-DELM
      ML=INT(AM)+1
      DO 63 M1=1,ML
      FM=M1+MIN-1
      SP=SQRT(HPH**2-FM**2)
      SM=SQRT(HMH**2-FM**2)
      SLOG=ALOG((HPH+SP)/(HMH+SM))
      Q(M1)=Q(M1)+(Q(201)-DAM*Q(202)+0.5*DAM**2*Q(203))*SLOG+(Q(202)-DAM
     1*Q(203))*(SP-SM)+0.25*Q(203)*(HPH*SP-HMH*SM+FM**2*SLOG)
   63 CONTINUE
      AM=AM+DELM
      DAM=DAM+DELM
      IF (DAM.GT.FLOAT(MAX)) GO TO 64
      Q(201)=0.0
      Q(202)=0.0
      Q(203)=0.0
      GO TO 61
   64 MX=MIN+300
      AM=0.0
   65 Q(MX)=0.5*SA(1)
      DO 66 IN=2,NAX1
   66 Q(MX)=Q(MX)+SA(IN)*COS(3.141592*AM*FLOAT(IN-1)/AMAX)
      IAM=AM
      IF (IAM.EQ.(MAX-MIN)) GO TO 67
      AM=AM+1.0
      MX=MX+1
      GO TO 65
   67 WRITE (2,68)
   68 FORMAT (1H1,18X,7HSMEARED,7X,7HSMEARED,19X,9HDESMEARED,10X,4HLOG,/
     1 6X,9HDESMEARED,/7X,1HM,5X,2HM2,3X,9HINTENSITY,6X,7HFOURIER,5X,11HD
     2IFFERENCE,4X,9HINTENSITY,7X,9HDESMEARED,4X,9HINTENSITY,7X,9HANGSTR
     3OMS,/32X,9HINTENSITY,34X,9HINTENSITY,3X,12H*(M SQUARED)//)
      DO 69 I=1,300
   69 B(I)=0.0
      DO 71 M1=1,MAAX
      Q(M1)=-Q(M1)/3.141592
      M=M1+MIN-1
      M2=M*M
      IGIS=Q(M+300)
      IVE=FLOAT(N(K3P,M1))-Q(M+300)
      EPOS=-1.E+8
      AG=M2*Q(M1)
      T1=M
      BETA=(AA*1.542)/(FK*T1)
      RRR=ABS(Q(M1))
```

```
FH100          74/74   OPT=   TRACE                          FTN  4.6+460          7
C        IF (BRR.GT.0.0) EFOS=ALOG(BRR)
         WRITE (2,70) M,M2,M1(K3B,M1),IGIS,IVE,O(M1),EFOS,AG,BETA
      70 FORMAT (4X,I4,I7,2X,I7,8X,I7,6X,I7,6X,F8.2,6X,F10.4,6X,F10.2,6X,F7
     1.2)
C     EXPERIMENTAL CORRELATION FUNCTION PROGRAM
C     ECA = GAMMA
C     AA  = SAMPLE TO REC. DISTANCE
C     MN  = POINT FROM WHICH POROD'S LAW IS OBEYED
C     RMAX = UPPER DISTANCE LIMIT OF ECF IN A
C     DR  = DISTANCE STEP IN A
C     TSA = I*M**3
C     FK  = AA*(ANGULAR STEP IN RADIANS)
C     B(M) = DESMEARED INTENSITY DATA
      71 B(M)=C(M1)
         IF (MN.EQ.1) STOP
         WRITE (2,72)
      72 FORMAT (///,12X,2HNR,23X,1HF,28X,7H3-D ECF,22X,7H1-D ECF)
         PI=3.14159272.0
      73 READ (1,74) M,FIL
         IF (M.EQ.0) GO TO 75
         B(M)=FIL
         GO TO 73
      74 FORMAT (I5,F14.3)
      75 R=0.0
         GAM=1.0
         GAMMA=1
         SOM=0.5
         IMAX=RMAX/DR+1.0
         C=6.283185*FK/(AA*FLA)
         C4=C**4*TSA/PI2
         DO 92 I=1,IMAX
         IF (I.EQ.1) GO TO 76
         SOMA=0.0
         SOMB=0.0
         DO 76 M=1,MN
         H=C*M
         FIH=B(M)*H**2
         FIHS=COS(H*R)*FIH
         SOMA=SOMA+FIHS
      76 SOMB=SOMB+FIH
         SOMA=C*(SOMA-0.5*FIHS)
         SOMB=C*(SOMB-0.5*FIH)
         Z=H*R
         Z2=Z*Z
         IF (Z.GE.10.0) GO TO 78
         VK=-1.0
         VX=3.0
         VY=Z**3/18.0
         SI=Z-VY
         DO 77 IT=1,23
         VK=-VK
         FS=VX
         VX=VX+2.0
         VER=FS*Z2/(VX**2*(VX-1.0))
         VY=VY*VER
      77 SI=SI+VK*VY
         GO TO 79
```

```
IAM H109          24/74   OPT=  TRACE                    FTN  4.6+560
      78 SI=PI2-(COS(Z)/Z)*(1.-2./Z2+24./(Z2**2))-(SIN(Z)/Z)*(1.-11./Z-6./(Z**2
     1)+120./(7*72*72))
      79 SA1=C4*(COS(7)/H+R*SI-R*PI2)
         SB=C4/H
         GA=(SOMA+SA1)/(SOMB+SB)
         SOM=SOM+GA
         GAMMA=(SOM-0.5*GA)/(I-1)
         GAM=2.*(I-1)*GAMMA-2.0*(I-2)*GAMMAB-GAMP
      80 GAMMAB=GAMMA
         GAMP=GAM
         WRITE (2,81) I,R,GAMMA,GAM
      81 FORMAT (3X,I7,18X,F11.2,2(19X,F11.3))
      82 R=R+DR
      83 CONTINUE
         STOP
         END
```

DETAILS DIAGNOSIS OF PROBLEM

AN IF STATEMENT MAY BE MORE EFFICIENT THAN A 2 OR 3 BRANCH CO

REFERENCE MAP (R=1)

N	TYPE	ARRAY	RELOCATION			
	REAL		7102	AA	REAL	
	REAL		7231	ACO	REAL	
	REAL		7200	AIN	REAL	
	REAL		7172	AMAX	REAL	
	REAL		7124	AQ	REAL	
	REAL		22260	B	REAL	ARRAY
	REAL		7235	C	REAL	
	REAL		7067	CC	REAL	
	REAL		7117	DC	REAL	
	REAL		7073	DR	REAL	
	REAL		7150	EAR	REAL	
	REAL		7242	FIN	REAL	
	REAL		7230	FIL	REAL	
	REAL		7103	FLA	REAL	
	REAL		7111	FS	REAL	
	REAL		7236	GAM	REAL	
	REAL		7233	GAMMA	REAL	
	REAL		7100	GR	REAL	
	REAL		7241	H	REAL	
	REAL		7204	HPH	REAL	
	INTEGER		7215	IAM	INTEGER	
	INTEGER		7137	ICO	INTEGER	

CARD NR.	SEVERITY	DETAILS	DIAGNOSIS OF PROBLEM
88	I		AN IF STATEMENT MAY BE MORE EFFICIENT THAN A 2 OR 3 BRANCH COMPU

SYMBOLIC REFERENCE MAP (R=1)

ENTRY POINTS
4137 H109

VARIABLES		SR	TYPE	ARRAY	RELOCATION				
21071	A		REAL			7102	AA	REAL	
7121	AC		REAL			7201	ACO	REAL	
7223	AG	1	REAL			7200	AIN	REAL	
7175	AM		REAL			7172	AMAX	REAL	
7115	AN		REAL			7124	AO	REAL	
7202	ASI		REAL			22260	B	REAL	ARRAY
7225	BETA	1	REAL			7235	C	REAL	
7236	CG		REAL			7167	CI	REAL	
7175	DAM		REAL			7117	DC	REAL	
7101	DALM		REAL			7144	DG	REAL	
7122	DO		REAL			7073	DS	REAL	
7222	EFOS	1	REAL			7150	FAP	REAL	
7151	FAEG		REAL			7242	FIH	REAL	
7243	FIHS		REAL			7230	FIL	REAL	
7072	FK		REAL			7103	FL	REAL	
7210	FM	1	REAL			7111	FS	REAL	
7255	GA		REAL			7232	GIM	REAL	
7260	GAMB		REAL			7233	GAMMA	REAL	
7257	GAMMAB		REAL			7160	GR	REAL	
7154	GRA	1	REAL			7241	H	REAL	
7205	HMH		REAL			7204	HPH	REAL	
7065	I		INTEGER			7215	IAM	INTEGER	
7100	IC		INTEGER			7137	ICO	INTEGER	

```
      PROGRAM SAXSC(INPUT,OUTPUT,TAPE50=INPUT,TAPE51=OUTPUT,PUNCH,
     1TAPE52=PUNCH)
C     SLIT-LENGTH COLLIMATION CORRECTION FOR GAUSSIAN WEIGHTING FUNCTION
C            (REVISED MARCH, 1969)
C
C     THIS PROGRAM SAXSC IS USED FOR CORRECTING SMALL ANGLE X-RAY  SCATTERING
C     INTENSITY FROM A FINITE SLIT SYSTEM WITH A GAUSSIAN WEIGHTING  FUNCTION
C     THE USER IS REFERRED TO  (P.W.SCHMIDT,ACTA CRYST.19,938 (1965))
C     THE PROCEDURE AND INPUT DATA ARE EXPLAINED AS FOLLOWS.
C     THE ANGULAR DATA INCREMENT IS ,A, MINUTES. THE INTENSITY VALUES F(I)
C     ARE GIVEN FOR SCATTERING ANGLES FROM A THROUGH A*IMAX.  (THE FORTRAN
C     SYMBOL * WILL BE USED TO DENOTE MULTIPLICATION.  ZEROES ARE USED FOR F(I)
C     FOR INTENSITIES AT WHICH EXPERIMENTAL DATA ARE NOT AVAILABLE.)  FIVE
C     INTENSITY VALUES ARE PUT ON EACH CARD IN (5E13.7) FORMAT
C          THE PROGRAM CALCULATES CORRECTED INTENSITIES FROM J0*A MILLIRADIANS
C     THROUGH N1*A MILLIRADIANS WITH AN ANGULAR INCREMENT N2*A MILLIRADIANS.
C     CORRECTED INTENSITIES ARE COMPUTED NEXT FROM (N1 + N4)*A MILLIRADIANS
C     THROUGH N3*A MILLIRADIANS WITH AN INCREMENT N4*A, AND THEN FROM
C     (N3 + N6)*A MILLIRADIANS THROUGH N5*A MILLIRADIANS WITH AN INCREMENT N6*A
C     PROVIDED N5 DOES NOT EXCEED IMAX.  CORRECTED INTENSITIES ARE NOT CALCUL-
C     ATED FOR ANGLES EXCEEDING IMAX*A MILLIRADIANS, REGARDLESS OF THE VALUES
C     OF THE NUMBERS ON CARD 3 BELOW.  (THIS IMAX VALUE IS THE VALUE FOR THE
C     CURVE BEING CORRECTED.)
C          IN THE USE OF THIS PROGRAM, THE CARDS ARE ARRANGED AS FOLLOWS.
C               CARD 1. A
C               CARD 2.  J0 AND IMAX.  (THE VALUE OF J0 ON THIS CARD MUST EQUAL
C                    THE SMALLEST J0 VALUE USED WITH ANY OF THE SCATTERING
C                    EQUAL THE LARGEST IMAX VALUE USED FOR ANY OF THE CURVES
C                    BEING CORRECTED.)
C               CARD 3. N1, N2, N3, N4, N5, N6
C               CARD 4. J0 AND IMAX FOR THE FIRST CURVE
C               CARD 5.  THE FIRST CARD OF THE SET OF CARDS WITH THE INTENSITIE
C                    F(1)
C     THE OTHER CARDS FOR THIS CURVE THEN FOLLOW.  FOR EXAMPLE, IF THERE ARE 80
C     F(I) IN THE FIRST CURVE, IMAX = 80, AND THERE 16 CARDS IN THE SET.  FOR
C     EACH SUCCEEDING CURVE, THE SET OF F(I) CARDS IS PRECEDED BY A CARD GIVING
C     J0 AND IMAX FOR THIS CURVE.
C          AFTER THE LAST CURVE HAS BEEN CORRECTED, THE COMPUTER GIVES A STATE-
C     MENT INDICATING THAT THE END OF THE DATA HAS BEEN REACHED.
C          USUALLY IT IS MOST CONVENIENT TO HAVE THE VALUES OF N3 AND N5 BE AT
C     LEAST AS LARGE AS N1 AND N3, RESPECTIVELY, WITH N2 AND N4 BEING NO LESS
C     THATN N4 AND N6, RESPECTIVELY.  HOWEVER, THESE CONDITIONS ARE NOT NECES-
C     SARY.  FOR EXAMPLE, IF CORRECTED VALUES ARE DESIRED ONLY FOR A SINGLE
C     ANGULAR INCREMENT, THE APPROPRIATE VALUES OF N1 AND N2 CAN BE CHOSEN, AND
C      N3, N4, N5, AND N6 CAN ALL BE SET EQUAL TO ZERO, OR THESE POSITIONS CAN
C     BE LEFT BLANK ON CARD 3.
C          THE LARGEST VALUES ALLOWED FOR THE NUMBERS ON CARDS 2, 3, AND 4 ARE
C      DETERMINED BY THE DIMENSION STATEMENT AT THE BEGINNING OF THE PROGRAM.
C     (THIS STATEMENT CAN BE CHANGED WHEN NECESSARY.)  NO IMAX VALUE ON CARDS
C      2 OR 4 CAN EXCEED [illegible], AND NO INPUT CURVES CAN HAVE MORE THAN 400 DATA
C     POINTS, ACCORDING TO THE DIMENSION STATEMENT USED IN THIS PROGRAM.  WITH
C     THE NUMBER 50 USED IN THE SECOND SUBSCRIPT OF T(I,JJ) IN THE DIMENSION
C     STATEMENT, CORRECTED INTENSITIES CAN BE CALCULATED AT UP TO 50 ANGLES.
C      THE ANGLES AT WHICH CORRECTED DATA ARE OBTAINED ARE SPECIFIED BY THE
C     NUMBERS ON CARDS 2, 3, AND 4.
C          THE CONSTANTS L0, L1, AND L2 IN THE INPUT AND OUTPUT STATEMENTS MUST
C     BE DEFINED AT THE BEGINNING OF THE PROGRAM.
```

```
C     THE ANGLE  S=2*SIN(THETA)/CAN WHERE SLAM - LAMBDA IN ANGSTROMS
C
C     COMPUTATION OF LEAST SQUARES FIT TO
      DIMENSION T(200,10), F(200)
      COMMON T
      DIMENSION FA(200)
      DIMENSION JJM(4)
      DIMENSION IDENT(5)
      DOUBLE PRECISION PBELPH,SQPI,A,SJ1(220),SJ2(220),
     1 SJ3(220), B, C, D, E, DL, EE, H, DIJ, V321J,V331J,
     2 T31IJ, DEL51, DEL52, DEL53, DEL42, VV
      LO=60
      L1=61
      PI=3.14159270 D0
      A1=2.D0*180.D0
      SQPI = 1.772453851D0
      PBELH = SQPI*11.D0BD0
      SLAM = 1.5417
    1 FORMAT(F6.4,I4)
    2 FORMAT(2I4)
    3 FORMAT(6I4)
    4 FORMAT(/,4X,10HANGLE( S ),9X,10HANGLE(MIN),8X,14HCORRECTED INT.,
     19X,14HMEASURED INT.,28HLORENTZ-GEOM. CORRECT. INT.      )
    5 FORMAT(5E13.7)
    6 FORMAT(/1X,F12.6,5X,F12.6,4X,E20.8,2X,-10.6,5X,E18.6)
    7 FORMAT(5X,F10.6,E15.6,5X,F10.6,2E15.6)
      READ(L0,1)APB,IFA
      READ (L0,2) J0, IMAX
      READ (L0,3) N1, N2, N3, N4, N5, NE
      A=(2.D0*APB*PI)/A1
      N = N1
      NN = N2
      J0J = J0
      JJ = 0
C     IF IFA .GT.0 YOU WANT DATA LORENTZ CORRECTED ONLY
      IF(IFA.GT.0) GO TO 200
  100 DO 105 J = J0, N, NN
      IM = IMAX - J + 12
      JJ = JJ + 1
      DO 102 I = 6, 10
      SJ1(I) = 0.0
      SJ2(I) = 0.0
  102 SJ3(I) = 0.0
      B = J
      IM1 = IM + 1
      DO 104 I = 11, IM1
      C = I - 10
      D = C*C + 200*C*C
      E = (C-100)*(C-100)+200*B*(C-100)
      DL=DSQRT(D)
      EE= DSQRT(E)
  103 SJ1(I)=DLOG((C+B+DL)/(C+B-100+EE))
      SJ2(I)=(C+B-0.50D)*SJ1(I)-DL+EE
  104 SJ3(I)= 0.50D*((C+B)**2-100/3D0+0.50D*B**2)*SJ1(I)
     1  -0.7500*(C+B)*DL+(0.750*(C+B)+0.2500)*EE
      H = A * PBELH
```

```
   XA=0
   DO 605 I = 10, IM
   C = I - 12
   UIJ=DEXP(-(H*H)*(C*C+200*B*C))/(H*SQPI)
   V32IJ=SJ2(I-1)  -200*SJ2(I-2)  +SJ2(I-3)
   V33IJ=SJ3(I)-300*SJ3(I-1  )+300*SJ3(I-2  )-SJ3(I-3  )
   T31IJ=UIJ* (SJ1(I-1  )-SJ1(I-2  )+V32IJ+V33IJ)
   DEL51= SJ1(I+1  )-500*SJ1(I)+1000*SJ1(I-1  )-1000*SJ1(I-2  )+500*
  1 SJ1(I-3  )-SJ1(I-4  )
   DEL52 = SJ2(I+1  )- 500* SJ2(I)+1000*SJ2(I-1  )-1000*SJ2(I-2  )
  1 + 500*SJ2(I-3  )-SJ2(I-4  )
   DEL53=SJ3(I+1)-500*SJ3(I)+1000*SJ3(I-1)-1000*SJ3(I-2)
  1 +  500*SJ3(I-3)-SJ3(I-4)
   DEL42=SJ2(I)-400*SJ2(I-1)+600*SJ2(I-2)-400*SJ2(I-3)+SJ2(I-4)
   VV=-200*DEL51+DEL52*900*DEL42+700*DEL53
   T(1,JJ) = T31IJ + (5.*UIJ*VV)/126.
 5 CONTINUE
 5 CONTINUE
   IF (N - N3) 110, 111, 111
 0 N = N3
   NN = N4
   J0 = N1 + N4
   JC1 = JJ - 1
   GO TO 100
 1 IF (N - N5) 112, 200, 200
 2 N = N5
   NN = N6
   J0 = N3 + N6
   JO2 = JJ - 1
   GO TO 100
   SLIT LENGTH CORRECTION
 0 READ (L0, 2) J0, IMAX
   IF(EOF(L0)) 700,701
 1 READ(L0,1002) (IDENT(I),I=1,5)
 2 FORMAT(5A10)
   WRITE(L1,1003) (IDENT(I),I=1,5)
   WRITE(62,1003) (IDENT(I),I=1,5)
 3 FORMAT(1X,5A10)
   READ (L0,5) (F(I), I = 1, IMAX)
   SLIO IS VALUE OF CONSTANT LIQUID SCATT. VIA VONK
   SET SLIO=0.0 IF NO SUBTRACTION DESIRED, AT END OF INT. SET
   IF PUNCHED DATA FOR H1O9 IS DESIRED PUT 1 IN COL. 10 OF LAST CARD
   TR IS SAMPLE TRANSMN, SINT IS INTY VALUE OF KRATKY STANDARD MEAS.
   READ(L0,8)SLIO,NPNCH,TR,SINT,E
 8 FORMAT(F5.3,I5,F5.3,F6.3,F6.3)
   THE VALUE OF 20.0 IN CFAC IS AN ARBITRARY NORMALIZNT CONSTANT
   CFAC = (1.0/TR)*(20.0/SINT)
   S=0
   DO 600 I= 1,IMAX
   S=2*SIN((APB*I)/(2*57.296))/1.5417
   F(I)=(F(I)-SLIO)*CFAC
   DIFFUSE BNT CORRECTION
   E IS THE  TRANSITION WIDTH
   F(I)=F(I)/(1.000-(2.0*E*((FI**5)**2)/3.000))
 0 CONTINUE
   IF(IFA.GT.0) GO TO 602
   WRITE (L1,4)
```

```
      IF (JC - N1) 201, 202, 202
  201 NN = N2
      JJ = (JC - J00)/N2
      IF (N1 - IMAX) 202, 203, 203
  202 N = N1
      GO TO 220
  203 N = IMAX
      GO TO 220
      IF (JC - N3) 205, 206, 206
  205 NN = N4
      JJ = JJ1 + (JC - N1)/N4
      IF (N2 - IMAX) 206, 207, 207
  206 N = N3
      GO TO 220
  207 N = IMAX
      GO TO 220
  208 NN = N6
      JJ = JJ2 + (JC - N3)/N6
      IF (N5 - IMAX) 209, 210, 210
  209 N = N5
      GO TO 220
  210 N = IMAX
  220 DO 230 J = J0, N, NN
      IMAX1 = IMAX + 12 - J
      JJ = JJ + 1
      SUM = 0.0
      DO 225 I = 10, IMAX1
      K = J + I - 12
  225 SUM = SUM + F(K)*T(I,JJ)
      X = J
      XA = A*X
      X = XA/SLAM
      Y = XA*57.29578*60.0
      FA(J)=SUM
      AC=(FLOAT(J)*A)**2
      FA(J)=FA(J)*AC
      WRITE (61,6) X,Y,SUM,F(J),FA(J)
C     PUNCHED OUTPUT FOR H109, CORR. FUNCT. ANAL.
      IF(NPNCH.EQ.1) 235,230
  235 CONTINUE
      FA(J) = FA(J)*100000.0
      IF(FA(J).LT.0)240,245
  240 FA(J) = 0.0
  245 CONTINUE
      WRITE(62,504) FA(J)
  504 FORMAT(10F6.1)
  230 CONTINUE
      IF (N - IMAX) 251, 260, 260
  251 IF(N - N3) 252, 261,261
  252 JC = N1 + N4
      GO TO 215
  261 IF(N - N5) 262, 260, 260
  262 JC = N3 + N6
      GO TO 205
  260 WRITE(61,601)
  601 FORMAT(' BCKGD CORR. INT.',5X,'LOW-NIZ-GEOM. CORR. INT. ')
      DO 503 I=J0,N,NN
```

```
      A = (FLOAT(I)/100.0)**2
      A(I)=F(I)*A
  230 WRITE(L1,502) F(I),A(I)
  502 FORMAT(/E18.8,7X,E18.8)
  300 CONTINUE
      DO 700 I = 1,300
  235 CONTINUE
      STOP
      END
```

```
00100 [illegible]
00110 [illegible]
00120 [illegible]
00130 [illegible]
00140 PRINT 17
00150 17 FORMAT(*TTO,TTF,TTST*)
00160 READ 1,TTO,TTF,TTST
00170 NJ=(TTF-TTO)/TTST
00180 NTO=NJ+1
00190 3 FORMAT(   ,I   .  )
00200 2 FORMAT(3(F4. ))
00210 CALL SET(    14,    14,  )
00220 READ(14,3)(SCE(I),I=1,NTO)
00222 DO 123 I=1,NTO
00224 SUME=SUME+SCE(I)
00226 123 CONTINUE
00230 5 PRINT 21
00240 21 FORMAT(*RIO,RIF,RIST,LTI*)
00250 READ 1,RIO,RIF,RIST,LTI
00260 PRINT 22
00270 22 FORMAT(*RMIO,RMIF,RMIST LTMI*)
00280 1 FORMAT(4(F8,X))
00290 READ 1,RMIO,RMIF,RMIST,LTMI
00300 PRINT 23
00310 23 FORMAT(*RGO,RGF,RGST,LTG*)
00320 READ 1,RGO,RGF,RGST,LTG
00360 PRINT 92
00370 92 FORMAT(*AO,AF,AST*)
00380 READ 67,AO,AF,AST
00385 67 FORMAT(3(F5.3,X))
00392 PRINT 67,AO,AF,AST
00400 PRINT 1,RIO,RIF,RIST,LTI
00410 PRINT 1,RMIO,RMIF,RMIST,LTMI
00420 PRINT 1,RGO,RGF,RGST,LTG
00432 NA=1+(AF-AO)/AST
00450 F=0
00470 C=0
00480 PIE=3.14159
00520 RIMF=RIO+(RIF-RIO)/2
00530 RMIMF=RMIO+(RMIF-RMIO)/2
00540 RGMF=RGO+(RGF-RGO)/2
00580 II=(RIF-RIO)/RIST
00590 IM=(RMIF-RMIO)/RMIST
00600 IG=(RGF-RGO)/RGST
00610 DO 57 KA=1,NA
00620 A=AO+(KA-1)*AST
00630 DO 66 JL=1,NTO
00640 TT(JL)=(TTO+(TTST*(JL-1)))/57.296
00650 VE=4*PIE*SIN(TT(JL)/2)/1.542
00660 DO 9 I=1,II
00670 RI=RIO+(I-1)*RIST
00680 PI=EXP(-(RI-RIMF)/LTI)
00690 DO 10 J=1,IM
00700 RMI=RMIO+(J-1)*RMIST
00710 PMI=EXP(-(RMI-RMIMF)/LTMI)
00720 [illegible]
00730 DO 11 K=1,IG
00740 RG=RGO+(K-1)*RGST
00750 RM=RMI+RG
      PG=EXP(-(RG-RGMF)/LTG)
00770 [illegible]=C*(SIN(VE*RI)+A*(SIN(VE*RG)-SIN(VE*RM)))
00780 FN =3*VE*(A*(RG*COS(VE*RG)-RM*COS(VE*RM))-RI*COS(VE*RI))
00790 X=(A*((RG**3)-(RM**3))+(RI**3))
```

```
00630      A=AC+(K-1)*.1
00636      DO 66 JL=1,NPC
00640      TT(JL)=(TTC+(TTS*(JL-1)))/57.296
00650      VL=4*II*SIN(TT(JL)/2)/1.542
00660      DO 9 I=1,II
00670      RI=II(+(I-1)*IIS)
00680      PI=EXI(-(II-IIS)/2II)
00690      DO 10 J=1,IJ
00700      RRI=IJI(+(J-1)*IIS)
00710      PJI=EXI(-(RRI-IJS)/2IJ)
00720      RR=RI+RRI
00730      DO 11 K=1,IC
00740      RRR(N)=CRI(+(K-1)*ICS)
00750      RC=RR+RRR(1)
00760      PC=EXI(-(RC-IC)/2IC)
00770      PW=3*(SIN(VL*II)+A*(SIN(VL*IC)-SIN(VL*IJ)))
00780      PWW=3*VL*(A*(1.+(COS(VL*RJ)-FC*COS(VL*RC))-FI*(COS(VL*II))
00790      X=(A*((FC**3)-(FJ**3))+(II**3))
00794      FL=(VL**3)*X
00800      F=(PWW+PW)/FL
00820      C=PI*PJI*PCI
00830      SCM(JL)=SCM(JL)+(I**2)*(X**2)*C
00850      11 CONTINUE
00860      10 CONTINUE
00870      9 CONTINUE
00940      C=0
00950      66 CONTINUE
00980      SUM=0
01000      DO 100 I=1,NPC
01020      SUMM=SUMM+SCM(I)
01030      100 CONTINUE
01040      PN=SUML/SUMM
01050      DIFF=0
01060      DO 200 I=1,NPC
01070      SCM(I)=SCM(I)*PN
01080      DEL=ABS(SCE(I)-SCM(I))/SCE(I)
01090      DIFF=DEL+DIFF
01100      TT(I)=TT(I)*57.296
01110      200 CONTINUE
01120      DEV=DIFF/NPC
01130      IF(KA.EQ.1)GO TO 55
01131      56 DEEV=DEV-DEVE
01132      IF(DEEV.GE.0)GO TO 57
01160      55 DEVE=DEV
01162      AE=A
01168      DO 12 JL=1,NPC
01190      SCE(JL)=SCM(JL)
01210      12 CONTINUE
01222      57 CONTINUE
01230      PRINT 8,DEVE,AE
01240      8 FORMAT(*DEVIATION = *,F6.4,4X,*AL = *,F5.3))
01250      PRINT 34
01260      34 FORMAT(*TT*,17X,*IIXI*,19X,*IJ(I*)
01270      PRINT 7,(TT(I),SCM(I),SCE(I),I=1,NPC)
01280      7 FORMAT(1P3E20.6,2X))
01310      PRINT 556
01320      556 FORMAT(*CHANGE PARAMETERS?  Y=1, N=2*)
01330      READ,NI
01340      IF(NE.EQ.1)GO TO 5
01350      STOP
01360      END
FINISH.
```

```
[illegible] FORMAT(I4,I4,[illegible])
00110* CALCULATE Z [illegible]
00120* AT VARIOUS ELEVATION ANGLES [illegible]
00130 DIMENSION Z([illegible]),[illegible]([illegible]),[illegible]([illegible]),[illegible]([illegible])
00132 PRINT 91
00134 91 FORMAT(*TYPE [illegible])
00140 READ 92,A
00142 92 FORMAT(F5.[illegible])
00145 1 FORMAT(3(F4.[illegible],[illegible]))
00146 11 FORMAT([illegible])
00148 PRINT [illegible]
[illegible]
00160 READ 1,TTMIN,TTMAX,TTDEL
00162 PRINT 94
00164 94 FORMAT(*TYPE [illegible],F4.[illegible] [illegible](F5.2,2X) *)
00166 READ 11,AZMIN,[illegible]
[illegible]
[illegible]
00190 READ 1,ELMIN,ELMAX,ELDEL
00200 NEL=1+(ELMAX-ELMIN)/ELDEL
00210 NTT=1+(TTMAX-TTMIN)/TTDEL
00220 NAZ=1+(AZMAX-AZMIN)/AZDEL
[illegible]
00235 PI=3.142
[illegible]
[illegible] PRINT 21
[illegible] 21 FORMAT(*TYPE [illegible])
[illegible] READ 2,PI
[illegible] 2 FORMAT(F4.[illegible])
[illegible] DO [illegible] K=1,NEL
[illegible] EL(K)=ELMIN+ELDEL*(K-1)
[illegible] AM=A*EL(K)
[illegible] AI=A/(EL(K)*[illegible])
[illegible] DO 5 I=1,NAZ
[illegible] AZ(I)=AZMIN+(I-1)*AZDEL
[illegible] AZI=AZ(I)*2*PI/360.0
[illegible] DO 5 J=1,NTT
[illegible] TT(J)=TTMIN+(J-1)*TTDEL
[illegible] TTI=TT(J)*2*PI/360.0
[illegible] [illegible]=[illegible](TTI/2)/1.[illegible]
[illegible] [illegible]=PI[illegible]
[illegible] [illegible]=[illegible]
[illegible] [illegible]=[illegible](-[illegible])**-2)
[illegible] [illegible]=[illegible](-[illegible])**-2)
[illegible] [illegible]=([illegible](AZI)[illegible])+[illegible])*([illegible])**[illegible])
[illegible] [illegible]=(1-([illegible]))/(1+([illegible])-2*[illegible]*COS(2*TI+2*[illegible]))
[illegible] [illegible]=(1-([illegible]))/(1+([illegible])-2*[illegible]*COS(2*TI+2*[illegible]))
[illegible] [illegible]=[illegible]*TI*[illegible]
00472 [illegible]=(3/([illegible]**3))*([illegible]([illegible])-[illegible]*COS([illegible]))
[illegible] [illegible]=([illegible])**2
[illegible] Z(I,J)=[illegible]
[illegible] 5 CONTINUE
[illegible] PRINT 1[illegible],[illegible],11,EL(K)
[illegible] 1[illegible] FORMAT(*[illegible]=*,1[illegible],[illegible],*[illegible]=*,[illegible]4.[illegible],[illegible],*EL=*,F4.[illegible])
[illegible] PRINT [illegible],AZ(I)
[illegible] [illegible] FORMAT(*AZ=*,[illegible],1[illegible].[illegible])
[illegible] PRINT [illegible]
[illegible] [illegible] FORMAT(*TT*,[illegible] *)
[illegible] DO 3[illegible] J=1,NTT
[illegible] PRINT 3[illegible],TT(J),Z(I,J)
[illegible] 3[illegible] FORMAT([illegible],[illegible].[illegible])
```

```
      [illegible]
      [illegible]
      [illegible]
      [illegible]
      [illegible]
      DO 5 K=1,NLL
      EL(K)=[illegible]
      AA=A*EL(K)
      AL=A/(EL(K)*[illegible])
      DO 5 I=1,NAA
      AZ(I)=AZMIN+(I-1)*AZLL
      AZ1=AZ(I)*2*PI/360.
      DO 6 J=1,NTT
      TT(J)=TTMIN+(J-1)*TTLL
      TT1=TT(J)*[illegible]
      [illegible]
      LA=LL*AA
      LL=PL*AL
      PA=LN(1-2*(TT*L*LA)**-2)
      PL=LN(1-2*(TT*L*LL)**-2)
      AF=(SIN(AZ1)**2)+([illegible])*([illegible])
      ZA=(1-(1-A**2))/(1+(TA**2)-2*TA*COS(2*PI*2*AA*AF))
      ZL=(1-(1-L**2))/(1+(TL**2)-2*TL*COS(2*2*PI*2*AL*AF))
      U=2*PI*TT
      F=(3/(U**3))*(SIN(U)-U*COS(U))
      F=(F*VI)**2
      Z(I,J)=ZA*ZL*F
    6 CONTINUE
      PRINT 10,A,PL,EL(K)
   10 FORMAT(*A=*,F5.2,3X,*PL=*,F4.2,3X,*EL=*,F4.2)
      PRINT 20,AZ(I)
   20 FORMAT(*AZ=*,3X,F5.2)
      PRINT 30
   30 FORMAT(*TT*,3X,*Z*)
      DO 36 J=1,NTT
      PRINT 35,TT(J),Z(I,J)
   35 FORMAT(F4.2,6X,F10.2)
   36 CONTINUE
    5 CONTINUE
    4 CONTINUE
      STOP
      END
READY.
```

```
00110 FORMAT(I10,F10.5,F10.5,F10.5,F10.5)
00115*THIS FORMAT CARD IS USED TO READ IN THE DATA FROM
00140* TYPE A LINE WITH 9999.
00150* AT END OF DATA TYPE A LINE WITH 1111.
00170*ANGLES AND CALCULATED INTERSECTIONS ARE STORED ON TAPE
00174*FOR USE OF THE PLOTTING PROGRAM(SAMPLE).
00180 DIMENSION A(10),N(10),A(19),L(19)
00190 REAL NC
00200*CNC IS THE FIELD COUNT IN FLOATING FORMAT;E.G.,1234..
00210 30 FORMAT(I10.1)
00215 REWIND 2
00217 REWIND 8
00225 CALL GET(5HTAPE,2,5HTABLE,5,1)
00230 50 READ(2,60)(A(I),N(I),I=1,3)
00240 60 FORMAT(7X,6(I4,2X))
00250 IF(A(1).EQ.9999) GO TO 75
00260 GO TO 80
00270 75 READ 65,NC
00280 GO TO 5.
00290 5 IF(N(1).EQ.1111) GO TO 150
00300 P=2.0
00310 DO 140 I=2,3
00320 CNL=60.0*A(I)+N(I)
00330 IF(CNL)130,130,120
00340 120 A(I)=CNC/CNL
00350 GO TO 140
00360 130 A(I)=0
00370 P=P-1.0
00380 GO TO 140
00390 140 CONTINUE
00400 X=0.0
00410 DO 190 I=2,5
00420 IF(P)164,164,170
00430 164 WRITE(8,165)
00440 165 FORMAT(*NO DATA*)
00450 GO TO 50
00460 170 L(I)=A(I)/P
00473 X=X+L(I)
00480 190 CONTINUE
00482  A(4)=(A(2)+A(3))/2.0
00485 ANG=A(1)+N(1)/60.
00490 WRITE(8,210)(ANG,(A(I),I=2,4))
00500 210 FORMAT(F7.4,2X,3(2X,F10.5))
00510 GO TO 50
00515 230 REWIND 3
00516 REWIND 2
00517 CALL RETRACE(5HTAPE,6,5HTABLE,0,0)
00540 STOP
00550 END
READY.
```

```
00100 PROGRAM SIZE(INPUT,OUTPUT,TAPE13)
00110 DIMENSION SCE(20),SC(20),SCE(20)
00120 1 FORMAT(*TYPE HMIN,HMAX,HLEL,3(F7.5,X)*)
00125 2 FORMAT(3(F7.5,X))
00130 3 FORMAT(6X,F5.2)
00140 4 FORMAT(*TYPE BETA,R0,F6.4,X,F6.2*)
00150 5 FORMAT(F8.4,X,F6.2)
00160 CALL GET(6HTAPE13,6HTAPE13,6,0)
00170 PRINT 1
00180 READ 2,HMIN,HMAX,HLEL
00190 NP=1+(HMAX-HMIN)/HLEL
00192 PRINT,NP
00200 READ(13,3)(SCE(I),I=1,NP)
00210 PRINT 4
00220 20 READ 5,BETA,R0
00230 PRINT 6
00240 6 FORMAT(*TYPE RMIN,RMAX,RLEL,3(F6.2,X)*)
00250 READ 7,RMIN,RMAX,RLEL
00260 7 FORMAT(3(F6.2,X))
00265 PI=3.14159
00270 NR=1+(RMAX-RMIN)/RLEL
00280 DO 10 I=1,NP
00290 H=HMIN+I*HLEL
00293 H=2*PI*H
00300 DO 11 J=1,NR
00310 R=RMIN+J*RLEL
00320 G=1/(1+(2*(((R-R0)/BETA)**2)))
00322 IF(I.GT.1)GO TO 31
00326 31 CONTINUE
00330 Z=EXP(-((H*R)**2)/3)
00340 SC(I)=SC(I)+(R**6)*Z*G
00360 11 CONTINUE
00365 10 CONTINUE
00366 TOT=0.0
00367 TOTE=0.0
00370 DO 27 I=1,NP
00371 TOTE=TOTE+SCE(I)
00372 TOT=TOT+SC(I)
00374 27 CONTINUE
00376 FT=TOT/TOTE
00380 DO 12 I=1,NP
00390 SC(I)=SC(I)/FT
00400 12 CONTINUE
00410 DIFF=0.0
00420 DO 13 I=1,NP
00430 DIFF=DIFF+ABS(SCE(I)-SC(I))/SCE(I)
00440 13 CONTINUE
00445 DIFF=DIFF/NP
00450 PRINT 14,BETA,R0,DIFF
00460 14 FORMAT(*BETA=*,F7.4,2X,*R0 = *,F6.2,2X,*DIFF = *,2X,F8.5)
00465 DO 21 I=1,NP
00470 PRINT 15,(SCE(I),SC(I))
00480 15 FORMAT(2(F9.5,3X))
00485 21 CONTINUE
00490 PRINT 16
00500 16 FORMAT(*NEW PARAMETERS ?, Y=1*)
00505 17 FORMAT(I1)
00510 READ 17,NY
00520 IF(NY.GT.1)GO TO 50
00530 GO TO 20
00540 50 CONTINUE
00550 STOP
00560 END
```

```
00100 PROGRAM TRAP(INPUT,OUTPUT)
00102 3 FORMAT(4(F6.4,X))
00104 PRINT 5
00106 5 FORMAT(*PRINT LI,LHC,LI,LI2 4(F6.4,X)*)
00110 REAL S,LI,LHC,LI,LI2
00120 LLLL=100.0
00130 DO 10 I=1,50
00135 II=I+1
00140 LI1=LI/(II-1)
00145 LI2=LI-LI1
00150 LHC1=LI-LI1
00160 LHC2=LI2-LI2
00180 LHCA=LHC1+LHC2
00190 LLL=ALOG(LHC-LHCA)
00200 IF(LLL.GT.LLLL)GO TO 10
00210 LLLL=LLL
00220 IL=I
00230 10 CONTINUE
00240 LI1L=LI/IL
00250 LI2L=LI-LI1L
00260 LHC1L=LI-LI1L
00270 LHC2L=LI2-LI2L
00280 PRINT,LLLL,IL
00300 PRINT 15,LI1,LI2
00302 15 FORMAT(*LI1L = *,X,F6.4,2X,*LI2L =*,X,F6.4)
00304 PRINT 16,LHC1,LHC2
00306 16 FORMAT(*LHC1L = *,X,F6.4,3X,*LHC2L =*,X,F6.4)
00320 E=(LI2)/(LI1L+LI2L)
00330 PRINT 20,E
00340 20 FORMAT(*E=*,X,F7.5)
00350 STOP
```

```
00100 PROGRAM SHELLL(INPUT,OUTPUT)
00110 DIMENSION SUM(100),TT(100)
00120 67 FORMAT(3(F4.2,X))
00130 4 FORMAT(F5.3)
00140 6 FORMAT(3(F7.5))
00150 7 FORMAT(I3)
00160 PRINT 24
00170 24 FORMAT(*TTO,TTF,TTST FF*)
00180 READ,TTO,TTF,TTST
00190 PN=(TTF-TTO)/TTST
00200 NPO=PN+1
00210 3 FORMAT(6X,F8.0)
00220 2 FORMAT(3(F4.2))
00230 5 PRINT 21
00240 21 FORMAT(*RI  F2*))
00250 READ 1,RI
00260 PRINT 22
00270 22 FORMAT(*RM F2*))
00280 1 FORMAT(F2)
00290 READ 1,RM
00300 PRINT 23
00310 23 FORMAT(*RO F2*))
00320 READ 1,RO
00330 PRINT 44
00340 44 FORMAT(*L F5.3*)
00350 READ 4,L
00360 PRINT 91
00370 91 FORMAT(*AIO,AIF,AIST 3(F4.2,X)*)
00380 READ 67,AIO,AIF,AIST
00390 PRINT 92
00400 92 FORMAT(*AO,AF,AST 3(F4.2,X)*)
00410 READ 67,AO,AF,AST
00420 PRINT 8
00430 8 FORMAT(*NFACT I3*)
00440 READ 7,NFACT
00450 93 FORMAT(*ELO,ELF,ELST 3(F4.2,X)*)
00460 94 FORMAT(3(F5.2,2X))
00470 NEL=1+(AF-AO)/AST
00480 PRINT 95
00490 95 FORMAT(*AZO,AZF,AZST 3(F5.2,2X)*)
00500 READ 94,AZO,AZF,AZST
00510 NAZ=1+(AZF-AZO)/AZST
00520 PRINT 67,AO,AF,AST
00530 PRINT 1,RI
00540 PRINT 1,RM
00550 PRINT 1,RO
00552 V10=RI**3
00554 V20=RM**3
00556 V30=RO**3
00558 V0=V30-V20+V10
00559 LF0=(V10+L*(V30-V20))/V0
00560 F=0
00570 PI=3.14159
00580 DO 58 KL=1,NEL
00590 AI=AIO+(KL-1)*AIST
00600 A=AO+(KL-1)*AST
00610 RIA=AI*RI
00612 RMA=A*RM
00614 ROA=RO+RM*(A-1)
00615 V1=RIA*(RI**2)
00616 V2=RMA*(RM**2)
00617 V3=ROA*(RO**2)
```

```
00480 PRINT 95
00490 95 FORMAT(*AZC,AZF,AZST 3(F5.2,2X)*)
00500 REAL 94,AZC,AZF,AZST
00510 NAZ=1+(AZF-AZC)/AZST
00520 PRINT 67,AC,AF,AST
00530 PRINT 1,RI
00540 PRINT 1,RM
00550 PRINT 1,RC
00552 V10=PI**3
00554 V20=RM**3
00556 V30=RC**3
00558 V0=V30-V20+V10
00559 LF0=(V10+L*(V30-V20))/V0
00560 F=0
00570 PI=3.14159
00580 DO 58 KL=1,NEL
00590 AI=AIC+(KL-1)*AIST
00600 A=AC+(KL-1)*AST
00610 RIA=AI*RI
00612 RMA=A*RM
00614 ROA=RC+RM*(A-1)
00615 V1=RIA*(RI**2)
00616 V2=RMA*(RM**2)
00617 V3=ROA*(RC**2)
00620 LS=L*((RC**3)-(RM**3))/((1.0A)*(RC**2)-RMA*(RM**2))
00622 V=V1-V2+V3
00625 LSS=LS*(RIA/RI)
00630 PRINT,LSS,RIA,RMA,1.0A
00650 DO 57 KAZ=1,NAZ
00660 AZ=AZC+(KAZ-1)*AZST
00670 DO 66 JL=1,NPO
00680 TT(JL)=(TTO+(TTS1*(JL-1)))/57.296
00690 FS=(COS(TT(JL)/2)*COS(AZ))**2
00700 GI=(1-FS)*((RI/RIA)**2)
00710 GM=(1-FS)*((RM/RMA)**2)
00720 GC=(1-FS)*((RC/ROA)**2)
00730 FF=(4*PI*SIN(TT(JL)/2))/1.542
00735 FFI=FF*RIA*((GI+FS)**0.5)
00740 FFM=FF*(RMA)*((GM+FS)**0.5)
00750 FFO=FF*(ROA)*((GC+FS)**0.5)
00760 FN=3*(SIN(FFI)+LSS*(SIN(FFO)-SIN(FFM)))
00770 FNN=3*(LSS*(FFM*COS(FFM)-FFO*COS(FFO))-FFI*COS(FFI))
00780 FL=(FFI+FFM+FFO)**3
00790 F=(FN+FNN)/FL
00800 SCM(JL)=F**2
00810 66 CONTINUE
00820 IF(KL.NE.1)GO TO 88
00830 IF(KAZ.NE.1)GO TO 88
00840 SUMM=0.0
00850 DO 101 I=1,NPO
00860 SUMM=SUMM+SCM(I)
00870 101 CONTINUE
00880 88 DO 102 I=1,NPO
00890 SCM(I)=SCM(I)*(NFACT/SUMM)*(V0/V)
00900 102 CONTINUE
00910 PRINT 100,A,AI,AZ
00920 100 FORMAT(*A=*,3X,F4.2,3X,*AI=*,3X,F4.2,3X,*AZ=*,3X,F4.1)
00930 PRINT 110,(TT(I),SCM(I),I=1,NPO)
00940 110 FORMAT(F8.6,2X,F15.6)
00950 57 CONTINUE
00960 58 CONTINUE
00970 STOP
00980 END
READY.
```

```
      [illegible] 11)
      [illegible]
     +), [illegible]
      L1=[illegible]
      L=[illegible]
      READ( , )N
      N1=N-L1
      N=N-L
      READ(5,2)(X(I),Y(I),I=1,N)
    2 FORMAT(F7.4,2X,F10.5)
      DO 10 I=1,N
      Y1(I)=Y(I)
      LL=I+L
      IF(LL.LE.N)Z(I)=ALOG(Y(LL))
   10 CONTINUE
      DO 20 [illegible]=1,[illegible]
      CALL [illegible](Y2, [illegible])
      CALL [illegible]
   20 CONTINUE
      DO 30 I=1,N
      LL1=I+L1-L
      IF(LL1.LE.N) [illegible](I)=[illegible](LL1)
   30 CONTINUE
      CALL [illegible]
      CALL [illegible]( ,1, 1, 1.)
      DO 40 I=1,N
      LL1=I+L1-L
      IF(LL1.[illegible].N)Y2(LL1)=Z1(I)
      Y2(I)=EXP(Y2(I))
      IL=I+L
      IF(IL.LE.N)Y1(IL)=Y2(I)
   40 CONTINUE
      DO 50 J=1,[illegible]
         CALL [illegible](Y1, [illegible])
      CALL [illegible](Y1, [illegible])
   50 CONTINUE
      WRITE(11,98)
   98 FORMAT(1H0)
      WRITE(11,99)(X(I),Y(I),Y1(I),I=1,N)
   99 FORMAT(3F11.6)
      END
```

```
00100 PROGRAM ...
00110 DIMENSION F(20),FF(100),FFF(100),POR(300)
00120 1 FORMAT(3(F6.2,X))
00130 3 FORMAT(3(F4.2,2X))
00140 34 FORMAT(F7.4)
00150 4 FORMAT(3(F5.1,X))
00160 PRINT 5
00170 5 FORMAT(*TYPE TTO,TTF,TTST,3(F4.2,2X)*)
00180 READ 3,TTO,TTF,TTST
00190 PRINT 6
00200 6 FORMAT(*TYPE G1,G2,W 3(F5.1,X)*)
00210 READ 4,G1,G2,W
00220 PRINT 4,G1,G2,W
00230 PRINT 35
00240 35 FORMAT(*TYPE A,F7.4*)
00250 READ 34,A
00260 PI=3.14159
00270 SQPI=1.7724
00280 NP=1+(TTF-TTO)/TTST
00290 PRINT 7
00300 7 FORMAT(*TYPE AZO,AZF,AZST 3(F7.3,X)*)
00310 READ 8,AZO,AZF,AZST
00320 8 FORMAT(3(F7.3,X))
00330 PRINT 9
00340 9 FORMAT(*TYPE AORO,AORF,AORST 3(F6.2,X)*)
00350 READ 1,AORO,AORF,AORST
00360 NAZ=1+(AZF-AZO)/AZST
00370 NAOR=1+(AORF-AORO)/AORST
00380 PRINT,NAOR
00390 AORSTR=AORST*(2.0*PI)/360.0
00400 AORORR=AORO*(2.0*PI)/360.0
00410 AORFR=AORF*(2.0*PI)/360.0
00420 PRINT 10
00430 10 FORMAT(*TYPE FACT,F5.2*)
00440 READ 15,FACT
00450 15 FORMAT(F5.2)
00480 AZL1=1.5708-ATAN((G1+G2)/W)
00483 PRINT,AZL1
00490 TOF=0.0
00500 SP=0.0
00510 PRINT 20
00520 20 FORMAT(*TYPE BOR,F6.3*)
00530 READ 25,BOR
00540 25 FORMAT(F6.3)
00550 PRINT 21
00560 21 FORMAT(*TYPE CHI*)
00570 READ 22,CHI
00580 22 FORMAT(F6.4)
00590 PRINT,BOR,CHI
00600 DO 90 K=1,NAOR
00610 AOR=(AORO+(K-1)*AORST)*(2.0*PI)/360.0
00620 POR(K)=1/(1+(2*(((AOR-CHI)/BOR)**2)))
00630 SP=SP+POR(K)
00640 90 CONTINUE
00650 DO 91 K=1,NAOR
00660 AOR=(AORO+(K-1)*AORST)*(2.0*PI)/360.0
00670 POR(K)=POR(K)/SP
00680 ANG=(COS(AOR-1.5708))**2
00690 TOF=TOF+POR(K)*ANG
00700 91 CONTINUE
00710 TOF=((3*TOF)-1)/2.0
00720 DO 120 I=1,NAZ
00730 AZ=(AZO+(I-1)*AZST)*(2.0*PI)/360.0
00740 PORS=0.0
00750 FR=0.0
00760 DO 95 J=1,NP
                    ...TTST)*(2.0*PI)/360.0
```

```
00620 POR(K)=1/(1+(2*(((ACR-CRI)/BCR)**2)))
00630 SP=SP+POR(K)
00640 90 CONTINUE
00650 DO 91 K=1,NACR                                                    275
00660 AOR=(ACRO+(K-1)*ACRST)*(2.0*PI)/360.0
00670 POR(K)=POR(K)/SP
00680 ANG=(COS(AOR-1.5708))**2
00690 TOF=TOF+POR(K)*ANG
00700 91 CONTINUE
00710 TOF=((3*TOF)-1)/2.0
00720 DO 120 I=1,NAZ
00730 AZ=(AZO+(I-1)*AZST)*(2.0*PI)/360.0
00740 PORS=0.0
00750 FR=0.0
00760 DO 95 J=1,NP
00770 TTR=(TTO+(J-1)*TTST)*(2.0*PI)/360.0
00780 S=2*SIN(TTR/2)/1.542
00790 PORS=0.0
00800 FR=0.0
00810 DO 87 IN=1,NACR
00820 AZD=(IN-1)*ACRSTR
00830 AORL=AZ+AZD
00840 IF(AORL.LT.1.57)GO TO 505
00850 K=1+(PI-AORL)/AORSTR
00860 GO TO 506
00870 505 K=1+(AORL/ACRSTR)
00880 506 PAZD=POR(K)
00890 B1=S*COS(AZD)
00900 B2=S*SIN(AZD)
00910 IF(B1.EQ.0)GO TO 89
00920 IF(B2.EQ.0)GO TO 89
00930 B1P=PI*B1
00950 IF(AZD.LE.AZD1)GO TO 882
00960 F=(SIN(B1P*G1)/B1P)*(SIN(PI*B2*W)/(PI*B2))
00970 F=F**2
00980 GO TO 915
01050 882 F1=SIN(B1P*G1)+A*(SIN(B1P*(3*G1+2*G2))-SIN(B1P*(G1+2*G2)))
01060 F1=F1/B1P
01070 F2=(SIN(PI*B2*W))/(PI*B2)
01080 F=(F1*F2)**2
01090 915 CONTINUE
01100 FF(IN)=F*PAZD
01110 PORS=PORS+PAZD
01120 IF(IN.EQ.1)GO TO 87
01130 D=ABS(FF(IN)-FF(IN-1))*(AORSTR/2.0)
01140 IF(FF(IN).GE.FF(IN-1))GO TO 88
01150 FR=FR+(FF(IN)*ACRSTR+D)
01160 GO TO 87
01170 88 FR=FR+(FF(IN-1)*AORSTR+D)
01180 89 CONTINUE
01190 87 CONTINUE
01200 FFF(J)=FR/PORS
01210 95 CONTINUE
01220 AZ=AZ*360.0/(2.0*PI)
01230 PRINT 96,AZ
01240 96 FORMAT(*AZ=*,F6.2)
01250 FN=FACT/1027.84
01260 111 FORMAT(*A =  *,F7.4)
01270 PRINT 99
01280 99 FORMAT(*TT    I*)
01290 DO 100 J=1,NP
01300 FFF(J)=FFF(J)*FN
01310 TT=TTO+(J-1)*TTST
01320 PRINT 103,TT,FFF(J)
01330 103 FORMAT(2(F10.5,5X))
01340 100 CONTINUE
```

```
00850 K=1+(PI-AORL)/AORSTR
00860 GO TO 506
00870 505 K=1+(ACRL/AORSTR)
00880 506 PAZL=POR(K)                                                    276
00890 B1=S*COS(AZL)
00900 B2=S*SIN(AZL)
00910 IF(B1.EQ.0)GO TO 89
00920 IF(B2.EQ.0)GO TO 89
00930 BIP=PI*B1
00950 IF(AZL.LE.AZD1)GO TO 882
00960 F=(SIN(BIP*G1)/BIP)*(SIN(PI*B2*W)/(PI*B2))
00970 F=F**2
00980 GO TO 915
01050 882 F1=SIN(BIP*G1)+A*(SIN(BIP*(3*G1+2*G2))-SIN(BIP*(G1+2*G2)))
01060 F1=F1/BIP
01070 F2=(SIN(PI*B2*W))/(PI*B2)
01080 F=(F1*F2)**2
01090 915 CONTINUE
01100 FF(IN)=F*PAZL
01110 PORS=PORS+PAZL
01120 IF(IN.EQ.1)GO TO 87
01130 D=ABS(FF(IN)-FF(IN-1))*(AORSTR/2.0)
01140 IF(FF(IN).GE.FF(IN-1))GO TO 88
01150 FR=FR+(FF(IN)*AORSTR+D)
01160 GO TO 87
01170 88 FR=FR+(FF(IN-1)*AORSTR+D)
01180 89 CONTINUE
01190 87 CONTINUE
01200 FFF(J)=FR/PORS
01210 95 CONTINUE
01220 AZ=AZ*360.0/(2.0*PI)
01230 PRINT 96,AZ
01240 96 FORMAT(*AZ=*,F6.2)
01250 FN=FACT/1027.84
01260 111 FORMAT(*A = *,F7.4)
01270 PRINT 99
01280 99 FORMAT(*TT    I*)
01290 DO 100 J=1,NP
01300 FFF(J)=FFF(J)*FN
01310 TT=TTO+(J-1)*TTST
01320 PRINT 103,TT,FFF(J)
01330 103 FORMAT(2(F10.5,5X))
01340 100 CONTINUE
01350 PRINT 221,TOF
01360 221 FORMAT(*OR. FUNCT. = *,F12.8)
01365 GO TO 222
01370 PRINT 102
01380 102 FORMAT(*ORIENTATION DISTR.*)
01390 DO 105 K=1,NAOR
01400 AOR=AORO+(K-1)*AORST
01410 PRINT 106,AOR,POR(K)
01420 106 FORMAT(F6.2,2X,F14.9)
01430 105 CONTINUE
01440 222 CONTINUE
01450 120 CONTINUE
01460 STOP
01470 END
```

```
00100 PROGRAM MICELLE(INPUT,OUTPUT,TAPE14)
00110 DIMENSION F(20),FF(100),FFF(100),FOR(100),ZE(20),ZE(20)
00120 CALL GET(6HTAPE14,6HTAPE14,0,0)
00130 33 FORMAT(6X,F5.2)
00132 34 FORMAT(F7.4)
00134 41 FORMAT(2(F5.1,X),F6.3))
00140 1 FORMAT(3(F6.2,X))
00150 3 FORMAT(3(F4.2,2X))
00160 4 FORMAT(3(F5.1,X))
00170 PRINT 5
00180 5 FORMAT(*TYPE TTO,TTF,TTST,3(F4.2,2X)*)
00190 READ 3,TTO,TTF,TTST
00192 PRINT 11
00194 11 FORMAT(*TYPE NO. OF LAYERS I2*)
00196 READ 12,NLY
00197 12 FORMAT(I2)
00200 PRINT 6
00210 6 FORMAT(*TYPE GMM1,GM1,GL1 3(F5.1,X)*)
00220 READ 4,GMM1,GM1,GL1
00230 PRINT 4,GMM1,GM1,GL1
00240 PRINT 17
00250 17 FORMAT(*TYPE GMM2,GM2,GL2*)
00260 READ 4,GMM2,GM2,GL2
00262 PRINT 4,GMM2,GM2,GL2
00270 PI=3.14159
00272 DIFFB=50.0
00275 C=0.0
00280 PRINT 18
00290 18 FORMAT(*TYPE WMIN,WMAX,WDEL*)
00300 READ 4,WMIN,WMAX,WDEL
00305 PRINT 4,WMIN,WMAX,WDEL
00306 PRINT 35
00307 35 FORMAT(*TYPE A,F7.4*)
00308 READ 34,A
00310 NG1=1+(GM1-GMM1)/GL1
00320 NG2=1+(GM2-GMM2)/GL2
00330 NW=1+(WMAX-WMIN)/WDEL
00335 PRINT,NG1,NG2,NW
00340 SQPI=1.7724
00350 NP=1+(TTF-TTO)/TTST
00360 8 FORMAT(3(F5.1,X))
00370 READ(14,33)(ZE(I),I=1,NP)
00380 DO 14 J=1,NP
00390 FACT=FACT+ZE(J)
00400 14 CONTINUE
00410 PRINT,FACT
00420 PRINT 9
00430 9 FORMAT(*TYPE AORO,AORF,AORST 3(F6.2,X)*)
00440 READ 1,AORO,AORF,AORST
00450 NAOR=1+(AORF-AORO)/AORST
00460 AORSTR=AORST*(2.0*PI)/360.0
00470 AORFR=AORF*(2.0*PI)/360.0
00480 PRINT 20
00490 20 FORMAT(*TYPE BOR,F6.3*)
00500 READ 25,BOR
00510 25 FORMAT(F6.3)
00520 PRINT 25,BOR
00530 AZ=30.0*(2.0*PI)/360.0
00532 DO 90 K=1,NAOR
00534 AOR=(AORO+(K-1)*AORST)*(2.0*PI)/360.0
00536 FOR(K)=(SQPI/(2*BOR))*EXP(-((AOR*BOR)**2))
00538 90 CONTINUE
00540 DO 130 II=1,NG1
```

```
00450 NAOR=1+(AORF-AOR())/AORST
00460 AORSTR=AORST*(2.0*PI)/360.0
00470 AORFR=AORF*(2.0*PI)/360.0
00480 PRINT 20
00490 20 FORMAT(*TYPE BOR,F6.3*)
00500 READ 25,BOR
00510 25 FORMAT(F6.3)
00520 PRINT 25,BOR
00530 AZ=30.0*(2.0*PI)/360.0
00532 DO 90 K=1,NAOR
00534 AOR=(AORO+(K-1)*AORST)*(2.0*PI)/360.0
00536 POR(K)=(SQPI/(2*BOR))*EXP(-((AOR*BOR)**2))
00538 90 CONTINUE
00540 DO 130 II=1,NG1
00550 G1=GMM1+(II-1)*GL1
00560 DO 128 JJ=1,NG2
00570 G2=GMM2+(JJ-1)*GL2
00580 DO 126 KK=1,NW
00590 W=WMIN+(KK-1)*WEEL
00600 SUMM=0.0
00610 PORS=0.0
00620 FR=0.0
00630 DO 95 J=1,NP
00640 TTR=(TTO+(J-1)*TTST)*(2.0*PI)/360.0
00650 S=2*SIN(TTR/2)/1.542
00660 PORS=0.0
00670 FR=0.0
00674 AZD1=1.5708-ATAN((G1+G2)/W)
00716 DO 87 IN=1,NAOR
00720 AZD=(IN-1)*AORSTR
00721 AORD=AZ+AZD
00722 IF(AORD.LT.1.57)GO TO 505
00723 K=1+(PI-AORD)/AORSTR
00724 GO TO 506
00725 505 K=1+(AORD/AORSTR)
00727 506 PAZD=POR(K)
00730 B1=S*COS(AZD)
00740 B2=S*SIN(AZD)
00750 IF(B1.EQ.0)GO TO 89
00760 IF(B2.EQ.0)GO TO 89
00770 B1P=PI*B1
00775 IF(NLY.EQ.2)GO TO 86
00776 IF(AZD.LE.AZD1)GO TO 78
00777 F=(SIN(B1P*G1)/B1P)*(SIN(PI*B2*W)/(PI*B2))
00778 F=F**2
00779 GO TO 82
00780 78 F1=SIN(B1P*G1)+A*(SIN(B1P*(3*G1+2*G2))-SIN(B1P*(G1+2*G2)))
00782 GO TO 83
00784 86 F1=SIN(B1P*(2*G1+G2))
00786 83 CONTINUE
00790 F1=F1/B1P
00800 F2=SIN(PI*B2*W)/(PI*B2)
00810 F=(F1*F2)**2
00815 82 CONTINUE
00820 FF(IN)=F*PAZD
00830 PORS=PORS+PAZD
00840 IF(IN.EQ.1)GO TO 87
00850 D=ABS(FF(IN)-FF(IN-1))*(AORSTR/2.0)
00860 IF(FF(IN).GE.FF(IN-1))GO TO 88
00870 FR=FR+(FF(IN)*AORSTR+D)
00880 GO TO 87
00890 88 FR=FR+(FF(IN-1)*AORSTR+D)
00900 89 CONTINUE
00910 87 CONTINUE
00920 FFF(J)=FR/PORS
```

```
00784 86 F1=SIN(DIF*(2*G1+G2))
00786 83 CONTINUE
00790 F1=F1/DIF
00800 F2=SIN(PI*B2*W)/(PI*B2)
00810 F=(F1*F2)**2
00815 82 CONTINUE
00820 FF(IN)=F*PAZD
00830 PORS=PORS+PAZD
00840 IF(IN.EQ.1)GO TO 87
00850 D=ABS(FF(IN)-FF(IN-1))*(AORSTP/2.0)
00860 IF(FF(IN).GE.FF(IN-1))GO TO 88
00870 FR=FR+(FF(IN)*AORSTR+D)
00880 GO TO 87
00890 88 FR=FR+(FF(IN-1)*AORSTR+D)
00900 89 CONTINUE
00910 87 CONTINUE
00920 FFF(J)=FR/PORS
00930 95 CONTINUE
00940 SUMM=0.0
00950 DO 97 JK=1,NP
00960 SUMM=SUMM+FFF(JK)
00970 97 CONTINUE
00990 FN=FACT/SUMM
01000 DO 100 JK=1,NP
01010 FFF(JK)=FFF(JK)*FN
01020 100 CONTINUE
01030 DIFF=0.0
01040 DO 101 IJ=1,NP
01050 DIFF=DIFF+ABS(ZE(IJ)-FFF(IJ))/ZE(IJ)
01060 101 CONTINUE
01065 PRINT,DIFF
01070 IF(DIFF.GT.DIFFB)GO TO 303
01080 DIFFB=DIFF
01090 G1B=G1
01100 G2B=G2
01110 WB=W
01120 DO 202 IJ=1,NP
01130 ZB(IJ)=FFF(IJ)
01140 202 CONTINUE
01150 303 CONTINUE
01155 C=C+1.0
01160 126 CONTINUE
01170 128 CONTINUE
01180 130 CONTINUE
01185 PRINT,C
01186 PRINT 110,NLY
01187 110 FORMAT(*NO. OF LAYERS =*,I2)
01188 PRINT 108,A
01189 108 FORMAT(*A = *,F7.4)
01190 PRINT 109
01200 109 FORMAT(5X,*TT*,8X,*IEXP*,8X,*IFIT*)
01210 DO 350 KI=1,NP
01220 TT=TTO+(KI-1)*TTST
01230 PRINT 103,TT,ZE(KI),ZB(KI)
01240 103 FORMAT(3(F10.5,5X))
01250 350 CONTINUE
01260 PRINT 115,G1B,G2B,WB
01270 115 FORMAT(*G1B=*,F5.1,3X,*G2B=*,F5.1,3X,*WB=*,F5.1)
01275 DIFFB=DIFFB/NP
01280 PRINT 111,DIFFB
01290 111 FORMAT(*REL. ERROR = *,F10.5)
01300 STOP
01310 END
```